Infinite Elements for Elasto- and Poroelastodynamics

Zur Erlangung des akademischen Grades eines
Doktors der technischen Wissenschaften
ausgeführte Dissertation

eingereicht an der
Fakultät für Bauingenieurwissenschaften
der Technischen Universität Graz

von

Mathias Nenning

Berichter: Univ.-Prof. Dr.-Ing. Martin Schanz
Univ.-Prof. Dr.-Ing. Otto von Estorff

Graz, August 2010

Abstract

Wave propagation phenomena in unbounded domains occur in many engineering applications, e.g., soil structure interactions. The considered problem is often modeled by the theory of elasticity which is in some applications a sufficient accurate approximation. Nevertheless, the interaction of the solid- and the fluid phase attribute a time dependent character to the mechanical response of the saturated soil, which can be modeled by Biot's theory of poroelasticity. When simulating unbounded domains, infinite elements are a possible choice to describe the far field behavior, whereas the near field is described through conventional finite elements. Hence, an infinite element is presented to treat wave propagation problems in unbounded elastic and saturated porous media. Infinite elements are based on special shape functions to approximate the semi-infinite geometry as well as the Sommerfeld radiation condition, i.e., the waves decay with distance and are not reflected at infinity. To provide the wave information the infinite elements are formulated in Laplace domain. The time domain solution is obtained by using the convolution quadrature method as inverse Laplace transformation. The temporal behavior of the near field is calculated using a standard time integration scheme, i.e., the Newmark-method. Finally, the near- and far field are combined using a substructure technique in any time step. The accuracy as well as the necessity of the proposed infinite elements, when unbounded domains are considered, is demonstrated with different examples.

Zusammenfassung

In vielen Bereichen des Ingenieurwesens sind Wellenausbreitungsvorgänge zu beobachten und zu berechnen. Ein Beispiel hierfür ist die Boden-Bauwerksinteraktion bei Erdbebenanregung. Der Boden wird dabei oft linear elastisch modelliert. Dies kann jedoch nur eine erste Näherung sein, da die Interaktion mit dem Porenwasser vernachlässigt wird. Mit der poroelastischen Theorie von Biot wird dies jedoch berücksichtigt. Unendlich ausgedehnte Gebiete können durch Verwendung der Finiten Elemente Methode in Kombination mit so genannten infiniten Elementen modelliert werden. Dabei werden finite Elemente dazu verwendet um das Verhalten des Nahfeldes und infinite Elemente um das Verhalten des Fernfeldes zu modellieren. Entsprechend befaßt sich diese Arbeit mit der Formulierung eines infiniten Elements, um die Wellenausbreitung in elastischen- bzw. poroelastischen Gebieten unendlicher Ausdehnung zu untersuchen. Die infiniten Elemente besitzen spezielle Ansatzfunktionen um die Sommerfeldsche Abstrahlbedingung zu approximieren. Im wesentlichen muss modelliert werden, dass Wellen ins Unendliche auslaufen und nicht reflektiert werden. Dies kann im Laplacebereich durch Exponentialfunktionen geschehen. Deswegen wird im Fernfeld die Faltungsquadraturmethode zur Zeitdiskretisierung herangezogen und im Nahfeld das Newmark Zeitintegrationsverfahren. Das Nah- und Fernfeld werden unter Verwendung einer Substrukturtechnik gekoppelt, um das zeitliche Verhalten des gesamten Gebietes zu erhalten. Die Arbeitsweise der infiniten Elemente wird an Beispielen aufgezeigt. Dabei wird deutlich, dass eine Berechnung ohne infinite Elemente zu falschen Ergebnissen führt. Die vorgestellten infiniten Elemente erweisen sich als effektiv.

CONTENTS

Notation

Throughout this thesis the indical notation is used. The summation convention is applied over repeated indices and Latin indices receive the values 1, 2 and 1, 2, 3 in two-dimensions $(2d)$ and three-dimensions $(3d)$, respectively. Sometimes the summation over repeated indices is explicitly stated for a better understanding. Commas $()_{,i}$ denote spatial derivatives and dots $\dot{()}$ denote the time derivative.

As long as no other meaning is explicitly given to a certain quantity within the text, its meaning corresponds to the following notation list.

General symbols

$[a,b]$	Closed interval a,b
(a,b)	Open interval a,b
$(a,b]$, $[a,b)$	Half open intervals a,b
$a,b,\ldots,\alpha,\beta,\ldots$	Scalar values
$\mathbf{a},\mathbf{b},\ldots$	Vectors
δ_{ij}	Kronecker symbol
ε_{ijk}	Permutation symbol
s	Complex Laplace parameter, $\mathrm{s} \in \mathbb{C} :\ \mathrm{Re}(\mathrm{s}) > 0$
$\mathscr{L}\{f(t)\}, \hat{f}(\mathrm{s})$	Laplace transform of $f(t)$
g	Real or complex valued function
$f_{,i}$	Gradient of f
$f_{i,i}$	Divergence of f_i
$f_{i,j}$	Gradient of f_i
$()_{,i}$	partial derivative with respect to x_i
$\dot{()}$	time derivative
$\mathbf{A}$	Second order tensor $[A_{ij}]_{1\leq i,j\leq 3}$
$\mathbf{a}\cdot\mathbf{b}, \langle\mathbf{a},\mathbf{b}\rangle$	Scalar product $\mathbf{a}\cdot\mathbf{b} = \langle\mathbf{a},\mathbf{b}\rangle := \sum_{i=1}^{3} a_i b_i$
$\mathbf{a}\otimes\mathbf{b}$	Outer product $[a_i b_j]_{1\leq i,j\leq 3}$
$\mathbf{a}\times\mathbf{b}$	Vector product $\mathbf{a}\times\mathbf{b} := \sum_{i=1}^{3} \varepsilon_{ijk} a_j b_k$
$\mathbf{A} : \mathbf{B}$	Double contraction, double dot product
$\mathrm{Ei}(z)$	Exponential integral of z
$\mathrm{H}(t)$	Heaviside step function, $\mathrm{H}(t) = 0, t < 0$; $\mathrm{H}(t) = 1, t > 0$

Special symbols

x_i	Location
c, c_P, c_S, c_R	Wave velocity, compressional wave velocity, shear wave velocity, velocity of Rayleigh wave
c_1, c_2	Poroelastic fast compressional wave velocity, poroelastic slow compressional wave velocity
k	wave number
t	Time
ε_{ii}	Volume dilatation
K	Bulk modulus
ε_{ij}	Linear strain tensor
ω_{ij}	Linear rotation tensor
σ_{ij}	Cauchy stress tensor
$C_{ijk\ell}$	Fourth order elasticity tensor
E	Young's modulus
ν	Poisson's ratio
n_i	Normal vector
ϕ	Porosity of the solid skeleton of porous media
V^s, V^f, V	Volume of the solid phase, fluid phase, and bulk material
$\varepsilon^s_{ij}, \varepsilon^f_{ij}$	Strain tensor of the solid skeleton and the fluid
u_i, u^f_i	Solid and fluid displacement
w_i	relative displacement of the fluid phase to the solid skeleton
p	Pore pressure of the interstitial fluid of porous material
$\sigma^s_{ij}, \sigma^f_{ij}$	Stress tensor of the solid and fluid phase
$\sigma^{\text{tot}}_{ij}, \sigma^{\text{eff}}_{ij}$	Total and effective stress tensor of porous media
K^f, K^s, K	Compression modulus of the fluid, solid grains, and bulk material
G	Shear modulus
α	Biot's effective stress coefficient
ζ	Variation of fluid volume per unit reference volume
q_i	Specific flux
ϱ_a	Biot's apparent mass density
κ	Permeability
Tr	Boundary trace operator
Ω	d-dimensional domain Ω $(d = 1, 2, 3)$
Γ	Boundary of domain Ω
$\overline{\Omega}$	Closed domain Ω $(\overline{\Omega} = \Gamma \cup \Omega)$
Γ_{D}	Boundary with prescribed Dirichlet data
Γ_{N}	Boundary with prescribed Neumann data
$\mathcal{V}$	Space of possible solutions of the boundary value problem
$\mathcal{V}_g$	Functions of $\mathcal{V}$ fulfilling Neumann boundary conditions

$\mathcal{V}_0$	Functions of $\mathcal{V}$ which are zero on the Dirichlet boundary
$\mathcal{V}^h$	Set of all finite element shape functions and their linear combination
$\mathcal{V}_g^h$	Functions of $\mathcal{V}^h$ fulfilling Neumann boundary conditions
$\mathcal{V}_0^h$	Functions of $\mathcal{V}^h$ which are zero on the Dirichlet boundary
τ_e	Finite element
$\widehat{\tau}$	Reference element
$\overline{\Omega}_h$	Triangulation of Ω
E_N	Total number of finite elements in $\overline{\Omega}_h$
e_N	Set containing all finite elements
$\tilde{\varphi}$	Global defined shape function
$\varphi, \vartheta, \psi, S$	Local shape function defined on $\widehat{\tau}$
m	Mapping function defined on $\widehat{\tau}$
$\bar{n}_h$	Set containing all nodes of $\overline{\Omega}_h$
n_h	Set containing all nodes of $\Omega \cup \Gamma_{\mathsf{N}}$
n_D	Set containing all nodes of Γ_{D}
$\bar{N}_h$	Number of nodes in $\overline{\Omega}_h$
N_h	Number of nodes in $\Omega_h \cup \Gamma_{\mathsf{N}}^h$
$\widehat{n}_e$	Set containing all nodes of $\widehat{\tau}$
$\widehat{N}_e$	Nodes of $\widehat{\tau}$
$\mathbf{J}_e$	Jacobi matrix of τ_e
Γ_{D}^h	Discrete boundary of Γ_{D}
Γ_{N}^h	Discrete boundary of Γ_{N}
Υ_b	Finite element on the boundary Γ_{N}^h (e.g. edge in two dimensions)
$B_{\Gamma^h}^{\mathsf{N}}$	Set of finite elements Υ_b living on the boundary Γ_{N}^h
$\widehat{\Upsilon}$	Reference element in relation to Υ_b
$\widehat{n}_b$	Set containing all nodes of $\widehat{\Upsilon}$
$\widehat{N}_b$	Nodes of $\widehat{\Upsilon}$
φ_Γ	Shape function defined on $\widehat{\Upsilon}$
m_Γ	Mapping function defined on $\widehat{\Upsilon}$
N_G	Number of quadrature points
$\overline{a}$	Characteristic length of infinite element
r	Radial distance measure of infinite element
$\mu(\xi_3)$	Phase term
$D(\xi_3)$	Radial weight
n_B	Set containing all nodes on the base face of the infinite element
n_B^P	Number of nodes on the base face of the infinite element
n_S	Set containing all source points of the infinite element
n_M	Set containing all mapping points of the infinite element

1 INTRODUCTION

The numerical treatment of unbounded domains is of considerable interest in many engineering applications, e.g., soil structure analysis, earthquake-, or geotechnical engineering. Numerical approximation methods have to be used since the partial differential equations describing the physical problem are only solvable for special cases. Especially, the fast growing computer technology of the past have encouraged the use and development of such numerical approximation schemes.

The most versatile and developed numerical approximation scheme is the Finite Element Method (FEM). The FEM is applicable to various kinds of engineering problems, which can be highly non-linear or exhibit inhomogeneous material behavior, e.g., the FEM has been utilized to linear- and non-linear problems as well as to isotropic and anisotropic problems in elastostatics and elastodynamics. The standard FEM yields sparse populated matrices which are often symmetric and, therefore, many efficient solutions procedures have been developed. Nevertheless, the finite element method is restricted to bounded problems.

The use of so-called infinite elements in combination with the finite element method is a possible choice for the investigation of unbounded domains. An infinite element is simply an element which attempts to represent the behavior of the solution in the unbounded domain. Thus, the unbounded domain is decomposed into a near field, where the spatial discretization is performed using conventional finite elements and into a far field, which is spatially discretized with infinite elements. Infinite elements can be easily coupled (nodes of the finite and infinite elements match each other at their interface) to finite elements and retain the banded structure of the matrices. Due to the fact that the near field is discretized with standard finite elements the application to, e.g., non-linear problems can be still accomplished. However, various other numerical methods for unbounded domains exist.

One common choice for the numerical treatment of unbounded domains is the Boundary Element Method (BEM). The BEM makes use of so-called fundamental solutions, which are analytical solutions of the governing differential equations due to a point source within an unbounded domain. The fact that the fundamental solution is exact brings in the advantage of improved accuracy. Moreover, the fundamental solutions automatically fulfills the Sommerfeld radiation condition, whereas other approximation methods only can try to approximate it. Especially for wave propagation problems the boundary element method is more accurate as the finite element method, as it represents the solution of the wave equation within the domain exactly. Another advantage of the boundary element method

is that only a spatial discretization of the surface of the considered domain has to be performed. Especially when a spatial discretization of a complex three-dimensional geometry is needed the finite element approach may lead to a tedious task, whereas the spatial discretization of the surface can be conducted more easily. On the other hand, singularities are present when using the boundary element method, which need special attention during the numerical integration. Nevertheless, the BEM is restricted to liner differential equations since the fundamental solutions for non-linear problems are generally not attainable. A common approach to overcome this restriction is the coupling of BEM with FEM, although special care has to be taken regarding the stability of the resulting equations system. The latest development of a coupled finite element scheme with the boundary element method can be found in the work of Rüberg [118] for the case of an elastic material. Compared to the classical finite element method the boundary element method in it's original formulation requires more computational effort. Here, it must be mentioned that the so-called fast boundary element methods have made great advance in the recent past and, thus, got competitive to the finite element method. The book of Rjasanow and Steinbach [117] gives an insight into these fast boundary element methods. A good overview of the classical boundary element method for the application to elastic problems is given in the book of Gaul et al. [73], which also reveals a historical development of the method. The BEM for the poroelastic case is elaborated by Schanz [123].

Another approach to approximate unbounded domains is the use of so called artificial or absorbing boundary conditions (ABC). This method introduces an artificial boundary, which deceives the solution that it actually extends to infinity. These artificial boundary conditions are then applied to the boundary of the standard finite element method. It is not trivial to find proper choices of such boundary conditions for various wave problems, since the artificial boundary condition has to represent the unbounded domain in an appropriate manner. In the context of wave propagation problems, an artificial boundary condition is also called a *Non-Reflecting Boundary Condition (NRBC)*. Artificial Boundary Conditions for the dynamic analysis of poroelastic media can be found, for instance, in [2, 3]. Time-domain analysis of dam-reservoir-foundation-systems using Absorbing Boundaries were investigated by Feltrin [71].

The unbounded domain can also be represented by using an absorbing boundary layer. This special layer is attached to the conventional finite element mesh. When a traveling wave enters the absorbing layer it is attenuated and, therefore, its amplitude decreases. Nevertheless, the thickness of the boundary layer as well as the absorbing properties remain to be chosen in such a way that the waves are sufficiently absorbed. This characteristic yields the denotation *Perfectly Matched Layer*, or *PML*, for the absorbing layer. The application of perfectly matched layers to transient and time-harmonic elastodynamics is discussed, e.g., by Basu [19] and Basu and Chopra [20, 21]. The use of perfectly matched layers in poroelastodynamics is treated by Zeng et al. [151].

In this work, the approach of using infinite elements in combination with conventional

finite elements will be used. Hence, an infinite element will be developed to represent an elastic as well as a poroelastic unbounded domain in an appropriate manner. Although, the approach of the infinite element is rather simple, as will be seen in the ongoing, the numerical results are sufficiently accurate.

1.1 State of the art

First publications on infinite elements were the thesis of Ungless [140] and the paper of Zienkiewicz and Bettess [157]. There exist mainly two different types of infinite elements. First, the use of a *decay function* together with a shape function which causes the field quantity to approach the sought value at infinity, while the finite size of the infinite element is retained. Second, conventional shape function are used to describe the variation of the field quantity, while the geometry is mapped from a finite to an infinite domain. Using the latter, brings in the advantage that the application of standard integration formulas is possible, e.g., standard Gauß integration [161]. Mapped infinite elements perform well for the static case in elastic media [161]. Such mapped infinite elements were also applied successfully to quasi-static materially nonlinear problems [99]. The application of infinite elements to wave propagation problems makes it necessary to include outwardly propagating wave-like factors in their formulation. This concept was originally proposed by Bettess and Zienkiewicz [33]. For acoustic media a wide variety of formulations exists and are well developed. A comprehensive overview for the acoustic case is given by Astley [10]. Whereas in the acoustic case only one traveling wave is present, in a homogeneous elastic half space there are actually three distinct waves, in particular compressional-, shear-, and Rayleigh waves [79]. These waves travel with three different wave speeds. The simplest approach is to include the characteristic of only one wave within the infinite element formulation. Depending on the spatial location of the infinite element, the dominant wave is incorporated into the infinite element formulation, e.g., see [148]. Moreover, an exponential decay of the field quantity is often assumed, instead of the correct asymptotic decay in three dimensions of $1/r$ (r is the distance measure to the applied load) [148, 154]. Infinite elements, capable of simulating all three wave types in the time harmonic case are developed by Zhao and Valliappan [152] and Yun et al. [150], but they also assume an exponential decay of the solution. Medina and Penzien [100] proposed an interesting infinite element for time harmonic applications, considering all three wave types. They perform very well but the evaluation of the shape functions turned out to be extremely tedious and they also assume an exponential decay of the field quantity.

Whereas the development of infinite elements for elastodynamic problems is well established the application of appropriate infinite elements to poroelastic issues is rather small. An infinite element formulation for wave propagation problems in one-dimensional poroelastic material has been accomplished by Khalili et al. [86]. Later they extended their work

to the two-dimensional case [87]. Their work covers time harmonic problems and the infinite element formulation considers the occurrence of the two compressional waves only.

Of course, the application of infinite elements is widespread and applied to many different fields of engineering. Here are some examples in compressed form such as consolidation [129], mass transport [153], electromagnetics [68], heat transfer [137], ground freezing [9], fluid-structure interaction [33, 162], and soil-structure interaction [52, 53, 100, 101, 111, 148, 150].

1.2 Overview

In *chapter 2*, the governing equations of linear elastodynamics and poroelastodynamics are shortly recalled. The porous material is modeled by Biot's theory. Additionally, the dynamic versions of the governing equations are condensed to their static and quasi-static counterparts of the elastic and poroelastic material, respectively. Concerning the poroelastic material, different formulations by means of different numbers of degrees of freedom will be discussed. Moreover, the wave speeds of plane body waves in infinite elastic and poroelastic materials will be derived. This section will be closed with a short overview of numerical approximation schemes for unbounded domains.

Chapter 3 is devoted to finite element formulations of the governing equations presented in chapter 2. Especially, for the poroelastic material different approaches of the numerical approximation will be discussed. The spatial discretization is performed using the standard finite element method. Then, the temporal discretization with respect to the Newmark method and the convolution quadrature method is presented.

The main scope of this work, the application of infinite elements to unbounded problems in elasto- and poroelastodynamics, is treated in *chapter 4*. The shape functions of the infinite elements are defined in Laplace domain to provide the wave-like behavior, which is approximated by exponential functions. To evaluate the occurring integrals, containing these exponential functions, in the variational formulation a special quadrature rule will be presented. The time domain solution of the far field is calculated with the convolution quadrature method. As mentioned before, the temporal behavior of the near field is treated by the Newmark-method. In order to obtain the time domain solution of the whole domain, a substructure technique will be presented which yields the time domain solution of the near- and far field. Beside these developments for dynamic problems the static solution is obtained as side effect.

The validation of the proposed infinite elements will be conducted in *chapter 5*. Here, the solution of the proposed approximation scheme will be compared to either analytical or semi-analytical solutions or to solutions obtained by the boundary element method.

The thesis will be concluded with a short summary in *chapter 6*, which is followed by an brief outlook on possible future work in this topic.

2 WAVE EQUATIONS FOR ELASTODYNAMICS AND POROELASTODYNAMICS

2.1 Linear elastodynamics

In the following, the basic equations of dynamic elasticity are summarized. A more detailed illustration can be found, e.g., in the textbooks of Becker and Gross [24], Sommerfeld [132], and Altenbach and Altenbach [5]. If the main focus is on the topic of wave propagation the books of Graff [79] and Achenbach [1] give a detailed description. The presentation of the governing equation here follows the textbooks of Gaul et al. [73] and Becker and Gross [24].

2.1.1 Governing equations

To obtain the governing equation of elastodynamics the *kinematic relations*, the *balance* or *conservation laws* and the *constitutive equations* have to be formulated.

To describe the deformation of a continuum, the displacement field $u_i = u_i(\mathbf{x},t)$ at any point $\mathbf{x}$ and time t is introduced. The linear strain tensor ε_{ij} within the elastic continuum is given by

$$\varepsilon_{ij} = \frac{1}{2}\left(u_{i,j} + u_{j,i}\right) \ . \tag{2.1}$$

From the above equation (2.1), it is obvious that the linear strain tensor ε_{ij} is symmetric $\varepsilon_{ij} = \varepsilon_{ji}$. The strain tensor ε_{ij} is the symmetric part of the deformation gradient $u_{i,j}$, which is defined by

$$\begin{aligned} u_{i,j} &= \frac{1}{2}\left(u_{i,j} + u_{j,i}\right) + \frac{1}{2}\left(u_{i,j} - u_{j,i}\right) \\ &= \qquad \varepsilon_{ij} \qquad + \qquad \omega_{ij} \ , \end{aligned}$$

where ω_{ij} represents the rotation tensor. Since ω_{ij} represent just a rigid body rotation of the elastic solid, no stresses are generated. The rotation tensor ω_{ij} therefore represents a rigid body translation. For this reason only the strain tensor is of interest in the law of elasticity.

The stress-strain relation is given by the constitutive equation. In the case of a homogeneous elastic material this relation is given for any point in the elastic material by

$$\sigma_{ij} = C_{ijk\ell}\varepsilon_{k\ell} \ , \tag{2.2}$$

where $C_{ijk\ell}$ is the *fourth order elasticity tensor* and σ_{ij} is the *second order stress tensor*. Since elastic behavior is assumed, the elasticity tensor $C_{ijk\ell}$ is independent of the time t. For an *isotropic* material, the mechanical response is independent of the direction of stress loading and, furthermore, the elasticity tensor consists only on two independent components and offers several symmetries [24], i.e.

$$C_{ijk\ell} = C_{jik\ell} = C_{ik\ell k} \ . \tag{2.3}$$

Thus, using the symmetric properties of the material tensor (2.3) with the linear geometry relation (2.1) yields the stress tensor

$$\sigma_{ij} = C_{ijk\ell}\varepsilon_{k\ell} = C_{ijk\ell}\frac{1}{2}(u_{k,\ell} + u_{\ell,k}) = \frac{1}{2}(C_{ijk\ell}u_{k,\ell} + C_{ij\ell k}u_{k,\ell}) = C_{ijk\ell}u_{k,\ell} \ . \tag{2.4}$$

The elasticity tensor for isotropic material may also be expressed as

$$C_{ijk\ell} = \left(K - \frac{2}{3}G\right)\delta_{ij}\delta_{k\ell} + G\left(\delta_{ik}\delta_{j\ell} + \delta_{i\ell}\delta_{jk}\right) \ , \tag{2.5}$$

where K and G are the compression- and shear modulus. These two quantities can also be expressed in terms of the well known Young's modulus E and the Poisson's ratio ν [24]

$$K = \frac{E}{3(1-2\nu)} \qquad G = \frac{E}{2(1+\nu)}$$
$$E = \frac{9KG}{3K+G} \qquad \nu = \frac{3K-2G}{6K+2G} \ .$$

Inserting (2.5) into (2.2) leads to

$$\sigma_{ij} = \left(K - \frac{2}{3}G\right)u_{k,k}\delta_{ij} + G(u_{i,j} + u_{j,i}) \tag{2.6}$$

the stress tensor in dependence of the material parameters K and G. To complete the set of governing equations, the *equation of motion* has to be formulated. The balance of momentum yields *Cauchy's equation of motion*

$$\sigma_{ij,j} + f_i = \varrho\ddot{u}_i \ , \tag{2.7}$$

with the body forces f_i and the uniformly distributed mass density ϱ. The notation $\dot{()}$ denotes the first time derivative and, consequently, $\ddot{()}$ the second time derivative. Taking the divergence of (2.6) and inserting it in (2.7) yields the equation of motion in the form

$$(K + \frac{1}{3}G)u_{j,ji} + Gu_{i,jj} + f_i = \varrho\ddot{u}_i \ . \tag{2.8}$$

The Laplace transform $\hat{f}(\mathrm{s}) = \mathscr{L}\{f(t)\}$ of equation (2.8), when vanishing initial boundary conditions are assumed, i.e., $u_i(0) = 0$ and $\dot{u}_i(0) = 0$, is given by

$$(K + \frac{1}{3}G)\hat{u}_{j,ji} + G\hat{u}_{i,jj} + f_i = \mathrm{s}^2 \varrho \hat{u}_i \ , \tag{2.9}$$

with the complex Laplace parameter s.

2.1.2 Plane body waves in elastic material

In this section, the occurrence of plane body waves in unbounded elastic materials will be investigated. The main steps follow the procedures as shown in the books of Graff [79] and Achenbach [1]. Consider a plane wave expressed by

$$u_i = A_i \, \mathrm{f}(n_k x_k - ct) \ , \tag{2.10}$$

where A_i gives the particle displacement of the wave, n_k is the wave normal unit vector, and x_k denotes the position vector. Thus, equation (2.10) represents a plane wave whose planes of constant phase are traveling with wave velocity c normal to n_k. Since the material is of isotropic nature the wave velocity c is independent of the direction. A plane wave in Laplace domain may be expressed by

$$\hat{u}_i = A_i \, \mathrm{e}^{-\frac{\mathrm{s}}{c} n_k x_k} \ .$$

Inserting equation (2.10) into the elastic equation of motion (2.8) yields, when body forces are neglected

$$(K + \frac{1}{3}G)A_j n_j n_i \, \mathrm{f}'' + GA_i n_j n_j \, \mathrm{f}'' - A_i \varrho c^2 \, \mathrm{f}'' = 0 \ , \tag{2.11}$$

where the prime, i.e., $()'$, denotes the spatial derivative. Since $n_j n_j = 1$, equation (2.11) reduces to

$$(K + \frac{1}{3}G)A_j n_j n_i + (G - \varrho c^2)A_i = 0 \ , \tag{2.12}$$

which can only be satisfied if the particle displacement is orthogonal to the wave front $A_i n_i = 0$ or the particle displacement is in direction of the wave front $n_i = {}^{A}/_{A_i}$ [1]. The latter simplifies (2.12) to

$$\big((K + \frac{4}{3}G) - \varrho c^2)A_i = 0 \ ,$$

which yields the *compressional (longitudinal)* wave speed

$$c_P = \sqrt{\frac{K + \frac{4}{3}G}{\varrho}} \ . \tag{2.13}$$

For this case, the rotation vanishes, i.e., $\nabla \times u_i = \mathbf{0}$ ($\varepsilon_{ijk}\partial u_j/\partial x_i \mathbf{e}_k = \mathbf{0}$), and, therefore, this type of wave is also called *irrotational wave*. Former solution, i.e., $A_i n_i = 0$, shortens (2.12) to

$$(G - \varrho c^2) A_i = 0 \,,$$

yielding the *shear (transverse)* wave speed

$$c_S = \sqrt{\frac{G}{\rho}} \,. \tag{2.14}$$

Since, here, the divergence of the displacement vector vanishes, i.e., $\nabla \cdot u_i = 0$ ($u_{i,i} = 0$), this type of wave is also called *rotational wave*. From equations (2.13) and (2.14) follows that

$$\frac{c_P}{c_S} = \sqrt{\frac{(K + \frac{4}{3}G)}{G}} = \sqrt{\frac{2(1-\nu)}{1-2\nu}} > 1 \qquad \forall \nu \in [-1, \tfrac{1}{2}) \,, \tag{2.15}$$

i.e., the compressional wave is always faster than the shear wave. Note that in (2.15) also negative Poisson ratios are considered. Materials and structures with negative Poisson's ratio can be manufactured and such materials are also an actual field of research, e.g. [94].

Rayleigh surface wave

Lord Rayleigh [113] first investigated surface waves and found the properties that their effects decreases rapidly with depth and that their velocity of propagation is smaller than that of the body waves. The speed of the so called *Rayleigh wave* can be approximated by

$$\frac{c_R}{c_S} = \frac{0.87 + 1.12\nu}{1 + \nu} \,. \tag{2.16}$$

The wave propagation velocities in elastic material are independent on the frequency [79]. This is obvious when taking a closer look at the definitions of the wave speeds of the compressional- and shear wave in equations (2.13) and (2.14), respectively, which are frequency independent. Consequently, the approximation of the Rayleigh wave speed (2.16) indicates that also this wave speed is frequency independent.

2.2 Linear poroelastodynamics - Biot's theory

The behavior of fluid infiltrated materials, such as water saturated soils, oil impregnated rocks or air filled foams is of interest in many branches of science. In order to describe the behavior of fluid saturated materials, their two-phasic character has to be considered. A common way is to describe it on the macroscopic level. This means that all quantities of the microscopic level are smeared out on the basis of an averaging process as it is shown for example in the book of de Boer [58]. The homogenization process for saturated porous media is given by Bonnet and Auriault [39] and Auriault et al. [14].

One possibility to model such materials is given by the *Theory of Porous Media (TPM)*, which is based on the theory of mixtures and derived from the well known methods of continuum mechanics. The TPM in its current understanding is based on the publications by Bowen [41, 42] and was improved and developed continuously in the last years by de Boer and Ehlers [59] and Ehlers [66, 67]. A comprehensive survey of the historical development of the TPM is given in the book of de Boer [58].

Another theory for porous media was developed by Biot [34] for linear, isotropic poroelastic media containing a viscous fluid. In Biot's theory (BT), which is based on the work of von Terzaghi [142], a fully saturated material is assumed. This work was extended later by Biot to the anisotropic case [35]. Wave propagation phenomena were investigated by Biot in two papers, one for the low frequency range [37] and one for the high frequency range [36]. In a porous medium different kinds of body waves occur, two compressional waves and one shear wave. The first compressional wave is called the *fast*, whereas the second one is called the *slow* wave. The most important characteristic of the slow wave is that it is higly attenuated. The validity of Biot's model and the experimental observation of the *slow wave* have been confirmed by Plona [110], Brown et al. [47], and Berryman [30]. A comparative study of Biot's theory and the TPM was published by Schanz and Diebels [125]. They observed that for incompressible constituents, and some other restrictions, Biot's theory and the TPM lead to the same governing equations. This is not the case when compressible constituents are considered. For a more detailed illustration of the differences of these two models the interested reader is referred to [125].

The *Simple Mixture Model* of Wilmanski [144], deduced by taking into account thermodynamical fundamental laws, is also capable to model porous material. Compared to the model of Biot, the Simple Mixture Model neglects some effects. A detailed comparison of these two methods is given by Wilmanski [145].

Although Biot's theory is more based on physical intuition, it has the widest acceptance in geophysics and geomechanics. Within this chapter, the governing equations of Biot's theory for poroelastic materials are given briefly, which are used for numerical studies in this thesis.

Considering a fully saturated porous media in terms of Biot's theory [37], the porosity of the solid skeleton is defined by

$$\phi = \frac{V^f}{V} \ ,$$

where V^f is the volume of interconnected pores and V is the Volume of the porous material given by $V = V^f + V^s$, with V^s denoting the volume of the solid skeleton. The porous medium is assumed to be statistically isotropic and homogenous in such a way that for all cross sections the same porosity ϕ is obtained. Superscript $()^s$ and $()^f$ denote solid and fluid constituents, respectively. The strain tensor of the elastic isotropic solid skeleton is given through, by assuming small strains,

$$\varepsilon^s_{ij} = \frac{1}{2}\left(u_{i,j} + u_{j,i}\right) \ ,$$

where u_i denotes the solid displacement.

2.2.1 Constitutive equations

The partial stress of the solid and the fluid phase using a Lagrangian description is given by Biot [35]

$$\begin{aligned} \sigma^s_{ij} &= 2G\varepsilon^s_{ij} + \left(K - \frac{2}{3}G + \frac{Q^2}{R}\right)\varepsilon^s_{kk}\delta_{ij} + Q\varepsilon^f_{kk}\delta_{ij} \\ \sigma^f_{ij} &= -\phi p\delta_{ij} = \left(Q\varepsilon^s_{kk} + R\varepsilon^f_{kk}\right)\delta_{ij} \ , \end{aligned} \tag{2.17a}$$

where G is the shear modulus and K the compression modulus of the solid skeleton. The parameters Q and R describe the coupling between the solid and the fluid phase and can be expressed, following the work of Detournay and Cheng [60], as

$$R = \frac{\phi^2 K^f (K^s)^2}{K^f\left(K^s - K\right) + \phi K^s\left(K^s - K^f\right)} \qquad Q = \frac{\phi(\alpha - \phi) K^f (K^s)^2}{K^f\left(K^s - K\right) + \phi K^s\left(K^s - K^f\right)} \ .$$

The sign convention of stresses and strains follow that of elasticity, namely tensile stress and strains are denoted positive. The pore pressure p, therefore, causes a negative stress in the fluid. Biot used in his earlier work [34] an alternative representation of equations (2.17), namely the total stress $\sigma^{\text{tot}}_{ij} = \sigma^s_{ij} + \sigma^f_{ij}$,

$$\sigma^{\text{tot}}_{ij} = 2G\varepsilon^s_{ij} + \left(K - \frac{2}{3}G\right)\varepsilon^s_{kk}\delta_{ij} - \alpha\delta_{ij}p \ , \tag{2.18}$$

where α denotes Biot's effective stress coefficient. Equation (2.18) indicates that the pore pressure in an isotropic porous material only influences the normal stresses, not the shear

stresses. Without the pore pressure p, equation (2.18) degenerates to the classical relation for an elastic homogenous material and may be, therefore, rewritten by introducing the effective stress acting on the solid skeleton

$$\sigma_{ij}^{\text{tot}} = \sigma_{ij}^{\text{eff}} - \alpha \delta_{ij} p \ . \tag{2.19}$$

The effective stress tensor σ_{ij}^{eff} may be also written in a more general form as

$$\sigma_{ij}^{\text{eff}} = C_{ijk\ell} \varepsilon_{k\ell}^{s} \tag{2.20}$$

with the symmetric isotropic linear elasticity tensor $C_{ijk\ell}$. Biot's effective stress coefficient is defined by [107]

$$\alpha = 1 - \frac{K}{K^s} \ .$$

Furthermore, the mass conservation law applied to the fluid flow is used to describe the porous material. The variation of fluid volume per unit reference volume ζ is introduced

$$\zeta = \alpha u_{i,i} + \frac{\phi^2}{R} p$$

or represented as time derivative

$$\dot{\zeta} = \alpha \dot{u}_{i,i} + \frac{\phi^2}{R} \dot{p} \ . \tag{2.21}$$

The first term of the right-hand side of equation (2.21) describes the additional storage caused by the expansion of the solid skeleton and the second term denotes a storage due to the compressibility of the solid grains and fluid [158]. The variation of the fluid volume is defined by the mass balance, here, given through the continuity equation

$$\dot{\zeta} + q_{i,i} = 0 \ , \tag{2.22}$$

with the specific flux $q_i = \phi(\dot{u}_i^f - \dot{u}_i) = \dot{w}_i$. Here, the variable $w_i = \phi(u_i^f - u_i)$ is introduced, denoting the relative displacement [158] of the fluid phase relative to the solid skeleton. Hence, the time derivative $\dot{w}_i$ is the average relative velocity of seepage measured over the total area. The term ζ could be interpreted as a motion of the fluid caused by the strain of the solid skeleton. The divergence of the flux may be written as

$$\dot{w}_{i,i} + \alpha \dot{u}_{i,i} + \frac{\phi^2}{R} \dot{p} = 0 \ , \tag{2.23}$$

obtained by inserting equation (2.21) into (2.22).

2.2.2 Balances of momentum

In the preceding section, the constitutive and kinematic relations of the porous material are given. To complete the set of needed equations the balances of momentum have to be formulated. Following Biot's approach the balances of momentum of the solid skeleton and the fluid are given by

$$\sigma^s_{ij,j} + (1-\phi)\, f^s_i = (1-\phi)\, \varrho_s \ddot{u}_i - \frac{\varrho_a}{\phi}\ddot{w}_i - \frac{\phi}{\kappa}\dot{w}_i \,, \tag{2.24a}$$

$$\sigma^f_{ij,j} + \phi f^f_i = \phi\, \varrho_f \ddot{u}_i + \left(\varrho_f + \frac{\varrho_a}{\phi}\right)\ddot{w}_i + \frac{\phi}{\kappa}\dot{w}_i \,, \tag{2.24b}$$

respectively. In the above equations (2.24), the body forces for the solid skeleton f^s_i and the fluid f^f_i per unit mass (generally gravity) are introduced. The density of the bulk material, the solid skeleton and the fluid are defined by ϱ, ϱ_s, and ϱ_f, respectively. The relation between the bulk density and the densities of the different constituents is defined by

$$\varrho = (1-\phi)\, \varrho_s + \phi\, \varrho_f \,.$$

The additional mass term, the *apparent mass density* ϱ_a, in equations (2.24) is introduced by Biot [37] to describe to dynamic interaction between the solid skeleton and the fluid. The apparent mass density can be written as $\varrho_a = C\phi\, \varrho_f$, where the factor C is a parameter depending on the geometry of the pores (tortuosity) and the frequency of excitation. Bonnet and Auriault [39] presented some measurements for the factor C for low frequencies. For a sphere of glass beds $C = 0.66$ is evaluated and will be assumed in this thesis. The permeability κ is assumed to be isotropic and frequency independent. For the high frequency range, for example, Johnson et al. [83], Biot [36], and Auriault et al. [14] suggest to use a frequency dependent permeability. However, a time domain representation of the governing equations just allows for a frequency independent model of the permeability. Since in this thesis a direct time domain solution is aimed at, a constant permeability will be used throughout this thesis. The balance of momentum can be also stated for the total solid-fluid mixture

$$\sigma^{\mathrm{tot}}_{ij,j} + F_i = \varrho \ddot{u}_i + \varrho_f \ddot{w}_i \,, \tag{2.25}$$

with $F_i = (1-\phi)\, f^s_i + \phi\, f^f_i$. For the pore fluid, the equation of motion is already given in equation (2.24b) and can be rewritten as

$$q_i = -\kappa \left(p_{,i} + \frac{1}{\phi^2}\left(\phi\, \varrho_f + \varrho_a\right)\ddot{w}_i + \varrho_f \ddot{u}_i - f^f_i \right) \,, \tag{2.26}$$

which can also be expressed, after rearranging equation (2.26) and solving for the fluid pressure p, as

$$p_{,i} + \frac{1}{\phi^2}\left(\phi\, \varrho_f + \varrho_a\right)\ddot{w}_i + \rho_f \ddot{u}_i + \frac{1}{\kappa}\dot{w}_i = f^f_i \,. \tag{2.27}$$

The above equations (2.26) and (2.27) are also well known as the dynamic version of *Darcy's law*.

Thus, the poroelastic material is described through the solid displacement u_i, the pore pressure, and the relative displacement w_i as primary unknowns. The full form (u_i, p, w_i) can be applied to saturated porous media filled with compressible or incompressible fluid [158]. Instead of using the relative displacement w_i as unknown, also the fluid displacement u_i^f can be chosen as primary variable [158].

2.2.3 Elimination of the pore pressure

Is the fluid of the porous medium assumed compressible, i.e., $R \neq \infty$, the pore pressure can be eliminated [158]. Thus, from equation (2.23) the pore pressure can be expressed, after integrating over time, as

$$p = -\frac{R}{\phi^2}\left(w_{i,i} + \alpha u_{i,i}\right) \tag{2.28}$$

and can be substituted into the balances of momentum. When a weak variational form of this irreducible form is sought, this is done best by directly inserting the pore pressure into the variational forms of (2.25) and (2.27), i.e., the pore pressure is inserted into (3.30) and (3.32).

If the fluid is assumed incompressible then the full form has to be used (u_i, p, w_i) or a penalty formulation has to be accomplished as proposed by Zienkiewicz and Shiomi [158]. Thus, the system become irreducible and the remaining variables are the solid displacement u_i and the relative displacement w_i.

2.2.4 Elimination of the relative displacement in time domain

The elimination of the relative displacement w_i in time domain is possible if inertia terms in the equation of motion (2.25) are neglected. This can be done with confidence for quasi-static, slow motion phenomena, which are typical for the consolidation behavior of soil. This approach can be found, e.g., in the book of Lewis and Schrefler [95].

For medium speed phenomena Zienkiewicz et al. [160] and Zienkiewicz [156] proposed only to neglect inertia terms related to the fluid. This approximation is valid for most problems of earthquake analysis and frequencies slower than this [158]. In the following, this simplification will be referred as the method where fluid inertia terms are neglected. Thus, in order to derive the mentioned formulation, equation (2.25) is taken and all relative acceleration terms are omitted, yielding

$$\sigma_{ij,j}^{\mathrm{tot}} + F_i = \varrho \ddot{u}_i \; . \tag{2.29}$$

Elimination of the relative displacement of equation (2.26) results in

$$q_i = -\kappa \left(p_{,i} + \varrho_f \ddot{u}_i - f_i^f \right) . \tag{2.30}$$

Substituting equation (2.22) into equation (2.21) yields

$$q_{i,i} + \alpha \dot{u}_{i,i} + \frac{\phi^2}{R} \dot{p} = 0 \, , \tag{2.31}$$

with the approximated specific flux defined in equation (2.30). Equations (2.29) and (2.31) define a coupled set of differential equation in which the solid displacement u_i and the pore pressure p remain as unknowns.

As shown by Bonnet [38], it is possible to eliminate the relative displacement w_i without omitting any inertia terms. But to do so, it is necessary to formulate the equations describing the porous medium in Laplace domain (or Frequency domain), as shown by Schanz and Cheng [124], Simon et al. [128], or Kim et al. [89, 90].

2.2.5 Laplace domain

The application of the Laplace transformation, by assuming vanishing initial conditions, i.e.,

$$\begin{aligned} u_i(0) &= 0 \qquad & p(0) &= 0 \qquad & w_i(0) &= 0 \\ \dot{u}_i(0) &= 0 \qquad & \dot{p}(0) &= 0 \qquad & \dot{w}_i(0) &= 0 \, , \end{aligned} \tag{2.32}$$

to the total balance of mass (2.25) yields

$$\hat{\sigma}_{ij,j}^{\mathrm{tot}} + \hat{F}_i = \mathrm{s}^2 \varrho \hat{u}_i + \mathrm{s}^2 \varrho_f \hat{w}_i \, . \tag{2.33}$$

The Laplace transform of the balance of momentum of the solid (2.24a) and fluid (2.24b) reads as

$$\begin{aligned} \hat{\sigma}_{ij,j}^{s} + (1-\phi)\, \hat{f}_i^s &= \mathrm{s}^2 (1-\phi)\, \varrho_s \hat{u}_i - \mathrm{s}^2 \frac{\varrho_a}{\phi} \hat{w}_i - \mathrm{s} \frac{\phi}{\kappa} \hat{w}_i \\ \hat{\sigma}_{ij,j}^{f} + \phi \hat{f}_i^f &= \mathrm{s}^2 \phi \varrho_f \hat{u}_i + \mathrm{s}^2 \left(\varrho_f + \frac{\varrho_a}{\phi} \right) \hat{w}_i + \mathrm{s} \frac{\phi}{\kappa} \hat{w}_i \, , \end{aligned} \tag{2.34a}$$

respectively and the continuity equation (2.23) in it's transformed version is given by

$$\mathrm{s} \hat{w}_{i,i} + \mathrm{s} \alpha \hat{u}_{i,i} + \mathrm{s} \frac{\phi^2}{R} \hat{p} = 0 \, . \tag{2.35}$$

2.2.6 Elimination of the relative displacement in Laplace domain

The elimination of the relative fluid displacement w_i can be accomplished in Laplace domain and, thus, otherwise as in time domain without omitting any inertia terms [38]. The reason for this is that the relative displacement also occurs a second time derivative. In order to eliminate the relative displacement, w_i from equation (2.34a) is expressed as

$$\hat{w}_i = -\underbrace{\frac{\kappa\phi^2\varrho_f \mathrm{s}^2}{\mathrm{s}\phi^2 + \kappa \mathrm{s}^2(\varrho_a + \phi\varrho_f)}}_{\beta} \frac{1}{\mathrm{s}^2\rho_f}\left(\hat{p}_{,i} + \varrho_f \mathrm{s}^2 \hat{u}_i - \hat{f}_i^f\right) , \tag{2.36}$$

with the abbreviation β, which will be used further. The final set of equations to describe the porous media is obtained by inserting the relative displacement (2.36) into equations (2.33) and (2.35) and some algebraic manipulations

$$\hat{\sigma}_{ij,j}^{\mathrm{eff}} - (\alpha-\beta)\hat{p}_{,i} - \mathrm{s}^2(\varrho - \beta\varrho_f)\hat{u}_i = \beta\hat{f}_i^f - \hat{F}_i \tag{2.37a}$$

$$\frac{\beta}{\mathrm{s}\varrho_f}\hat{p}_{,ii} - \frac{\mathrm{s}\phi^2}{R}\hat{p} - \mathrm{s}(\alpha-\beta)\hat{u}_{i,i} = \frac{\beta}{s\varrho_f}\hat{f}_{i,i}^f . \tag{2.37b}$$

The effective stress may also be expressed in terms of the solid displacement using equation (2.20).

2.2.7 Plane body waves in poroelastic media

Plane waves in an infinite porous media are investigated in this section. Basically the same steps as in section 2.1.2 are performed. Without loss of generality equations (2.37) are used, since this formulation suffices to determine plane waves in a poroelastic material. Hence, consider the following ansatz for a plane wave in Laplace domain

$$\hat{u}_i = A_i \mathrm{e}^{-\frac{\mathrm{s}}{c}n_k x_k} \qquad\qquad \hat{p} = B\,\mathrm{e}^{-\frac{\mathrm{s}}{c}n_k x_k} \tag{2.38}$$

for the solid displacement and the pore pressure, respectively. A_i and B give the particle displacement of the wave. Since the fluid can only transmit compressional waves the particle displacement is in the direction of the wave normal and may be defined through a scalar value $B = B_k n_k$. The wave normal unit vector is given by n_k and x_k denotes the position vector. The solution (2.38) describes the propagation of plane body waves with the wave velocity c in a porous infinite medium, whose wave fronts are perpendicular to the normal vector n_k.

Inserting the ansatz (2.38) into equations (2.37) and taking into account that the effective stress for a homogenous isotropic solid skeleton is given by

$$\hat{\sigma}_{ij}^{\mathrm{eff}} = 2G\hat{\varepsilon}_{ij}^s + \left(K - \frac{2}{3}G\right)\hat{\varepsilon}_{kk}^s\delta_{ij} ,$$

yields, when body forces are neglected,

$$GA_i n_j n_j \frac{s^2}{c^2} + (K + \frac{1}{3}G) A_j n_j n_i \frac{s^2}{c^2} - (\alpha - \beta) B n_i \frac{s}{c} - s^2(\varrho - \beta\varrho_f) A_i = 0 \quad (2.39a)$$

$$\frac{\beta}{s\varrho_f} \frac{s^2}{c^2} n_i n_i B - \frac{s\phi^2}{R} B - \frac{s^2}{c}(\alpha - \beta) A_i n_i = 0 \,. \quad (2.39b)$$

Consider now the case that the particle motion is parallel to the propagation of the wave, i.e., $A = A_i n_i$. From equation (2.39b) the Amplitude B can be expressed as

$$B = \frac{Rsc\varrho_f(\alpha - \beta)}{\phi^2 c^2 \varrho_f - R\beta} A_i n_i \,. \quad (2.40)$$

Inserting (2.40) into (2.39a) and considering that $n_i n_i = 1$ and $A_i = A n_i$ leads to an equation for the wave velocity c of the form

$$\left[K + \frac{4}{3}G + (\alpha - \beta)^2 \frac{Rc\varrho_f}{\phi^2 c\varrho_f - R\beta} - c^2(\varrho - \beta\varrho_f) \right] \frac{s^2}{c^2} A_i = 0 \,. \quad (2.41)$$

Equation (2.41) can only be satisfied if the term in the square brackets vanishes. Hence, from equation (2.41) two compressional waves are obtained with wave speeds

$$c_{1,2}^2 = \frac{R\beta(\beta\varrho_f - \varrho) - (K + \frac{4}{3}G)\phi^2\varrho_f - (\alpha - \beta)^2 R\varrho_f}{2\phi^2\varrho_f(\varrho_f\beta - \varrho)}$$
$$\pm \frac{\sqrt{\left[R\beta(\beta\varrho_f - \varrho) - (K + \frac{4}{3}G)\phi^2\varrho_f - (\alpha - \beta)^2 R\varrho_f\right]^2 + 4R\beta\phi^2\varrho_f(\varrho_f\beta - \rho)(K + \frac{4}{3}G)}}{2\phi^2\varrho_f(\varrho_f\beta - \rho)} \,, \quad (2.42)$$

namely the *fast* and *slow* compressional wave. The *fast* wave propagates in a medium when the fluid and solid movement are in phase. This locking may arise through viscous or inertial coupling forces. The slow wave needs relative movement of the fluid and the solid skeleton. This relative motion is highly dependent on the permeability κ and the viscosity of the interstitial fluid [81].

Considering the case that the particle motion is perpendicular to the direction of wave propagation, i.e., $A_i n_i = 0$, equation (2.39a) simplifies to

$$\frac{s^2}{c^2} \left[G - c^2(\varrho - \beta\varrho_f) \right] A_i = 0 \quad (2.43)$$

and implies that also the amplitude B in equation (2.40) vanishes. From equation (2.43) follows the shear wave speed

$$c_S^2 = \frac{G}{\varrho - \beta\varrho_f} \,.$$

Since the compressional waves speeds c_1, c_2 and the shear wave speed c_S are frequency dependent they are also called *dispersive* waves.

Plane body waves when fluid inertia is neglected Following the same procedure as above, the wave velocities can also be computed for the governing equations (2.29)-(2.31). This yields the compressional waves speeds

$$c_{1,2}^2 = \frac{R\left(\alpha^2 + s\kappa\varrho - s\alpha\kappa\varrho_f\right) + (K + \frac{4}{3}G)\phi^2}{2\phi^2\varrho} \pm \frac{\sqrt{\left[R\left(\alpha^2 + s\kappa\varrho - s\alpha\kappa\varrho_f\right) + (K + \frac{4}{3}G)\phi^2\right]^2 - 4(K + \frac{4}{3}G)Rs\kappa\varrho\phi^2}}{2\phi^2\varrho} \tag{2.44}$$

and the shear wave speed

$$c_S^2 = \frac{G}{\varrho} .$$

Note that the shear wave speed is in this case independent of the frequency and, thus, is called a non-dispersive wave.

Rayleigh surface wave

As in the elastic halfspace, also in a poroelastic halfspace the Rayleigh wave occurs [4]. For the case of an elastic material the *Rayleigh wave* speed c_R can be approximated by equation (2.16). This approximation can also be applied to porous materials as long as low frequency problems are considered, as investigated by Yang [147]. This is the case for many soil- and geomechanical applications and, thus, this approximation will be used throughout the whole thesis.

2.3 Notes on unbounded domains

Infinite domains or unbounded domains appear in various mathematical models in applied mechanics or applied physics, i.e., wave propagation in an elastic or a poroelastic halfspace. Unbounded domains are characterized by a spatial domain of infinite length, area, or volume. The most essential thing in unbounded wave problems is that all waves are traveling outward and do not return. This phenomena is ensured by the statement of so called *radiation conditions*. These radiation conditions vary whether a static, a time-harmonic, or a transient problem is under consideration.

In static problems a sufficiently accurate solution is attainable when the clamped boundary is far enough away. Consequently, in this case the radiation condition is only fulfilled approximately. Moreover, this kind of calculation has to be performed based on heuristics

methods. This is not the case for dynamic unbounded problems, unless so much damping is present that the waves are dissipated until they return from the boundary. For time harmonic problems, the most established radiation condition is formulated by Sommerfeld [130, 131]. This radiation condition is denoted as *Sommerfeld radiation condition* and ensures that the far field condition is fulfilled, i.e., no incoming waves are present and the correct decay of the field quantity is obtained. While for the time harmonic case the far field condition must be explicitly stated, this is not the case for transient problems [76]. This is the case since initial conditions for the underlying problem have to be defined. If vanishing initial conditions are assumed at infinity, no incoming waves occur, and, therefore, the Sommerfeld radiation condition is fulfilled [76]. Here, in this work, vanishing initial conditions are assumed for elastic (3.3) and also for poroelastic (3.28) initial boundary value problems. Thus, the radiation conditions are automatically fulfilled.

When using the finite element method for unbounded wave propagation problems, the spatial discretization can only be realized for a finite domain. In order to fulfill the radiation condition the reflection of outgoing waves at the artificial boundary of the discretized finite domain must be prevented. Several methods are developed to model this behavior and summarized in section 2.4. More information covering this topic can be found, e.g., for the scalar wave equation and the elastic equation of motion in the work of Bonnet [40].

2.4 Methods for unbounded domains

Various different numerical approaches up to now are explored and even improved for different problems. In the following, a short overview for different numerical methods will be given, capable of dealing with unbounded domains for various types of differential equations. In the ongoing the method of using so called *infinite elements* will be illustrated in more detail in section 4.

In general, all these methods are based on the strategy that the unbounded region is truncated at some point. Hence, the unbounded domain is divided into a finite inner region Ω_i of interest and a remaining unbounded exterior region Ω_e, as depicted in figure 2.1. The body B represents any scattering or radiating source which is located within the inner region Ω_i and owns the boundary ∂B. The domain Ω_i is enclosed by it's boundary $\Gamma = \partial\Omega_\mathrm{i}$ with the outward normal vector $\mathbf{n}$. Thus, the remaining exterior domain is defined by $\Omega_\mathrm{e} = \mathbb{R}^d \setminus \overline{\Omega}_\mathrm{i}$, where d denotes the spatial dimension ($\overline{\Omega}_\mathrm{i} = \Omega_\mathrm{i} \cup \Gamma$). The main purpose of the exterior region is to act like an energy absorber, capable of avoiding any spurious reflections and to represent the far field behavior appropriately. Different approaches exist to model the far field behavior and are summarized shortly in the following.

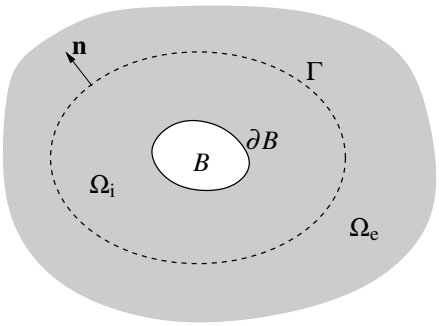

Figure 2.1: Decomposition of the unbounded domain into an inner region Ω_i and exterior region Ω_e.

Boundary Element Method (BEM) The Boundary Element Method is a computational method which uses fundamental solutions and suitable boundary integral equations to formulate the differential equations, describing the underlying physical problem, on the surface. Thus, the spatial dimension of the discretized geometry is reduced by one. The discretization process yields a set of linear algebraic equations which yields the solution on the boundary. Once, the solution on the surface is obtained, unknown field variables in the whole space can be computed using the surface integral equations. A major advantage of the boundary element method is that the radiation condition of unbounded problems is already incorporated in the formulation itself and, therefore, the far field behavior is modeled exactly. Additionally, the fact that the fundamental solution is exact brings in the advantage of improved accuracy. On the other hand the need of a fundamental solution is also a drawback of this method. Thus, for some operators, for instance, for inhomogeneous, nonlinear and some anisotropic operators, no or no suitable fundamental solution is obtainable [73]. Nevertheless, non-linear analysis are performed within the BEM, although it turns out to be a lavish task [115]. A more common approach to deal with non-linear problems is the coupling of BEM with FEM, e.g., [141]. Moreover, singularities are present using the boundary element method, which need special attention for the numerical integration. Various different formulations of the BEM exist [76]. To get more insight into this method the reader is referred, for instance, for the elastic case, to the book of Gaul et al. [73], which also reveals a historical development of the method. The application of the BEM to poroelastodynamics is elaborated by Schanz [123] and Messner and Schanz [102].

Artificial Boundary Conditions (ABC) Another common approach to treat unbounded domains is the use of so called Artificial or Absorbing Boundary Conditions (ABC). The first step is to introduce an artificial boundary Γ, as in figure 2.1, to make the unbounded domain Ω finite. Then, boundary conditions have to be imposed on the boundary Γ, which try to approximate the behavior of the far field. For example, a simple Dirichlet boundary condition will set the solution to zero on the boundary. Of course this will reflect waves on the fixed boundary. To find proper choices of boundary conditions for various wave prob-

lems is a subject of ongoing research. This task is not trivial, since this artificial boundary condition has to represent accurately the behavior of the infinite domain outside Ω_i. Thus, an ABC tries to fool the solution in "thinking" that it extends forever with no boundary. In the context of wave propagation problems, an artificial boundary condition is also called a *Non-Reflecting Boundary Condition* (NRBC). Various non-reflecting boundary conditions have been proposed in the literature [75]. A classical approximate absorbing boundary is developed by Lysmer and Kuhlemeyer [98] and consists of a viscous dashpot model. Although this model is local and cheaply computed, it requires large bounded domains for satisfactory accuracy. Even more, this model is only capable to absorb outward traveling waves on a small range of angles of incidence. One popular method is the so called Dirichlet to Neumann (DtN) map proposed by Keller and Givoli [85], Givoli [75], and Givoli and Keller [77], which is non-local in time and space. This approach yields fully populated system matrices and destroys the sparse matrix of the FEM and subsequently increases computational costs. Basically, a DtN just relates the field variable to it's normal derivative on the whole boundary. This relation can either be performed numerically or analytically. When it can be obtained analytically then often in form of a series expansion. Thus, in order to obtain an accurate solution the number of used terms must be sufficient. Another family of methods are local and approximate. These methods are proposed by Engquist and Majda [69, 70] and Bayliss and Turkel [23]. The local DtN map is appealing due to their increased numerical efficiency but still lack in accuracy in some situations, especially for waves impinge obliquely to the boundary and not normally [75]. A comparison for the Helmholtz equation of the local and non-local NRBC is given by Givoli et al. [78]. The use of artificial boundary conditions in poroelastodynamics can be found, for instance, in [2, 3]. Time-domain analysis of dam-reservoir-foundation-systems using absorbing boundaries were investigated by Feltrin [71].

PML Instead of finding an absorbing boundary condition, an absorbing boundary layer is constructed to fulfill the radiation condition in unbounded domains. Here, the unbounded domain is truncated at an artificial boundary Γ. In place of finding the proper boundary condition on the introduced boundary Γ, the finite domain Ω_i is now surrounded by an artificial absorbing material. Note that this boundary layer is independent on the boundary conditions. When a waves enters the absorbing layer it is attenuated by the absorbing layer and, therefore, it's amplitude decreases. Even if, there is a reflection at the outer boundary of the absorbing layer the amplitude of the reflected wave is very small. Nevertheless, the thickness of the boundary layer as well the absorbing properties remain to be chosen in such a way that waves are absorbed sufficiently. Moreover, the absorbing layer has to be constructed in such a manner that there is no reflection when the waves enter the absorbing layer. This characteristic, which can be accomplished as shown by Berenger [29], yields the denotation *Perfectly Matched Layer*, or *PML*, for the absorbing layer. The PML was first initiated by Berenger [29] for the application to electromagnetism (Maxwell's equations). These ideas are also applicable to other wave equations. Various interpretations of

the PML are offered by different authors, e.g. [50, 120, 155]. The most popular interpretation of the PML is the co-ordinate stretching explanation, provided by Chew et al. [50]. Here, the real coordinate in the infinite domain (layer) is replaced by a complex extension, which causes the waves to decay within the perfectly matched layer. Thus, depending on the proper complex coordinate stretching the performance of the PML varies [21]. Various application of the PML exist in the literature and only a small extract is given here of this fast developing method. The transient and time-harmonic case for elastodynamics is discussed for example by Basu [19] and Basu and Chopra [20, 21]. The application of perfectly matched layers to poroelastodynamics is discussed by Zeng et al. [151].

3 FINITE ELEMENT METHOD

The finite element method (FEM), also called finite element analysis (FEA), is a numerical method for approximately solving many field problems. This is needed since an exact solution is not possible in most cases. Today the finite element method is the most common numerical method used in any field of engineering, surely also by virtue of increasing computational possibilities.

One of the first numerical methods developed was the Rayleigh-Ritz approximation [116]. It is based on the following idea: Choose a finite number of trial functions $\varphi_1, \ldots, \varphi_N$ and find among their linear combinations $u = \sum a_i \varphi_i$ the coefficients a_i $(a_1, \ldots, a_N)$ which minimizes the potential energy of the problem, with the field quantity u. Therefore, a set of N algebraic equations has to be solved instead of the differential equation. The minimization process seeks automatically for the solution which is closest to u. Nevertheless, every trial function (also called Ritz or shape function) must be admissible: that is, each must satisfy compatibility conditions and essential boundary conditions. Even more, the shape functions should be chosen in such a manner that they are convenient enough for the potential energy to be computed and minimized. At the same time they should be general enough to approximate the general solution u with sufficient accuracy. This makes the Rayleigh-Ritz method not applicable to general problems. It is also not clear how to choose proper additional shape functions to increase accuracy and the integrals which has to be computed may get complicated soon.

This is what the finite element method is able to handle better. The idea of the finite element method is simple. First the structure is subdivided into a finite number of segments, called *finite elements*. Their size is arbitrary; they may all be of the same size or all different. The elements are connected at nodes. The particular arrangement of the finite elements is called *mesh*. Within the finite element the field quantity is approximated by so called *shape functions*. This lead to a set of algebraic equations in the field quantity (unknowns at nodes). The boundary conditions are also more easily applied on a local element as in the Rayleigh-Ritz method where they have to be applied globally. The accuracy may be increased by choosing a higher polynomial order of the shape functions or the polynomial order is retained and the mesh is refined (increasing the number of finite elements). This is simpler as choosing an appropriate global shape function as in the Rayleigh-Ritz method. Also sparse system matrices are gained in the finite element method which reduces computational costs.

A wide range of text books on the finite element method exists. The books of Bathe [22], Braess [43], Cook et al. [55], Hughes [82], Jung and Langer [84], Strang and Fix [135],

Szabó and Babuška [138], Zienkiewicz and Taylor [159], and Zienkiewicz et al. [164, 165] are only some examples of available textbooks on this topic.

In the following, the finite element formulation for the elastodynamic case will be accomplished. Also the finite element formulation for poroelastodynamics, in all it's different approaches of unknowns, will be presented.

3.1 Elastodynamics

3.1.1 Strong and weak formulation

The partial differential equation (2.7) comprise a temporal evolution and, therefore, the unknown function doesn't only depend on the spatial dimension d but also on time t. Thus, the unknown function u_i may be written as

$$u_i = u_i(\mathbf{x},t) \ , \quad (\mathbf{x},t) \in \overline{\Omega} \times [0,T] \ , \tag{3.1}$$

which means that u_i is a function of $\mathbf{x} \in \overline{\Omega}$ and $t \in [0,T]$, the closed time interval of length $T > 0$. In the ongoing, the condensed pair $(\mathbf{x},t)$ will be used, which belongs in this case to the $(d+1)$-dimensional region $\overline{\Omega} \times [0,T]$. The Symbol $\overline{\Omega}$ denotes the spatial domain Ω including the boundary Γ ($\overline{\Omega} = \Omega \cup \Gamma$). Solving a time dependent boundary value problem involves to impose time dependent boundary data. Therefore, the boundary trace u_i^Γ is introduced

$$u_i^\Gamma(\mathbf{y}) = \mathrm{Tr}\ u_i(\mathbf{x}) = \lim_{\Omega \ni \mathbf{x} \to \mathbf{y} \in \Gamma} u_i(\mathbf{x}) \ . \tag{3.2}$$

In equation (3.2) the operator Tr was introduced for taking the trace. The boundary data are also time dependent and may be written as

$$\begin{aligned} g_i^{\mathsf{D}}(\mathbf{y},t) \ , &\quad (\mathbf{y},t) \in \Gamma_{\mathsf{D}} \times (0,T) \\ \sigma_{ij}(\mathbf{y},t) n_j(\mathbf{y},t) = g_i^{\mathsf{N}}(\mathbf{y},t) \ , &\quad (\mathbf{y},t) \in \Gamma_{\mathsf{N}} \times (0,T) \ , \end{aligned}$$

assuming that the disjoint boundary sections Γ_{D} and Γ_{N} do not vary with time. The boundary sections Γ_{D} and Γ_{N} are subsets of the boundary Γ, where Dirichlet g_i^{D} and Neumann g_i^{N} boundary conditions are applied, respectively. The Dirichlet data $g_i^{\mathsf{D}}(\mathbf{y},t)$ corresponds to prescribed displacements, the Neumann data $g_i^{\mathsf{N}}(\mathbf{y},t)$ to prescribed stresses. The boundary Γ admits the decomposition $\overline{\Gamma} = \overline{\Gamma_{\mathsf{D}} \cup \Gamma_{\mathsf{N}}}$ where the overline $\overline{()}$ denotes the closure of a set. Moreover, it is assumed that $\Gamma_{\mathsf{D}} \cap \Gamma_{\mathsf{N}} = \varnothing$, i.e., that point $\mathbf{x}$ on the boundary is either in Γ_{D} or Γ_{N}. This means that no Point $\mathbf{x}$ is contained in both Γ_{D} and Γ_{N}. The outward normal vector is denoted by n_j.

For a well posed boundary value problem also initial conditions have to be specified

$$\begin{aligned} u_i^0(\mathbf{x}) &= u_i(\mathbf{x},0^+) \ , \quad \mathbf{x}\in\Omega \\ \dot{u}_i^0(\mathbf{x}) &= \dot{u}_i(\mathbf{x},0^+) \ , \quad \mathbf{x}\in\Omega \ , \end{aligned} \tag{3.3}$$

where 0^+ denotes the approach to zero from the positive direction ($t>0$). Since the second time derivative $\ddot{u}_i(\mathbf{x},t)$ occurs (i.e., acceleration) two initial conditions are to be specified. The given initial conditions have to coincide with the given boundary data

$$(\mathrm{Tr}\, u_i^0)(\mathbf{y}) = g_i^{\mathsf{D}}(\mathbf{y},0^+) \quad \text{and} \quad (\mathrm{Tr}\, \dot{u}_i^0)(\mathbf{y}) = g_i^{\mathsf{D}}(\mathbf{y},0^+) \ , \qquad \mathbf{y}\in\Gamma_{\mathsf{D}} \ .$$

The other parameters involving the initial boundary value problem, as the material tensor $C_{ijk\ell}$ and the density ϱ are assumed to be constant in space and time, i.e., $C_{ijk\ell}(\mathbf{x},t) = C_{ijk\ell}$ and $\varrho(\mathbf{x},t) = \varrho$. The *strong form* of the initial boundary problem may now be stated:

Given $f_i(\mathbf{x},t), g_i^{\mathsf{D}}(\mathbf{y},t), g_i^{\mathsf{N}}(\mathbf{y},t), u_i^0(\mathbf{x})$ and $\dot{u}_i^0(\mathbf{x})$ given as in (3.1) through (3.3), find $u_i(\mathbf{x},t)$ such that

$$\begin{aligned} \sigma_{ij,j}(\mathbf{x},t) + f_i(\mathbf{x},t) &= \varrho\ddot{u}_i(\mathbf{x},t) && (\mathbf{x},t)\in\Omega\times(0,T) \\ u_i^{\Gamma}(\mathbf{y},t) &= g_i^{\mathsf{D}}(\mathbf{y},t) && (\mathbf{y},t)\in\Gamma_{\mathsf{D}}\times(0,T) \\ \sigma_{ij}(\mathbf{y},t)n_j(\mathbf{y},t) &= g_i^{\mathsf{N}}(\mathbf{y},t) && (\mathbf{y},t)\in\Gamma_{\mathsf{N}}\times(0,T) \\ u_i(\mathbf{x},0^+) &= u_i^0(\mathbf{x}) && \mathbf{x}\in\Omega \\ \dot{u}_i(\mathbf{x},0^+) &= \dot{u}_i^0(\mathbf{x}) && \mathbf{x}\in\Omega \ . \end{aligned} \tag{3.4}$$

The strong form (3.4) is valid for any point $\mathbf{x}$ in the domain Ω.

In order to formulate the weak formulation two special types of function have to be introduced. The first one is the *space of (trial) solutions*. Possible solutions of this space require to fulfill the Dirichlet boundary conditions $u_i^{\Gamma} = g_i^{\mathsf{D}}$ on Γ_{D}. Here and in the following, the condensed pair $(\mathbf{y},t)$ or accordingly $(\mathbf{x},t)$ will be suppressed. Furthermore, these solution functions have to require that their derivatives are square integrable, i.e., they are H^1*-functions* ($u_i\in H^1$)[81, 114]. Thus, the collection of *solutions*, denoted by $\mathcal{V}_g$, may be written as

$$\mathcal{V}_g = \{u_i \ : \ u_i\in H^1 \ , \ u_i = g_i^{\mathsf{D}} \text{ on } \Gamma_{\mathsf{D}}\} \ .$$

The second set of functions is called *weighting* or *test functions*. This set of functions is similar to the set of solutions $\mathcal{V}_g$ but they have to fulfill homogenous Dirichlet boundary conditions g_i^D. This collection is denoted by

$$\mathcal{V}_0 = \{\bar{u}_i \ : \ \bar{u}_i\in H^1 \ , \ \bar{u}_i = 0 \text{ on } \Gamma_{\mathsf{D}}\} \ .$$

More on function spaces and their proper choice may be found for example in the books of Steinbach [134], Reddy [114], and Brezzi and Fortin [45].

Next, in order to obtain the variational formulation, the strong form given in equation (3.4) is pre-multiplied by the test function $\bar{u}_i \in \mathcal{V}_0$ and integrated over the domain Ω, yielding

$$\int_\Omega \bar{u}_i \sigma_{ij,j} \, \mathrm{d}\Omega - \int_\Omega \bar{u}_i \varrho \ddot{u}_i \, \mathrm{d}\Omega + \int_\Omega \bar{u}_i f_i \, \mathrm{d}\Omega = 0 \, . \tag{3.5}$$

Integrating equation (3.5) by parts and applying the *divergence theorem* $\int_\Omega (\bar{u}_i \sigma_{ij})_{,j} \, \mathrm{d}\Omega = \int_\Gamma \bar{u}_i \sigma_{ij} n_j \, \mathrm{d}\Gamma$ leads to

$$\int_\Omega \bar{u}_{i,j} \sigma_{ij} \, \mathrm{d}\Omega + \varrho \int_\Omega \bar{u}_i \ddot{u}_i \, \mathrm{d}\Omega - \int_\Omega \bar{u}_i f_i \, \mathrm{d}\Omega = \int_{\Gamma_\mathsf{N}} (\mathrm{Tr}\, \bar{u}_i) g_i^\mathsf{N} \, \mathrm{d}\Gamma_\mathsf{N} \, , \tag{3.6}$$

where only the surface integral over Γ_N remains, since the test functions $\bar{u}_i$ vanishes on Γ_D. The final *weak formulation* is obtained by inserting the material properties (2.2) with the relation (2.4) in (3.6)

$$\int_\Omega \bar{u}_{i,j} C_{ijk\ell} u_{k,\ell} \, \mathrm{d}\Omega + \varrho \int_\Omega \bar{u}_i \ddot{u}_i \, \mathrm{d}\Omega - \int_\Omega \bar{u}_i f_i \, \mathrm{d}\Omega = \int_{\Gamma_\mathsf{N}} (\mathrm{Tr}\, \bar{u}_i) g_i^\mathsf{N} \, \mathrm{d}\Gamma_\mathsf{N} \, . \tag{3.7}$$

The initial conditions of the strong form (3.4) may also be expressed for the weak form

$$\varrho \int_\Omega \bar{u}_i u_i \, \mathrm{d}\Omega = \varrho \int_\Omega \bar{u}_i u_i^0 \, \mathrm{d}\Omega \quad \text{and} \quad \varrho \int_\Omega \bar{u}_i \dot{u}_i \, \mathrm{d}\Omega = \varrho \int_\Omega \bar{u}_i \dot{u}_i^0 \, \mathrm{d}\Omega \quad \text{at} \quad t = 0 \, .$$

The variational formulation is a weaker one than the strong form since it demands less smoothness on the solution u_i. Under consideration of special regularity conditions (smoothness) the solution of the weak form is also a solution of the strong form [114]. Of course, a solution of the strong form is also a solution of the weak form.

The main focus of the finite element method is now to approximate the function spaces $\mathcal{V}_g$ and $\mathcal{V}_0$ by function spaces which are denoted by $\mathcal{V}_g^h$ and $\mathcal{V}_0^h$. The variational functions are then solved in this finite-dimensional context.

3.1.2 Spatial discretization

The spatial discretization of the domain Ω, in which a solution of the boundary value problem is sought for, requires a partition into non-overlapping subdomains, so called finite elements

$$\overline{\Omega} \approx \overline{\Omega}_h = \bigcup_{e=1}^{E_N} \tau_e \, ,$$

where E_N is the total number of geometric finite elements τ_e. Here and in the following, the index h denotes that the corresponding quantity is understood in a spatial discretized sense. A common choice of finite elements in two dimensions are triangles and quadrilateral, whereas in three dimensions tetrahedrons and hexahedrons dominate. Moreover, the finite element mesh consists of *nodal points* $\mathbf{p}_i$. Nodes are locates at least at vertices of finite elements, but in order to improve accuracy more nodes may be introduced. So, in any case a finite element mesh contains of a total number of nodes $\bar{N}_h$, which have position vectors $\mathbf{p}_1, \mathbf{p}_2, \ldots, \mathbf{p}_{\bar{N}_h}$. Since the finite elements are non-overlapping they fulfill the following characteristic for every $e, e' \in e_N = \{1, 2, \ldots, E_N\}$ with $e \neq e'$

$$\tau_e \cap \tau_{e'} = \begin{cases} \varnothing \quad \text{or} \\ \text{a common node or} \\ \text{a common edge or} \\ \text{a common face (for } d = 3 \text{ only)} \, . \end{cases}$$

The set containing the element numbering is appointed to $e_N = \{1, 2, \ldots, E_N\}$. Once, the triangulation of the domain is established, the shape functions of the finite elements can be specified. In a finite element mesh there is a total number of $\bar{N}_h$ shape functions that is one shape function for every node. Each shape function $\tilde{\varphi}^i(\mathbf{x}_j)$ has the property that it is only nonzero on the elements that are connected to the node i and $\tilde{\varphi}_i(\mathbf{x}_j)$ is equal to 1 at node i. At every other node it is zero, i.e.,

$$\tilde{\varphi}^i(\mathbf{x}_j) = \delta_{ij} = \begin{cases} 1 & \text{if } i = j \\ 0 & \text{if } i \neq j \, , \end{cases} \tag{3.8}$$

where $\tilde{\varphi}$ revers to a global defined shape function. Using these shape functions, the unknowns of any variational formulation may be approximated as

$$u_i(\mathbf{x}, t) \approx u_i^h(\mathbf{x}, t) = \sum_{j=1}^{\bar{N}_h} \tilde{\varphi}^j(\mathbf{x}) \bar{u}_i^j(t) \, . \tag{3.9}$$

In equation (3.9) only an approximation in space is done, the time is still continuous. This will lead in the ongoing to a so called *semi-discrete* finite element formulation. Since the shape functions are now introduced, the space of finite element functions is defined by

$$\mathcal{V}^h = \Big\{ \sum_{j \in \bar{n}_h} \tilde{\varphi}^j \Big\} = \text{span} \, \{ \tilde{\varphi}^j \ : \ j \in \bar{n}_h \}$$

Next, the function spaces $\mathcal{V}_g^h$ and $\mathcal{V}_0^h$ will be defined. $\mathcal{V}_0^h$ is a subspace of $\mathcal{V}_0$, whose members vanish on the Dirichlet boundary and is defined by

$$\mathcal{V}_0^h = \big\{ \bar{u}_i^h \ : \ \bar{u}_i^h = \sum_{j \in \bar{n}_h} \tilde{\varphi}^j \bar{u}_i^j \big\} \tag{3.10}$$

Furthermore, the subspace $\mathcal{V}_g^h$, which is a subspace of $\mathcal{V}_g$, is defined by

$$\mathcal{V}_g^h = \left\{ u_i^h \ : \ u_i^h = \sum_{j \in n_h} \tilde{\varphi}^j u_i^j + \sum_{j \in n_D} \tilde{\varphi}^j g_i^{j,\mathsf{D}} \right\} , \tag{3.11}$$

whose members assume the prescribed Dirichlet boundary data $g_i^{j,\mathsf{D}}$. The sets n_h, n_D and $\bar{n}_h$ are given by

$$\bar{n}_h = \{1,2,\ldots,\bar{N}_h\} \ , \ n_h = \{1,2,\ldots,N_h\} \ , \ n_D = \{N_h+1, N_h+2,\ldots,\bar{N}_h\} \ ,$$

where N_h are nodes which belong to $\Omega \cup \Gamma_{\mathsf{N}}$. The index h gives some indication how close the approximated subspaces $\mathcal{V}_g^h, \mathcal{V}_0^h$ are to $\mathcal{V}_g, \mathcal{V}_0$. As the number of elements E_N grows, the parameter h gets smaller, i.e., the mesh is refined. This means that in the limit $E_N \to \infty$, $h \to 0$, $\mathcal{V}_g^h$ approaches $\mathcal{V}_g$. A more precise illustration can be found in [114]. In the above equations (3.10) and (3.11) the same shape functions are used for the test and weighting functions. This is called a *Bubnov-Galerkin-Method*. Another class of approximation, where the weighting function $\bar{u}_i^h$ is not in $\mathcal{V}_0^h$, is called *Petrov-Galerkin-Method*, e.g.,

$$\mathcal{V}_0^h = \left\{ \bar{u}_i^h \ : \ \bar{u}_i^h = \sum_{j \in n_h} \tilde{\psi}^j \bar{u}_i^j \right\} .$$

Using the above approximation yields now the semi-discrete variational form of (3.7)

$$\int_{\Omega^h} \bar{u}_{i,j}^h C_{ijk\ell} \bar{u}_{k,\ell}^h \, \mathrm{d}\Omega^h + \varrho \int_{\Omega^h} \bar{u}_i^h \ddot{u}_i^h \, \mathrm{d}\Omega^h - \int_{\Omega^h} \bar{u}_i^h f_i^h \, \mathrm{d}\Omega^h = \int_{\Gamma_{\mathsf{N}}^h} (\mathrm{Tr}\ \bar{u}_i^h) g_i^{\mathsf{N},h} \, \mathrm{d}\Gamma_{\mathsf{N}}^h \ . \tag{3.12}$$

Inserting the approximations $\bar{u}_i^h \in \mathcal{V}_0^h$ with arbitrary coefficients $\bar{u}_i^j$ and $u_i^h \in \mathcal{V}_g^h$ in (3.12) yields the semi-discrete finite element formulation

$$\begin{aligned} \int_{\Omega^h} \tilde{\varphi}_{,j}^N C_{ijk\ell} \tilde{\varphi}_{,\ell}^M u_k^M \, \mathrm{d}\Omega^h + \varrho \delta_{ik} \int_{\Omega^h} \tilde{\varphi}^N \tilde{\varphi}^M \ddot{u}_k^M \, \mathrm{d}\Omega^h &= \int_{\Omega^h} \tilde{\varphi}^N f_i^h \, \mathrm{d}\Omega^h \\ + \int_{\Gamma_{\mathsf{N}}^h} (\mathrm{Tr}\ \tilde{\varphi}^N) g_i^{\mathsf{N},h} \, \mathrm{d}\Gamma_{\mathsf{N}}^h - \int_{\Omega^h} \tilde{\varphi}_{,j}^N C_{ijk\ell} \tilde{\varphi}_{,\ell}^{\overline{M}} g_k^{\overline{M},\mathsf{D}} \, \mathrm{d}\Omega^h - \varrho \delta_{ik} \int_{\Omega^h} \tilde{\varphi}^N \tilde{\varphi}^{\overline{M}} \ddot{g}_k^{\overline{M},\mathsf{D}} \, \mathrm{d}\Omega^h \ . \end{aligned} \tag{3.13}$$

where the superscripts N, M belong to the set n_h, i.e., $N, M \in n_h$ and the superscript $\overline{M}$ belongs to the set n_D ($\overline{M} \in n_D$). Thus, equation (3.13) yields $N_h \times d$ linear independent equations

$$K_{ik}^{NM} u_k^M + M_{ik}^{NM} \ddot{u}_k^M = f_i^N \ , \tag{3.14}$$

in which the complete right-hand side is put into the force vector $f_i^N = (f_i^N)^f + (f_i^N)^{\mathsf{N}} + (f_i^N)^K + (f_i^N)^M$. Using a proper time integration scheme the resulting equation system can

be solved for the nodal unknowns u_k^M. Equation (3.14) written in matrix notation reads as

$$\mathbf{M}\ddot{\mathbf{u}} + \mathbf{K}\mathbf{u} = \mathbf{f}\,,$$

with the so called stiffness- and mass matrix $\mathbf{K}$ and $\mathbf{M}$, respectively. The right-hand side is denoted by $\mathbf{f}$, also well known as load vector, which is a collection of the body forces $\mathbf{f}^f$, Neumann boundary data $\mathbf{f}^{\mathsf{N}}$ and terms due to prescribed Dirichlet data $\mathbf{f}^K$ and $\mathbf{f}^M$, i.e.,

$$\mathbf{f} = \mathbf{f}^f + \mathbf{f}^{\mathsf{N}} + \mathbf{f}^K + \mathbf{f}^M\,.$$

The unknown node data is identified by $\mathbf{u}$ and $\ddot{\mathbf{u}}$, which are called displacement and acceleration vector in case of elastodynamics.

3.1.3 Element point of view

Until now, only global shape functions were considered. When programming the finite element method, matters can be considerably simplified by setting up a *reference element* $\widehat{\tau}$. This reference element is isolated from the actual finite element mesh and is referred to its own local coordinate system $\boldsymbol{\xi}$. The relation between a point $\boldsymbol{\xi}$ in the reference element $\widehat{\tau}$ and a coordinate $\mathbf{x}$ in the domain τ_e is given by mappings of the form (see Fig. 3.1)

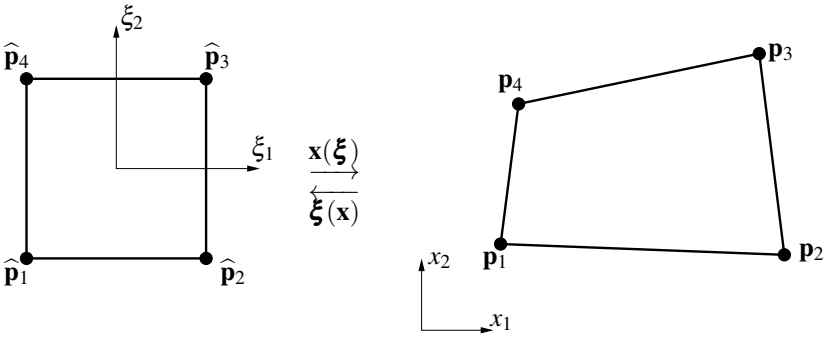

Figure 3.1: Reference element for bi-linear quadrilateral element.

$$\mathbf{x}(\boldsymbol{\xi}) = \sum_{n\in\widehat{n}_e} \mathsf{m}^n(\boldsymbol{\xi})\mathbf{p}_n \qquad \boldsymbol{\xi}\in\widehat{\tau} \quad , \quad \mathbf{p}_n \in \tau_e\,, \tag{3.15}$$

where $\widehat{n}_e = \{1,2,\ldots,\widehat{N}_e\}$ is the set of a local node numbering, $\widehat{N}_e$ is the number of total nodes of the reference element ($\widehat{N}_e$ must be equal to the number of nodes of the global element), and $\mathsf{m}^n(\xi)$ are the so called *mapping functions*, which are defined on the reference element $\widehat{\tau}$. In equation (3.15), $\mathbf{p}_n \in \mathbb{R}^d$ are the global points defining the geometry of the

global element τ_e. Since $n \in \widehat{n}_e$ is a local number, a relation to the global node numbering $N \in \bar{n}_h$ has to be established for every element

$$\tau_e : \quad n \leftrightarrow N = N(e,n), \quad e \in e_N \ , \ n \in \widehat{n}_e \tag{3.16}$$

such that every point $\mathbf{p}_N$ with global numbering can be assigned to the local numbering, i.e.,

$$\mathbf{p}_n \overset{N(e,n)}{\longleftrightarrow} \mathbf{p}_N \ .$$

Here and in the following, if not otherwise stated, subscripts $m,n,\ldots$ pertain to the local numbering system. Capital letters $M,N,\ldots$ will pertain to the global numbering system. Using equation (3.15) yields a distinct relation between a point $\mathbf{p}_n$ and a local point $\widehat{\mathbf{p}}_n$, such that the relation

$$\mathbf{p}_n = \mathbf{x}(\widehat{\mathbf{p}}_n) = \sum_{n \in \widehat{n}_e} \mathsf{m}^n(\widehat{\mathbf{p}}_n)\mathbf{p}_n$$

is given (see Fig. 3.1), which holds only if

$$\mathsf{m}^n(\mathbf{p}_m) = \delta_{nm} \ .$$

The global shape functions $\tilde{\varphi}^N(\mathbf{x})$ can now also be expressed using local shape functions φ^n, $n \in \widehat{n}_e$, defined on the reference element $\widehat{\tau}$ using the relation (3.16)

$$\tilde{\varphi}^N(\mathbf{x}) = \begin{cases} \bigcup\limits_{e \in B_e} \varphi^n(\boldsymbol{\xi}(\mathbf{x})) & \mathbf{x} \in \tau_e \\ 0 & \text{otherwise, i.e., } \mathbf{x} \in \overline{\Omega}_h \setminus \bigcup\limits_{e \in B_e} \tau_e \ . \end{cases}$$

The introduced set B_e contains all elements which belong to the global numbered node N, i.e., $\mathbf{p}_N \in \tau_e$. The local shape functions $\varphi^n(\boldsymbol{\xi})$ are defined on the reference element $\widehat{\tau}$ and consists of polynomials to retain at least C_0 continuity [165]. For example the shape functions of the bi-linear quadrilateral element

$$\tau_\square = \{(\xi_1,\xi_2) \in \mathbb{R}^2 \ : \ 0 \leq (\xi_1,\xi_2) \leq 1\}$$

are constructed. The shape function for a specific node $n \in \widehat{n}_e$ can be written as bi-linear approximation of the form

$$\varphi^n(\boldsymbol{\xi}) = C_1^n + C_2^n\xi_1 + C_3^n\xi_2 + C_4^n\xi_1\xi_2 \ ,$$

where the coefficients C_i^n remain to be determined. Collecting all shape functions $\varphi^n(\boldsymbol{\xi})$ into a vector $\boldsymbol{\varphi}_{\widehat{N}_e}(\boldsymbol{\xi}) = [\varphi^1,\ldots,\varphi^{\widehat{N}_e}]$, the shape functions can be expressed as a multiplication of a vector containing the monomials $\boldsymbol{\psi}(\boldsymbol{\xi}) = [1,\xi_1,\xi_2,\ldots]$ with the coefficient matrix $\mathsf{C} = [\mathsf{C}^1,\ldots,\mathsf{C}^{\widehat{N}_e}]$, $\mathsf{C} \in \mathbb{R}$, containing the coefficient vectors C^n

$$\boldsymbol{\varphi}_{\widehat{N}_e}(\boldsymbol{\xi}) = \boldsymbol{\psi}(\boldsymbol{\xi}) \cdot \mathsf{C} \ .$$

The property (3.8), which also holds for local defined shape functions, i.e.,

$$\varphi^n(\boldsymbol{\xi} m) = \delta_{nm}, \qquad n,m \in \widehat{n}_e \ ,$$

yields the condition $\boldsymbol{\varphi}_{\widehat{N}_e}(\widehat{\mathbf{p}}_n) = \mathsf{e}_n^{\mathsf{T}}$, with the n-th unit vector e_n. Introducing the matrix $\mathsf{X} = [\boldsymbol{\psi}(\widehat{\mathbf{p}}_1), \ldots, \boldsymbol{\psi}(\widehat{\mathbf{p}}_{\widehat{N}_e})]^{\mathsf{T}}$, which contains the monomials evaluated at the distinct nodes $\widehat{\mathbf{p}}_n$ of the local element, yields the coefficient matrix

$$\mathsf{X} \cdot \mathsf{C} = \mathsf{I} \quad \Longrightarrow \quad \mathsf{C} = \mathsf{X}^{-1}$$

and, accordingly, the set of shape functions $\varphi^n(\boldsymbol{\xi})$

$$\boldsymbol{\varphi}_{\widehat{N}_e}(\boldsymbol{\xi}) = \boldsymbol{\psi}(\boldsymbol{\xi}) \cdot \mathsf{X}^{-1} \ .$$

For the case of a bi-linear quadrilateral the set of monomials is given through $\boldsymbol{\psi}(\boldsymbol{\xi}) = [1, \xi_1, \xi_2, \xi_1\xi_2]$. The corresponding matrix X and its inverse is given by

$$\mathsf{X} = \begin{bmatrix} \boldsymbol{\psi}(\left[\begin{smallmatrix}-1\\-1\end{smallmatrix}\right]) \\ \boldsymbol{\psi}(\left[\begin{smallmatrix}1\\-1\end{smallmatrix}\right]) \\ \boldsymbol{\psi}(\left[\begin{smallmatrix}1\\1\end{smallmatrix}\right]) \\ \boldsymbol{\psi}(\left[\begin{smallmatrix}-1\\1\end{smallmatrix}\right]) \end{bmatrix} = \begin{bmatrix} 1 & -1 & -1 & 1 \\ 1 & 1 & -1 & -1 \\ 1 & 1 & 1 & 1 \\ 1 & -1 & 1 & -1 \end{bmatrix} \quad \Longrightarrow \quad \mathsf{X}^{-1} = \begin{bmatrix} 1/4 & 1/4 & 1/4 & 1/4 \\ -1/4 & 1/4 & 1/4 & -1/4 \\ -1/4 & -1/4 & 1/4 & 1/4 \\ 1/4 & -1/4 & 1/4 & -1/4 \end{bmatrix} .$$

Finally, the set of shape functions is defined by

$$\boldsymbol{\varphi}_{\square}(\boldsymbol{\xi}) = \begin{bmatrix} 1 & \xi_1 & \xi_2 & \xi_1\xi_2 \end{bmatrix} \cdot \begin{bmatrix} 1/4 & 1/4 & 1/4 & 1/4 \\ -1/4 & 1/4 & 1/4 & -1/4 \\ -1/4 & -1/4 & 1/4 & 1/4 \\ 1/4 & -1/4 & 1/4 & -1/4 \end{bmatrix} = \begin{bmatrix} 1/4(1-\xi_1)(1-\xi_2) \\ 1/4(1+\xi_1)(1-\xi_2) \\ 1/4(1+\xi_1)(1+\xi_2) \\ 1/4(1-\xi_1)(1+\xi_2) \end{bmatrix}^{\mathsf{T}} .$$

This process gaining shape functions has some considerable disadvantages. Occasionally, no inverse of X exists as Zienkiewicz et al. [165] and references therein states. Nevertheless, other methods to derive shape functions exists. For example, shape functions can be deduced by tensor products of one-dimensional Lagrange polynomials, e.g., [82, 84]. In general, shape functions persists of complete polynomials such as for the 4-noded and 9-noded quadrilateral. But there also exists a group of elements which consists of less nodes than are needed for complete polynomials, such as the 8-noded quadrilateral. This group of elements are so-called serendipity elements. Of course, there exist a lot of different types of elements, but to cover all of them as well their behavior would blast this section. The interested reader is therefore referred to common textbooks, e.g., [22, 82, 84, 165]. Is the set of shape functions $\varphi^n(\boldsymbol{\xi})$ also used to define the mapping relation (3.15), then the element is said to be *isoparametric*.

Using the set of local shape functions $\varphi^n = \varphi^n(\boldsymbol{\xi}(\mathbf{x}))$ the stiffness- and mass matrix is obtained by

$$\mathbf{K} = K_{ik}^{NM} = \bigcup_{e=1}^{E_N} \left(K_{ik}^{nm}\right)_e = \bigcup_{e=1}^{E_N} \int_{\widehat{\tau}_e} \varphi_{,j}^n C_{ijk\ell} \varphi_{,\ell}^m \, \mathcal{J}_e \, \mathrm{d}\boldsymbol{\xi} \tag{3.17a}$$

$$\mathbf{M} = M_{ik}^{NM} = \bigcup_{e=1}^{E_N} \left(M_{ik}^{nm}\right)_e = \bigcup_{e=1}^{E_N} \delta_{ik} \int_{\widehat{\tau}_e} \varphi^n \varphi^m \, \mathcal{J}_e \, \mathrm{d}\boldsymbol{\xi} \ , \tag{3.17b}$$

using the relation between the global and local node numbering

$$\begin{aligned} \tau_e : \quad & n \leftrightarrow N \ = N(e,n), \quad e \in e_N \ , \ n \in \widehat{n}_e \\ & m \leftrightarrow M = M(e,m), \quad e \in e_N \ , \ m \in \widehat{n}_e \ . \end{aligned} \tag{3.18}$$

The integrals in (3.17) contain the determinant of the *Jacobian matrix* $\mathbf{J}_e(\boldsymbol{\xi})$ of the corresponding element $e \in E_N$, e.g., $\mathcal{J}_e(\boldsymbol{\xi}) = \det \mathbf{J}_e(\boldsymbol{\xi})$ due to the transformation from global to local coordinates. The Jacobian matrix is defined by [165]

$$\mathbf{J}_e = \left(J_{ij}\right)_e = \frac{\mathrm{d}\, x_i}{\mathrm{d}\, \xi_j} \ ,$$

with $\mathbf{x}$ given by (3.15). In equation (3.17a) the spatial derivative with respect to global coordinates $\mathbf{x}$ by local coordinates $\boldsymbol{\xi}$ occur. Local derivatives are defined by

$$\frac{\partial}{\partial \mathbf{x}} = \mathbf{J}_e \frac{\partial}{\partial \boldsymbol{\xi}}$$

and, accordingly, the global derivatives are given by the relation [22]

$$\frac{\partial}{\partial \boldsymbol{\xi}} = \mathbf{J}_e^{-1} \frac{\partial}{\partial \mathbf{x}} \ .$$

Thus, the coefficients of the stiffness matrix are given by

$$\mathbf{K} = K_{ik}^{NM} = \bigcup_{e=1}^{E_N} \left(K_{ik}^{nm}\right)_e = \bigcup_{e=1}^{E_N} \int_{\widehat{\tau}_e} \left(\varphi_{,\eta}^n J_{j\eta}^{-1}\right) C_{ijk\ell} \left(\varphi_{,\zeta}^m J_{\ell\zeta}^{-1}\right) \mathcal{J}_e \, \mathrm{d}\boldsymbol{\xi} \ ,$$

where the subscripts η, ζ denote a spatial derivative of the local shape functions with respect to local coordinates $\boldsymbol{\xi}$. Up to now the stiffness- and mass matrix are built but it remains to define the right-hand side $\mathbf{f}$.

Building the right-hand side needs to define a new set $B_{\Gamma^h}^{\mathsf{N}}$, containing all edges in two- or faces Υ_b in three dimensional problems. The discrete boundary Γ_{N}^h can therefore be expressed as

$$\Gamma_{\mathsf{N}}^h = \bigcup_{b \in B_{\Gamma^h}^{\mathsf{N}}} \Upsilon_b \ .$$

Analogue to the relation (3.18) also a relation between the global and the local node numbering of every edge or face Υ_b is established

$$\Upsilon_b : \quad n \leftrightarrow N = N(b,n), \quad b \in B_{\Gamma^h}^{\mathsf{N}} \, , \, n \in \widehat{n}_b \, , \, N \in \bar{n}_h \, , \tag{3.19}$$

with $\widehat{n}_b = \{1,2,\ldots,\widehat{N}_b\}$ defining the set of local node numbering of the edge or face with the total number $\widehat{N}_b$ of nodes. Furthermore, a reference element, denoted by $\widehat{\Upsilon}$, is introduced, as well as shape functions φ_Γ and mapping functions m_Γ, which are defined on the boundary. Using the introduced notations, the right-hand side, caused by the Neumann boundary conditions $g_i^{\mathsf{N},h}(\mathbf{y},t),\ \mathbf{y} \in \Gamma_{\mathsf{N}}^h$, is defined by

$$\mathbf{f}^{\mathsf{N}} = \left(f_i^N\right)^{\mathsf{N}} = \bigcup_{b=1}^{B_{\Gamma^h}^{\mathsf{n}}} \left(f_i^N\right)_e^{\mathsf{N}} = \bigcup_{b=1}^{B_{\Gamma^h}^{\mathsf{N}}} \int_{\widehat{\Upsilon}_b} \varphi_\Gamma^n g_i^{\mathsf{N},h} \, \mathcal{J}_b \, \mathrm{d}\boldsymbol{\xi} \, . \tag{3.20}$$

Note that in equation (3.20) the relation between the global and local node numbering (3.19) is used. The determinant of the Jacobian of the corresponding element $b \in B_{\Gamma^h}^{\mathsf{n}}$ is denoted by $\mathcal{J}_b$. The mapping between a point $\boldsymbol{\xi}$ of the reference edge or face $\widehat{\Upsilon}$ and a coordinate $\mathbf{y}$ in the domain Υ_b is given by

$$\mathbf{y}(\boldsymbol{\xi}) = \sum_{n \in \widehat{n}_b} \mathsf{m}_\Gamma^n(\boldsymbol{\xi}) \mathbf{p}_n \, , \qquad \boldsymbol{\xi} \in \widehat{\Upsilon} \, , \, \mathbf{p}_n, \mathbf{y} \in \Upsilon_b \, ,$$

keeping in mind that relation (3.19) is also valid for points $\mathbf{p}_n \leftrightarrow \mathbf{p}_N$. The right-hand side contribution of equation (3.13), resulting from body forces $\mathbf{f}^f$ and the prescribed Dirichlet data $\mathbf{f}^K$ and $\mathbf{f}^M$, are built in the same manner as the stiffness- and mass matrix (3.17a) and are defined as

$$\begin{aligned}
\mathbf{f}^f = \left(f_i^N\right)^f &= \bigcup_{e=1}^{E_N} \left(f_i^n\right)_e^f = \bigcup_{e=1}^{E_N} \int_{\widehat{\tau}_e} \varphi^n f_i^h \, \mathcal{J}_e \, \mathrm{d}\boldsymbol{\xi} \\
\mathbf{f}^K = \left(f_i^N\right)^K &= \bigcup_{e=1}^{E_N} \left(f_i^n\right)_e^K = \bigcup_{e=1}^{E_N} \int_{\widehat{\tau}_e} \left(\varphi_{,\eta}^n J_{j\eta}^{-1}\right) C_{ijk\ell} \left(\varphi_{,\zeta}^{\overline{m}} J_{\ell\zeta}^{-1}\right) g_k^{\overline{m},\mathsf{N}} \, \mathcal{J}_e \, \mathrm{d}\boldsymbol{\xi} \\
\mathbf{f}^M = \left(f_i^N\right)^M &= \bigcup_{e=1}^{E_N} \left(f_i^n\right)_e^M = \bigcup_{e=1}^{E_N} \delta_{ik} \int_{\widehat{\tau}_e} \varphi^n \varphi^{\overline{m}} \ddot{g}_k^{\overline{m},\mathsf{N}} \, \mathcal{J}_e \, \mathrm{d}\boldsymbol{\xi} \, ,
\end{aligned}$$

with the relation

$$\tau_e : \quad \overline{M} \leftrightarrow \overline{m} = \overline{m}(e,\overline{M}), \quad e \in e_N \, , \, \overline{M} \in n_D \, , \, \overline{m} \in \widehat{n}_e \, . \tag{3.21}$$

3.1.4 Laplace domain

Contrary to the time dependent case initial conditions are considered during the Laplace transformation [61]. Assuming vanishing initial conditions

$$\begin{aligned} u_i(\mathbf{x},0^+) &= 0\,, \quad \mathbf{x}\in\overline{\Omega} \\ \dot{u}_i(\mathbf{x},0^+) &= 0\,, \quad \mathbf{x}\in\overline{\Omega}\,, \end{aligned}$$

the elastodynamic boundary value problem is stated in the strong form in Laplace domain as follows.

Given $\hat{f}_i(\mathbf{x}), \hat{g}_i^{\mathsf{D}}(\mathbf{y}), \hat{g}_i^{\mathsf{N}}(\mathbf{y})$, find $\hat{u}_i(\mathbf{x})$ such that

$$\begin{aligned} \hat{\sigma}_{ij,j}(\mathbf{x}) + \hat{f}_i(\mathbf{x}) &= \mathrm{s}^2\varrho\hat{u}_i(\mathbf{x}) \quad && \mathbf{x}\in\Omega \\ \hat{u}_i^{\Gamma}(\mathbf{y}) &= \hat{g}_i^{\mathsf{D}}(\mathbf{y}) && \mathbf{y}\in\Gamma_{\mathsf{D}} \\ \hat{\sigma}_{ij}(\mathbf{y})n_j(\mathbf{y}) &= \hat{g}_i^{\mathsf{N}}(\mathbf{y}) && \mathbf{y}\in\Gamma_{\mathsf{N}}\,, \end{aligned} \tag{3.22}$$

with the stress tensor $\hat{\sigma}_{ij} = C_{ijk\ell}\hat{u}_{k,\ell}$. In the following, the functions will be written without the dependent variables $\mathbf{x}$ and $\mathbf{y}$. The variational or weak form of the strong form (3.22) is obtained by performing the same steps as in the time domain. Therefore, after partial integration and applying the divergence theorem $\int_\Omega(\hat{\tilde{u}}_i\hat{\sigma}_{ij})_{,j}\,\mathrm{d}\Omega = \int_\Gamma \hat{\tilde{u}}_i\hat{\sigma}_{ij}n_j\,\mathrm{d}\Gamma$, the weak form with $\hat{u}_i\in\mathcal{V}_g$ and $\hat{\tilde{u}}_i\in\mathcal{V}_0$ reads as

$$\int_\Omega \hat{\tilde{u}}_{i,j}C_{ijk\ell}\hat{u}_{k,\ell}\,\mathrm{d}\Omega + \mathrm{s}^2\varrho\int_\Omega \hat{\tilde{u}}_i\hat{u}_i\,\mathrm{d}\Omega - \int_\Omega \hat{\tilde{u}}_i\hat{f}_i\,\mathrm{d}\Omega = \int_{\Gamma_{\mathsf{N}}} (\mathrm{Tr}\;\hat{\tilde{u}}_i)\hat{g}_i^{\mathsf{N}}\,\mathrm{d}\Gamma_{\mathsf{N}}\,.$$

Following the procedure in section 3.1.2, the approximation

$$\begin{aligned} \hat{u}_i &\approx \hat{u}_i^h = \sum_{M\in n_h}\tilde{\varphi}^M\hat{u}_i^M + \sum_{M\in n_D}\tilde{\varphi}^M\hat{g}_i^{M,D} \\ \hat{\tilde{u}}_i &\approx \hat{\tilde{u}}_i^h = \sum_{N\in n_h}\tilde{\varphi}^N\hat{\tilde{u}}_i^N\,, \end{aligned}$$

yields the discrete weak formulation

$$\begin{aligned} \int_{\Omega^h}\tilde{\varphi}^N_{,j}C_{ijk\ell}\tilde{\varphi}^M_{,\ell}u_k^M\,\mathrm{d}\Omega^h + \mathrm{s}^2\varrho\delta_{ik}\int_{\Omega^h}\tilde{\varphi}^N\tilde{\varphi}^M\hat{u}_k^M\,\mathrm{d}\Omega^h &= \int_{\Omega^h}\tilde{\varphi}^N f_i^h\,\mathrm{d}\Omega^h \\ + \int_{\Gamma_{\mathsf{N}}^h}(\mathrm{Tr}\;\tilde{\varphi}^N)\hat{g}_i^{\mathsf{N},h}\,\mathrm{d}\Gamma_{\mathsf{N}}^h - \int_{\Omega^h}\tilde{\varphi}^N_{,j}C_{ijk\ell}\tilde{\varphi}^{\overline{M}}_{,\ell}\hat{g}_k^{\overline{M},\mathsf{D}}\,\mathrm{d}\Omega^h &- \mathrm{s}^2\varrho\delta_{ik}\int_{\Omega^h}\tilde{\varphi}^N\tilde{\varphi}^{\overline{M}}\hat{g}_k^{\overline{M},\mathsf{D}}\,\mathrm{d}\Omega^h\,, \end{aligned}$$

or written in a more compressed form

$$\underbrace{\left(K_{ik}^{NM} + \mathrm{s}^2M_{ik}^{NM}\right)}_{(\hat{\tilde{K}}_{ik}^{NM})}\hat{u}_k^M = \hat{f}_i^N\,. \tag{3.23}$$

In equation (3.23), the so called dynamic stiffness matrix $(\hat{\overline{K}}_{ik}^{NM})$ or $\hat{\overline{\mathbf{K}}}$ is introduced. The coefficients of the stiffness- K_{ik}^{NM} and mass matrix M_{ik}^{NM} are the same as in (3.17a) and (3.17b), respectively. Note that they are also independent of the Laplace parameter s and, therefore, have to be calculated just once for different s. Only the components of the force vector $\hat{f}_i^N = (f_i^N)^f + (\hat{f}_i^N)^{\mathsf{N}} + (\hat{f}_i^N)^K + (\hat{f}_i^N)^M$, containing boundary data, differ from (3.14) and are given as

$$\begin{aligned}
\left(\hat{f}_i^N\right)^{\mathsf{N}} &= \bigcup_{b=1}^{B_{\Gamma^h}^{\mathsf{n}}} \left(\hat{f}_i^N\right)_e^{\mathsf{N}} = \bigcup_{b=1}^{B_{\Gamma^h}^{\mathsf{N}}} \int_{\hat{\Upsilon}_b} \varphi_{\Gamma}^n \hat{g}_i^{\mathsf{N},h} \, \mathcal{J}_b \, \mathrm{d}\boldsymbol{\xi} \\
\left(\hat{f}_i^N\right)^K &= \bigcup_{e=1}^{E_N} \left(\hat{f}_i^n\right)_e^K = \bigcup_{e=1}^{E_N} \int_{\hat{\tau}_e} \left(\varphi_{,\eta}^n J_{j\eta}^{-1}\right) C_{ijk\ell} \left(\varphi_{,\zeta}^{\overline{m}} J_{\ell\zeta}^{-1}\right) \hat{g}_k^{\overline{m},\mathsf{N}} \, \mathcal{J}_e \, \mathrm{d}\boldsymbol{\xi} \\
\left(\hat{f}_i^N\right)^M &= \bigcup_{e=1}^{E_N} \left(\hat{f}_i^n\right)_e^M = \bigcup_{e=1}^{E_N} \mathrm{s}\delta_{ik} \int_{\hat{\tau}_e} \varphi^n \varphi^{\overline{m}} \hat{g}_k^{\overline{m},\mathsf{N}} \, \mathcal{J}_e \, \mathrm{d}\boldsymbol{\xi} \ ,
\end{aligned}$$

by considering the relations given in (3.18), (3.19), and (3.21).

Remark on elastostatics The strong and weak form for elastostatic problems can be deduced in the same manner as for the dynamic case. Basically, both the strong and weak form are obtained by neglecting all inertia terms of the dynamic formulation presented above. This is also valid for the discrete variational form. Since the deduction of the finite element formulation for elastostatics is rather straightforward it will be skipped in this thesis.

3.2 Poroelastodynamics

In this section, the finite element formulations for different approaches of the governing equations, which describe the behavior of a porous material, are given. An overview of finite element formulations for a porous medium is given by Zienkiewicz and Shiomi [158] and Simon et al. [127]. The former paper illustrates the full form (u_i, p, u_i^f) as well formulations where simplifications are used. Such simplifications are useful and permitted for slow motion phenomena as already discussed in section 2.2. The latter one also uses the full form, but uses instead of the fluid displacement u_i^f the relative displacement w_i as unknown, i.e., the set of unknowns is (u_i, p, w_i). A finite element formulation for partial saturated porous media is given by Ravichandran [112]. There, the full form is considered where the solid displacement, the liquid displacement, the gas displacement, the pore water pressure, and the pore gas pressure are assumed to be the unknowns. Consolidation phenomena of saturated as well of partially saturated media are discussed in detail by Lewis and Schrefler [95]. Also mixed finite element formulations for porous media exist and are discussed for example by Simon et al. [127] or Korsawe et al. [93].

In this thesis, the finite element formulation of the full form (u_i, p, w_i) will be reviewed. Moreover, the finite element approximation of the irreducible u_i, w_i formulation and the simplified u_i, p form is presented. The different finite element formulations of the porous material follows the one of section 3.1, where the finite element formulation for an initial boundary value is given in detail for elastodynamics. Thus, only the main steps will be presented.

3.2.1 The full form u_i, p, w_i

The primary unknowns in the finite element formulation of the full form are the solid displacement u_i, the pore pressure p, and the relative displacement w_i. If the fluid has to be considered as an incompressible material the full form is the only possible one to describe the porous material appropriately [158]. For the finite element formulation of the full form the total balance of momentum (2.25), the continuity equation (2.23), and the balance of momentum of the pore fluid (2.27) are used and are given in the strong form as

$$\sigma_{ij,j}^{\mathrm{tot}} + F_i - \varrho \ddot{u}_i - \varrho_f \ddot{w}_i = 0 \tag{3.24a}$$

$$\dot{w}_{i,i} + \alpha \dot{u}_{i,i} + \frac{\phi^2}{R} \dot{p} = 0 \tag{3.24b}$$

$$p_{,i} + \frac{1}{\phi^2} \left(\phi \varrho_f + \varrho_a \right) \ddot{w}_i + \rho_f \ddot{u}_i + \frac{1}{\kappa} \dot{w}_i - f_i^f = 0 \,. \tag{3.24c}$$

The unknown variables are therefore

$$\begin{aligned} u_i &= u_i(\mathbf{x},t) \\ p &= p(\mathbf{x},t)\ , \qquad (\mathbf{x},t) \in \overline{\Omega} \times [0,T] \\ w_i &= w_i(\mathbf{x},t)\ . \end{aligned}$$

The boundary conditions for the porous material may be defined as:

- For the total balance of momentum (3.24a) the boundary Γ is decomposed into the part where the Dirichlet data g_i^u is prescribed Γ_{D}^u and the Neumann part Γ_{N}^u where the total stress vector $t_i^{\mathrm{tot}} = \sigma_{ij}^{\mathrm{tot}} n_j$ is applied with the unit normal vector n_j, i.e.,

$$\begin{aligned} \Gamma &= \Gamma_{\mathsf{D}}^u \cup \Gamma_{\mathsf{N}}^u \\ u_i(\mathbf{y},t) &= g_i^u \quad , \qquad (\mathbf{y},t) \in \Gamma_{\mathsf{D}}^u \times (0,T) \\ \sigma_{ij}^{\mathrm{tot}} n_j(\mathbf{y},t) &= t_i^{\mathrm{tot}} \quad , \qquad (\mathbf{y},t) \in \Gamma_{\mathsf{N}}^u \times (0,T)\ . \end{aligned} \tag{3.25}$$

- The boundary for the continuity equation (3.24b) is again divided into the part Γ_{D}^p on which the values g^p are prescribed and Γ_{N}^p where the normal flux g^q is prescribed, i.e.,

$$\begin{aligned} \Gamma &= \Gamma_{\mathsf{D}}^p \cup \Gamma_{\mathsf{N}}^p \\ p(\mathbf{y},t) &= g^p \quad , \qquad (\mathbf{y},t) \in \Gamma_{\mathsf{D}}^p \times (0,T) \\ q_i n_i(\mathbf{y},t) &= g^q \quad , \qquad (\mathbf{y},t) \in \Gamma_{\mathsf{N}}^p \times (0,T)\ . \end{aligned} \tag{3.26}$$

- Finally, the boundary for the fluid phase (3.24c) is decomposed into the part Γ_{D}^w on which the values g_i^w are prescribed and Γ_{N}^w where the fluid pressure $t_i^p = n_i p$ is prescribed, i.e.,

$$\begin{aligned} \Gamma &= \Gamma_{\mathsf{D}}^w \cup \Gamma_{\mathsf{N}}^w \\ w_i(\mathbf{y},t) &= g_i^w \quad , \qquad (\mathbf{y},t) \in \Gamma_{\mathsf{D}}^w \times (0,T) \\ n_i p(\mathbf{y},t) &= t_i^p \quad , \qquad (\mathbf{y},t) \in \Gamma_{\mathsf{N}}^w \times (0,T)\ . \end{aligned} \tag{3.27}$$

In the above relations (3.25)-(3.26) the superscripts u,p, and w are used to denote that the considered quantity corresponds to the solid displacement, the pore pressure, or the relative displacement, respectively. Note that both boundary conditions (3.26) and (3.27) correspond to the fluid phase. Consequently, depending on the chosen FEM formulation (different FEM formulations will be presented in the following) the corresponding set of boundary conditions have to be applied. The finite element formulation, therefore, has to be adopted to the underlying problem, which has to be solved or the prescribed boundary

conditions have to be reformulated for the preferred FEM formulation. Furthermore, the initial conditions of the problem have to be specified, thus, they are defined by

$$\begin{aligned} (u_i)^0 &= u_i(\mathbf{x},0^+) & (\dot{u}_i)^0 &= \dot{u}_i(\mathbf{x},0^+) \\ (p)^0 &= p(\mathbf{x},0^+) & (\dot{p})^0 &= \dot{p}(\mathbf{x},0^+) \quad , \qquad \mathbf{x}\in\Omega\ . \\ (w_i)^0 &= w_i(\mathbf{x},0^+) & (\dot{w}_i)^0 &= \dot{w}_i(\mathbf{x},0^+) \end{aligned} \tag{3.28}$$

Any other variables occurring in the initial boundary value problem (3.24) will be assumed to be constant in space and time.

Weak form of the full form u_i, p, w_i

In order to formulate the weak form the solution and trial spaces are defined through

$$\begin{aligned} \mathcal{V}_g^u &= \{u_i \ : \ u_i \in H^1 \ , \ u_i = g_i^u \text{ on } \Gamma_{\mathsf{D}}^u\} \\ \mathcal{V}_0^u &= \{\bar{u}_i \ : \ \bar{u}_i \in H^1 \ , \ \bar{u}_i = 0 \text{ on } \Gamma_{\mathsf{D}}^u\}\ , \\ \mathcal{V}_g^p &= \{p \ : \ p \in H^1 \ , \ p = g^p \text{ on } \Gamma_{\mathsf{D}}^p\} \\ \mathcal{V}_0^p &= \{\bar{p} \ : \ \bar{p} \in H^1 \ , \ \bar{p} = 0 \text{ on } \Gamma_{\mathsf{D}}^p\}\ , \\ \mathcal{V}_g^w &= \{w_i \ : \ w_i \in H^1 \ , \ w_i = g_i^w \text{ on } \Gamma_{\mathsf{D}}^w\} \\ \mathcal{V}_0^w &= \{\bar{w}_i \ : \ \bar{w}_i \in H^1 \ , \ \bar{w}_i = 0 \text{ on } \Gamma_{\mathsf{D}}^w\}\ , \end{aligned}$$

for the solid displacement, the pore pressure, and the relative displacement, respectively. For simplicity, the explicit statement of the initial conditions in the weak form will be omitted. Also, the Dirichlet boundary conditions will not be incorporated in the weak formulations to ensure a more readable form.

In order to obtain the weak form of the total balance of momentum equation (3.24a) is pre-multiplied with $\bar{u}_i \in \mathcal{V}_0^u$ and integrated over Ω, yielding

$$\int_\Omega \bar{u}_i \sigma_{ij,j}^{\mathrm{tot}} \,\mathrm{d}\Omega - \int_\Omega \bar{u}_i \varrho \ddot{u}_i \,\mathrm{d}\Omega - \int_\Omega \bar{u}_i \varrho_f \ddot{w}_i \,\mathrm{d}\Omega = -\int_\Omega \bar{u}_i F_i \,\mathrm{d}\Omega\ . \tag{3.29}$$

Integrating equation (3.29) by parts and applying the divergence theorem $\int_\Omega (\bar{u}_i \sigma_{ij}^{\mathrm{tot}})_{,j} \,\mathrm{d}\Omega = \int_\Gamma \bar{u}_i \sigma_{ij}^{\mathrm{tot}} n_j \,\mathrm{d}\Gamma$, yields with inserted Neumann boundary conditions (3.25),

$$\int_\Omega \bar{u}_{i,j} \sigma_{ij}^{\mathrm{tot}} \,\mathrm{d}\Omega + \varrho \int_\Omega \bar{u}_i \ddot{u}_i \,\mathrm{d}\Omega + \varrho_f \int_\Omega \bar{u}_i \ddot{w}_i \,\mathrm{d}\Omega = \int_\Omega \bar{u}_i F_i \,\mathrm{d}\Omega + \int_{\Gamma_{\mathsf{N}}^u} (\mathrm{Tr}\ \bar{u}_i) t_i^{\mathrm{tot}} \,\mathrm{d}\Gamma_{\mathsf{N}}^u\ .$$

Inserting relation (2.19) with (2.4) results in

$$\int_\Omega \bar{u}_{i,j} C_{ijk\ell} u_{k,\ell} \,\mathrm{d}\Omega - \alpha \int_\Omega \bar{u}_{i,i} p \,\mathrm{d}\Omega + \varrho \int_\Omega \bar{u}_i \ddot{u}_i \,\mathrm{d}\Omega + \varrho_f \int_\Omega \bar{u}_i \dot{w}_i \,\mathrm{d}\Omega = \int_\Omega \bar{u}_i F_i \,\mathrm{d}\Omega + \int_{\Gamma^u_{\mathsf{N}}} (\mathrm{Tr}\ \bar{u}_i) t_i^{\mathrm{tot}} \,\mathrm{d}\Gamma^u_{\mathsf{N}} \,. \tag{3.30}$$

The weak form of the continuity equation is derived by pre-multiplying equation (3.24b) with the test function $\bar{p} \in \mathcal{V}_0^p$ and integrated over the domain Ω yielding

$$\int_\Omega \bar{p} \dot{w}_{i,i} \,\mathrm{d}\Omega + \alpha \int_\Omega \bar{p} \dot{u}_{i,i} \,\mathrm{d}\Omega + \frac{\phi^2}{R} \int_\Omega \bar{p} \dot{p} \,\mathrm{d}\Omega = 0 \,.$$

Integration by parts and applying the divergence theorem $\int_\Omega (\bar{p}\dot{w}_i)_{,i} \,\mathrm{d}\Omega = \int_\Gamma \bar{p}\dot{w}_i n_i \,\mathrm{d}\Gamma$ results in, after applying the Neumann boundary condition (3.26),

$$-\int_\Omega \bar{p}_{,i} \dot{w}_i \,\mathrm{d}\Omega + \alpha \int_\Omega \bar{p} \dot{u}_{i,i} \,\mathrm{d}\Omega + \frac{\phi^2}{R} \int_\Omega \bar{p} \dot{p} \,\mathrm{d}\Omega = -\int_{\Gamma^p_{\mathsf{N}}} (\mathrm{Tr}\ \bar{p}) g^q \,. \tag{3.31}$$

Note that in equation (3.31) the relation $\dot{w}_i = q_i$ was taken into account.

To derive the weak form of the balance of momentum of the fluid phase equation (3.24c) is pre-multiplied with the test function $\bar{w}_i \in \mathcal{V}_0^w$ and integrated over the domain Ω. Performing some algebraic manipulations results in

$$\int_\Omega \bar{w}_i p_{,i} \,\mathrm{d}\Omega + \frac{1}{\phi}\left[\phi \varrho_f + \varrho_a\right] \int_\Omega \bar{w}_i \dot{w}_i \,\mathrm{d}\Omega + \varrho_f \int_\Omega \bar{w}_i \ddot{u}_i \,\mathrm{d}\Omega + \frac{1}{\kappa} \int_\Omega \bar{w}_i \dot{w}_i \,\mathrm{d}\Omega = \int_\Omega \bar{w}_i f_i^f \,\mathrm{d}\Omega \,. \tag{3.32}$$

Since the Neumann boundary conditions for the fluid phase are already applied in the weak form of the continuity relation (3.31), no Neumann boundary conditions have to be introduced in the weak form of the relative displacement (3.32).

Discretized weak form of the full form u_i, p, w_i

The discretized variational form will only be stated on element level to retain a more readable form. This means that the Dirichlet boundary conditions will be left aside. Thus, the boundary conditions have to be considered in a later step. There exist several methods and a good overview of such methods is given in the book of Jung and Langer [84]. The discrete approximation of the solid displacement, the pore pressure, and the relative displacement is done by

$$u_i \approx \sum_{n \in \widehat{n}_e^u} \varphi^n u_i^n \quad , \quad p \approx \sum_{n \in \widehat{n}_e^p} \vartheta^n p^n \quad , \quad w_i \approx \sum_{n \in \widehat{n}_e^w} \psi^n \bar{w}_i^n \,, \tag{3.33}$$

respectively. Since the approximation order of the different constituents can be different, the corresponding reference element consist of three possible number of nodes, namely $\widehat{n}_e^u, \widehat{n}_e^p$, and $\widehat{n}_e^w$ for the fluid displacement, the pore pressure, and the relative displacement, respectively. The test functions are accordingly approximated by

$$\bar{u}_i \approx \sum_{n \in \widehat{n}_e^u} \varphi^n \bar{u}_i^n \quad , \quad \bar{p} \approx \sum_{n \in \widehat{n}_e^p} \vartheta^n \bar{p}^n \quad , \quad \bar{w}_i \approx \sum_{n \in \widehat{n}_e^w} \psi^n \bar{w}_i^n \; . \tag{3.34}$$

The discrete form of the total balance of momentum is obtained by inserting the above approximations into the weak form (3.30), which yields a set of linear equations of the form

$$\bar{u}_i^n \left[K_{ik}^{nm} u_k^m - G1_i^{nm} p^m + M1_{ik}^{nm} \ddot{u}_k^m + M2_{ik}^{nm} \ddot{w}_k^m - (f_i^n)^u \right] = 0 \; .$$

Since $\bar{u}_i^n$ is arbitrary, the term in the square brackets must vanish and the above equation reduces to

$$K_{ik}^{nm} u_k^m - G1_i^{nm} p^m + M1_{ik}^{nm} \ddot{u}_k^m + M2_{ik}^{nm} \ddot{w}_k^m = (f_i^n)^u \; . \tag{3.35}$$

The single components of the left-hand side of equation (3.35) are given as follows

$$\begin{aligned}
K_{ik}^{nm} &= \int_{\widehat{\tau}_e} \varphi_{,j}^n C_{ijk\ell} \varphi_{,\ell}^m \, \mathcal{J}_e \, \mathrm{d}\boldsymbol{\xi} \\
G1_i^{nm} &= \alpha \int_{\widehat{\tau}_e} \varphi_{,i}^n \vartheta^m \, \mathcal{J}_e \, \mathrm{d}\boldsymbol{\xi} \\
M1_{ik}^{nm} &= \varrho \delta_{ik} \int_{\widehat{\tau}_e} \varphi^n \varphi^m \, \mathcal{J}_e \, \mathrm{d}\boldsymbol{\xi} \\
M2_{ik}^{nm} &= \varrho_f \delta_{ik} \int_{\widehat{\tau}_e} \varphi^n \psi^m \, \mathcal{J}_e \, \mathrm{d}\boldsymbol{\xi}
\end{aligned} \tag{3.36}$$

and the right-hand side reads as

$$(f_i^n)^u = \int_{\widehat{\tau}_e} \varphi^n F_i \, \mathcal{J}_e \, \mathrm{d}\boldsymbol{\xi} + \int_{\widehat{\Gamma}_b} \varphi_\Gamma^n t_i^{\mathrm{tot}} \, \mathcal{J}_b \, \mathrm{d}\boldsymbol{\xi} \; .$$

To obtain the discrete form of the continuity relation the approximations (3.33) and (3.34) are inserted into the weak form (3.31), which yields a set of linear equations of the form

$$\bar{p}^n \left[-C3_k^{nm} \dot{w}_k^m + P^{nm} \dot{p}^m + C2_k^{nm} \dot{u}_k^m + (f1^n)^p \right] = 0 \; .$$

Again, since $\bar{p}_i^n$ is arbitrary, the term in the square brackets must vanish and the above equation reduces to

$$-C3_k^{nm} \dot{w}_k^m + P^{nm} \dot{p}^m + C2_k^{nm} \dot{u}_k^m = -(f1^n)^p \; . \tag{3.37}$$

The single components of the left-hand side of equation (3.37) reads as

$$C2_k^{nm} = \alpha \int_{\widehat{\tau}_e} \vartheta^n \varphi^m_{,k} \, \mathcal{J}_e \, \mathrm{d}\boldsymbol{\xi}$$

$$P^{nm} = \frac{\phi^2}{R} \int_{\widehat{\tau}_e} \vartheta^n \vartheta^m \, \mathcal{J}_e \, \mathrm{d}\boldsymbol{\xi}$$

$$C3_k^{nm} = \int_{\widehat{\tau}_e} \vartheta^n_{,k} \psi^m \, \mathcal{J}_e \, \mathrm{d}\boldsymbol{\xi}$$

and the right-hand side reads as

$$(f1^n)^p = \int_{\widehat{\Upsilon}_b} \vartheta^n_\Gamma g^q \, \mathcal{J}_b \, \mathrm{d}\boldsymbol{\xi} \ .$$

Inserting the approximations (3.33) and (3.34) into the weak form (3.32) yields the discrete weak form of the fluid phase

$$G2_i^{nm} p^m + M3_{ik}^{nm} \ddot{w}_k^m + (M2_{ik}^{nm})^T \ddot{u}_k^m + C1_{ik}^{nm} \dot{\bar{w}}_k^m = (f1_i^n)^w \ ,$$

for arbitrary $\bar{w}_i^n$. The above components of the left-hand side are given in detail by

$$G2_i^{nm} = \int_{\widehat{\tau}_e} \psi^n \vartheta^m_{,i} \, \mathcal{J}_e \, \mathrm{d}\boldsymbol{\xi}$$

$$M3_{ik}^{nm} = \delta_{ik} \frac{1}{\phi} \left[\phi \, \varrho_f + \varrho_a \right] \int_{\widehat{\tau}_e} \psi^n \psi^m \, \mathcal{J}_e \, \mathrm{d}\boldsymbol{\xi}$$

$$(M2_{ik}^{nm})^T = \delta_{ik} \varrho_f \int_{\widehat{\tau}_e} \psi^n \varphi^m \, \mathcal{J}_e \, \mathrm{d}\boldsymbol{\xi}$$

$$C1_{ik}^{nm} = \delta_{ik} \frac{1}{\kappa} \int_{\widehat{\tau}_e} \psi^n \psi^m \, \mathcal{J}_e \, \mathrm{d}\boldsymbol{\xi}$$

and the right-hand side is given by

$$(f1_i^n)^w = \int_{\widehat{\tau}_e} \psi^n f_i^f \, \mathcal{J}_e \, \mathrm{d}\boldsymbol{\xi}.$$

The whole system u_i, p, w_i To give an overview of the whole equation system of the porous medium in its full form, it is presented in matrix notation

$$\begin{bmatrix} \mathbf{M1} & \mathbf{0} & \mathbf{M2} \\ \mathbf{0} & \mathbf{0} & \mathbf{0} \\ \mathbf{M2}^T & \mathbf{0} & \mathbf{M3} \end{bmatrix} \begin{bmatrix} \ddot{\mathbf{u}} \\ \ddot{\mathbf{p}} \\ \ddot{\mathbf{w}} \end{bmatrix} + \begin{bmatrix} \mathbf{0} & \mathbf{0} & \mathbf{0} \\ \mathbf{C2} & \mathbf{P} & -\mathbf{C3} \\ \mathbf{0} & \mathbf{0} & \mathbf{C1} \end{bmatrix} \begin{bmatrix} \dot{\mathbf{u}} \\ \dot{\mathbf{p}} \\ \dot{\mathbf{w}} \end{bmatrix} + \begin{bmatrix} \mathbf{K} & \mathbf{G}_1 & \mathbf{0} \\ \mathbf{0} & \mathbf{0} & \mathbf{0} \\ \mathbf{0} & \mathbf{G2} & \mathbf{0} \end{bmatrix} \begin{bmatrix} \mathbf{u} \\ \mathbf{p} \\ \mathbf{w} \end{bmatrix} = \begin{bmatrix} \mathbf{f}^u \\ -\mathbf{f1}^p \\ \mathbf{f1}^w \end{bmatrix} . \tag{3.38}$$

The above equation system is not symmetric. If a symmetric equation system is desired this can be obtained by using the time integrated form of the continuity equation (3.24b), which shifts the equation from the so called damping matrix to the stiffness matrix. For completeness also this case will be presented.

3.2.2 The symmetric full form u_i, p, w_i

In order to derive the weak and discrete form of the time integrated continuity relation equation (3.24b) is integrated in time, multiplied with the test function $\bar{p} \in \mathcal{V}_0^p$ and integrated over the domain Ω, yielding

$$-\int_\Omega \bar{p} w_{i,i} \,\mathrm{d}\Omega - \alpha \int_\Omega \bar{p} u_{i,i} \,\mathrm{d}\Omega - \frac{\phi^2}{R} \int_\Omega \bar{p} p \,\mathrm{d}\Omega = 0 \,.$$

Note that in this case the boundary conditions of the fluid will be incorporated in the balance of momentum of the fluid and, thus, different handled as for the non-symmetric formulation. Inserting the approximations (3.33) and (3.34) results in the discrete variational formulation

$$-(G1_k^{nm})^T u_k^m - (P_k^{nm}) p^m - (G3_k^{nm})^T w_k^m = 0 \,,$$

with the yet unknown components defined by

$$(G1_k^{nm})^T = \alpha \int_{\widehat{\tau}_e} \vartheta^n \varphi_{,k}^m \mathcal{J}_e \,\mathrm{d}\boldsymbol{\xi}$$

$$(G3_k^{nm})^T = \int_{\widehat{\tau}_e} \vartheta^n \psi_{,k}^m \mathcal{J}_e \,\mathrm{d}\boldsymbol{\xi} \,.$$

Next, the weak and discrete form of the momentum of balance of the fluid phase is derived. For a symmetric formulation equation (3.24c) is pre-multiplied with the test function $\bar{w}_i \in \mathcal{V}_0^w$ and integrated over the domain Ω. Additional algebraic manipulations result in

$$\int_\Omega \bar{w}_i p_{,i} \,\mathrm{d}\Omega + \frac{1}{\phi}\left[\phi \varrho_f + \varrho_a\right] \int_\Omega \bar{w}_i \ddot{w}_i \,\mathrm{d}\Omega + \varrho_f \int_\Omega \bar{w}_i \ddot{u}_i \,\mathrm{d}\Omega + \frac{1}{\kappa} \int_\Omega \bar{w}_i \dot{w}_i \,\mathrm{d}\Omega = \int_\Omega \bar{w}_i f_i^f \,\mathrm{d}\Omega \,. \tag{3.39}$$

To introduce natural boundary conditions the first integral of equation (3.39) is integrated by parts. Taking into account the divergence theorem $\int_\Omega (\bar{w}_i \sigma_{ij}^f)_{,j} \,\mathrm{d}\Omega = \int_\Gamma \bar{w}_i \sigma_{ij}^f n_j \,\mathrm{d}\Gamma$ and applying the Neumann boundary conditions (3.27) yields

$$\begin{aligned} -\int_\Omega \bar{w}_{i,i} p \,\mathrm{d}\Omega + \frac{1}{\phi}\left[\phi \varrho_f + \varrho_a\right] \int_\Omega \bar{w}_i \ddot{w}_i \,\mathrm{d}\Omega + \varrho_f \int_\Omega \bar{w}_i \ddot{u}_i \,\mathrm{d}\Omega + \frac{1}{\kappa} \int_\Omega \bar{w}_i \dot{w}_i \,\mathrm{d}\Omega = \\ \int_\Omega \bar{w}_i f_i^f \,\mathrm{d}\Omega - \int_{\Gamma_{\mathsf{N}}^w} (\mathrm{Tr}\ \bar{w}_i) t_i^p \,\mathrm{d}\Gamma_{\mathsf{N}}^w \,. \end{aligned} \tag{3.40}$$

The approximations (3.33) and (3.34) inserted in equation (3.40) yield the discrete variational formulation

$$-G3_i^{nm} p^m + M3_{ik}^{nm} \ddot{w}_k^m + (M2_{ik}^{nm})^T \ddot{u}_k^m + C1_{ik}^{nm} \dot{w}_k^m = (f2_i^n)^w \; .$$

The still unknown component of the left-hand side is

$$G3_i^{nm} = \int\limits_{\widehat{\tau}_e} \psi_{,i}^n \vartheta^m \, \mathcal{J}_e \, \mathrm{d}\boldsymbol{\xi}$$

and the right-hand side is

$$(f2_i^n)^w = \int\limits_{\widehat{\tau}_e} \psi^n f_i^f \, \mathcal{J}_e \, \mathrm{d}\boldsymbol{\xi} - \int\limits_{\widehat{\Gamma}_b} \psi_\Gamma^n t_i^p \, \mathcal{J}_b \, \mathrm{d}\boldsymbol{\xi} \; .$$

Finally, the whole symmetric system written in matrix notation reads as

$$\begin{bmatrix} \mathbf{M1} & \mathbf{0} & \mathbf{M2} \\ \mathbf{0} & \mathbf{0} & \mathbf{0} \\ \mathbf{M2}^T & \mathbf{0} & \mathbf{M3} \end{bmatrix} \begin{bmatrix} \ddot{\mathbf{u}} \\ \ddot{\mathbf{p}} \\ \ddot{\mathbf{w}} \end{bmatrix} + \begin{bmatrix} \mathbf{0} & \mathbf{0} & \mathbf{0} \\ \mathbf{0} & \mathbf{0} & \mathbf{0} \\ \mathbf{0} & \mathbf{0} & \mathbf{C1} \end{bmatrix} \begin{bmatrix} \dot{\mathbf{u}} \\ \dot{\mathbf{p}} \\ \dot{\mathbf{w}} \end{bmatrix} + \begin{bmatrix} \mathbf{K} & -\mathbf{G1} & \mathbf{0} \\ -\mathbf{G1}^T & -\mathbf{P} & -\mathbf{G3}^T \\ \mathbf{0} & -\mathbf{G3} & \mathbf{0} \end{bmatrix} \begin{bmatrix} \mathbf{u} \\ \mathbf{p} \\ \mathbf{w} \end{bmatrix} = \begin{bmatrix} \mathbf{f}^u \\ \mathbf{0} \\ \mathbf{f2}^w \end{bmatrix} . \tag{3.41}$$

If the boundary conditions for the flux and the pore pressure (3.27) are given, the symmetric system can be used. In the other case, when the boundary conditions for the pore pressure and the relative displacement (3.26) are given, the system (3.38) has to be used. Alternatively, the boundary conditions have to be reformulated appropriately for the desired FEM formulation.

3.2.3 The irreducible form u_i, w_i

If the fluid of the porous media is assumed compressible the pore pressure can be eliminated (2.28) [158]. The remaining primary variables are consequently the solid- and relative displacement.

Weak form

For simplicity, the pore pressure (2.28) is directly inserted into the weak form of the balance of momentum of the total mixture (3.30), yielding

$$\begin{aligned} \int\limits_\Omega \bar{u}_{i,j} C_{ijk\ell} u_{k,\ell} \, \mathrm{d}\Omega - \alpha \int\limits_\Omega \bar{u}_{i,i} \left[-\frac{R}{\phi^2} \left(w_{k,k} + \alpha u_{k,k} \right) \right] \mathrm{d}\Omega + \varrho \int\limits_\Omega \bar{u}_i \ddot{u}_i \, \mathrm{d}\Omega \\ + \varrho_f \int\limits_\Omega \bar{u}_i \ddot{w}_i \, \mathrm{d}\Omega = \int\limits_\Omega \bar{u}_i F_i \, \mathrm{d}\Omega + \int_{\Gamma_{\mathsf{N}}^u} (\mathrm{Tr}\, \bar{u}_i) t_i^{\mathrm{tot}} \, \mathrm{d}\Gamma_{\mathsf{N}}^u \; . \end{aligned}$$

and reads after rearranging as

$$\int_\Omega \bar{u}_{i,j} C_{ijk\ell} u_{k,\ell} \,\mathrm{d}\Omega + \frac{R}{\phi^2}\alpha \int_\Omega \bar{u}_{i,i} w_{k,k} \,\mathrm{d}\Omega + \frac{R}{\phi^2}\alpha^2 \int_\Omega \bar{u}_{i,i} u_{k,k} \,\mathrm{d}\Omega + \varrho \int_\Omega \bar{u}_i \ddot{u}_i \,\mathrm{d}\Omega + \varrho_f \int_\Omega \bar{u}_i \ddot{w}_i \,\mathrm{d}\Omega = \int_\Omega \bar{u}_i F_i \,\mathrm{d}\Omega + \int_{\Gamma_\mathsf{N}^u} (\mathrm{Tr}\ \bar{u}_i) t_i^{\mathrm{tot}} \,\mathrm{d}\Gamma_\mathsf{N}^u \,.$$

Inserting the approximations (3.33) and (3.34) yields the discrete form

$$K_{ik}^{nm} u_k^m + G5_{ik}^{nm} w_k^m + G4_{ik}^{nm} u_k^m + M1_{ik}^{nm} \ddot{u}_k^m + M2_{ik}^{nm} \ddot{u}_k^m = (f_i^n)^u \,,$$

where the new components are

$$G4_{ik}^{nm} = \frac{R}{\phi^2}\alpha^2 \int_{\widehat{\tau}_e} \varphi_{,i}^n \varphi_{,k}^m \,\mathcal{J}_e \,\mathrm{d}\boldsymbol{\xi}$$

$$G5_{ik}^{nm} = \frac{R}{\phi^2}\alpha \int_{\widehat{\tau}_e} \varphi_{,i}^n \psi_{,k}^m \,\mathcal{J}_e \,\mathrm{d}\boldsymbol{\xi} \,.$$

The weak form for the fluid phase is obtained in the same manner. Thus, the pore pressure (2.28) is directly inserted into the weak form of the balance of momentum of the fluid (3.40) and is written as

$$-\int_\Omega \bar{w}_{i,i} \left[-\frac{R}{\phi^2} \left(w_{k,k} + \alpha u_{k,k} \right) \right] \mathrm{d}\Omega + \frac{1}{\phi} \left[\phi \varrho_f + \varrho_a \right] \int_\Omega \bar{w}_i \ddot{w}_i \,\mathrm{d}\Omega + \varrho_f \int_\Omega \bar{w}_i \ddot{u}_i \,\mathrm{d}\Omega + \frac{1}{\kappa} \int_\Omega \bar{w}_i \dot{w}_i \,\mathrm{d}\Omega = \int_\Omega \bar{w}_i f_i^f \,\mathrm{d}\Omega - \int_{\Gamma_\mathsf{N}^w} (\mathrm{Tr}\ \bar{w}_i) t_i^p \,\mathrm{d}\Gamma_\mathsf{N}^w \,,$$

which can be rearranged to

$$\frac{R}{\phi^2} \int_\Omega \bar{w}_{i,i} w_{k,k} \,\mathrm{d}\Omega + \frac{R}{\phi^2}\alpha \int_\Omega \bar{w}_{i,i} u_{k,k} \,\mathrm{d}\Omega + \frac{1}{\phi} \left[\phi \varrho_f + \varrho_a \right] \int_\Omega \bar{w}_i \ddot{w}_i \,\mathrm{d}\Omega + \varrho_f \int_\Omega \bar{w}_i \ddot{u}_i \,\mathrm{d}\Omega + \frac{1}{\kappa} \int_\Omega \bar{w}_i \dot{w}_i \,\mathrm{d}\Omega = \int_\Omega \bar{w}_i f_i^f \,\mathrm{d}\Omega - \int_{\Gamma_\mathsf{N}^w} (\mathrm{Tr}\ \bar{w}_i) t_i^p \,\mathrm{d}\Gamma_\mathsf{N}^w \,.$$

Inserting the approximations (3.33) and (3.34) yields the discrete form

$$G6_{ik}^{nm} w_k^m + (G5_{ik}^{nm})^T u_k^m + M3_{ik}^{nm} \ddot{w}_k^m + (M2_{ik}^{nm})^T \ddot{u}_k^m + C1_{ik}^{nm} \dot{w}_k^m = (f2_i^n)^w$$

with the new components given as

$$(G5_{ik}^{nm})^T = \frac{R}{\phi^2}\alpha \int_{\widehat{\tau}_e} \psi_{,i}^n \varphi_{,k}^m \,\mathcal{J}_e \,\mathrm{d}\boldsymbol{\xi}$$

$$G6_{ik}^{nm} w_k^m = \bar{w}_i^n \frac{R}{\phi^2} \int_{\widehat{\tau}_e} \psi_{,i}^n \psi_{,k}^m \,\mathcal{J}_e \,\mathrm{d}\boldsymbol{\xi} \,.$$

The whole u_i, w_i-system written in matrix notation is

$$\begin{bmatrix} \mathbf{M1} & \mathbf{M2} \\ \mathbf{M2}^T & \mathbf{M3} \end{bmatrix} \begin{bmatrix} \ddot{\mathbf{u}} \\ \ddot{\mathbf{w}} \end{bmatrix} + \begin{bmatrix} \mathbf{0} & \mathbf{0} \\ \mathbf{0} & \mathbf{C1} \end{bmatrix} \begin{bmatrix} \dot{\mathbf{u}} \\ \dot{\mathbf{w}} \end{bmatrix} + \begin{bmatrix} \mathbf{K}+\mathbf{G4} & \mathbf{G5} \\ \mathbf{G5}^T & \mathbf{G6} \end{bmatrix} \begin{bmatrix} \mathbf{u} \\ \mathbf{w} \end{bmatrix} = \begin{bmatrix} \mathbf{f}^u \\ \mathbf{f2}^w \end{bmatrix} . \tag{3.42}$$

It is observable that also the irreducible system (3.42) is symmetric. For the case of an incompressible fluid the reduced u_i, w_i-form is only applicable if a penalty formulation is used [158]. Penalty methods for incompressible constituents may be found nearly in every book about the finite element method, e.g., [22, 82, 165].

3.2.4 The u_i, p form in time domain

As already mentioned in section 2.2.3 the elimination of the relative displacement w_i can only be accomplished when inertia terms in the equation of motion (2.25) are neglected. This simplification is reasonable for medium speed phenomena [158]. Thus, the remaining variables are the solid displacement u_i and the pore pressure p. The application of this simplified model will be validated with some numerical examples (cf. section 5.2). In the following, the discrete variational formulation will be derived.

Weak form

The relevant weak form is derived in the same manner as above. Therefore, the simplified total balance of momentum (2.29) is pre-multiplied with the test function $\bar{u}_i \in \mathcal{V}_0^u$ and integrated over the domain Ω

$$\int_\Omega \bar{u}_i \sigma_{ij,j}^{\mathrm{tot}} \,\mathrm{d}\Omega - \int_\Omega \bar{u}_i \varrho \ddot{u}_i \,\mathrm{d}\Omega + \int_\Omega \bar{u}_i F_i \,\mathrm{d}\Omega = 0 \,. \tag{3.43}$$

Next, the first integral of (3.43) is integrated and the divergence theorem $\int_\Omega (\bar{u}_i \sigma_{ij}^{\mathrm{tot}})_{,j} \,\mathrm{d}\Omega = \int_\Gamma \bar{u}_i \sigma_{ij}^{\mathrm{tot}} n_j \,\mathrm{d}\Gamma$ is applied, which yields with inserted boundary conditions (3.25)

$$\int_\Omega \bar{u}_{i,j} \sigma_{ij}^{\mathrm{tot}} \,\mathrm{d}\Omega + \varrho \int_\Omega \bar{u}_i \ddot{u}_i \,\mathrm{d}\Omega = \int_\Omega \bar{u}_i F_i \,\mathrm{d}\Omega + \int_{\Gamma_{\mathsf{N}}^u} (\mathrm{Tr}\ \bar{u}_i) t_i^{\mathrm{tot}} \,\mathrm{d}\Gamma_{\mathsf{N}}^u \,.$$

Inserting relation (2.19) with (2.4) results in

$$\int_\Omega \bar{u}_{i,j} C_{ijk\ell} u_{k,\ell} \,\mathrm{d}\Omega - \alpha \int_\Omega \bar{u}_{i,i} p \,\mathrm{d}\Omega + \varrho \int_\Omega \bar{u}_i \ddot{u}_i \,\mathrm{d}\Omega = \int_\Omega \bar{u}_i F_i \,\mathrm{d}\Omega + \int_{\Gamma_{\mathsf{N}}^u} (\mathrm{Tr}\ \bar{u}_i) t_i^{\mathrm{tot}} \,\mathrm{d}\Gamma_{\mathsf{N}}^u \,.$$

Applying the approximations (3.33) and (3.34) yields the discrete form of the approximated total balance of momentum for any nonzero $\bar{u}_i^n$

$$K_{ik}^{nm} u_k^m - G1_i^{nm} p + M1_{ik}^{nm} \ddot{u}_k^m = (f_i^n)^u \,,$$

with the single components defined in (3.36). To obtain the weak form related to the pore pressure the simplified flux (2.30) is inserted into equation (2.31). Taking into account the relation $\dot{w}_i = q_i$ results in

$$\kappa \int_\Omega \bar{p}_{,i} p_{,i} \,\mathrm{d}\Omega + \kappa \varrho_f \int_\Omega \bar{p}_{,i} \ddot{u}_i \,\mathrm{d}\Omega + \alpha \int_\Omega \bar{p} \dot{u}_{i,i} \,\mathrm{d}\Omega + \frac{\phi^2}{R} \int_\Omega \bar{p} \dot{p} \,\mathrm{d}\Omega = \kappa \int_\Omega \bar{p}_{,i} f_i^f \,\mathrm{d}\Omega - \int_{\Gamma_\mathrm{N}^p} (\mathrm{Tr}\ \bar{p}) g^q .$$

The discrete form for nonzero $\bar{p}^n$ is obtained by inserting the approximations (3.33) and (3.34)

$$G7^{nm} p^m + M4_k^{nm} \ddot{u}_k^m + C2_k^{nm} \dot{u}_k^m + P^{nm} \dot{p}^m = (f2^n)^p \ ,$$

with the coefficients

$$\begin{aligned} G7^{nm} &= \kappa \int_{\widehat{\tau}_e} \vartheta_{,i}^n \vartheta_{,i}^m \mathcal{J}_e \,\mathrm{d}\boldsymbol{\xi} \\ M4^{nm} &= \kappa \varrho_f \delta_{ij} \int_{\widehat{\tau}_e} \vartheta_{,i}^n \varphi^m \mathcal{J}_e \,\mathrm{d}\boldsymbol{\xi} \\ (f2^n)^p &= \kappa \int_{\widehat{\tau}_e} \vartheta_{,i}^n f_i^f \mathcal{J}_e \,\mathrm{d}\boldsymbol{\xi} - \int_{\widehat{\Upsilon}_b} \vartheta_\Gamma^n q^q \mathcal{J}_b \,\mathrm{d}\boldsymbol{\xi} \ . \end{aligned}$$

The whole system written in matrix notation reads as

$$\begin{bmatrix} \mathbf{M1} & \mathbf{0} \\ \mathbf{M4} & \mathbf{0} \end{bmatrix} \begin{bmatrix} \ddot{\mathbf{u}} \\ \ddot{\mathbf{p}} \end{bmatrix} + \begin{bmatrix} \mathbf{0} & \mathbf{0} \\ \mathbf{C2} & \mathbf{P} \end{bmatrix} \begin{bmatrix} \dot{\mathbf{u}} \\ \dot{\mathbf{p}} \end{bmatrix} + \begin{bmatrix} \mathbf{K} & -\mathbf{G1} \\ \mathbf{0} & \mathbf{G7} \end{bmatrix} \begin{bmatrix} \mathbf{u} \\ \mathbf{p} \end{bmatrix} = \begin{bmatrix} \mathbf{f}^u \\ \mathbf{f2}^p \end{bmatrix} , \tag{3.44}$$

which is not symmetric.

3.2.5 The u_i, p form in Laplace domain

For completeness, also the finite element formulation of the u_i, p form in Laplace domain will be presented. This formulation is of most interest, since an analytic one-dimensional infinite element can be deduced for this poroelastic form, as will be shown in section 4.3.1. Moreover, no relative inertia terms have to be neglected to derive the u_i, p formulation in Laplace domain. This is the case when a u_i, p formulation in time domain is desired (cf. section 2.2.6). Assuming vanishing initial conditions (2.32) during the Laplace transformation, the strong form of the problem reads as

$$\hat{\sigma}_{ij,j}^{\mathrm{tot}} - \mathrm{s}^2(\varrho - \beta\varrho_f)\hat{u}_i + \beta \hat{p}_{,i} + \hat{F}_i = 0 \tag{3.45a}$$

$$\hat{q}_{i,i} + \mathrm{s}\alpha \hat{u}_{i,i} + \mathrm{s}\frac{\phi^2}{R}\hat{p} = 0 \ , \tag{3.45b}$$

by using equations (2.33) and (2.35), with inserted relative displacement $\hat{w}_i$ of (2.36), respectively. Moreover, the relation $\hat{q}_i = \mathrm{s}\hat{w}_i$ is used. The unknown functions are

$$\begin{aligned} \hat{u}_i &= \hat{u}_i(\mathbf{x}) \ , \quad \mathbf{x} \in \overline{\Omega} \\ \hat{p} &= \hat{p}(\mathbf{x}) \ , \quad \mathbf{x} \in \overline{\Omega} \ . \end{aligned}$$

The Laplace transformed boundary conditions (3.25) and (3.26) for the solid phase and fluid phase, respectively, are given as

$$\begin{aligned} \Gamma &= \Gamma^u_{\mathsf{D}} \cup \Gamma^u_{\mathsf{N}} \\ \hat{u}_i(\mathbf{y}) &= \hat{g}^u_i \quad , \qquad \mathbf{y} \in \Gamma^u_{\mathsf{D}} \\ \hat{\sigma}^{\mathrm{tot}}_{ij} n_j(\mathbf{y}) &= \hat{t}^{\mathrm{tot}}_i \quad , \qquad \mathbf{y} \in \Gamma^u_{\mathsf{N}} \ , \end{aligned} \tag{3.46}$$

$$\begin{aligned} \Gamma &= \Gamma^p_{\mathsf{D}} \cup \Gamma^p_{\mathsf{N}} \\ \hat{p}(\mathbf{y}) &= \hat{g}^p \quad , \qquad \mathbf{y} \in \Gamma^p_{\mathsf{D}} \\ \hat{q}_i n_i(\mathbf{y}) &= \hat{g}^q \quad , \qquad \mathbf{y} \in \Gamma^p_{\mathsf{N}} \ . \end{aligned} \tag{3.47}$$

The variational weak form is obtained by performing the same steps as in time domain.

Discrete weak form of the total balance of momentum To obtain the weak form, equation (3.45a) is pre-multiplied with the test function $\hat{\tilde{u}} \in \mathcal{V}^u_0$ and integrated over the domain Ω, yielding

$$\int_\Omega \hat{\tilde{u}}_i \hat{\sigma}^{\mathrm{tot}}_{ij,j} \, \mathrm{d}\Omega - \mathrm{s}^2(\varrho - \beta \varrho_f) \int_\Omega \hat{\tilde{u}}_i \hat{u}_i \, \mathrm{d}\Omega + \beta \int_\Omega \hat{\tilde{u}}_i \hat{p}_{,i} \, \mathrm{d}\Omega + \int_\Omega \hat{\tilde{u}}_i \hat{F}_i \, \mathrm{d}\Omega = 0 \ . \tag{3.48}$$

Integrating equation (3.48) by parts and applying the divergence theorem $\int_\Omega (\hat{\tilde{u}}_i \hat{\sigma}^{\mathrm{tot}}_{ij})_{,j} \Omega = \int_\Gamma \hat{\tilde{u}}_i \hat{\sigma}^{\mathrm{tot}}_{ij} n_j \Gamma$, yields with inserted boundary condition (3.46)

$$\begin{aligned} \int_\Omega \hat{\tilde{u}}_{i,j} C_{ijk\ell} \hat{u}_{k,\ell} \, \mathrm{d}\Omega - \alpha \int_\Omega \hat{\tilde{u}}_{i,i} \hat{p} \, \mathrm{d}\Omega + \mathrm{s}^2(\varrho - \beta \varrho_f) \int_\Omega \hat{\tilde{u}}_i \hat{u}_i \, \mathrm{d}\Omega - \beta \int_\Omega \hat{\tilde{u}}_i \hat{p}_{,i} \, \mathrm{d}\Omega = \\ \int_\Omega \hat{\tilde{u}}_i \hat{F}_i \, \mathrm{d}\Omega + \int_{\Gamma^u_{\mathsf{N}}} (\mathrm{Tr}\ \hat{\tilde{u}}_i) \hat{t}^{\mathrm{tot}}_i \, \mathrm{d}\Gamma^u_{\mathsf{N}} \ . \end{aligned} \tag{3.49}$$

Note that equation (3.49) is derived using the relation (2.19) with (2.4). Inserting the Laplace transformed approximations (3.33) and (3.34) into the weak form (3.49) yields a set of linear equations

$$K^{nm}_{ik} \hat{w}^m_k - G1^{nm}_i \hat{p}^m + H1^{nm}_{ik} \hat{u}^m_k - H2^{nm}_i \hat{p}^m = (\hat{f}^n_i)^u \ . \tag{3.50}$$

The yet unassigned components of equation (3.50) are

$$H1_{ik}^{nm} = \mathrm{s}^2(\varrho - \beta\varrho_f)\delta_{ik}\int_{\widehat{\tau}_e} \varphi^n\varphi^m\,\mathcal{J}_e\,\mathrm{d}\boldsymbol{\xi}$$

$$H2_{i}^{nm} = \beta\,\delta_{ik}\int_{\widehat{\tau}_e} \varphi^n\psi^m_{,i}\,\mathcal{J}_e\,\mathrm{d}\boldsymbol{\xi}$$

and the right-hand side reads as

$$(\hat{f}_i^n)^u = \int_{\widehat{\tau}_e} \varphi^n\hat{F}_i\,\mathcal{J}_e\,\mathrm{d}\boldsymbol{\xi} + \int_{\widehat{\Upsilon}_b} \varphi^n_\Gamma\hat{t}_i^{\mathrm{tot}}\,\mathcal{J}_b\,\mathrm{d}\boldsymbol{\xi}\ .$$

Discrete weak form of the fluid phase Here, equation (3.45b) is multiplied with the test function $\hat{\bar{p}} \in \mathcal{V}_0^p$ and integrated over the domain Ω, resulting in

$$\int_\Omega \hat{\bar{p}}\hat{q}_{i,i}\,\mathrm{d}\Omega + \mathrm{s}\alpha\int_\Omega \hat{\bar{p}}\hat{u}_{k,k}\,\mathrm{d}\Omega + \mathrm{s}\frac{\phi^2}{R}\int_\Omega \hat{\bar{p}}\hat{p}\,\mathrm{d}\Omega = 0\ . \tag{3.51}$$

Partial integration and the application of the divergence theorem to equation (3.51) yields, after inserting the boundary conditions (3.47),

$$\int_\Omega \hat{\bar{p}}_{,i}\hat{q}_i\,\mathrm{d}\Omega - \mathrm{s}\alpha\int_\Omega \hat{\bar{p}}\hat{u}_{k,k}\,\mathrm{d}\Omega - \mathrm{s}\frac{\phi^2}{R}\int_\Omega \hat{\bar{p}}\hat{p}\,\mathrm{d}\Omega = -\int_{\Gamma_{\mathrm{N}}^p}(\mathrm{Tr}\ \hat{\bar{p}})\hat{g}^q\ .$$

Using the relation $\hat{q}_i = \mathrm{s}\hat{w}_i$ with the definition of the relative displacement (2.36) results in the final weak form of the fluid phase

$$-\frac{\beta}{\mathrm{s}\varrho_f}\int_\Omega \hat{\bar{p}}_{,k}\hat{p}_{,k}\,\mathrm{d}\Omega - \beta\mathrm{s}\int_\Omega \hat{\bar{p}}_{,k}\hat{u}_k\,\mathrm{d}\Omega - \mathrm{s}\alpha\int_\Omega \hat{\bar{p}}\hat{u}_{k,k}\,\mathrm{d}\Omega - \mathrm{s}\frac{\phi^2}{R}\int_\Omega \hat{\bar{p}}\hat{p}\,\mathrm{d}\Omega = -\int_{\Gamma_{\mathrm{N}}^p}(\mathrm{Tr}\ \hat{\bar{p}})\hat{g}^q\ . \tag{3.52}$$

Inserting the Laplace transformed approximations (3.33) and (3.34) into the above weak form (3.52) yields

$$-H3^{nm}\hat{p}_k^m - H4_k^{nm}\hat{u}^m - \mathrm{s}C2_k^{nm}\hat{u}_k^m - \mathrm{s}P^{nm}\hat{p}^m = (\hat{f}3^n)^p\ . \tag{3.53}$$

The new components of (3.53) are as follows

$$H3^{nm} = \frac{\beta}{\mathrm{s}\varrho_f}\int_{\widehat{\tau}_e} \vartheta^n_{,k}\vartheta^m_{,k}\,\mathcal{J}_e\,\mathrm{d}\boldsymbol{\xi}$$

$$H4_k^{nm} = \mathrm{s}\beta \int_{\widehat{\tau}_e} \vartheta_{,k}^n \varphi^m \, \mathcal{J}_e \, \mathrm{d}\boldsymbol{\xi}$$

and the right-hand side reads as

$$(\hat{f}3^n)^p = \int_{\widehat{\Upsilon}_b} \vartheta_\Gamma^n \hat{g}^q \, \mathcal{J}_b \, \mathrm{d}\boldsymbol{\xi} \ .$$

The whole system written in matrix notation is

$$\begin{bmatrix} \mathbf{K} - \mathbf{H2} & -\mathbf{G1} + \mathbf{H1} \\ -\mathbf{H4} - \mathrm{s}\mathbf{C2} & -\mathbf{H3} - \mathrm{s}\mathbf{P} \end{bmatrix} \begin{bmatrix} \hat{\mathbf{u}} \\ \hat{\mathbf{p}} \end{bmatrix} = \begin{bmatrix} \hat{\mathbf{f}}^u \\ \hat{\mathbf{f}}^p \end{bmatrix} .$$

The finite element formulation in Laplace domain for any other poroelastic formulation, i.e., the u_i, p-form in time domain, the u_i, w_i-, and the u_i, p, w_i-form is obtained by performing the same steps as above.

Remark on the quasi-static solution The main interest in quasi-static poroelasticity is to calculate the consolidation of the porous material. To obtain more insight about the behavior of saturated porous media under quasi-static circumstances the reader is referred to, e.g., the work of Zienkiewicz et al. [160]. The quasi-static solution of the above formulations is simply deduced by neglecting all inertia terms. Since this procedure is rather straight forward, the derivation of the quasi-static solution will be skipped in this thesis.

3.2.6 Approximation order of mixed poroelastic formulation

In the previous section, various finite element formulations for a poroelastic material were presented. It remains to choose a proper approximation order of the single constituents. However, it must be emphasized that arbitrary combinations of approximation orders can lead to unphysical behavior of the solutions or to poor numerical performance. Their proper choice is limited by the Babuška-Brezzi condition [15, 16, 44], which has to be satisfied. For the general case, a wide choice of shape functions for the different constituents is possible. For example, all primary unknowns of any finite element formulation of poroelastic material can be approximated by the same order [127, 158]. However, since first order spatial derivatives are present in the weak formulations, C_0 shape functions have to be used at least [165].

For the case of the u_i, p finite element formulation, i.e., the solid displacement and pore pressure are the primary variables, Lewis and Schrefler [95] and Zienkiewicz et al. [163] reveal to use different approximation orders for the undrained limit. In this limit, the permeability matrix **G7** and compressibility matrix **P** are set to zero. Thus, in the equation

(3.44) zero diagonal terms appear. The resulting matrices of this limiting case are then identical to such matrices occurring when solving problems of incompressible elasticity or fluid dynamics [163, 165]. To ensure solvability of the system, the approximation order of the pore pressure should be chosen one order less than the solid displacement.

Concerning the approximation order of the different variables of full form (u_i, p, w_i) the information given by literature is quite rare. Ravichandran [112] and Gajo et al. [72] propose also for the general case to approximate the pressure field one order less than the displacement variables u_i, w_i. Besides, computational costs can be limited if the approximation order of any primary variable can be reduced.

However, as long as no numerical instabilities are detectable the shape functions of the single constituents will be chosen to be of the same kind, if not otherwise stated. This ensures that every component is approximated with the same quality within the equation system.

3.2.7 Transformation of variables

When programming the finite element formulation of porous media it is of numerical benefit to transform the present variables, as it is worked out in detail by Chen and Dargush [48] and Kielhorn [88]. In the following, the main steps of the transformation procedure are presented. In order not to alter the governing equations of the poroelastic material, the linear transformations

$$\tilde{x}_i = \frac{x_i}{A} \,, \quad \tilde{t}_i = \frac{t_i}{B} \,, \quad \tilde{C}_{ijk\ell} = \frac{C_{ijk\ell}}{C} \tag{3.54}$$

of spatial coordinates, time coordinates, and material data, respectively, is performed using three constant values $A, B, C \in \mathbb{R}^+$. The obtained dimensionless variables due to the transformation will be shown on some examples. Thus, taking into account the transformations (3.54), the new spatial derivative is

$$\frac{\partial u_i}{\partial x_j} = \frac{A \partial \tilde{u}_i}{A \partial \tilde{x}_j} = \tilde{u}_{i,\tilde{j}} \,,$$

whereas the first and second time derivative yields

$$\begin{aligned} \frac{\partial u_i}{\partial t} &= \frac{A \partial \tilde{u}_i}{B \partial \tilde{t}} = \frac{A}{B} \dot{\tilde{u}}_i \\ \frac{\partial^2 u_i}{\partial t^2} &= \left(\frac{\partial}{\partial t} \right) \left(\frac{\partial u_i}{\partial t} \right) = \left(\frac{\partial}{B \partial \tilde{t}} \right) \left(\frac{A \partial \tilde{u}_i}{B \partial \tilde{t}} \right) = \frac{A}{B^2} \frac{\partial^2 \tilde{u}_i}{\partial \tilde{t}^2} = \frac{A}{B^2} \ddot{\tilde{u}}_i \,. \end{aligned}$$

The divergence of the stress tensor is related to his transformation by

$$\sigma_{ij,j} = \frac{\partial \sigma_{ij}}{\partial x_j} = \frac{C \partial \tilde{\sigma}_{ij}}{A \partial \tilde{x}_j} = \frac{C}{A} \tilde{\sigma}_{ij,\tilde{j}} \quad \Longleftrightarrow \quad \sigma_{ij,j} = \frac{C}{A} \tilde{\sigma}_{ij,\tilde{j}} \,.$$

Inserting the linear transformation into the governing equations of section 2.2 yields the remaining dimensionless variables for the permeability and any density

$$\tilde{\kappa} = \frac{BC}{A^2}\kappa \qquad \tilde{\varrho} = \frac{A^2}{B^2C}\varrho \; .$$

Bad conditioned equation systems occurring in numerical solution schemes due to the poroelastic material is obvious, since the material data varies in a high range (see table 5.6). The goal is, therefore, to transform the variables in the form

$$\tilde{C}_{ijk\ell} = \tilde{\kappa} = \tilde{\rho} = \lambda \; , \qquad \lambda \in \mathbb{R}^+ \; ,$$

which will lead to the following equations

$$\frac{1}{C}E = \lambda \qquad \frac{BC}{A^2}\kappa = \lambda \qquad \frac{A^2}{B^2C}\rho = \lambda \; . \tag{3.56}$$

Solving equations (3.56) for the unknown parameters yields

$$A = \frac{\kappa}{\lambda^2}\sqrt{E\varrho} \qquad B = \frac{\varrho\kappa}{\lambda^2} \qquad C = \frac{E}{\lambda} \; .$$

Kielhorn [88] investigated different approaches on a final choice of the three parameters A, B and C. In this thesis, the choice $\lambda = 1$ will be used. The benefits gained by using dimensionless variables is evident when considering the condition number of resulting system matrices. It can be reduced by an order of roughly 10^{11} [88].

3.3 Temporal discretization

3.3.1 Newmark method

As shown in sections 3.1 and 3.2, the semi-discrete approximation (3.9) of transient field problems leads to a set of ordinary differential equations of the form

$$\mathbf{M}\ddot{\mathbf{u}} + \mathbf{C}\dot{\mathbf{u}} + \mathbf{K}\mathbf{u} = \mathbf{f} \,. \tag{3.57}$$

Analytic solutions of the given problem are in general not available and for this reason a numerical approximation scheme is required. A vast body of literature considering this topic is accessible where different methods are illustrated with their accuracy, convergence, and stability properties, e.g, Chopra [51]. Numerical approximation schemes are also well discussed in common Finite Element books which cover the dynamic case, e.g. [22, 55, 82, 165]. Although many such methods exist, only the well-known *Newmark* method [106] will be used in this thesis.

In order to simplify the notation, first only a single degree of freedom system

$$m\ddot{u}(t) + c\dot{u}(t) + ku(t) = f \qquad t \in (0,\infty) \tag{3.58}$$

is considered, where m,c, and k are positive real valued constants and u and f are scalar valued functions of time only. As before, $\dot{()}$ and $\ddot{()}$ represents the first and second time derivative, respectively. The initial-value problem (3.58) is subjected to initial conditions

$$u(0^+) = u_0 \qquad \text{and} \qquad \dot{u}(0^+) = u_1 \,. \tag{3.59}$$

If the numerical approximation scheme of (3.59) is accomplished it is an easy task to extend it to a system of ordinary differential equations.

At first, the time interval of interest, denoted by $(0,T)$, is split into N-equal time steps Δt. Thus, the time grid

$$t_n = n\Delta t \qquad n = 0,1,2,\ldots,N \tag{3.60}$$

is taken constant for simplicity, whereas the method wouldn't actually require this. Following the procedure presented by Newmark [106], the approximation of the discrete acceleration $\ddot{u}_{n+1}$ and velocity $\dot{u}_{n+1}$ at time step $n+1$ is given by

$$\ddot{u}_{n+1} = b_1(u_{n+1} - u_n) - b_2\dot{u}_n - b_3\ddot{u}_n \tag{3.61a}$$
$$\dot{u}_{n+1} = b_4(u_{n+1} - u_n) - b_5\dot{u}_n - b_6\ddot{u}_n \,, \tag{3.61b}$$

respectively, with the introduced constants $b_1,\ldots,b_6$ defined by

$$b_1 = \tfrac{1}{\beta\Delta t^2} \qquad b_2 = \tfrac{1}{\beta\Delta t} \qquad b_3 = \tfrac{1}{2\beta} - 1$$
$$b_4 = \tfrac{\gamma}{\beta\Delta t} \qquad b_4 = \tfrac{\gamma}{\beta} - 1 \qquad b_6 = \Delta t\left(\tfrac{\gamma}{2\beta} - 1\right) \,.$$

The time discrete form of (3.58) at time step $n+1$ reads as

$$m\ddot{u}_{n+1} + c\dot{u}_{n+1} + ku_{n+1} = f_{n+1} \ . \tag{3.62}$$

Note that in (3.61a) and (3.62) the approximations

$$u_n \approx u(t_n), \quad \dot{u}_n \approx \dot{u}(t_n), \quad \ddot{u}_n \approx \ddot{u}(t_n)$$

for any time step n are used. Furthermore, the abbreviation $f_{n+1} = f(t_{n+1})$ is used. Inserting the equations (3.61) into (3.62) yields the expression for the only remaining unknown u_{n+1}

$$(b_1 m + b_4 c + k)\, u_{n+1} = f_{n+1} + (b_1 u_n + b_2 \dot{u}_n + b_3 \ddot{u}_n)\, m + (b_4 u_n + b_5 \dot{u}_n + b_6 \ddot{u}_n)\, c \ . \tag{3.63}$$

For $n = 0$ it remains to calculate the acceleration $\ddot{u}_0$, which can easily done by using the original differential equation (3.58) or the approximated form (3.62)

$$m\ddot{u}_0 = f_0 - c\dot{u}_0 - ku_0 \ ,$$

with the initial conditions from (3.59). The parameters β and γ define the variation of acceleration over a time step and determine the stability and accuracy characteristics of the method. Typical selection for $\gamma = 1/2$ and $1/6 \leq \beta \leq 1/4$ is satisfactory from all points of view, including that of accuracy [51]. The choice of $\gamma = 1/2$ and $\beta = 1/4$ corresponds to constant acceleration whereas $\gamma = 1/2$ and $\beta = 1/6$ describes a linear variation of acceleration. The Newmark method is unconditionally stable for the inequality

$$2\beta \geq \gamma \geq \tfrac{1}{2} \ .$$

However, numerical dissipation is desired, the choice $\gamma > 1/2$ would be an adequate choice, despite the second order accuracy of the numerical integration scheme is lost [82]. For now, the choice

$$\beta = \tfrac{1}{4} \quad \text{and} \quad \gamma = \tfrac{1}{2}$$

is fixed throughout this thesis unless stated otherwise.

Applying the Newmark scheme to a system of differential equations, the scalar values m, c and k basically has to be understood as matrices $\mathbf{M}, \mathbf{C}$ and $\mathbf{K}$, which are commonly called mass-, damping- and stiffness matrix, respectively. The unknowns $u_{n+1}, \dot{u}_{n+1}$ and $\ddot{u}_{n+1}$ has to be understood as vectors with size of degrees of freedom of the system. Thus, the Newmark scheme applied to the system (3.57) yields for equation (3.63) the following set of algebraic equations

$$\underbrace{(b_1\mathbf{M} + b_4\mathbf{C} + \mathbf{K})}_{\overline{\mathbf{K}}}\, \mathbf{u}_{n+1} = \mathbf{f}_{n+1} + \underbrace{(b_1\mathbf{u}_n + b_2\dot{\mathbf{u}}_n + b_3\ddot{\mathbf{u}}_n)\,\mathbf{M} + (b_4\mathbf{u}_n + b_5\dot{\mathbf{u}}_n + b_6\ddot{\mathbf{u}}_n)\,\mathbf{C}}_{\mathbf{r}_{n+1}} \ . \tag{3.64}$$

for the unknowns $\mathbf{u}_{n+1}$. Analogously, the acceleration vector $\ddot{\mathbf{u}}_{n+1}$ and velocity vector $\dot{\mathbf{u}}_{n+1}$ can be calculated from equations (3.61a) and (3.61b), respectively. The matrix $\mathbf{M}$ has to be positive-definite, the matrices $\mathbf{C}$ and $\mathbf{K}$ are positive-semi-definite [82]. The resulting matrix on the left-hand side is commonly termed dynamic stiffness matrix, while the right-hand side is referred as dynamic force vector. Note that if the time step Δt is chosen constant, the dynamic stiffness matrix has to calculated only once. Thus, it is often preferred to assemble $\overline{\mathbf{K}}$ and to pre-compute a factorization of it, which can be efficiently reused at every time step. It only remains, therefore, to compute the right-hand side at every time step.

3.3.2 Convolution quadrature method

Convolution integrals like

$$y(t) := (f * g)(t) = \int_0^t f(t-\tau)g(\tau)\,\mathrm{d}\,\tau \quad , \qquad t \geq 0 \tag{3.65}$$

describe the response of a linear system to an input signal $g(t)$ when $f(t)$ is the impulse response of the system. The problem to be solved is to evaluate the convolution $f(t) * g(t)$ at discrete times approximately, when only the Laplace transform $\hat{f}(\mathrm{s})$ of $f(t)$ is known. The *Convolution Quadrature Method* (CQM) developed by Lubich [96, 97] serves this purpose. The CQM may also be used to calculate numerically the inverse Laplace transformation of a function.

The CQM is well illustrated in the book of Schanz [123]. For this reason only the main steps of the method will be presented here. The interested reader is also referred to the original works of Lubich [96, 97] to gain more insight into the method.

Taking into account a discrete time grid with equally spaced time steps Δt, as given in equation (3.60), the convolution (3.65) can be approximated at discrete time steps n by the quadrature rule [123]

$$y_n(n\Delta t) = \sum_{k=0}^{n} \omega_{n-k}(\Delta t)g(k\Delta t)\ . \tag{3.66}$$

The so called quadrature weights ω_n are given by

$$\omega_n(\Delta t) = \frac{1}{2\pi \mathrm{i}} \int_{\mathcal{S}_\mathcal{R}} \hat{f}\left(\frac{\gamma(z)}{\Delta t}\right) z^{-n-1}\,\mathrm{d}\,z\ , \tag{3.67}$$

with $\mathcal{S}_\mathcal{R} := \{z \in \mathbb{C}\ :\ |z| = \mathcal{R}\}$ being the circumference of the circle with radius $\mathcal{R}$ in the domain of analyticity of $\hat{f}\,(\gamma(z)/\Delta t)$. The above integral is treated numerically by using a

trapezoidal rule [123].

$$\omega_n(\Delta t) = \frac{\mathcal{R}^{-n}}{L} \sum_{\ell=0}^{L-1} \hat{f}\left(\frac{\gamma\left(\mathcal{R}\,\mathrm{e}^{\mathrm{i}\ell\frac{2\pi}{L}}\right)}{\Delta t}\right) \mathrm{e}^{-\mathrm{i}n\ell\frac{2\pi}{L}} . \tag{3.68}$$

The derivation of the quadrature rule (3.66) incorporates the use of a linear multistep method, which has to fulfill certain stability requirements [123]. An example of such a multistep method, which fulfills the stability requirements, is the *Backward Differential Formula* of order two (BDF2), which will be used within this thesis. The characteristic polynomial of this method is given by

$$\gamma(z) = \frac{3}{2} - 2z + \frac{1}{2}z^2 .$$

Thus, the CQM only uses two approximations to calculate the convolution integral (3.65), namely the linear multistep method and the trapezoidal rule (3.68) to calculate the quadrature weights ω_n. It remains to specify the parameter L, which is the number of intervals, the integration path $\mathcal{S}_\mathcal{R}$ is split into, when approximating the integral in (3.67). The computation of $\hat{f}(\mathrm{s})$ in (3.68) is performed with an error bounded by ε, the choice of $L = N$, and $\mathcal{R}^N = \sqrt{\varepsilon}$ [123]. The choice $L = N$ yields the advantage that the computation of the weights in (3.68) can be performed very efficiently using the technique of the Fast Fourier Transform (FFT) [46]. Numerical studies concerning the proper choice of parameters can be found in the book of Schanz [123].

Moreover, the convolution quadrature method (3.66) can be used as inverse Laplace transform method. It turns out that the CQM is superior compared to other inverse Laplace transform methods [124].

The convolution quadrature method can also be applied to a set of differential equations, e.g., to equation (3.23). The scalar values $y_n(n\Delta t)$ and $g(n\Delta t)$ have to be understood then as vectors and the weights $\omega_n(\Delta t)$ as matrix. Consequently, the convolution quadrature method can be used as inverse Laplace transformation of equation (3.23). The multiplication in Laplace domain (3.23) corresponds to a convolution in time domain, which can be approximated by the convolution quadrature method

$$\hat{\overline{\mathbf{K}}}(\mathrm{s})\hat{\mathbf{u}}(\mathrm{s}) \bullet\!\!-\!\!\circ \int_0^t \overline{\mathbf{K}}(t-\tau)\mathbf{u}(\tau)\,\mathrm{d}\,\tau \approx \sum_{k=0}^{n} \boldsymbol{\omega}_{n-k}\big(\hat{\overline{\mathbf{K}}}(\mathrm{s}),\Delta t\big)\mathbf{u}(k\Delta t) = \mathbf{f}(n\Delta t) .$$

At each time step $t_n = n\Delta t$ the current displacement vector $\mathbf{u}(n\Delta t)$ is the only unknown. Thus, the right-hand side is constructed from the current loading as well from foregoing solutions. The resulting equation system for the unknown solution vector $\mathbf{u}(k\Delta t)$ reads as

$$\boldsymbol{\omega}_0\big(\hat{\overline{\mathbf{K}}}(\mathrm{s}),\Delta t\big)\mathbf{u}(n\Delta t) = \mathbf{f}(n\Delta t) - \underbrace{\sum_{k=0}^{n-1} \boldsymbol{\omega}_{n-k}\big(\hat{\overline{\mathbf{K}}}(\mathrm{s}),\Delta t\big)\mathbf{u}(k\Delta t)}_{\mathbf{r}_n} . \tag{3.69}$$

The coefficient matrix $\boldsymbol{\omega}_0$ has to be inverted only once when using a direct solver, whereas the right-hand side vector $\mathbf{r}_n$ has to be calculated for every time step.

3.4 Numerical evaluation of finite integrals

The volume integrals occurring in finite element formulations are in general approximated by using numerical integration schemes on the reference element. Numerical integration methods use N_G sampling points $\boldsymbol{\xi}_i$ and assigns weights W_i to approximate the integral

$$\int_{\widehat{\tau}} f(\boldsymbol{\xi})\,\mathrm{d}\boldsymbol{\xi} \approx \sum_{i=1}^{N_G} f(\boldsymbol{\xi}_i) W_i \,.$$

The *Gauß quadrature* is the most popular method in order to generate element matrices, since it minimizes the number of sampling points for a given accuracy. Since the integration is performed on a reference element $\widehat{\tau}$, tabulated sampling points $\boldsymbol{\xi}_i$ and weights W_i can be used. For this reason the implementation of the numerical integration is straightforward. For the one-dimensional case, the Gauß integration rule integrates polynomial of degree $2m-1$ exactly when using m sampling points. Gauß integration points and weights for the two- and three dimensional case are obtained by tensor products. Such integration formulas are exact in the two dimensional case for polynomial of the form

$$f(x) = \sum_{0\le i\le \ell, 0\le j\le m} a_{ij} \xi_1^{\ell} \xi_2^{m}$$

and in the three dimensional case for

$$f(x) = \sum_{0\le i\le \ell, 0\le j\le m, 0\le k\le n} a_{ijk} \xi_1^{\ell} \xi_2^{m} \xi_3^{n} \,.$$

Here, ℓ, m, and n denote the degree of polynomial for which the Gauß quadrature rule is exact in the one dimensional case and $a_{ij}, a_{ijk} \in \mathbb{R}$ are constants [84].

Tables containing Gauß quadrature points and weights can be found, in general, in any textbook covering the finite element technique, e.g., Zienkiewicz et al. [165] or Cook et al. [55]. Proofs and additional details can be found in, e.g., [136] or [57].

4 INFINITE ELEMENTS

In chapter 3, the finite element method was introduced treating bounded domains. In the following, the application of infinite elements within the finite element method is introduced, which is a possible choice for the investigation of unbounded domains. An infinite element is simply an element which attempts to represent the behavior of the solution in the unbounded domain. Infinite elements are easily coupled to finite elements and retain the banded structure of finite element matrices.

A good overview of the development of infinite elements as well as possible applications is given in the book of Bettess [31]. In the following, a short historical review of different approaches of infinite elements will be given. First published publications about infinite elements were the thesis of Ungless [140] and the paper of Zienkiewicz and Bettess [157]. There exist mainly two different types of developed infinite elements:

1. The use of a *decay function* together with a shape function which causes the field quantity to approach the sought value at infinity, while the finite size of the infinite element is retained.

2. Using conventional shape functions to describe the variation of the field quantity, while the geometry is mapped from a finite to an infinite domain.

Different mappings are possible, for example the mapping proposed by Beer and Meek [26], but maybe the most promising is presented by Zienkiewicz et al. [161], due to its simplicity of the mapping. This mapping retains the applicability of standard integration formulas, e.g., standard Gauß integration. For another point of view, the reader is referred to [31, 32] or Beer's discussion [25].

Mapped infinite elements perform well for the static case in elastic media [161]. Such mapped infinite elements were also applied successfully to quasi-static materially nonlinear problems [99].

The application of infinite elements to wave propagation problems, makes it necessary to include outwardly propagating wave-like factors in their formulation. This concept was originally proposed by Bettess and Zienkiewicz [33]. For acoustic media a wide variety of formulations exists. Basically, two different approaches exist, namely the unconjugated and the conjugated infinite elements. The former are better known as Bettess infinite elements and are based on a Bubnov-Galerkin variational approach. This means that the test and trial functions are identical [162]. Thus, a symmetric system matrix can be retained. The applicability of these elements to transient problems is computationally expensive

since they are non-local in time. Furthermore, special integration techniques has to be applied to handle the oscillating integrals.

The notation conjugated infinite element stems from the fact that the test function is chosen to be the complex conjugate of the trial function. This highly interesting element was originated by Astley et al. [12, 13]. Astley called this type *wave envelope* elements. Due to the conjugated test function, oscillatory terms are canceled out within the weighted Petrov-Galerkin variational formulation. This leads to a considerable simplification, since the occurring integrals can be evaluated numerically using standard integration formulas. Even more, the application to transient problems is straightforward [12]. A comparison of the conjugated and unconjugated infinite element method for the Helmholtz equation is discussed by Gerdes [74]. The performance of the wave envelope element is even enhanced by Dreyer [62], Dreyer and von Estorff [63], and Dreyer et al. [64] for the time harmonic case. Improved stability for time domain calculations is accomplished by Cipolla [54]. A more detailed development of existing infinite element formulations concerning the acoustic media can be found in the review article of Astley [10].

In the elastodynamic case, it turns out to be a little bit more complicated since there is no longer just one unique wave occurring. In a homogeneous elastic half space there are actually three distinct waves present, in particular, a compressional-, shear-, and Rayleigh wave (cf. section 2.1.2). These waves travel with three different wave speeds. However, the simplest approach is to include only the characteristic of one wave within the infinite element formulation. Depending on the spatial location of the infinite element, the dominant wave is consequently incorporated into the infinite element formulation. Moreover, an exponential decay of the field quantity is often assumed, instead of the correct asymptotic decay in 3-dimensions of $1/r$, where r is the distance measure from the applied point source (singular point) [148, 154]. Infinite elements, capable of simulating all three wave types in the time harmonic case are developed by Zhao and Valliappan [152] and Yun et al. [150], though they also assume an exponential decay of the solution. Medina and Penzien [100] proposed also an interesting infinite element considering all three wave types. They performed very well but the evaluation of the shape functions turned out to be extremely tedious and they also assume an exponential decay of the field quantity. Due to the fact that different wave types must be considered in the shape function of the infinite element, the unconjugated element doesn't yield the advantages as it does for only one wave type. This is because still oscillating terms will remain in the variational formulation. Thus, special integration schemes must be applied to solve such integrals numerically. Also, the application for transient problems is therefore limited. However, as far as the author knows, no such attempt has been accomplished. For the time harmonic case also the application of the conjugated infinite element was performed [109]. Transient wave propagation problems in elastic media have been performed by Yerli et al. [149] for the two-dimensional case. The formulation of this infinite elements was performed in Laplace domain. The time domain formulation was obtained by a numerical inverse Laplace transformation [65]. Even more an exponential decay of the field quantity is assumed.

An infinite element formulation for wave propagation problems in one-dimensional poroelastic material was accomplished by Khalili et al. [86]. Later they extended their work to the two-dimensional case [87]. Their work covers time harmonic problems and the infinite element formulation just considers the occurrence of the two compressional waves.

Of course, the application of infinite elements is widespread and applied to many different fields of engineering. Here are some more examples in compressed form such as consolidation [129], mass transport [153], electromagnetism [68], heat transfer [137], ground freezing [9], fluid-structure interaction [33, 162], and soil-structure interaction [52, 53, 100, 101, 111, 148, 150].

In the following, an infinite element will be presented capable of handling all waves that are present in the underlying media. The developed infinite element is of the mapped type to ensure the correct asymptotic decay for the three-dimensional case. Although the approach of the infinite element is rather simple, as will be seen in the ongoing, the numerical results are sufficiently accurate.

4.1 Infinite elements for elastodynamics

As a starting point of this section, a one-dimensional infinite element for an elastic column will be developed. The proper performance of this infinite element will than be confirmed by the comparison with an analytical infinite element (cf. section 5.1.2). Furthermore, this one-dimensional infinite element will be extended to three-dimensional problems.

4.1.1 1d elastodynamic infinite element

First, the derivation of an analytical infinite element for the one-dimensional elastodynamic case will be presented. This is done for mainly two reasons, first, to compare the performance of the later derived approximated infinite element to the analytical one and, second, to gain an idea how the approximated infinite element must be constructed to perform well.

Analytic infinite element

The analytical infinite element can be deduced from the analytical finite element. In order to derive the analytical finite element, the general solution of an elastic column is needed. Thus, the solution of a one-dimensional elastic column of length ℓ, cross sectional area A, constant young's modulus $E = K + \frac{4}{3}G$, and density ϱ, as depicted in figure 4.1, will be presented. The solution will be derived in Laplace domain as this solution is needed to derive the analytical infinite element in the following. The time domain solution is

presented in appendix A.1. The analytic solution of a column is extensively discussed by Graff [79] for the elastic case and by Schanz for the viscoelastic case [121]. Therefore, only the main steps are presented here.

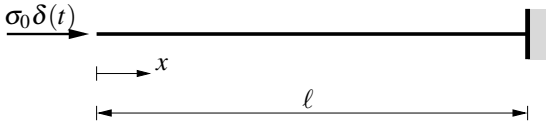

Figure 4.1: One-dimensional elastic column under time dependent loading.

Governing equation The governing equation of a one-dimensional column in Laplace domain is obtained by restricting (2.9) to the x-direction. Assuming vanishing body forces yields

$$\hat{u}(x,\mathrm{s})_{,xx} - \frac{\mathrm{s}^2}{c_P^2}\hat{u}(x,\mathrm{s}) = 0\ . \tag{4.1}$$

In equation 4.1, c_P denotes the compressional wave speed, which is defined by

$$c_P = \sqrt{\frac{K+\frac{4}{3}G}{\varrho}}\ .$$

Note that vanishing initial conditions $u(0^+) = 0$ and $\dot{u}(0^+) = 0$ are assumed during the Laplace transformation. The general solution of the homogenous differential equation (4.1) is

$$\hat{u}(x,\mathrm{s}) = C_1\,\mathrm{e}^{\frac{\mathrm{s}}{c_P}x} + C_2\,\mathrm{e}^{-\frac{\mathrm{s}}{c_P}x}\ , \tag{4.2}$$

where the constants C_i, with $i = 1,2$, have to be determined through prescribed boundary conditions. Assuming boundary conditions of the form (The symbol $\bullet\!\!-\!\!\circ$ denotes the Laplace transformation)

$$\begin{aligned}\hat{u}(0,\mathrm{s}) = 0 \quad &\bullet\!\!-\!\!\circ \quad 0 = u(0,t),\\ \hat{\sigma}(0,\mathrm{s}) = -\hat{\sigma}_0 \bullet\!\!-\!\!\circ -\sigma_0\delta(t) &= \sigma(0,t)\ ,\end{aligned}$$

yields, with the definition of the stress

$$\hat{\sigma}(x,\mathrm{s}) = \left(K+\tfrac{4}{3}G\right)u_{,x}\ ,$$

the solution of the elastic column

$$\hat{u}(x,\mathrm{s}) = \frac{\hat{\sigma}c_P}{(K+\frac{4}{3}G)\mathrm{s}}\left[\frac{\mathrm{e}^{-\frac{\mathrm{s}}{c_P}x} - \mathrm{e}^{-\frac{\mathrm{s}}{c_P}(2\ell-x)}}{1+\mathrm{e}^{-2\frac{\mathrm{s}}{c_P}\ell}}\right]. \tag{4.3}$$

Next, the analytical finite element (length h, A, $E = K+\frac{4}{3}G$, ϱ), as depicted in figure 4.2, will be derived. The analytical finite element in Laplace domain is nothing else as the

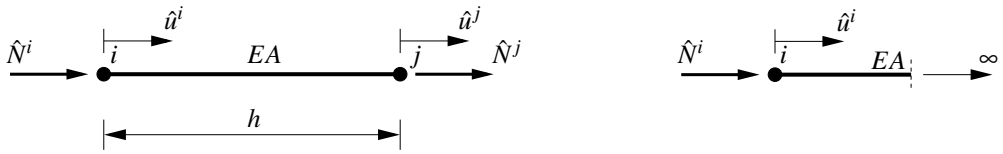

(a) finite (b) infinite

Figure 4.2: Analytic finite and infinite element of an elastic column.

dynamic stiffness relation, obtained by performing a Dirichlet to Neumann map using the analytical solution of the homogeneous elastic column (4.2), which results in

$$\begin{bmatrix} \hat{u}^i_{,x} \\ \hat{u}^j_{,x} \end{bmatrix} = \frac{\mathrm{s}}{c_P\left(1-\mathrm{e}^{-2\frac{\mathrm{s}}{c_P}h}\right)} \begin{bmatrix} 1+\mathrm{e}^{-2\frac{\mathrm{s}}{c_P}h} & -2\,\mathrm{e}^{-\frac{\mathrm{s}}{c_P}h} \\ -2\,\mathrm{e}^{-\frac{\mathrm{s}}{c_P}h} & 1+\mathrm{e}^{-2\frac{\mathrm{s}}{c_P}h} \end{bmatrix} \begin{bmatrix} \hat{u}^i \\ \hat{u}^j \end{bmatrix} . \tag{4.4}$$

The nodal displacements are defined by $\hat{u}^i$ and $\hat{u}^j$, whereas the strains acting on the nodal points are represented by $\hat{u}^i_{,x}$ and $\hat{u}^j_{,x}$. A nodal force is defined by the relation $\hat{N}^i = EA\hat{u}^i_{,x}$.

The analytical infinite element is obtained by shifting the nodal point j to infinity and setting the displacement $\hat{u}^j$ to zero. Thus, the limit $h \to \infty$ is taken. Applying the aforementioned steps to equation (4.4), yields

$$\hat{u}^i_{,x} = \tfrac{\mathrm{s}}{c_P}\hat{u}^i \tag{4.5}$$

the analytical infinite element. The above relations are now ready to be coupled to the discrete variational finite element formulation of a one-dimensional elastic column. A more pleasant method to obtain the analytical infinite element is to use directly the analytical solution of an infinite column and will be shown in the following.

Analytical infinite column

The analytical infinite element can also be deduced from the analytical solution of an infinite column and will be shown here. By looking at the homogeneous solution of the elastic column (4.2), it is observable that the solution consist of two propagating waves of the same speed c_P. One wave propagates along the positive x-direction, whereas the other one propagates in negative x-direction. The term containing the negative exponential terms represents the wave traveling in positive x-direction (decreasing amplitude). This is the only wave we want to preserve, since no wave can originate from infinity. This statement is confirmed by the Sommerfeld radiation condition, which is defined for the one-dimensional elastic column as [76]

$$\hat{u}(x,\mathrm{s})_{,x} + \frac{\mathrm{s}}{c_P}\hat{u}(x,\mathrm{s}) = 0 . \tag{4.6}$$

Thus, taking into account the radiation condition (4.6) the general solution of the infinite elastic column (4.2) reduces to

$$\hat{u}(x,\mathrm{s}) = C\,\mathrm{e}^{-\frac{\mathrm{s}}{c_P}x}\,, \tag{4.7}$$

where C denotes a constant, which remains to be adapted to given boundary conditions. Applying an impulse load as boundary condition

$$\hat{\sigma}(0,\mathrm{s}) = -\hat{\sigma}_0 \bullet\!\!-\!\!\circ -\sigma_0\delta(t) = \sigma(0,t) \tag{4.8}$$

at the top of the column, results in the solution

$$\hat{u}(x,\mathrm{s}) = \frac{\hat{\sigma}_0}{E}\frac{c_P}{\mathrm{s}}\,\mathrm{e}^{-\frac{\mathrm{s}}{c_P}x}\,. \tag{4.9}$$

Note that the stress-strain relation $\hat{\sigma}(x,\mathrm{s}) = E\hat{u}_{,x}(x,\mathrm{s})$ was used to incorporate the boundary condition (4.8). The above solution can also be computed by taking the limit of an infinite length of the displacement of the finite column (4.3).

In order to derive the analytical infinite element from the analytical solution of the infinite elastic column, the displacement $\hat{u}(x,\mathrm{s})$ in (4.7) is expressed in dependence of the nodal displacement $\hat{u}^i$ (cf. figure 4.2(b))

$$\hat{u}(x,\mathrm{s}) = \mathrm{e}^{-\frac{\mathrm{s}}{c_P}x}\,\hat{u}^i\,.$$

The stress within the column is defined by

$$\hat{\sigma}(x,\mathrm{s}) = -E\frac{\mathrm{s}}{c_P}\,\mathrm{e}^{-\frac{\mathrm{s}}{c_P}x}\,\hat{u}^i\,.$$

With the relation $\hat{\sigma}^i = -\hat{\sigma}(0,\mathrm{s})$ at node i and the strain stress relation $\hat{\sigma}(x,s) = E\hat{u}(x,s)_{,x}$, the dynamic stiffness relation is obtained for the infinite column

$$\hat{u}^i_{,x} = \tfrac{\mathrm{s}}{c_P}\hat{u}^i\,. \tag{4.10}$$

Again, the matrix entry of the analytical infinite element is obtained (cf. equations (4.5) and (4.10)), which can be inserted in any variational formulation of a one-dimensional elastic column.

Approximated infinite element

The need of an approximated infinite element is necessary, since in general, no analytical solution for three-dimensional problems are obtainable. Thus, an approximated infinite element will be presented. First, only the one-dimensional case will be considered. The approximated infinite element developed here follows mainly the construction of the

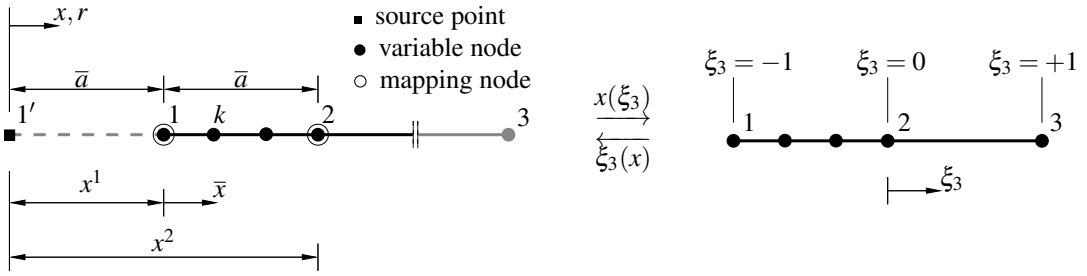

(a) Infinite element in physical space

(b) Corresponding mapped element in local coordinates

Figure 4.3: One-dimensional infinite element.

Astley-Leis mapped element [13]. The geometry of the proposed infinite element, see figure 4.3, is defined as follows. Let $1'$ denote a source point, the location where for example a load is applied. The radial direction of the infinite element is defined through the line $1'-1$, where the point 1 denotes the base point of the finite element. The base point 1 is also the location where the infinite element is coupled to the conventional finite element mesh. The radial distance $\overline{a}$ is defined through the distance of the base point 1 and the source point $1'$. The second point 2 of the infinite element, defined for mapping issues, is located in outward radial direction with distance $\overline{a}$ from the base point 1. The distance between the two mapping points 1 and 2 must not be chosen to be equal to the distance $1'$ and 1. However, in many physical problems, the source point is often a singular point about which the field quantity decays. This behavior can only be represented by the proposed infinite element, if the distance $1-2$ is chosen to be equal to $\overline{a}$. Point 3 of the element is located at infinity and will not be further considered, since throughout this work vanishing field quantities are assumed at infinity. The mapping from the physical space to local coordinates is performed using the $1/r$-mapping introduced by Marques and Owen [99]. Thus, the mapping is defined by

$$x(\xi_3) = \mathsf{m}^1(\xi_3)x^1 + \mathsf{m}^2(\xi_3)x^2 \tag{4.11}$$

with the mapping functions

$$\mathsf{m}^1(\xi_3) = \frac{-2\xi_3}{1-\xi_3} \quad , \quad \mathsf{m}^2(\xi_3) = \frac{1+\xi_3}{1-\xi_3} \, . \tag{4.12}$$

The above mapping functions ensure compatibility of the finite element mesh with the connected infinite element at the coupling node 1 and also represent the infinite extension in radial direction of the element. Thus, the relation between the radial distance measure r and the local coordinate is given by

$$\xi_3 = 1 - \frac{2\overline{a}}{r} \quad , \quad r - \overline{a} = \overline{a}\frac{1+\xi_3}{1-\xi_3} \, . \tag{4.13}$$

Note that through the particular mapping points located at infinity ($r \to \infty$) are mapped to the local coordinate $\xi_3 = 1$.

The next step is to define the shape functions. To give an idea how the shape functions are constructed, the coordinate $\bar{x}$ is introduced. Taking into account the analytical solution of the infinite column (4.7), the displacement within the infinite element can be written as

$$u(\bar{x}) = \mathrm{e}^{-\frac{s}{c_P}\bar{x}} u(\bar{a}) \; .$$

Consequently, the associated shape function for any node k within the infinite element in local coordinates will be defined as

$$\varphi^k(\xi_3) = P_p^k(\xi_3)\, \mathrm{e}^{-\frac{s}{c_P}\mu(\bar{a},\xi_3)} \; , \tag{4.14}$$

with the phase term $\mu(\bar{a},\xi)$. The phase term consists of the distance $\bar{a}$ and a radial weight

$$\mu(\xi_3) = \bar{a}\frac{1+\xi_3}{1-\xi_3} \; . \tag{4.15}$$

Note that the geometric factor is equal to the mapping function $\mathsf{m}^2(\xi_3)$ in (4.12). Thus, the phase-like term vanishes at $\xi_3 = -1$ and approaches the distance $\bar{a}$ for $\xi_3 = 0$. The exponential factor in (4.14) represents, therefore, a radial wave-like factor of the form $\exp(\frac{s}{c_P}(r-\bar{a}))$ within each element [13]. $P_p^k(\xi_3)$ denotes a polynomial of order p corresponding to the radial node k, which represents the approximation in radial direction. Depending on the number of nodes located within the mapping points 1 and 2, the approximation order can be customized. In the ongoing equally spaced points within the interval $\xi_3 \in [-1,0]$ are assumed. A polynomial expression of the form

$$P_p = c_0 + c_1\xi_3 + c_2\xi_3^2 + \cdots + c_p\xi_3^p \; ,$$

as it is used in conventional finite element formulations to approximate the field variable, can be expressed by using the mapping relation (4.13) as

$$P_p = \gamma_0 + \frac{\gamma_1}{r} + \frac{\gamma_2}{r^2} + \cdots + + \frac{\gamma_p}{r^p} \; . \tag{4.16}$$

The term γ_0 represents the solution at infinity and, therefore, implies to be zero, if the solution vanishes at infinity, as it is the common case in many unbounded problems. Since the solution of many field problems behaves of the form (4.16), the solution can be approximated accurately by a proper choice of the polynomial P_p [161].

The test function of the infinite element is defined by

$$\bar{\varphi}^k(\xi_3) = D(\xi_3)\varphi^k(\xi_3) = D(\xi_3)P_p^k(\xi_3)\, \mathrm{e}^{-\frac{s}{c_P}\mu(\bar{a},\xi_3)}$$

and is distinguished from the trial function only by the additional weight

$$D(\xi_3) = \frac{(1-\xi_3)^2}{4} \,. \tag{4.17}$$

Taking into account the relation (4.13), the radial weight $D(\xi_3)$ corresponds to an additional weight of the form $1/r^2$, which ensures the finiteness of integrals occurring in the discrete variational formulation. Thus, the need of square integrability is fulfilled. Note that also the test function fulfills a compatible matching of the base node with any adjacent node of the discrete finite element mesh.

Radial interpolation polynomials

In general, the most intuitive way to construct interpolation functions is the use of the well known *Lagrange polynomials*. The proper choice of interpolation functions is essential in order to obtain a well conditioned equation system [63]. Consequently, iterative solvers, such as for example GMRES [119], can be successfully applied to solve the resulting equation system. The selection of suitable polynomials is even more an essential point, since the matrices of the exterior domain are non-symmetric. The optimal choice of interpolation functions was investigated by Dreyer and von Estorff [63]. They recommend for problems of exterior acoustics the use of *Jacobi polynomials*. His studies reveals that the resulting system matrices are better suited for iterative solvers. This is due to the fact that the system matrices possess a better condition number, which is a first aid for the application of iterative solvers [62]. Consequently, the interpolation functions are constructed by using Jacobi Polynomials, as suggested by Dreyer [62], if not otherwise stated. Moreover, it must be mentioned that even *Legendre polynomials* lead to a better conditioned system matrices as when *Lagrange polynomials* were used, at least for the case of exterior acoustics [11]. In the following, the common Lagrange polynomials are presented as well the Legendre and Jacobi polynomials.

Lagrange polynomials In the case of the Astley-Leis element [13], Lagrange polynomials are used for the interpolation function. Thus, the interpolation function of order p is given for a radial node k by

$$P_p^k(\xi_3) = \prod_{\substack{i=1 \\ i\neq k}}^{p} \frac{\xi_3 - (\xi_3)_i}{(\xi_3)_k - (\xi_3)_i} \,.$$

Lagrange polynomials fulfill the property to be one at the node they belong to and zero at any other node $P_p^k((\xi_3)_\ell) = \delta_{k\ell}$. Hence, the continuity at the base node 1 is given, the location where the infinite element is connected to conventional finite elements. The more

data points are used for the interpolation, the higher the degree of the resulting polynomial. Hence, they will exhibit greater oscillation between the data points and, thus, a poor numerical performance must be taken into account when equally spaced integration points are used. To reduce these oscillation appropriate unequally distributed interpolation points have to be chosen [122].

Legendre polynomials Legendre polynomials can be generated by Rodrigues formula

$$P^k(\xi_3) = \frac{1}{2^k k!} \frac{\mathrm{d}^k}{\mathrm{d}\,\xi_3^k} \left(\xi_3^2 - 1\right)^k \ .$$

Legendre polynomial satisfy the following orthogonality property

$$\int_{-1}^{+1} P_i(\xi_3) P_j(\xi_3)\, \mathrm{d}\,\xi_3 = \frac{2}{2i+1} \delta_{ij} \ .$$

Jacobi polynomials Jacobi polynomials are generalized *Legendre polynomials* and are defined by

$$P^k_{(\alpha,\beta)}(\xi_3) = \frac{(-1)^k}{2^k k!} (1-\xi_3)^{-\alpha} (1+\xi_3)^{-\beta} \frac{\mathrm{d}^k}{\mathrm{d}\,\xi_3^k} \left[(1-\xi_3)^{\alpha+k} (1+\xi_3)^{\beta+k} \right] \ .$$

These polynomials are *orthogonal polynomials* and satisfy therefore the relation

$$\int_{-1}^{+1} P^i_{(\alpha,\beta)} P^j_{(\alpha,\beta)} (1-\xi_3)^{\alpha} (1+\xi_3)^{\beta}\, \mathrm{d}\,\xi_3 = \phi(\alpha,\beta,j)\delta_{ij} \ ,$$

where $\phi(\alpha,\beta,j)$ is a function depending on the parameters α,β and j. To ensure compatibility between the finite and infinite elements at their interface, the interpolation condition (3.8) has to be fulfilled. However, Legendre and Jacobi polynomials don't automatically satisfy this interpolation condition. Thus, the first polynomial within the portion of radial shape functions $p+1$ has to fulfill $P^1_p(-1) = 1$, whereas all other polynomials have to satisfy $P^i_p(-1) = 0$, with $1 < i \leq p+1$. This can be easily achieved by applying adequate constant shifts to the polynomials.

4.1.2 3d elastodynamic infinite element

In the three-dimensional case the existence of multiple waves has to be considered. In a semi-infinite halfspace three different wave types are observable, as revealed in section 2.1.2. Thus, the infinite element of the one-dimensional case must be extended in such a way that all outwardly propagating waves are represented appropriately.

Geometric discretization

The geometry of an infinite element, which follows mainly the proposed infinite element of Astley et al. [13], for the three-dimensional case is depicted in figure 4.4. The set con-

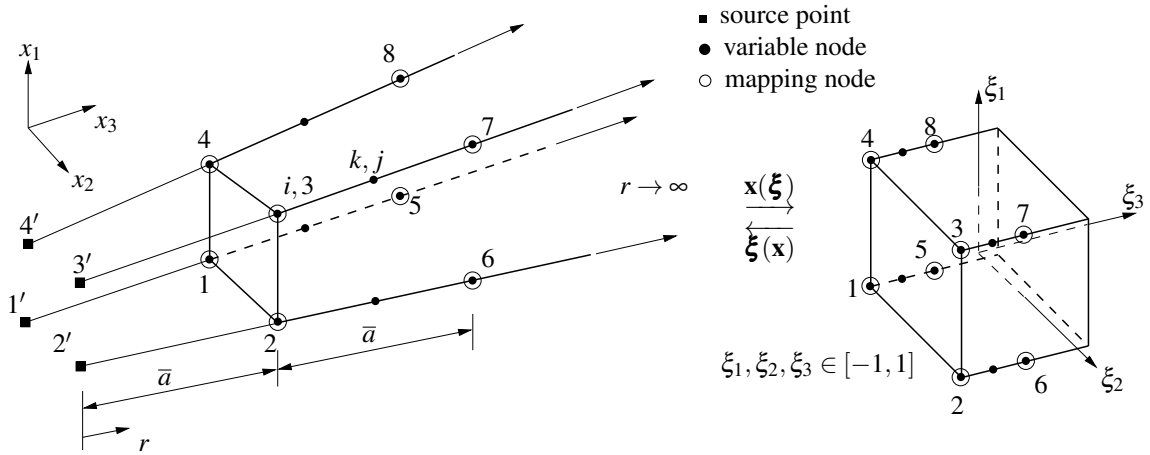

(a) Infinite element in physical space

(b) Corresponding mapped element in local coordinates

Figure 4.4: Three-dimensional infinite element.

taining the points on the base face (x_1x_2-plane) is defined with $n_B = \{1, 2, \ldots, n_B^P\}$, where n_B^P denotes the number of base points for the approximation of the field quantity (e.g., $n_B^P = 4$, as it is depicted in figure 4.4). Thus, the infinite element is not restricted to a linear approximation order on the base face. The radial direction of the infinite element is defined by the so called source points which are defined by the set $n_S = \{1', 2', \ldots, (n_B^P)'\}$. Source points denote locations, where the load is applied and may collapse to a single point. Consequently, the radial direction of the infinite element is given through corresponding source and base points (see figure 4.4(a)) as well through radial distances a_i, with $i \in n_B$. In any case, it must be ensured that the source points for every infinite element are chosen in such a way that the single infinite elements do not intersect each other. This is of course ensured when the source point is chosen to be the same for every infinite element. Moreover, the radial directions also lead to the mapping points $n_M = \{n_B^P + 1, \ldots, 2n_B^P\}$, i.e., in the special case of figure 4.4, $n_M = \{5, 6, 7, 8\}$. These mapping points are located deliberately at related distances a_i measured from the base points n_B. The distance between points n_M and n_B must not be chosen to be equal to the related radial distances a_i. However, in many physical problems, the source point is often a singular point, from which on the field quantity decays. This behavior can only be represented by the proposed infinite element, if the distances between the related points n_M and n_B is chosen to be equal to a_i. The mapping from the physical to the local space is independent of the approximation order of the field quantity. The mapping in radial direction is performed in the same manner

as for the one-dimensional infinite element (4.11), which yields a $1/r$-like mapping. The mapping on the base face is deduced using conventional finite element shape functions, denoted by $S^i(\xi_1,\xi_2)$, with $i \in n_B$. The geometric mapping from the physical to the local space is defined by

$$\mathbf{x}(\boldsymbol{\xi}) = \mathsf{m}^1(\xi_3)\sum_{i=1}^{n_B^P} S^i(\xi_1,\xi_2)\mathbf{p}^i + \mathsf{m}^2(\xi_3)\sum_{i=1}^{n_B^P} S^i(\xi_1,\xi_2)\mathbf{p}^{i+n_B^P}\,, \tag{4.18}$$

where $\mathbf{p}^i$ denotes the geometrical points of the infinite element and $\mathsf{m}^1(\xi_3)$, $\mathsf{m}^2(\xi_3)$ the mapping functions in radial direction, already defined in (4.12). The above mapping relation (4.18) assures the compatibility condition at the base nodes between the infinite and conventional finite elements. As well as in the one-dimensional case, the proposed mapping relation maps points located at $r \to \infty$ to $\xi_3 = +1$ in the local element.

Shape function

Actually, the shape functions of the three-dimensional infinite element are constructed from shape functions of a conventional finite element defined on the base face and the shape function of the one-dimensional infinite element of section 4.1.1 (page 64). In other words, the one-dimensional infinite element is simply placed at every node $i \in n_B$ on the base face. Since the one-dimensional infinite element is capable of representing only one outward traveling wave, the shape function has to be extended. The wave behavior of the far field in an elastic material can be approximately represented by exponential functions in Laplace domain. Moreover, the occurrence of different waves can be approximated in the far field by the superposition of plane waves [79, 111, 152]. Thus, taking into account the occurrence of multiple waves in three-dimensional media, the shape function for a radial node j can be expressed as

$$\varphi^j(\boldsymbol{\xi}) = \frac{1}{2}(1-\xi_3)S^i(\xi_1,\xi_2)P_p^k(\xi_3)\frac{1}{n_c}\sum_{\ell=1}^{n_c} \mathrm{e}^{-\frac{s}{c_\ell}\mu(\overline{a},\xi_3)}\,, \tag{4.19}$$

where n_c denotes the number of waves to be approximated and c_ℓ the respective wave speed. In general, in an elastic half space three different types of waves occur, namely, a compressional-, a shear-, and a Rayleigh wave with wave speeds c_P, c_S, and c_R, respectively. The phase term is defined in the same way as in (4.15), with the exception that the characteristic length $\overline{a}$ is defined as

$$\overline{a} = \frac{1}{n_B^P}\sum_{i=1}^{n_B^P} a_i\,. \tag{4.20}$$

The radial approximation is represented by a polynomial $P_p^k(\xi_3)$ of order p with corresponding radial node k. The approximation order depends on the number of nodes located

within the mapping points n_B and n_M. Furthermore, equally spaced nodes within the interval $\xi_3 \in [-1,0]$ are assumed for the construction of the polynomials $P_p^k(\xi_3)$. The interpolation polynomials can be constructed in different ways, as described on page 67. The node numbering j is a function of the base node numbering i and the radial node numbering k

$$j(k,i) \quad , \quad i \in n_B \quad , \quad 1 \leq k \leq p+1 \quad , \quad 1 \leq j \leq (p+1)n_B^P \, .$$

The factor $\frac{1}{2}(1-\xi_3)$ is introduced to preserve the interpolation condition $\varphi^j(\boldsymbol{\xi}) \to 0$ as $\xi_3 \to +1$. Hence, the Sommerfeld radiation condition is fulfilled. The radial behavior of the shape function $\varphi^j(\boldsymbol{\xi})$ in radial direction is of the form, when ξ_2 and ξ_3 are held constant

$$\varphi^j \approx \left[\frac{\gamma_1}{r} + \frac{\gamma_2}{r^2} + \cdots + \frac{\gamma_p}{r^p}\right] \sum_{\ell=1}^{n_c} \mathrm{e}^{-\frac{s}{c_\ell}\mu(\bar{a},\xi_3)} \, .$$

It remains to define the test function, which is nothing else as the trial function premultiplied with the additional weight (4.17)

$$\bar{\varphi}^j(\boldsymbol{\xi}) = D(\xi_3)\varphi^j(\boldsymbol{\xi}) \, .$$

Again, the additional weight $D(\xi_3)$ ensures finiteness of integrals occurring in the discrete variational formulation. Thus, the need of square integrability is fulfilled. Even more, the test function fulfills the interpolation condition, which preserves a compatible matching of finite and infinite elements at their interface.

Remark on 2d elastodynamic infinite elements In two dimensional exterior wave propagation problems, the amplitude decays differently compared to the three-dimensional case. Whereas the amplitude in three-dimensional problems decays like $1/r$, the amplitude in two-dimensional problems decays like $1/\sqrt{r}$, as explained in more detail in references [31, 54, 162]. The geometric discretization as well the shape function are derived in the same manner as for the three-dimensional case. The only two differences are that, first, the ξ_1 direction is eliminated and, thus, the base shape function remains to be only a function of the coordinate ξ_2, i.e., $S^i(\xi_2)$. Second, the decay is now defined by a factor of $\sqrt{(1-\xi_3)/2}$ to obtain the $1/\sqrt{r}$-like decay. Thus, the shape function is defined by

$$\varphi^j(\boldsymbol{\xi}) = \sqrt{\tfrac{1}{2}(1-\xi_3)}S^i(\xi_2)P_p^k(\xi_3)\frac{1}{n_c}\sum_{\ell=1}^{n_c} \mathrm{e}^{-\frac{s}{c_\ell}\mu(\bar{a},\xi_3)} \tag{4.21}$$

and the corresponding test function is expressed as

$$\bar{\varphi}^j(\boldsymbol{\xi}) = D(\xi_3)\varphi^j(\boldsymbol{\xi}) \, ,$$

where the single components represents the same meaning as for the three-dimensional case (cf. section 4.1.2).

4.2 Infinite elements for elastostatics

The elastostatic infinite element can be simply deduced from the dynamic infinite element by eliminating the wave-like factors. Thus, the mapping relation (4.18) is the same constant and the trial and test function for three-dimensional problems are defined as

$$\varphi^j(\boldsymbol{\xi}) = \frac{1}{2}(1-\xi_3)S^i(\xi_2,\xi_3)P_p^k(\xi_3)$$

and

$$\bar{\varphi}^j(\boldsymbol{\xi}) = D(\xi_3)\varphi^j(\boldsymbol{\xi}) \ ,$$

respectively.

4.3 Infinite elements for poroelastodynamics

In the beginning of this section, an analytical infinite element for poroelastodynamics for one-dimensional problems will be presented. In accordance to the analytical element an approximated one-dimensional infinite element will be deduced. Furthermore, the approximated one-dimensional infinite element will be extended to three-dimensional problems.

4.3.1 Analytical 1d poroelastodynamic infinite element

The analytical poroelastic infinite element can only be derived for the u,p-form or the u,w-form. This is because only for these two formulations the governing equations (A.5) are reduced to two differential equations of second order. This is needed to obtain an analytical finite element or more specifically, a Dirichlet to Neumann map can only be performed for this set of governing equations. In other words, only for the u,p- or u,w-form a relation between the nodal displacements and the nodal stresses as well as for the nodal pressure and the nodal flux can be performed. Alternatively, also the relation of the nodal relative displacement and the fluid pressure can be used. Here, the former formulation will be used, i.e., the u,p-formulation. The analytical infinite poroelastic element, as depicted in figure 4.5, is deduced from the general analytical solution of a porous column, given by (A.11). Note that the relative displacement w of the solution (A.11) is not needed for the deduction of the analytical infinite poroelastic element. The analytical solution of the finite poroelastic column consists of the superposition of four wave terms. Two pairs of compressional waves travel with the wave velocities $c_1 = 1/\lambda_1$ and $c_2 = 1/\lambda_2$ into the positive and negative x-direction. In other words, the analytical solution contains two pairs of compressional waves, one with decaying and one with increasing amplitude. In order to formulate the infinite element only the decaying amplitudes are of interest, since

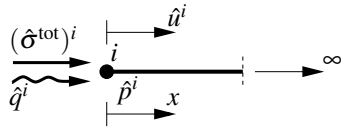

Figure 4.5: Analytic infinite poroelastic element.

no incoming wave from infinity is allowed. This ensures that the Sommerfeld radiation condition is satisfied, as explained in more detail for the elastic case in section 4.1.1. Thus, the general ansatz of the analytical infinite element reads as

$$\begin{bmatrix}\hat{u}(x,\mathrm{s})\\ \hat{p}(x,\mathrm{s})\end{bmatrix} = C_3 \begin{bmatrix}v_1^3\\ v_2^3\end{bmatrix} \mathrm{e}^{-\mathrm{s}\lambda_1 x} + C_4 \begin{bmatrix}v_1^4\\ v_2^4\end{bmatrix} \mathrm{e}^{-\mathrm{s}\lambda_2 x}\,, \tag{4.22}$$

with the Eigenvectors defined in (A.12). Inserting the boundary conditions

$$\hat{u}(0,\mathrm{s}) = \hat{u}^i \quad , \quad \hat{p}(0,\mathrm{s}) = \hat{p}^i$$

into (4.22) yields

$$C_3 = \frac{v_2^4 u^i - v_1^4 p^i}{v_1^3 v_2^4 - v_2^3 v_1^4} \quad , \quad C_4 = \frac{v_1^3 p^i - v_2^3 u^i}{v_1^3 v_2^4 - v_2^3 v_1^4}$$

and further on the solution for the solid displacement and pore pressure

$$\begin{bmatrix}\hat{u}(x,\mathrm{s})\\ \hat{p}(x,\mathrm{s})\end{bmatrix} = \frac{v_2^4 u^i - v_1^4 p^i}{v_1^3 v_2^4 - v_2^3 v_1^4}\mathbf{v}^1 \mathrm{e}^{-\mathrm{s}\lambda_1 x} + \frac{v_1^3 p^i - v_2^3 u^i}{v_1^3 v_2^4 - v_2^3 v_1^4}\mathbf{v}^2 \mathrm{e}^{-\mathrm{s}\lambda_2 x}\,. \tag{4.23}$$

The corresponding stress is obtained by inserting the solution (4.23) into the one-dimensional form of the constitutive relation (2.18)

$$\begin{aligned}\hat{\sigma}^{\mathrm{tot}}(x,\mathrm{s}) &= (K+\tfrac{4}{3}G)\hat{u}_{,x}(x,\mathrm{s}) - \alpha\hat{p}(x,\mathrm{s})\\ &= -\mathrm{s}(K+\tfrac{4}{3}G)\left[\lambda_1 \frac{v_2^4 u^i - v_1^4 p^i}{v_1^3 v_2^4 - v_2^3 v_1^4} v_1^1 \mathrm{e}^{-\mathrm{s}\lambda_1 x} + \lambda_2 \frac{v_1^3 p^i - v_2^3 u^i}{v_1^3 v_2^4 - v_2^3 v_1^4} v_1^2 \mathrm{e}^{-\mathrm{s}\lambda_2 x}\right] - \alpha\hat{p}(x,\mathrm{s})\end{aligned}$$

and the one-dimensional flux is defined by

$$\hat{q}(x,\mathrm{s}) = \mathrm{s}\hat{w}(x,\mathrm{s}) = -\frac{\beta}{\mathrm{s}\varrho_f}\left(\hat{p}_{,x}(x,\mathrm{s}) + \mathrm{s}^2\varrho_f\hat{u}(x,\mathrm{s})\right)$$

with the relative displacement defined by (2.36). Note that the body force $\hat{f}_i^f$ is neglected in the solution of the flux. The next step is to incorporate the nodal total stress $(\hat{\sigma}^{\mathrm{tot}})^i$ and flux q^i. This is realized by the boundary conditions stated at node i as

$$\hat{\sigma}^{\mathrm{tot}}(0,\mathrm{s}) = -(\hat{\sigma}^{\mathrm{tot}})^i \quad , \quad \hat{q}(0,\mathrm{s}) = -\hat{q}^i\,.$$

Hence, the nodal relation of the single components is defined as

$$\begin{bmatrix} (\hat{\sigma}^{\mathrm{tot}})^i \\ \hat{q}^i \end{bmatrix} = \frac{1}{\varrho_f(v_2^3 - v_2^4)} \begin{bmatrix} \varrho_f \mathrm{s}(K + \frac{4}{3}G)\left(v_2^3\lambda_2 - v_2^4\lambda_1\right) & \beta\left[v_2^3\left(v_2^4(\lambda_1 - \lambda_2) + \mathrm{s}\varrho_f\right) - \mathrm{s}\varrho_f v_2^4\right] \\ \varrho_f\alpha\left(v_2^3 - v_2^4\right) + \varrho_f(K + \frac{4}{3}G)(\lambda_1 - \lambda_2) & \beta\left(v_2^4\lambda_2 - v_2^3\lambda_1\right) \end{bmatrix} \begin{bmatrix} \hat{u}^i \\ \hat{p}^i \end{bmatrix}, \tag{4.24}$$

whereas the entries $v_1^3 = v_1^4 = 1$ are substituted. The above relation is now appropriate to be attached at a one-dimensional poroelastic finite element formulation of the u, p-form in Laplace domain. In three-dimension no analytical infinite element can be established. Therefore, an approximated infinite element will be deduced, which can be extended to three-dimensional problems.

4.3.2 1d approximated infinite element

In the following, an approximated infinite poroelastic infinite element will be presented. First, the infinite element proposed by Khalili et al. [86] will be shown and, second, a more efficient infinite element will be derived which is valid for most poroelastic material.

Khalili approach

The poroelastic infinite element proposed by Khalili et al. [86], which will be referred as Khalili in the future for simplicity, is depicted in figure 4.6. Node 1 one of the proposed

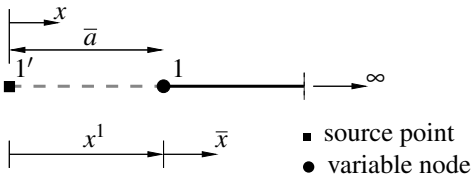

Figure 4.6: Infinite poroelastic element proposed by Khalili et al. [86].

element is located at distance $\bar{a}$ away from any impact point and corresponds to the global coordinate x^1. Furthermore, a local coordinate system $\bar{x}$, with the origin placed at node 1, is introduced for the infinite element. As already shown in the derivation of the analytical infinite element, the solution of a one-dimensional poroelastic column (A.11) at point x^1 is given, when only outward traveling waves are allowed, as

$$\begin{bmatrix} \hat{u}(\bar{a}, \mathrm{s}) \\ \hat{p}(\bar{a}, \mathrm{s}) \\ \hat{w}(\bar{a}, \mathrm{s}) \end{bmatrix} = C_3 \mathbf{v}^3 \, \mathrm{e}^{-\mathrm{s}\lambda_1\bar{a}} + C_4 \mathbf{v}^4 \, \mathrm{e}^{-\mathrm{s}\lambda_2\bar{a}} \ . \tag{4.25}$$

The solid displacement within the infinite element can be written in the local coordinate system as

$$\hat{u}(\bar{x},\mathrm{s}) = C_3 v_1^3 \,\mathrm{e}^{-\mathrm{s}\lambda_1(\bar{a}+\bar{x})} + C_4 v_1^4 \,\mathrm{e}^{-\mathrm{s}\lambda_2(\bar{a}+\bar{x})} \frac{\hat{u}(\bar{a},\mathrm{s})}{C_3 v_1^3 \,\mathrm{e}^{-\mathrm{s}\lambda_1\bar{a}} + C_4 v_1^4 \,\mathrm{e}^{-\mathrm{s}\lambda_2\bar{a}}} \,. \tag{4.26}$$

Note that the solid displacement is extended by the fraction of the distinct nodal displacement $\hat{u}(\bar{a},\mathrm{s})$ and the expanded form of $\hat{u}(\bar{a},\mathrm{s})$, given in (4.25). Equation (4.26) can be rearranged to

$$\hat{u}(\bar{x},\mathrm{s}) = \Bigg\{ \underbrace{\left[\frac{C_3 v_1^3 \,\mathrm{e}^{-\mathrm{s}\lambda_1\bar{a}}}{C_3 v_1^3 \,\mathrm{e}^{-\mathrm{s}\lambda_1\bar{a}} + C_4 v_1^4 \,\mathrm{e}^{-\mathrm{s}\lambda_2\bar{a}}} \right]}_{\hat{U}_1^{\mathrm{K}}} \mathrm{e}^{-\mathrm{s}\lambda_1\bar{x}} + \underbrace{\left[\frac{C_4 v_1^4 \,\mathrm{e}^{-\mathrm{s}\lambda_2\bar{a}}}{C_3 v_1^3 \,\mathrm{e}^{-\mathrm{s}\lambda_1\bar{a}} + C_4 v_1^4 \,\mathrm{e}^{-\mathrm{s}\lambda_2\bar{a}}} \right]}_{\hat{U}_2^{\mathrm{K}}} \mathrm{e}^{-\mathrm{s}\lambda_2\bar{x}} \Bigg\} \hat{u}(\bar{a},\mathrm{s}). \tag{4.27}$$

Consequently, the shape function for the solid displacement of a poroelastic infinite rod should be expressed as

$$\varphi^j(\bar{x}) = \hat{U}_1^{\mathrm{K}} \,\mathrm{e}^{-\mathrm{s}\lambda_1\bar{x}} + \hat{U}_2^{\mathrm{K}} \,\mathrm{e}^{-\mathrm{s}\lambda_2\bar{x}} \,,$$

where the superscript K denotes the affinity to the Khalili infinite element. It can be observed that the shape function (4.27) relates the variation of the field quantity $\hat{u}(\bar{x},\mathrm{s})$ within the infinite element to the nodal value $\hat{u}(\bar{a},\mathrm{s})$. The shape functions for the pore pressure and the relative displacement are derived in the same manner, yielding

$$\begin{aligned} \vartheta^j(\bar{x}) &= \hat{P}_1^{\mathrm{K}} \,\mathrm{e}^{-\mathrm{s}\lambda_1\bar{x}} + \hat{P}_2^{\mathrm{K}} \,\mathrm{e}^{-\mathrm{s}\lambda_2\bar{x}} \\ \psi^j(\bar{x}) &= \hat{W}_1^{\mathrm{K}} \,\mathrm{e}^{-\mathrm{s}\lambda_1\bar{x}} + \hat{W}_2^{\mathrm{K}} \,\mathrm{e}^{-\mathrm{s}\lambda_2\bar{x}} \,, \end{aligned}$$

with the coefficients given by

$$\begin{aligned} P_1^{\mathrm{K}} &= \frac{C_3 v_2^3 \,\mathrm{e}^{-\mathrm{s}\lambda_1\bar{a}}}{C_3 v_2^3 \,\mathrm{e}^{-\mathrm{s}\lambda_1\bar{a}} + C_4 v_2^4 \,\mathrm{e}^{-\mathrm{s}\lambda_2\bar{a}}} \quad , \qquad & P_2^{\mathrm{K}} &= \frac{C_3 v_2^3 \,\mathrm{e}^{-\mathrm{s}\lambda_2\bar{a}}}{C_3 v_2^3 \,\mathrm{e}^{-\mathrm{s}\lambda_1\bar{a}} + C_4 v_2^4 \,\mathrm{e}^{-\mathrm{s}\lambda_2\bar{a}}} \,, \\ W_1^{\mathrm{K}} &= \frac{C_3 v_3^3 \,\mathrm{e}^{-\mathrm{s}\lambda_1\bar{a}}}{C_3 v_3^3 \,\mathrm{e}^{-\mathrm{s}\lambda_1\bar{a}} + C_4 v_3^4 \,\mathrm{e}^{-\mathrm{s}\lambda_2\bar{a}}} \quad , \qquad & W_2^{\mathrm{K}} &= \frac{C_3 v_3^3 \,\mathrm{e}^{-\mathrm{s}\lambda_2\bar{a}}}{C_3 v_3^3 \,\mathrm{e}^{-\mathrm{s}\lambda_1\bar{a}} + C_4 v_3^4 \,\mathrm{e}^{-\mathrm{s}\lambda_2\bar{a}}} \,. \end{aligned}$$

The parameters U_i^{K}, P_i^{K}, and W_i^{K}, with $i = 1,2$, are a kind of wave weighting factors. In other words, the two compressional waves c_1 and c_2 are related to each other, which is modeled by the mentioned weighting factors. The most meaningful property of these weighting factors is that their sum is equal to one, i.e.,

$$U_1^{\mathrm{K}} + U_2^{\mathrm{K}} = 1 \,, \qquad P_1^{\mathrm{K}} + P_2^{\mathrm{K}} = 1, \qquad W_1^{\mathrm{K}} + W_2^{\mathrm{K}} = 1 \,.$$

The test function are chosen to be equal the trial function

$$\bar{\varphi}^j(\bar{x}) = \varphi^j(\bar{x}) \quad , \quad \bar{\vartheta}^j(\bar{x}) = \vartheta^j(\bar{x}) \quad , \quad \bar{\psi}^j(\bar{x}) = \psi^j(\bar{x}) \,.$$

It remains to define the yet unknown constants C_3 and C_4. This can be accomplished by defining problem specific boundary conditions, e.g., for a given total stress and pore pressure, in form of an impulse impact, at position $x = 0$

$$\hat{\sigma}^{\mathrm{tot}}(0,\mathrm{s}) = -\hat{\sigma}_0^{\mathrm{tot}} \bullet\!\!-\!\!\circ -\sigma_0^{\mathrm{tot}}\delta(t) = \sigma^{\mathrm{tot}}(0,t) \;, \quad \hat{p}(0,\mathrm{s}) = 0 \bullet\!\!-\!\!\circ 0 = p(0,t) \;.$$

The resulting constants are

$$C_3 = \frac{v_2^2\hat{\sigma}^{\mathrm{tot}}}{\mathrm{s}(K+\frac{4}{3}G)(v_1^1v_2^2\lambda_1 - v_2^1v_1^2\lambda_2)} \;, \quad C_4 = \frac{-v_2^1\hat{\sigma}^{\mathrm{tot}}}{\mathrm{s}(K+\frac{4}{3}G)(v_1^1v_2^2\lambda_1 - v_2^1v_1^2\lambda_2)} \;.$$

The validity of the proposed infinite element is shown in [86]. The extension to two-dimension can be found in [87]. Though the performance of the infinite element is very well, the shape functions have to be adapted to the kind of problem to be solved, since the shape functions contain the constants C_3 and C_4. These constants have to be fitted to given boundary conditions. Furthermore, the $1/r$-like decay is not considered and only the two compressional waves are considered, which is correct if pure one-dimensional problems are considered.

Mapped and simplified model of poroelastic infinite element shape functions

This approach follows mainly the poroelastic infinite element proposed by Khalili et al. [86], whereas the infinite element is now chosen to be of the mapped type. Thus, the one-dimensional infinite element is actually a combination of the infinite element presented by Khalili and the already introduced infinite element of the elastodynamic case, described in detail in section 4.1.1. Hence, the shape and corresponding test function are defined as

$$\begin{aligned}
\varphi^k(\xi_3) &= P_p^k(\xi_3)\left[\hat{U}_1^{\mathrm{K}}\,\mathrm{e}^{-\frac{\mathrm{s}}{c_1}\mu(\bar{a},\xi_3)} + \hat{U}_2^{\mathrm{K}}\,\mathrm{e}^{-\frac{\mathrm{s}}{c_2}\mu(\bar{a},\xi_3)}\right] \;,\; \bar{\varphi}^k(\xi_3) = D(\xi_3)\varphi^k(\xi_3) \;, \\
\vartheta^k(\xi_3) &= P_p^k(\xi_3)\left[\hat{P}_1^{\mathrm{K}}\,\mathrm{e}^{-\frac{\mathrm{s}}{c_1}\mu(\bar{a},\xi_3)} + \hat{P}_2^{\mathrm{K}}\,\mathrm{e}^{-\frac{\mathrm{s}}{c_2}\mu(\bar{a},\xi_3)}\right] \;,\; \bar{\vartheta}^k(\xi_3) = D(\xi_3)\vartheta^k(\xi_3) \;, \\
\psi^k(\xi_3) &= P_p^k(\xi_3)\left[\hat{W}_1^{\mathrm{K}}\,\mathrm{e}^{-\frac{\mathrm{s}}{c_1}\mu(\bar{a},\xi_3)} + \hat{W}_2^{\mathrm{K}}\,\mathrm{e}^{-\frac{\mathrm{s}}{c_2}\mu(\bar{a},\xi_3)}\right] \;,\; \bar{\psi}^k(\xi_3) = D(\xi_3)\psi^k(\xi_3) \;,
\end{aligned} \tag{4.28}$$

for the solid displacement, the pore pressure, and the relative displacement, respectively. The detailed meaning of the single components of (4.28) is the same as for the one-dimensional elastodynamic infinite element presented in section 4.1.1.

The simplified model is based on the fact, that the slow (or second) wave in a poroelastic material is highly damped and thus, for realistic, most common poroelastic material, not observable [123]. This corresponds to the case that the wave weighting factors approach $\hat{U}_1^{\mathrm{K}} = \hat{P}_1^{\mathrm{K}} = \hat{W}_1^{\mathrm{K}} \approx 1$, whereas $\hat{U}_2^{\mathrm{K}} = \hat{P}_2^{\mathrm{K}} = \hat{W}_2^{\mathrm{K}} \approx 0$. In this case it is reasonable to neglect the influence of the slow wave and to approximate only the fast (or first) wave. Thus,

the simplified model of the infinite element for a poroelastic material is identical to the elastodynamic infinite element, i.e., the shape and test function are defined as

$$\begin{aligned}
\varphi^k(\xi_3) &= P_p^k(\xi_3)\,\mathrm{e}^{-\frac{s}{c_1}\mu(\overline{a},\xi_3)}\,, \quad \bar{\varphi}^k(\xi_3) = D(\xi_3)\varphi^k(\xi_3) \\
\vartheta^k(\xi_3) &= P_p^k(\xi_3)\,\mathrm{e}^{-\frac{s}{c_1}\mu(\overline{a},\xi_3)}\,, \quad \bar{\vartheta}^k(\xi_3) = D(\xi_3)\varphi^k(\xi_3) \\
\psi^k(\xi_3) &= P_p^k(\xi_3)\,\mathrm{e}^{-\frac{s}{c_1}\mu(\overline{a},\xi_3)}\,, \quad \bar{\psi}^k(\xi_3) = D(\xi_3)\varphi^k(\xi_3)\,,
\end{aligned} \tag{4.29}$$

for the solid displacement, the pore pressure, and the relative displacement, respectively.

4.3.3 3d poroelastodynamic infinite element

The enhancement of the one-dimensional infinite element to the tree-dimensional is accomplished in the same manner as for the elastodynamic case, see section 4.1.2. Hence, an infinite element as shown in figure 4.4 is considered. Nevertheless, attention must be paid to the question which type of constituent is able to transfer which type of wave, since multiple waves are present in a three-dimensional problem. In an unbounded three-dimensional poroelastic media two compressional and a shear wave may be present with wave velocities c_1, c_2, and c_S, respectively, as revealed in section 2.2.7. In a poroelastic halfspace also the propagation of the Rayleigh wave can be observed [123], as it is also the case in an elastic halfspace [1, 79]. As it can be noticed in the general analytical solution of the poroelastic column (A.11), both compressional waves, with wave speeds c_1 and c_2, are transferred by the solid displacement, the pore pressure, and the relative displacement. Since an inviscid interstitial fluid is assumed, the shear and consequently, the Rayleigh wave with wave speeds c_S and c_R, can be only carried by the solid displacement. Thus, the shape and test function of the solid displacement u_i is defined as

$$\varphi^j(\boldsymbol{\xi}) = \frac{1}{2}(1-\xi_3)S^i(\xi_1,\xi_2)P_p^k(\xi_3)\frac{1}{n_c}\sum_{\ell=1}^{n_c}\mathrm{e}^{-\frac{s}{c_\ell}\mu(\overline{a},\xi_3)}\,, \quad \bar{\varphi}^j(\boldsymbol{\xi}) = D(\xi_3)\varphi^j(\boldsymbol{\xi})\,, \tag{4.30}$$

where n_c denotes the number of waves to be approximated. The parameter c_ℓ represents one of the wave velocities c_1, c_S, or c_R. For the pore pressure p and the relative displacement w_i are the shape and test functions defined by

$$\begin{aligned}
\vartheta^j(\boldsymbol{\xi}) &= \frac{1}{2}(1-\xi_3)S^i(\xi_1,\xi_2)P_p^k(\xi_3)\,\mathrm{e}^{-\frac{s}{c_1}\mu(\overline{a},\xi_3)}\,, \quad \bar{\vartheta}^j(\boldsymbol{\xi}) = D(\xi_3)\vartheta^j(\boldsymbol{\xi}) \\
\psi^j(\boldsymbol{\xi}) &= \frac{1}{2}(1-\xi_3)S^i(\xi_1,\xi_2)P_p^k(\xi_3)\,\mathrm{e}^{-\frac{s}{c_1}\mu(\overline{a},\xi_3)}\,, \quad \bar{\psi}^j(\boldsymbol{\xi}) = D(\xi_3)\psi^j(\boldsymbol{\xi})\,.
\end{aligned} \tag{4.31}$$

Any other parameters are the same as already defined for the elastodynamic infinite element of section 4.1.2.

If also the slow wave is to be considered, the approach of Khalili et al. [86, 87] is included. Therefore, the shape function for the solid displacement is defined as

$$\varphi^j(\boldsymbol{\xi}) = \frac{1}{2}(1-\xi_3)S^i(\xi_1,\xi_2)P_p^k(\xi_3)\frac{1}{3}\left(\left[\hat{U}_1^{\mathrm{K}}\,\mathrm{e}^{-\frac{s}{c_1}\mu(\bar{a},\xi_3)} + \hat{U}_2^{\mathrm{K}}\,\mathrm{e}^{-\frac{s}{c_2}\mu(\bar{a},\xi_3)}\right] + \mathrm{e}^{-\frac{s}{c_S}\mu(\bar{a},\xi_3)} + \mathrm{e}^{-\frac{s}{c_R}\mu(\bar{a},\xi_3)}\right) .$$

The shape function for the pore pressure and the relative displacement are given by

$$\vartheta^j(\boldsymbol{\xi}) = \frac{1}{2}(1-\xi_3)S^i(\xi_1,\xi_2)P_p^k(\xi_3)\left[\hat{P}_1^{\mathrm{K}}\,\mathrm{e}^{-\frac{s}{c_1}\mu(\bar{a},\xi_3)} + \hat{P}_2^{\mathrm{K}}\,\mathrm{e}^{-\frac{s}{c_2}\mu(\bar{a},\xi_3)}\right]$$
$$\psi^j(\boldsymbol{\xi}) = \frac{1}{2}(1-\xi_3)S^i(\xi_1,\xi_2)P_p^k(\xi_3)\left[\hat{W}_1^{\mathrm{K}}\,\mathrm{e}^{-\frac{s}{c_1}\mu(\bar{a},\xi_3)} + \hat{W}_2^{\mathrm{K}}\,\mathrm{e}^{-\frac{s}{c_2}\mu(\bar{a},\xi_3)}\right] ,$$

respectively. The test function for the three constituents are

$$\bar{\varphi}^j(\boldsymbol{\xi}) = D(\xi_3)\varphi^j(\boldsymbol{\xi}), \quad \bar{\vartheta}^j(\boldsymbol{\xi}) = D(\xi_3)\vartheta^j(\boldsymbol{\xi}), \quad \bar{\psi}^j(\boldsymbol{\xi}) = D(\xi_3)\psi^j(\boldsymbol{\xi}) .$$

Note that the parameters $U_i^{\mathrm{K}}, P_i^{\mathrm{K}}$, and W_i^{K}, with $i = 1,2$, contain still the constants C_3 and C_4, which have to be determined for the underlying problem. Of course, the application of the wave weighting factors U_i^{K}, P_i^{K}, and W_i^{K} to the three-dimensional case is just an approximation, since a one-dimensional model is used to define them.

The derivation of the two-dimensional poroelastic infinite element is rather straightforward, as it can be seen for the elastodynamic case (cf. section 4.1.2), and will therefore be omitted.

4.3.4 Quasi-static poroelastic infinite element

The quasi-static infinite element for poroelastic media is simple deduced by neglecting the wave-like terms in section (4.3.3) yielding the shape and test functions

$$\varphi^j(\boldsymbol{\xi}) = \frac{1}{2}(1-\xi_3)S^i(\xi_1,\xi_2)P_p^k(\xi_3) , \quad \bar{\varphi}^j(\boldsymbol{\xi}) = D(\xi_3)\varphi^j(\boldsymbol{\xi})$$
$$\vartheta^j(\boldsymbol{\xi}) = \frac{1}{2}(1-\xi_3)S^i(\xi_1,\xi_2)P_p^k(\xi_3) , \quad \bar{\vartheta}^j(\boldsymbol{\xi}) = D(\xi_3)\vartheta^j(\boldsymbol{\xi})$$
$$\psi^j(\boldsymbol{\xi}) = \frac{1}{2}(1-\xi_3)S^i(\xi_1,\xi_2)P_p^k(\xi_3) , \quad \bar{\psi}^j(\boldsymbol{\xi}) = D(\xi_3)\psi^j(\boldsymbol{\xi}) ,$$

for the solid displacement, the pore pressure, and the relative displacement, respectively.

General remarks The here proposed shape function are now ready to be inserted into any discrete variational formulation of section 3.1 to 3.2. Note that the test function for any infinite element is different from the trial function. Moreover, the Jacobian for infinite elements is calculated by using the mapping relation (4.18). The evaluation of the integrals, which contain exponential expressions, is performed by a Newton-Cotes scheme derived in the following section 4.4.

4.4 Numerical integration

During the evaluation of infinite element matrices, based on the shape functions of sections 4.1 and 4.3, integrals of the form

$$\int_{-1}^{+1} f(\xi_3)\,\mathrm{e}^{-z\frac{1+\xi_3}{1-\xi_3}}\,\mathrm{d}\,\xi_3 \tag{4.32}$$

have to be calculated. In equation (4.32), $z \in \mathbb{C}$ represent a Complex parameter, e.g., $z = \overline{a}\frac{\mathrm{s}}{c}$, where $\overline{a}$ denotes the characteristic length of the infinite element defined in (4.20) and c any wave velocity. The finiteness of the integral is ensured, since the real part of the Laplace parameter is positive by definition, i.e., $\mathrm{Re}(\mathrm{s}) > 0$ [61]. It can be verified that also the real part of the fraction s/c is always larger than zero. In order to evaluate this integrals numerically, a Newton Cotes type formula will be derived. Thus, integration points are chosen and corresponding integration weights are calculated. To explain the integration procedure a two point integration rule will be derived. The chosen points are for example

$$\xi_3^1 = -\tfrac{1}{3}\,, \quad \xi_3^2 = +\tfrac{1}{3}\,.$$

The polynomial $f(\xi_3)$ is approximated by Lagrange polynomials P_p^k, with $p = 1$ and $k = 1,2$, and is, therefore, expressed as

$$f(\xi_3) = f^1 P_1^1(\xi_3) + f^2 P_1^2(\xi_3)\,,$$

where $f^1 = f(\xi_3^1)$ and $f^2 = f(\xi_3^2)$ are the values of $f(\xi_3^k)$ evaluated at the integration points. Thus, the given integral (4.32) can be rewritten

$$\begin{aligned}\int_{-1}^{+1} f(\xi_3)\,\mathrm{e}^{-z\frac{1+\xi_3}{1-\xi_3}}\,\mathrm{d}\,\xi_3 &= f^1 \int_{-1}^{+1} P_1^1(\xi_3)\,\mathrm{e}^{-z\frac{1+\xi_3}{1-\xi_3}}\,\mathrm{d}\,\xi_3 + f^2 \int_{-1}^{+1} P_1^2(\xi_3)\,\mathrm{e}^{-z\frac{1+\xi_3}{1-\xi_3}}\,\mathrm{d}\,\xi_3 \\ &= f^1 w^1 + f^2 w^2\,,\end{aligned}$$

with the integrations weights w^1 and w^2, defined by the integrals. During the derivation of the integration weights, integrals of the product of the single monomials with the exponential term must be performed, yielding

$$\int_{-1}^{+1} (\xi_3)^0\,\mathrm{e}^{-z\frac{1+\xi_3}{1-\xi_3}}\,\mathrm{d}\,\xi_3 = 2 + 2z\mathrm{e}^z\left(\mathrm{Ei}(-z) + \frac{1}{2}\left(\log(-\tfrac{1}{z}) - \log(\tfrac{1}{z}) - \log(-z) + \log(z)\right)\right)$$

$$\int_{-1}^{+1} (\xi_3)^1\,\mathrm{e}^{-z\frac{1+\xi_3}{1-\xi_3}}\,\mathrm{d}\,\xi_3 =$$

$$2z\left[1 + (1+z)\,\mathrm{e}^z\left(\mathrm{Ei}(-z) + \frac{1}{2}\left(\log(-\tfrac{1}{z}) - \log(\tfrac{1}{z}) - \log(-z) + \log(z)\right)\right)\right]\,,$$

where $\mathrm{Ei}(-z)$ denotes the *Exponential Integral* [143]. Consequently, the integration weights results in

$$w^1 = 1-3z-z(2+3z)\,\mathrm{e}^z\left(\mathrm{Ei}(-z)+\frac{1}{2}\left(\log\left(-\tfrac{1}{z}\right)-\log\left(\tfrac{1}{z}\right)-\log\left(-z\right)+\log\left(z\right)\right)\right)$$
$$w^2 = 1+3z+z(4+3z)\,\mathrm{e}^z\left(\mathrm{Ei}(-z)+\frac{1}{2}\left(\log\left(-\tfrac{1}{z}\right)-\log\left(\tfrac{1}{z}\right)-\log\left(-z\right)+\log\left(z\right)\right)\right). \tag{4.33}$$

The proposed integration rule is exact for polynomials of degree $m-1$, when m is the number of integration points. Note that the integration weights are frequency dependent, whereas the integration points remain to be real valued. Thus, the integration weights have to be recalculated for every needed frequency. The integration on the base face of the infinite element in figure 4.4 is still performed with the standard *Gauß quadrature* (cf. section 3.4), whereas the integral of the infinite direction is evaluated using the above derived integration rule.

Efficient evaluation of integration weights

A crucial point in the evaluation of the integration weights of the integral (4.32) is the computation of the Exponential Integral $\mathrm{Ei}(-z)$. Different approaches are possible to evaluate this integral. Actually, the calculation is divided into three ranges of values of z, namely

- $\mathrm{Re}(z) < 5 \wedge \mathrm{Abs}(\mathrm{Im}(z)) < 5$: An efficient way of computing the Exponential Integral is proposed by Amos [7]. The FORTRAN subroutine supplied by Amos [6] is used.
- $5 \leq \mathrm{Re}(z) < 100 \wedge 5 \leq \mathrm{Abs}(\mathrm{Im}(z)) < 100$: The integration weights are calculated by interpolation from pre-calculated look-up tables. These look-up tables were generated using the software package Mathematica [146].
- $\mathrm{Re}(z) \geq 100 \vee \mathrm{Abs}(\mathrm{Im}(z)) \geq 100$: For values of $z \to \infty$ the asymptotic series expansion

$$\mathrm{Ei}(-z) \approx -\frac{\mathrm{e}^{-z}}{z}\sum_{k=0}^{\infty}\frac{k!}{(-z)^k}-\frac{1}{2}\left(\log(-\tfrac{1}{z})-\log(\tfrac{1}{z})-\log(-z)+\log(z)\right)$$

  is valid [143]. Inserting the above asymptotic series expansion into the weights (4.33) yields

$$w^1 = 1-3z-z(2+3z)\left(-\frac{1}{z}\sum_{k=0}^{\infty}\frac{k!}{(-z)^k}\right) = \frac{4}{z}-\frac{14}{z^2}+\frac{60}{z^3}-\frac{312}{z^4}+\ldots$$
$$w^2 = 1+3z+z(4+3z)\left(-\frac{1}{z}\sum_{k=0}^{\infty}\frac{k!}{(-z)^k}\right) = -\frac{2}{z}+\frac{10}{z^2}-\frac{48}{z^3}+\frac{264}{z^4}-\ldots.$$

Note that the above weights aren't equal, although the integration points are symmetric. The series expansion is truncated after a precision of at least eight digits is obtained. This is ensured by a comparison of the weights calculated with the above series expansion and exact calculated weights (4.33) using the computing package Mathematica [146]. For example, for a five point integration rule, twelve terms of the series expansion are used.

The derived quadrature rule is only exact for polynomials of a maximum order $m-1$, where m is the number of integration points. Special care must be taken when the above quadrature rule is used to evaluate the infinite element matrices resulting from the shape functions (4.21) (two-dimensional problems). In this case, the resulting integrals may contain polynomials of square root type. For this kind of polynomials no information can be given about the accuracy of the proposed integration scheme. Thus, to obtain a desired accuracy the number of integration points must be increased appropriately. Since, two-dimensional problems aren't covered in this thesis, no further investigations are performed concerning the appropriate integration of such integrals.

4.5 Time domain solution of coupled finite and infinite elements

When dealing with unbounded domains a special treatment is necessary to obtain a time domain solution. The Newmark algorithm can not be used as time stepping scheme in dynamic problems when infinite elements are used, since the shape functions of the infinite elements are defined in Laplace domain to provide the wave behavior (cf. section 4.1 and 4.1.1). In order to obtain a time domain solution an inverse Laplace transformation is needed. A method which serves this aim is the convolution quadrature method (CQM), as explained in detail in section 3.3.2. The drawback of CQM is that the quadrature weights have to be stored for every time step as well as all solution vectors of the past. Thus, the amount of computer storage needed is dependent on the number of time steps of the simulation. On the other side, once the quadrature weights are calculated, they can be reused for different load cases. On the contrary, the computer storage consumption of the Newmark time integration scheme is essentially smaller, since only a view matrices and solution vectors have to be stored. This brings up the idea to combine these two time stepping methods. Thus, the Newmark method will be applied to the time integration of the near field, whereas the time domain solution of the far field will be calculated using the CQM. This purpose can be accomplished by using the *substructure method* or *domain decomposition method*. Here, the domain of interest is divided into so called subdomains. These subdomains are then initially treated separately and subsequently merged together under consideration of *interface conditions*. Thus, the use of an optimized solution algorithm for each subdivision of the original domain is possible. An extensive survey of domain decomposition methods for the finite element method is given in the books of Toselli and Widlund [139] and

Steinbach [133] . Another area of research is the topic of conforming and non-conforming interface discretizations, e.g. [103, 118]. In the case that the discretizations of the single subdomains at the interface is conform, the interface conditions can be formulated directly at the nodes. This can be realized either by using the Lagrange multiplier method [118] or by assembling directly the single subdomains into global system matrices, e.g., [80]. If the interfaces are non-conforming, the Lagrange multipliers are approximated by conventional shape functions. This approach results in so called *connectivity matrices*, which ensures the interface conditions to be fulfilled [118].

The infinite elements are constructed in such a way that they match to the finite elements. Also, it is ensured that the approximation order at the interfaces coincide. Thus, in this work, the interface conditions will be fulfilled by assembling the finite and infinite elements into a global equation system, i.e., a direct coupling is performed. The solution for every time step is then obtained by solving this global equation system. For simplicity, the application of the proposed substructure method is explained for two subdomains, where in one domain the Newmark time stepping scheme will be applied and in the other domain the CQM is used to gain the time domain solution. Nevertheless, the use of more than two subdomains is possible and straightforward. Hence, the domain Ω_h, the discretization parameter h will be omitted in the following to retain a more readable form, is decomposed into two non-overlapping subdomains

$$\overline{\Omega} = \overline{\Omega}^{\mathrm{NEW}} \cup \overline{\Omega}^{\mathrm{CQM}} , \quad \Omega^{\mathrm{NEW}} \cap \Omega^{\mathrm{CQM}} = \varnothing , \tag{4.34}$$

as shown in figure 4.7. In equation (4.34) $\overline{\Omega}^{\mathrm{NEW}}$ and $\overline{\Omega}^{\mathrm{CQM}}$ denote the subdomains, where

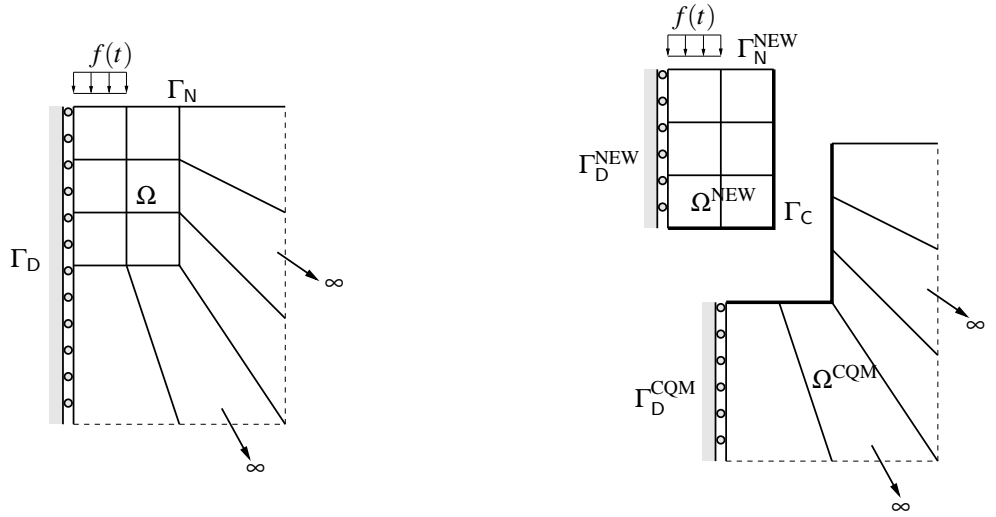

(a) Single domain

(b) Decomposition into two subdomains

Figure 4.7: Decomposition of the domain Ω into near Ω^{NEW} and far field Ω^{CQM}.

the Newmark integration scheme and the convolution quadrature method, respectively, is

applied to obtain the time domain solution. Due to the subdivision the *interface* Γ_C

$$\Gamma_C = \overline{\Omega}^{NEW} \cap \overline{\Omega}^{CQM}$$

is generated. Consequently, the boundary of each subdomain is composed of the interface Γ_C, a Neumann and Dirichlet part

$$\Gamma^{NEW} = \Gamma_C \cup \Gamma_D^{NEW} \cup \Gamma_N^{NEW} , \quad \Gamma^{CQM} = \Gamma_C \cup \Gamma_D^{CQM} \cup \Gamma_N^{CQM} .$$

Consequently, new unknowns are produced due to the subdivision of the domain Ω. To maintain a well posed equation system, *interface conditions* have to be formulated. For an elastic material the nodal forces have to be in equilibrium. Moreover, the displacements at a common node $N \in n_C$ of the single subdomains have to match each other, i.e.,

$$\begin{aligned} {}_n(f_i^N)^{NEW} + {}_n(f_i^N)^{CQM} &= 0 \\ {}_n(u_i^N)^{NEW} - {}_n(u_i^N)^{CQM} &= 0 , \end{aligned} \tag{4.35}$$

where the superscript f_i^N denotes the nodal force vector, u_i^N the nodal displacement vector and n the discrete time step. n_C represents all nodes belonging to the interface Γ_C. In a poroelastic material the interface conditions have to be formulated for every constituent, namely the solid and fluid phase. Thus, the interface conditions for the solid phase are

$$\begin{aligned} {}^u_n(f_i^N)^{NEW} + {}^u_n(f_i^N)^{CQM} &= 0 \\ {}_n(u_i^N)^{NEW} - {}_n(u_i^N)^{CQM} &= 0 . \end{aligned}$$

The interface conditions for the fluid phase are formulated as

$$\begin{aligned} {}^p_n(f_i^N)^{NEW} + {}^p_n(f_i^N)^{CQM} &= 0 \\ {}_n(p_i^N)^{NEW} - {}_n(p_i^N)^{CQM} &= 0 \end{aligned}$$

or as

$$\begin{aligned} {}^w_n(f_i^N)^{NEW} + {}^w_n(f_i^N)^{CQM} &= 0 \\ {}_n(w_i^N)^{NEW} - {}_n(w_i^N)^{CQM} &= 0 \end{aligned}$$

depending on whether boundary conditions (3.26) or (3.27) are used. In order to illustrate the coupling process the equations system of the single subdomains are reordered accordingly to the degrees of freedom belonging to the interior or the interface of the subdomains. Thus, the resulting equation system of the Newmark method (3.64) of domain Ω^{NEW} is decomposed as

$$\begin{bmatrix} \overline{\mathbf{K}}_{II}^{NEW} & \overline{\mathbf{K}}_{IC}^{NEW} \\ \overline{\mathbf{K}}_{CI}^{NEW} & \overline{\mathbf{K}}_{CC}^{NEW} \end{bmatrix} \begin{bmatrix} {}_n\mathbf{u}_I^{NEW} \\ {}_n\mathbf{u}_C^{NEW} \end{bmatrix} = \begin{bmatrix} {}_n\mathbf{f}_I^{NEW} + {}_n\mathbf{r}_I^{NEW} \\ {}_n\mathbf{f}_C^{NEW} + {}_n\mathbf{r}_C^{NEW} \end{bmatrix} , \tag{4.36}$$

where the superscripts I and C refer to the interior and interface of each subdomain, respectively. Moreover, the equation of the convolution quadrature for the unknown solution vector (3.69) is decomposed as

$$\begin{bmatrix} \overline{\boldsymbol{\omega}}_{\mathsf{II}}^{\mathrm{CQM}} & \overline{\boldsymbol{\omega}}_{\mathsf{IC}}^{\mathrm{CQM}} \\ \overline{\boldsymbol{\omega}}_{\mathsf{CI}}^{\mathrm{CQM}} & \overline{\boldsymbol{\omega}}_{\mathsf{CC}}^{\mathrm{CQM}} \end{bmatrix} \begin{bmatrix} {}_n\mathbf{u}_{\mathsf{I}}^{\mathrm{CQM}} \\ {}_n\mathbf{u}_{\mathsf{C}}^{\mathrm{CQM}} \end{bmatrix} = \begin{bmatrix} {}_n\mathbf{f}_{\mathsf{I}}^{\mathrm{CQM}} + {}_n\mathbf{r}_{\mathsf{I}}^{\mathrm{CQM}} \\ {}_n\mathbf{f}_{\mathsf{C}}^{\mathrm{CQM}} + {}_n\mathbf{r}_{\mathsf{C}}^{\mathrm{CQM}} \end{bmatrix} , \tag{4.37}$$

where the coefficient matrix $\boldsymbol{\omega}_0$ is replaced by $\overline{\boldsymbol{\omega}}$. The global equation system for time step n is, therefore, obtained by assembling the equations systems of the subdomains (4.36) and (4.37), yielding

$$\begin{bmatrix} \overline{\mathbf{K}}_{\mathsf{II}}^{\mathrm{NEW}} & \overline{\mathbf{K}}_{\mathsf{IC}}^{\mathrm{NEW}} & \mathbf{0} \\ \overline{\mathbf{K}}_{\mathsf{CI}}^{\mathrm{NEW}} & \overline{\mathbf{K}}_{\mathsf{CC}}^{\mathrm{NEW}} + \overline{\boldsymbol{\omega}}_{\mathsf{CC}}^{\mathrm{CQM}} & \overline{\boldsymbol{\omega}}_{\mathsf{CI}}^{\mathrm{CQM}} \\ \mathbf{0} & \overline{\boldsymbol{\omega}}_{\mathsf{IC}}^{\mathrm{CQM}} & \overline{\boldsymbol{\omega}}_{\mathsf{II}}^{\mathrm{CQM}} \end{bmatrix} \begin{bmatrix} {}_n\mathbf{u}_{\mathsf{I}}^{\mathrm{NEW}} \\ {}_n\mathbf{u}_{\mathsf{C}} \\ {}_n\mathbf{u}_{\mathsf{I}}^{\mathrm{CQM}} \end{bmatrix} = \begin{bmatrix} {}_n\mathbf{f}_{\mathsf{I}}^{\mathrm{NEW}} + {}_n\mathbf{r}_{\mathsf{I}}^{\mathrm{NEW}} \\ {}_n\mathbf{f}_{\mathsf{C}}^{\mathrm{NEW}} + {}_n\mathbf{f}_{\mathsf{C}}^{\mathrm{CQM}} + {}_n\mathbf{r}_{\mathsf{C}}^{\mathrm{NEW}} + {}_n\mathbf{r}_{\mathsf{C}}^{\mathrm{CQM}} \\ {}_n\mathbf{f}_{\mathsf{I}}^{\mathrm{CQM}} + {}_n\mathbf{r}_{\mathsf{I}}^{\mathrm{CQM}} \end{bmatrix} . \tag{4.38}$$

Taking into account the interface conditions, e.g. (4.35) for elastic material, the right-hand side of (4.38) simplifies to

$$\underbrace{\begin{bmatrix} \overline{\mathbf{K}}_{\mathsf{II}}^{\mathrm{NEW}} & \overline{\mathbf{K}}_{\mathsf{IC}}^{\mathrm{NEW}} & \mathbf{0} \\ \overline{\mathbf{K}}_{\mathsf{CI}}^{\mathrm{NEW}} & \overline{\mathbf{K}}_{\mathsf{CC}}^{\mathrm{NEW}} + \overline{\boldsymbol{\omega}}_{\mathsf{CC}}^{\mathrm{CQM}} & \overline{\boldsymbol{\omega}}_{\mathsf{CI}}^{\mathrm{CQM}} \\ \mathbf{0} & \overline{\boldsymbol{\omega}}_{\mathsf{IC}}^{\mathrm{CQM}} & \overline{\boldsymbol{\omega}}_{\mathsf{II}}^{\mathrm{CQM}} \end{bmatrix}}_{\mathbf{K}_{\mathrm{sys}}} \begin{bmatrix} {}_n\mathbf{u}_{\mathsf{I}}^{\mathrm{NEW}} \\ {}_n\mathbf{u}_{\mathsf{C}} \\ {}_n\mathbf{u}_{\mathsf{I}}^{\mathrm{CQM}} \end{bmatrix} = \begin{bmatrix} {}_n\mathbf{f}_{\mathsf{I}}^{\mathrm{NEW}} + {}_n\mathbf{r}_{\mathsf{I}}^{\mathrm{NEW}} \\ {}_n\mathbf{r}_{\mathsf{C}}^{\mathrm{NEW}} + {}_n\mathbf{r}_{\mathsf{C}}^{\mathrm{CQM}} \\ {}_n\mathbf{f}_{\mathsf{I}}^{\mathrm{CQM}} + {}_n\mathbf{r}_{\mathsf{I}}^{\mathrm{CQM}} \end{bmatrix} . \tag{4.39}$$

The resulting global system matrix $\mathbf{K}_{\mathrm{sys}}$ has to be inverted only once, as it is also the case in a pure Newmark equation system or CQM based time stepping scheme, if a direct solver is used, e.g., a direct solver based on LU-decomposition. The vector on the right-hand side of (4.39) has to be recomputed at every time step for each subdomain, depending on the used time stepping scheme. Note that based on the direct coupling strategy the nodal interface forces vanish and, therefore, must not be known a priori. The application of the suggested method to more than two subdomains can be performed analogously. The time step size of each subdomain is chosen to be equal. But this doesn't need to be necessarily the case [27, 28]. The proposed coupled time integration strategy will be validated in section 5.

5 NUMERICAL EXAMPLES

In this chapter, the performance of the proposed infinite element will be investigated. At first, typical examples will be considered where the analytical solution is available. Some reference solutions are given in Appendix A but will be explicitly mentioned when they are used. Additionally, the results of a halfspace with different boundary conditions will be explored. Since for arbitrary boundary conditions of a halfspace no analytical solutions are obtainable, the results of the coupled finite elements with the infinite elements will be compared to results obtained by a BEM calculation [102, 123]. In any of the following calculations body forces will be neglected. Before presenting the numerical examples some information about the implementation of the approximation methods will be given.

The numerical implementation is accomplished by using the open source library LIBMESH [92]. The near field is discretized using conventional finite elements (cf. for example [82] and [165]). If not otherwise stated in three-dimensional examples always 20-noded hexahedron elements will be used and denoted as "HEX20". The spatial discretization of the far field is performed using the infinite elements presented in chapter 4. The radial approximation is performed using Jacobi polynomials, as suggested by Dreyer and von Estorff [63]. The radial approximation order of the infinite elements will be fixed to be of first order, unless stated otherwise.

The evaluation of the volume integrals according to the variational formulations of chapter 3 with the shape functions of chapter 4 is performed in infinite direction by the Newton Cotes quadrature rule derived in section 4.4. The spatial integration of the finite portion of the infinite elements, i.e., the base face of the infinite elements, as well as of the conventional finite elements is performed using the Gauß quadrature presented in section 3.4. The temporal integration of the near field is performed using the Newmark quadrature introduced in section 3.3.1. If not otherwise stated the Newmark parameters are fixed to the values $\beta = 0.25$ and $\gamma = 0.5$. The time domain solution of the far field is calculated using the CQM presented in section 3.3.2. Here, the error bound is fixed to $\varepsilon = 10^{-5}$ and the underlying multistep method is chosen to be a BDF2. To calculate the temporal behavior of the whole domain, the near- and far field are combined using the substructure technique presented in section 4.5. Thus, for any example, which implies the application of infinite elements, denoted as "iFEM" in the following, it is assumed that the Newmark scheme is applied to finite elements and the CQM to infinite elements. The solution of the resulting equation system of the whole domain is obtained by using the direct solver package SPOOLES [8], which is supported by the numerical calculation package PETSC [17].

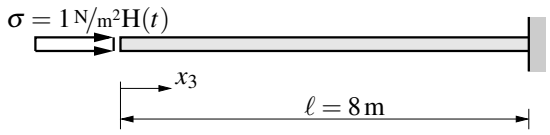

Figure 5.1: Schematic representation of the one-dimensional column with impact force.

5.1 Elastodynamic problems

In this following, different examples will be presented in order to investigate the presented coupled time stepping scheme of section 4.5 as well as the performance of the suggested infinite elements of section 4.1. The material data of the elastic homogeneous material, which corresponds to a soil, is given in table 5.1.

	$K\left[\frac{\mathrm{N}}{\mathrm{m}^2}\right]$	$G\left[\frac{\mathrm{N}}{\mathrm{m}^2}\right]$	$\varrho\left[\frac{\mathrm{kg}}{\mathrm{m}^3}\right]$
soil $1d$	$1.272 \cdot 10^8$	$8.48 \cdot 10^7$	1884
soil $3d$	$1.018 \cdot 10^8$	$1.696 \cdot 10^8$	1884

Table 5.1: Material data of a soil. For a pure one-dimensional problem (soil $1d$) the lateral contraction is set to zero, i.e., $\nu = 0$.

5.1.1 One-dimensional elastic column

The dynamic response of a one-dimensional column is examined as depicted in figure 5.1. The elastic column is assumed to be of 8 m length. The material data is given in table 5.1. Furthermore, it is assumed to be fixed at the bottom $x_3 = 8\,\mathrm{m}$. The column is subjected to a time dependent stress loading in terms of a Heaviside step function, i.e., $\mathbf{t} = [0\,0\,-1]^{\mathrm{T}}\mathrm{H}(t)\,\mathrm{N/m^2}$ at the top of the column ($x_3 = 0$). For the one-dimensional problem the analytical solution is given in equation (A.3).

In order to investigate the influence of different spatial- and temporal approximations, a three-dimensional finite element analysis will be carried out and compared to the analytical solution. Here, a column with the dimensions $2\times 2\times 8\,\mathrm{m}^3$ is assumed. Additionally, to the boundary conditions of the one-dimensional column, here, the side walls are assumed to be free to move and traction free. In order to compare the three-dimensional results with the analytical one, the lateral contraction is set to zero and, thus, the material data "soil $1d$" are taken from table 5.1 for the analysis.

First, various time steps will be investigated and it is common to use the so called CFL-factor

$$\chi = \frac{c\Delta t}{h_e} \tag{5.1}$$

to compare stability for different mesh and time step sizes. The CFL-factor was introduced by Courant, Friedrichs, and Lewy to measure the stability within finite difference schemes [56]. In equation (5.1), c denotes the wave velocity, Δt the time step, and h_e the measure for the spatial discretization. For the elastic case c is defined through the compressional wave speed c_P defined in (2.13). For the spatial discretization parameter h_e the smallest distance between two nodes will be assumed. Thus, for $0 < \chi \leq 1$ it is assured that the wave doesn't pass the distance between two nodes within one time step.

The spatial discretization is performed using the mesh sketched in figure 5.2(a), which will be referred as mesh I in the following. Here, the mesh consists of 4 HEX20 elements. Hence, the discretization parameter $h_e = 1\,\mathrm{m}$. Moreover, the different integration schemes presented in section 3.3.1 will be considered, as well their coupled solution. The different gray-scales in figures 5.2, therefore, represent domains where either the Newmark method or the CQM as time integration scheme is applied. Moreover, the application of only one integration scheme, i.e., the Newmark method or the CQM, to the whole domain will be analyzed. The Newmark parameters are chosen to be $\beta = 0.25$ and $\gamma = 0.5$.

In figures 5.3, the displacement of the elastic column at the top $u_3(0,t)$ is depicted for various discretization parameters $\chi \in \{0.1, 0.5, 0.7, 1.0, 2.0\}$, as well for the analytical solution. In figure 5.3(a), the results are obtained when the whole domain of mesh I is subjected to the Newmark method and in 5.3(b) to the CQM. The results obtained by using the coupling scheme presented in section 4.5 are shown in figure 5.3(c). The worst results are obtained in all three cases for $\chi = 2.0$. This is in a way obvious since for $\chi > 1$ the wave travels faster as the physical model is able to represent. This follows in a phase shift as well as in a reduced amplitude of the solution. These effects are stronger observable for the CQM as for the Newmark integration scheme. Nevertheless, the CFL-condition is violated for $\chi = 2.0$ the solutions do not show any instabilities, which is obvious for the case of the Newmark method. This method is unconditionally stable for $\beta = 0.25$ and $\gamma = 0.5$ (cf. section 3.3.1 or [82]). Despite the accuracy of the results are not acceptable for $\chi = 2.0$. The approach to smaller values of χ lead to more accurate results and, therefore, they come closer to the analytical solution, independent on the time stepping scheme, as can be seen in figures 5.3. For the value $\chi = 0.1$ a slight shaky behavior of the displacement can be noticed in figure 5.3(a) when the Newmark time stepping scheme is used. For this CFL-factor the best results are obtained. Furthermore, independent on the CFL-factor χ the CQM results in larger phase shifts as well in a higher damped amplitudes compared to the Newmark method. The coupling of these two methods, shown in figure 5.3(c), results in an averaging of these two time stepping schemes. Moreover, it must be mentioned that smaller values of χ correspond to a smaller time step, when the discretization parameter h_e is kept constant and follows in an increasing number of time steps N to be evaluated for the same observation time. The corresponding time step Δt and number of time steps N for any χ are listed in table 5.2. The number of time steps N is calculated by assuming an maximum observation time of $t = 0.34\,\mathrm{s}$, which corresponds to the time-plot-ranges in figures 5.4.

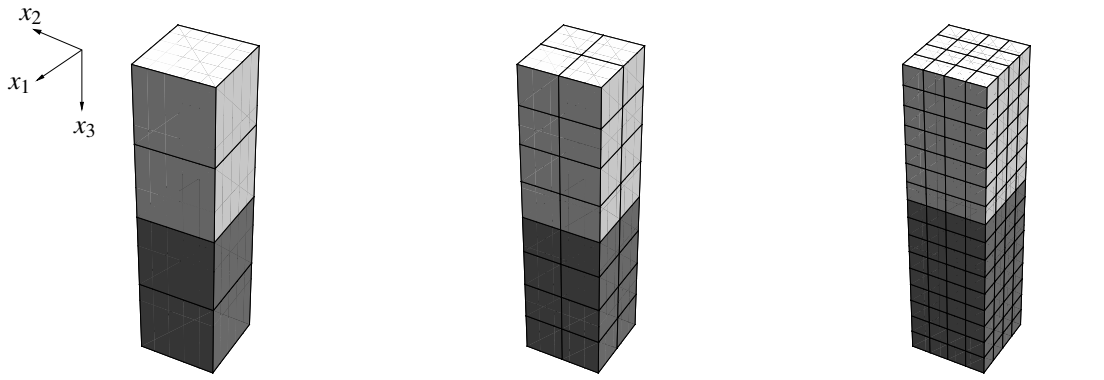

(a) Mesh I - 4 HEX20 (b) Mesh II - 32 HEX20 (c) Mesh III - 256 HEX20

Figure 5.2: Different spatial discretizations of a three-dimensional column of length $\ell = 8\,\mathrm{m}$.

Thus, taking into account computational costs the results for $\chi = 0.5$ and $\chi = 0.7$ provide quite good results, tough a coarse mesh is used. Consequently, for these two values of χ the effects of different spatial discretization will be investigated in the following.

Three different meshes with discretization parameters $h_e \in \{1.0, 0.5, 0.25\}\,\mathrm{m}$ will be investigated, as depicted in figures 5.2, and will be referred as mesh I, mesh II, and mesh III, respectively. The displacement $u_3(0,t)$ at the top of the elastic column is plotted for $\chi = 0.5$ and $\chi = 0.7$ in figures 5.4(a) and (b), respectively, for the three meshes. In figure 5.5, the results of figures 5.4(a) and (b) are added and shown for a smaller time range $t \in [0.285, 0.325]$. Accordingly to the two different gray-scales in figures 5.2 the Newmark method and the CQM are used in a coupled system to gain the time domain solution.

	mesh I $h_e = 1.0\,\mathrm{m}$		mesh II $h_e = 0.5\,\mathrm{m}$		mesh III $h_e = 0.25\,\mathrm{m}$	
χ [−]	Δt [s]	N	Δt [s]	N	Δt [s]	N
0.1	0.000272	1250	-	-	-	-
0.5	0.00136	250	0.000680	500	0.000341	1000
0.7	0.00190	180	0.000952	358	0.000476	716
1.0	0.00272	126	-	-	-	-
2.0	0.00544	64	-	-	-	-
	Compressional wave speed $c_P = 367.5\,\mathrm{m/s}$					
	Observation duration $t = 0.34\,\mathrm{s}$					

Table 5.2: Time and spatial discretization parameters for the one-dimensional column.

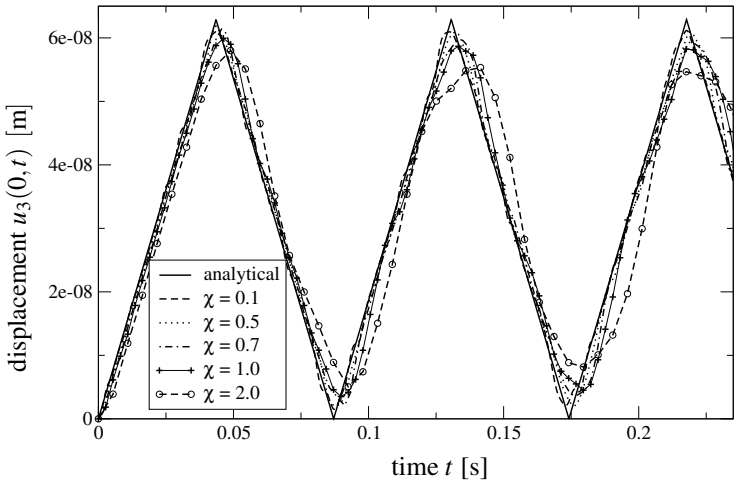

(a) Mesh I - Newmark method

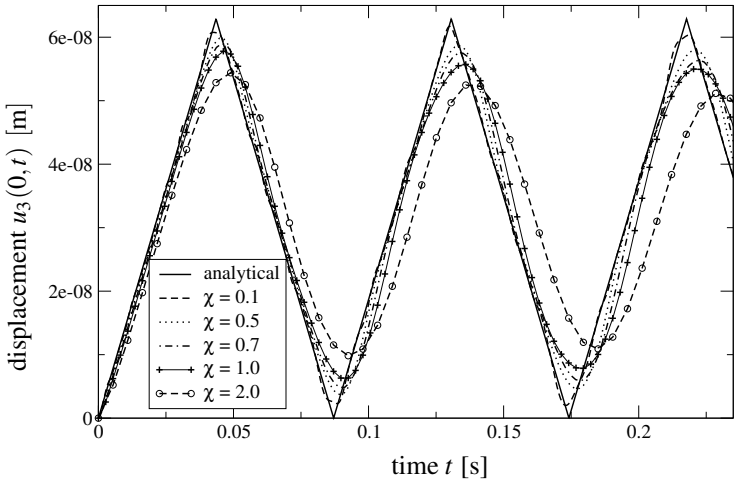

(b) Mesh I - CQM

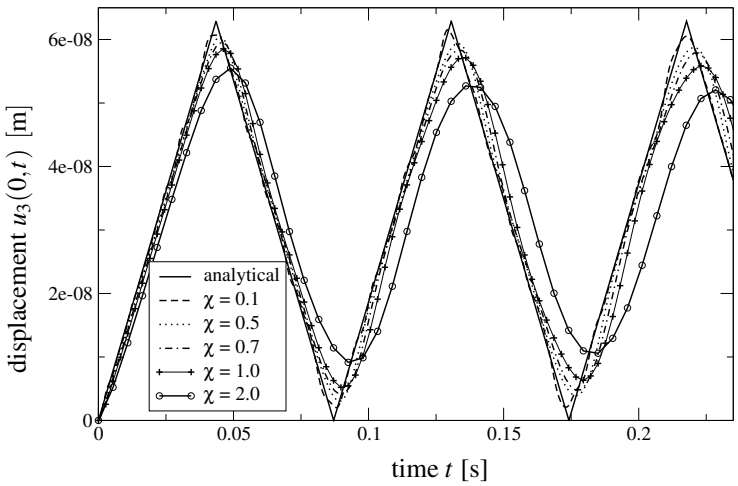

(c) Mesh I - coupled Newmark method (4 HEX20) with CQM (4 HEX20)

Figure 5.3: Displacement $u_3(0,t)$ of the three-dimensional column for different CFL-numbers χ.

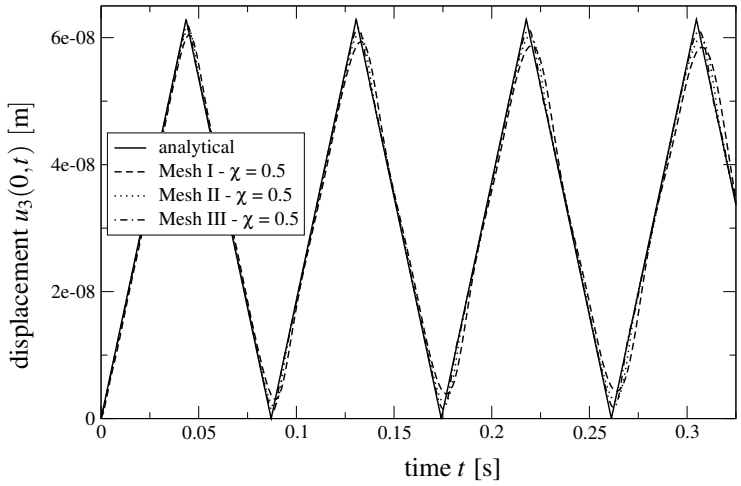

(a) CFL-factor $\chi = 0.5$ for different spatial discretizations

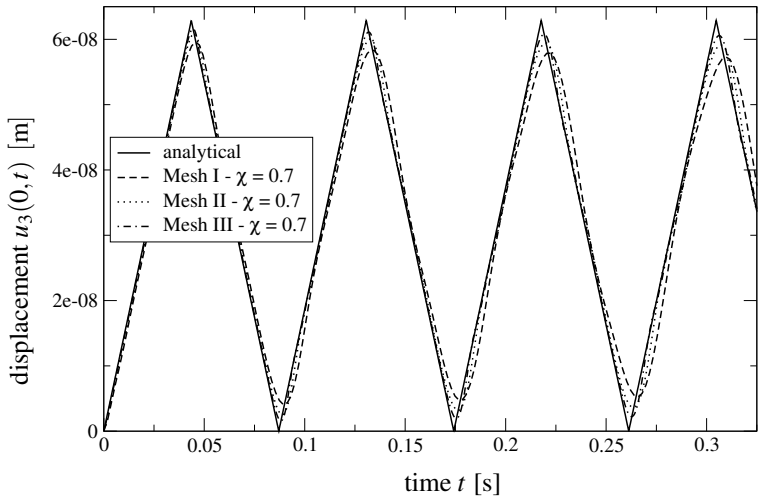

(b) CFL-factor $\chi = 0.7$ for different spatial discretizations

Figure 5.4: Displacement of the three-dimensional column for different CFL-numbers χ.

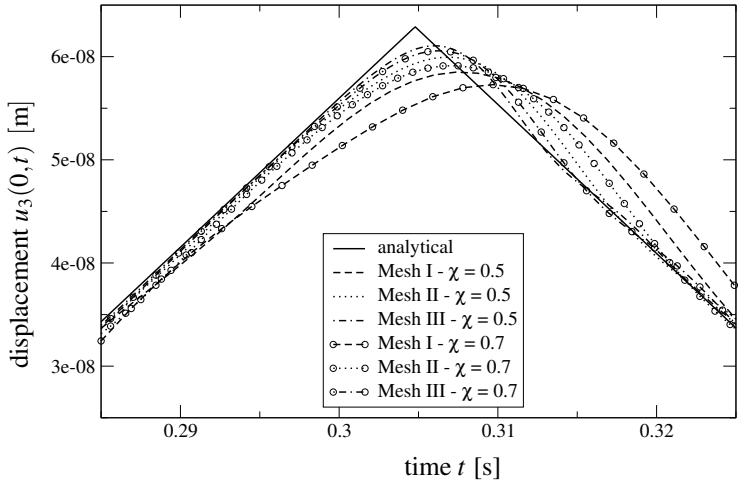

Figure 5.5: Displacement of the three-dimensional column for different spatial discretizations and the CFL-numbers $\chi = 0.5$ and $\chi = 0.7$.

In figures 5.4(a) and (b), it can be clearly identified that a finer spatial discretization yields better results even though χ is kept constant. Taking a closer look at figure 5.5 it can be observed that for mesh III the solutions for the different CFL-factors ($\chi = 0.5,\ \chi = 0.7$) only differ slightly from each other. Contrary to mesh II, the solutions of mesh I diverge from each other in a serious amount for the two different CFL-factors. Taking into account computational costs, i.e., number of time steps to be evaluated, mesh II yields the most promising results, as can be verified in figures 5.4 and 5.5.

5.1.2 One-dimensional infinite elastic column

Here, a one dimensional infinite elastic column as depicted in figure 5.6 will be investigated. A soil is assumed with the material data given in table 5.1. It is subjected to a

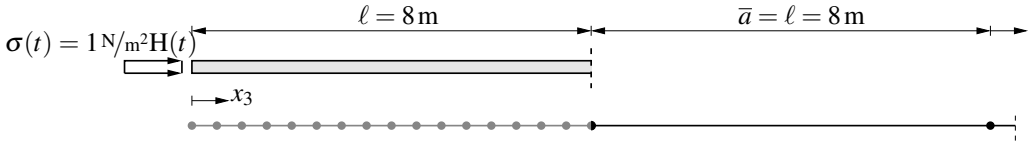

Figure 5.6: Infinite elastic column.

time dependent stress loading $\mathbf{t} = [0\,0\,-1]^{\mathrm{T}}\mathrm{H}(t)\,\mathrm{N/m^2}$ in terms of a Heaviside step function in time. Three different types of calculation will be performed in order to validate the proposed one-dimensional infinite element (section 4.1.1). First, a one-dimensional finite element calculation will be performed, where the far field is described by the analytical infinite element of section 4.1.1. The near field, assumed to be of 8 m length, is discretized with eight quadratic one-dimensional finite elements. For simplicity, here, the near and far field is discretized in time by the CQM. Second, the results of a three-dimensional column, as depicted in figure 5.7 will be examined. The near field is discretized with thirty-two

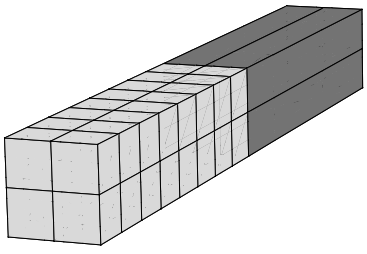

Figure 5.7: Spatial discretization of three-dimensional elastic infinite column.

HEX20. The spatial discretization of the far field is done by using four infinite elements with the modified shape function of (4.19) for each element. Modified for the reason that the factor $\frac{1}{2}(1-\xi_3)$ is dropped to obtain the one-dimensional behavior (review also the definition the pure one-dimensional shape function (4.14)). The radial approximation polynomial is chosen to be of constant order, i.e., $P_0^k = 1$ and, of course, only the compressional wave speed c_P will be approximated. The time domain solution is obtained by using the coupling strategy presented in section 4.5. The CFL-factor $\chi = 0.5$ is assumed for both calculations. Thus, the discretization parameter h_e (for the one- and three-dimensional mesh) yields the time step size $\Delta t = 0.00068\,\mathrm{s}$. The third calculation is performed using the analytical solution (A.4) and will be used to validate the other two calculations. In figure 5.8, the displacements at positions $x_3 = 0\,\mathrm{m}$ and $x_3 = 8\,\mathrm{m}$ are plotted. The analytical calculation is denoted by "analytical $u_3(\cdot,t)$", the solution of the discrete one-dimensional column by "1d FEM - analytical iFEM $u_3(\cdot,t)$", and the three-dimensional results by "3d FEM - iFEM $u_3(\cdot,t)$". It can be clearly observed that the different scenarios match each

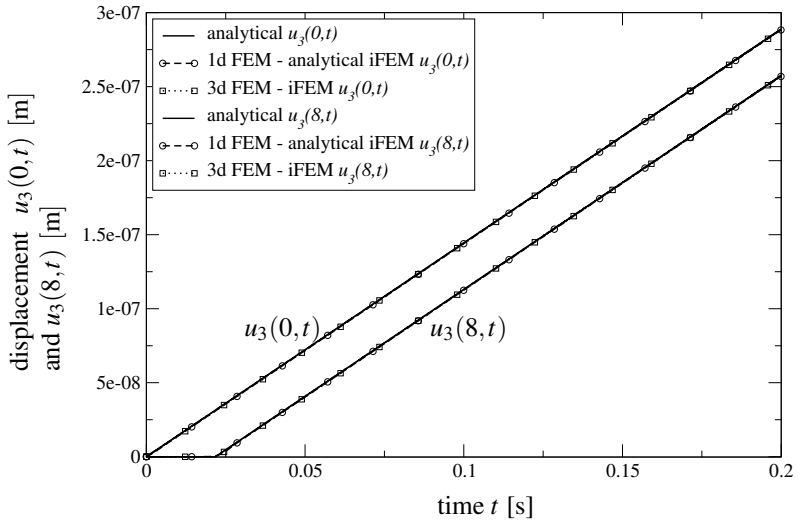

Figure 5.8: Displacement $u_3(0,t)$ and $u_3(8,t)$ of an infinite elastic column.

other. Neither the pure one-dimensional, nor the three-dimensional FEM-iFEM calculation diverge from the analytical solution. Thus, the temporal as well as the spatial discretization are chosen appropriate to obtain sufficient accurate solutions.

5.1.3 Elastic halfspace

In the next example, an elastic halfspace is considered. The underlying material is assumed to be a soil where the material data is given in table 5.1. A schematic representation of the halfspace is given in figure 5.9. The halfspace is subjected to a vertical loading on a area of $2\times2\,\mathrm{m}^2$ ($1\times1\,\mathrm{m}^2$ when the symmetric properties of the problem are used), wheres the remaining surface is traction free. In the following, the static and the dynamic case will be

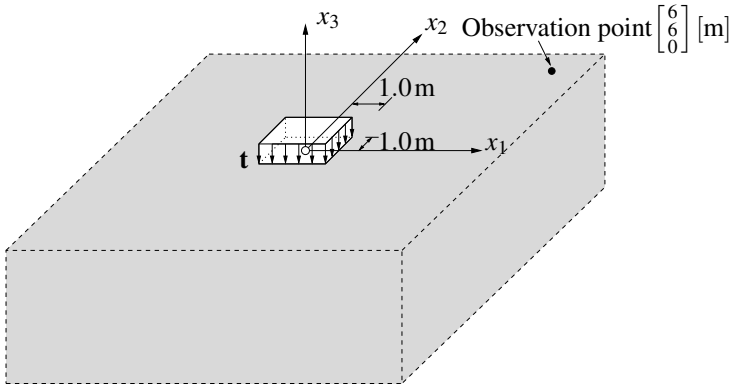

Figure 5.9: Schematic representation of the elastic halfspace.

investigated. Thus, for the static case the load vector is $\mathbf{t} = [0\,0\,-1]^{\mathrm{T}}\,\mathrm{N/m^2}$. In the dynamic case, the load vector acts in terms of a Heaviside step function, i.e., $\mathbf{t} = [0\,0\,-1]^{\mathrm{T}}\mathrm{H}(t)\,\mathrm{N/m^2}$. Since the underlying problem is unbounded the domain has to be truncated at some point when using the standard finite element method. Whereas in the static case this drawback can be circumvent by using a large finite discretized domain, this is nearly impossible for the dynamic case. Here, outward traveling waves are reflected at the introduced unphysical boundary and, thus, these reflected waves pollute the numerical results significantly as will be shown in the following. In order to transfer these waves to infinity without causing any reflections, infinite elements will be used. Hence, the unbounded domain is represented in an appropriate manner. The results obtained by using infinite elements will be compared, nevertheless, with a pure finite element calculation. Here, the bottom of the discretized domain is assumed to be fixed in vertical direction, whereas the sides to infinity are traction free. Both, the static and dynamic calculation are performed using the symmetric properties of the problem. Thus, the normal displacements at the symmetric planes, the x_1x_3- and x_2x_3-plane, are restrained.

Static case

The static calculation is performed using different spatial discretizations which are sketched in figures 5.10. The corresponding discretization parameters are given in table 5.3. The calculation are performed for two different mesh sizes of the finite domain, i.e., $h_e \in \{0.25, 0.5\}$, whereas the far field is approximated by infinite elements (figures 5.10(a) and 5.10(b)). Furthermore, a pure finite element mesh is considered as sketched in figure 5.10(c). Here, an additional layer of 7 m thickness consisting of conventional finite elements is attached. This layer is added to simulate the far field. The results of the numerical calculations are displayed in figures 5.11. The results are compared to the analytical so-

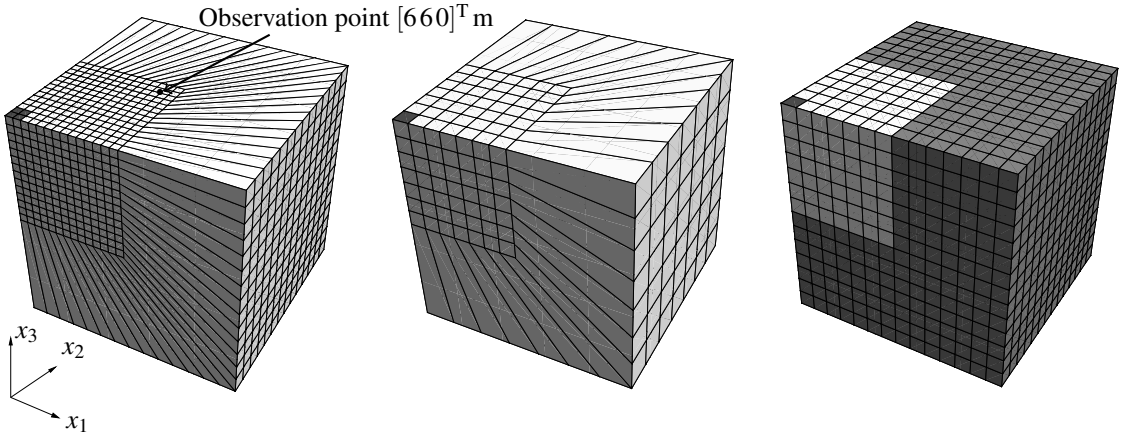

(a) Mesh 1: cube $7\times7\times7\,\mathrm{m}^3$ (b) Mesh 2: cube $7\times7\times7\,\mathrm{m}^3$ (c) Mesh 3: cube $14\times14\times14\,\mathrm{m}^3$

Figure 5.10: FEM-iFEM discretization. The dashed area in the upper left corner denotes the load area ($1.0\times1.0\,\mathrm{m}^2$).

lution, which is obtained by the integration of the analytical solution of the Boussinesq problem [24].

Mesh label	mesh 1	mesh 2	mesh 3
Finite domain	$7\times7\times7\,\mathrm{m}^3$	$7\times7\times7\,\mathrm{m}^3$	$14\times14\times14\,\mathrm{m}^3$
h_e	0.25 m	0.5 m	0.5 m
Near field	2744 HEX20	343 HEX20	343 HEX20
Far field	588 iFEM	147 iFEM	2401 HEX20
Degrees of freedom, elastic material, P_p^k with $p=1$	44022	7020	38475

Table 5.3: Spatial discretization parameters.

In figures 5.11(a) and 5.11(b), the vertical- and horizontal displacement are plotted, respectively. The displacements are plotted along the positive x_1-axis where the coordinates $x_2 = 0$ and $x_3 = 0$ are kept constant. First, the vertical displacement shown in figure 5.11(a) will be discussed. The approximation polynomial P_p^k of mesh 1 is chosen to be constant and denoted as “mesh 1, iFEM-CONST”. The results of this approximation match the analytical solution nearly perfect. The calculation using mesh 2 is done with a variation of the radial approximation polynomial of the infinite elements, due to the reason that the calculation using a constant polynomial P_p^k, denoted as “mesh 2, iFEM-CONST”, deviates

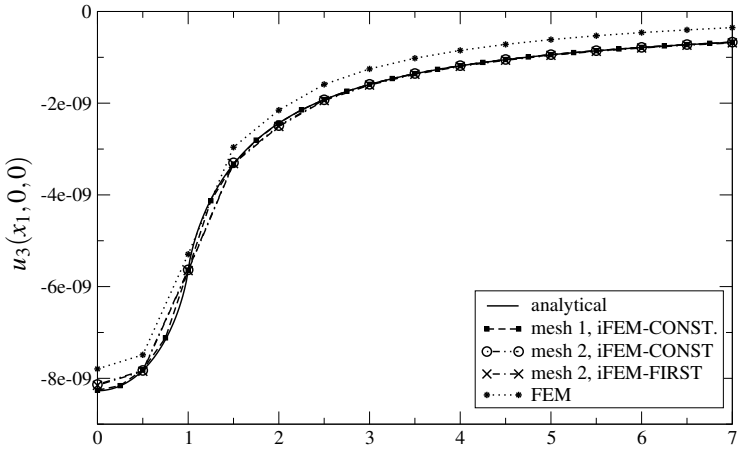

(a) Vertical displacement

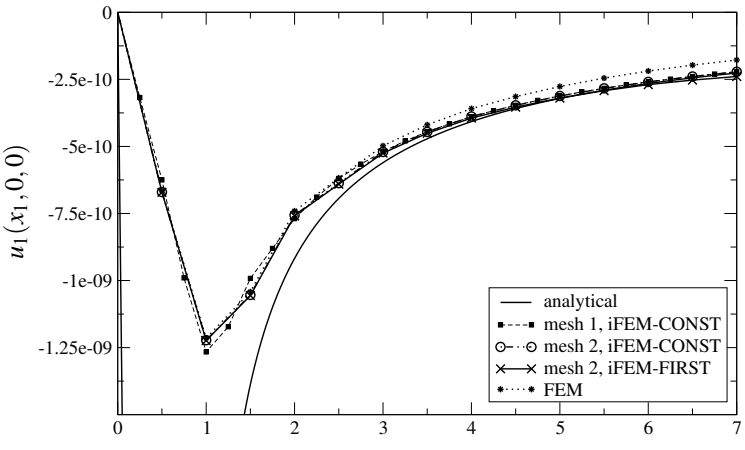

(b) Horizontal displacement

Figure 5.11: Results of the static halfspace. Vertical- and horizontal displacement along the axis $0\,\text{m} \leq x_1 \leq 7\,\text{m}$ and $x_2 = x_3 = 0$.

slightly from the analytical solution as x_1 approaches zero (figure 5.11(a)). Nevertheless, using a linear polynomial P_p^k, denoted as "mesh 2, iFEM-FIRST", doesn't significantly improve the results. The results obtained by using a constant or linear radial approximation polynomial are nearly not distinguishable from each other, as can be observed in figures 5.11. Nevertheless, all results obtained by using the infinite elements are superior compared to the pure finite element calculation for $x_1 > 1\,\text{m}$. Concerning the finite element calculation it must be mentioned that this approximation behaves to stiff for the whole range $0 \leq x_1 \leq 7\,\text{m}$, which results in a nearly positive constant shift in vertical direction.

Second, the horizontal displacement will be discussed which is plotted in figure 5.11(b). Here, the analytical solution exhibits a singular point. This singularity can not be reproduced by the numerical approximations. Thus, the numerical approximations deviate from the analytical solution as they approach the singularity. Moreover, the numerical approximations yield for the horizontal displacement (figure 5.11(b)) nearly the same results for the different spatial discretizations when infinite elements are used. When considering the range $4\,\mathrm{m} \leq x_1 \leq 7\,\mathrm{m}$ of the results obtained by using infinite elements, it can be identified that they approach the analytical solution. This behavior is not valid for the pure finite element calculation, which can not correctly represent the far field behavior.

In conclusion, it can be stated that for the static case the proposed infinite elements work properly, i.e., the far field behavior of the unbounded domains is approximated in an adequate manner.

Dynamic case

In the dynamic case, the load varies in time now as a Heaviside step function, i.e., $\mathbf{t} = [0\ 0\ -1]^{\mathrm{T}}\mathrm{H}(t)\,\mathrm{N/m^2}$, whereas the other boundary conditions are assumed to be the same as for the static case. They will be kept constant over the whole time range. Furthermore, vanishing initial conditions are assumed. In the following, different scenarios will be investigated, such as the influence of different mesh sizes, the number of different wave types approximated by the infinite elements, the effects of a varying size of the characteristic length $\overline{a}$ of the infinite element, and different radial approximation orders. In all cases, the vertical displacement u_3 at the observation point $[6\,6\,0]^{\mathrm{T}}\,\mathrm{m}$ will be taken under consideration for the comparative study. Additionally, the proposed method will be tested against an analytical solution by Pekeris [108]. The time integration is performed using the proposed coupled time stepping scheme presented in section 4.5.

It is of interest to check the theoretical arrival times of the different waves which are present. The wave velocity for the compressional-, shear-, and Rayleigh wave are defined in section 2.1.2. The resulting wave velocities for the soil, with the material parameters given in table 5.1, are listed in table 5.4. To calculate the arrival times of the different wave types the distance measure is performed from the outer corner point of the load area, i.e., $[1\,1\,0]^{\mathrm{T}}\,\mathrm{m}$. They are given in table 5.4. The arrival times of the different wave types at the observation point are given in column 1. In case if any reflection would take place at the transition from the near to the far field the arrival times at the observation point are given in column 2. Column 3 contains the arrival times from the truncated boundary of the pure finite element mesh.

Spatial- and time discretization As a starting point to validate the proposed infinite element the influence of different mesh sizes will be analyzed. Thus, mesh 1 and mesh 2

(see figure 5.10(a) and (b)) will be used. Note that in this case infinite elements are used to represent the far field behavior. The radial approximation polynomial P_p^k of the infinite elements is chosen to be of first order. Furthermore, the compressional-, the shear- and the Rayleigh wave are approximated by the infinite element. A comparison is also performed to a pure finite element mesh (mesh 3). Here, an *additional layer* of 7 m thickness of conventional finite elements is attached as depicted in 5.10(c). The additional layer is added to attempt to simulate the far field. The bottom is fixed, whereas the boundaries to the infinite side are assumed to be free to move and traction free. For all three meshes the CFL-factor will be fixed to $\chi = 0.5$. This results in a time step of $\Delta t = 0.00031$ s for mesh 1 and $\Delta t = 0.00062$ s for mesh 2 and mesh 3. Furthermore, a variation of the Newmark parameters will be performed, i.e., they will be set to $\beta = 0.3025$ and $\gamma = 0.6$, to achieve a slight numerical damping as proposed by Zienkiewicz and Shiomi [158].

	Wave speed [m/s]	Distance [m]		
		7.07	9.07	23.07
		Arrival time [s]	Reflection time [s]	
			iFEM	FEM
Comp. wave c_P	402.5	0.018	0.023	0.057
Shear wave c_S	232.4	0.030	0.039	0.099
Rayleigh wave c_R	213.8	0.033	0.042	0.11

Table 5.4: Distance measure from load corner point $[1\,1\,0]^{\mathrm{T}}$ m to observation point $[6\,6\,0]^{\mathrm{T}}$ m with corresponding wave arrival times.

The vertical displacement u_3 at the observation point $[6\,6\,0]^{\mathrm{T}}$ m is plotted in figures 5.12(a)-(c). The arrival times of the different wave types can be observed in figure 5.12(b). The arrival of the compressional wave at time $t = 0.018$ s is represented in an appropriate manner by every discretization setting. The arrival of the shear wave can be observed at time $t = 0.030$ s which overlaps with the arrival of the Rayleigh wave at time $t = 0.33$ s. It must be mentioned that the arrival times in table 5.4 only give the earliest arrival time of the corresponding wave and not the arrival time of the waves generated by the distributed load. This explain that the maximum amplitude due to the waves is approximately at time $t = 0.037$ m. Furthermore, it can be seen that the solution of the pure finite element mesh (mesh 3) matches the solution of mesh 2 as long as the reflected compressional wave from the outer boundary arrives at time $t = 0.057$ s (figure 5.12(b) and (a)). Hence, it follows that the behavior of the near field is not altered by the infinite elements. This statement is approved by the fact that deviations due to different spatial- and temporal discretizations can be eliminated, since mesh 2 and mesh 3 exhibit the same spatial- and temporal discretization of the near field. After the waves have passed the observation point the solutions approach the static solution (denoted by “analytical, static”) as can be identified

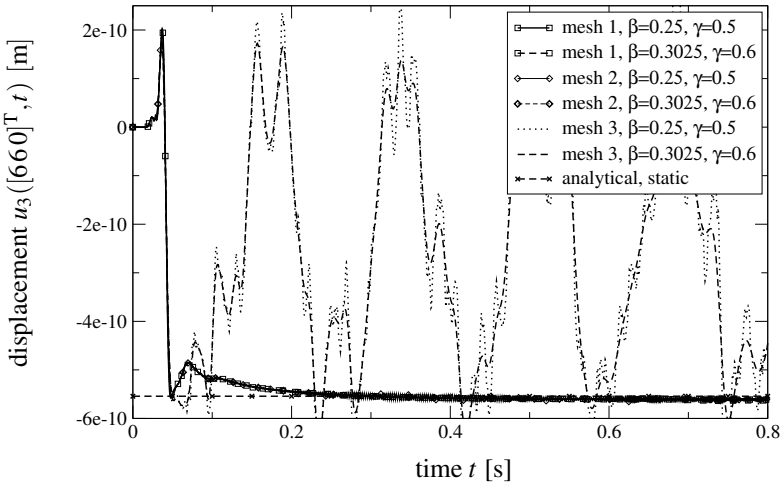

(a) Displacement u_3

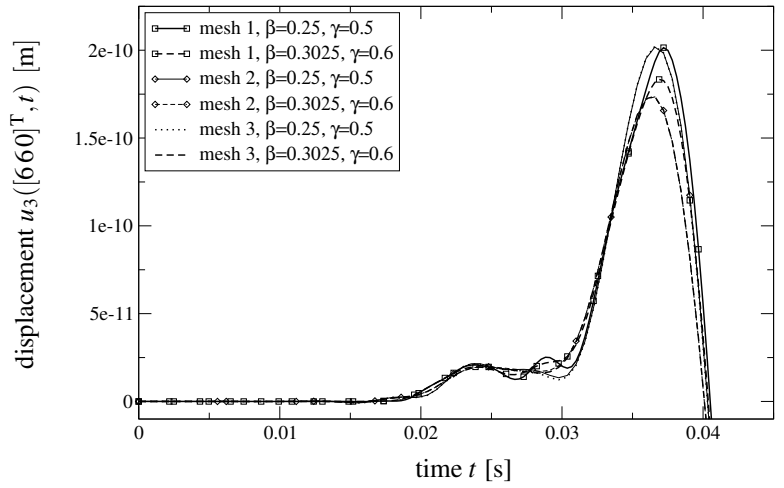

(b) Zoom section of figure 5.12(a) - Displacement u_3

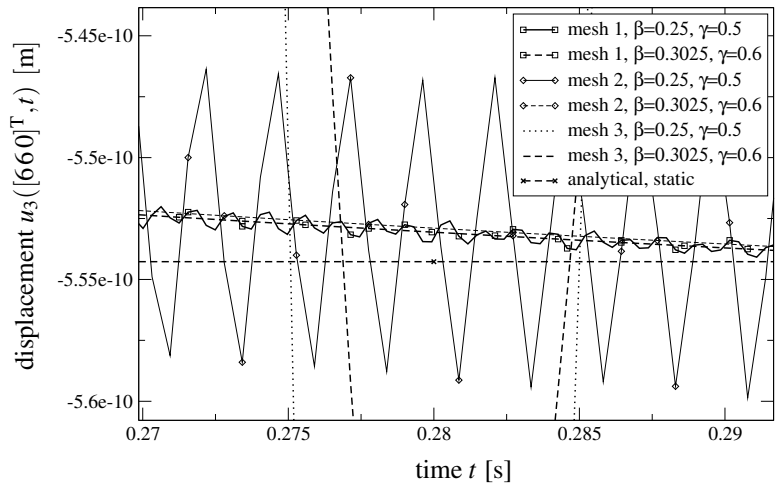

(c) Zoom section of figure 5.12(a) - Displacement u_3

Figure 5.12: Vertical displacement u_3 at observation point $[660]^T$ m for different time and spatial discretizations.

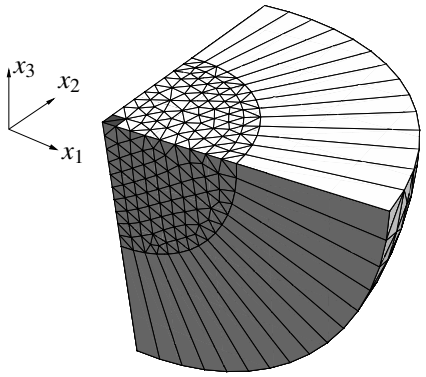

Figure 5.13: Mesh 4: 1/8-sphere $R = 9.5\,\mathrm{m}$. FEM-iFEM discretization. The dashed area in the upper left corner denotes the load area ($1.0 \times 1.0\,\mathrm{m}^2$).

Mesh label	mesh 4
Finite domain	$R = 9.5\,\mathrm{m}$
h_e	$0.5\,\mathrm{m}$
Near field	3533 TET10
Far field	306 iFEM
Degrees of freedom, elastic material, P_p^k with $p = 1$	18495

Table 5.5: Spatial discretization parameters.

in figures 5.12(a). The introduced numerical damping results in a small reduction of the Rayleigh pole, whereas the deflection due to the compressional wave is nearly unaffected, as can be noticed in figure 5.12(b). Nevertheless, the damping also eliminates the shaky behavior of the results, especially when looking at the results when they approach the static solution, as plotted in figure 5.12(c). In conclusion, it can be stated that the coarser mesh 2 yields nearly the same results as mesh 1. Using mesh 2 reduces the computational effort extremely. This is due to the fact that the degrees of freedom of mesh 2 are roughly only one sixth of mesh 1, as summarized in table 5.3. Furthermore, only half as much time steps are needed for mesh 2 as for mesh 1 when the total time is assumed to be the same.

Wave approximation In this paragraph, the influence of the number of approximated waves will be investigated. As shown in section 2.1.2, three different types of waves exist namely compressional-, shear-, and Rayleigh waves. The proposed infinite element with the shape function given in equation 4.19 is capable to approximate various wave types. Thus, in the following the displacement at the observation point $[6\,6\,0]^{\mathrm{T}}\,\mathrm{m}$ will be calculated for the cases that all wave types are approximated, the shear- and compressional wave are approximated, or when only the compressional wave is approximated. These three cases will be compared to each other. The corresponding curves are labeled in the following plots in such a way as mentioned before. Moreover, two different meshes will be used for the study, i.e., mesh 2 and the new introduced mesh 4, which is sketched in figure 5.13 with the detailed discretization parameters given in table 5.5. In fact, mesh 4 is used to ensure that the angle of incidence is always perpendicular when the outward propagating waves enter the transition from the near- to the far field. The radial approximation polynomial P_p^k of the infinite elements is chosen to be of first order for both meshes. For both

meshes the CFL-factor will be fixed to $\chi = 0.5$. This results in a time step of $\Delta t = 0.00062\,\mathrm{s}$ for both meshes, since they exhibit the same discretization parameter h_e. The Newmark parameters are chosen to be $\beta = 0.3025$ and $\gamma = 0.6$ to achieve a small numerical damping. The vertical displacement u_3 for this configuration setting is plotted in figures 5.14(a)

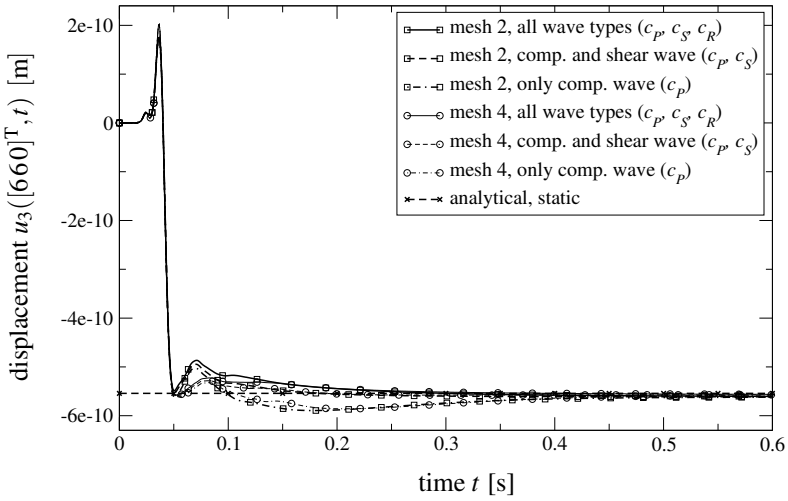

(a) Displacement u_3

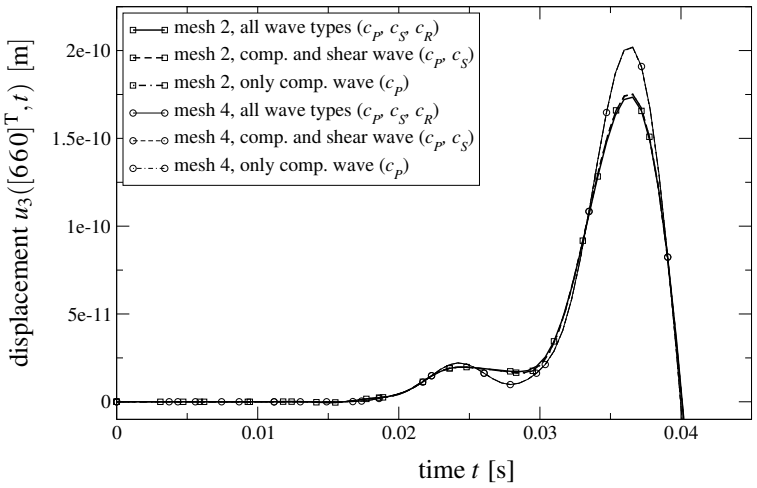

(b) Zoom section of 5.14(a) - Displacement u_3

Figure 5.14: Vertical displacement u_3 at observation point $[660]^T\,\mathrm{m}$ for different spatial discretizations and wave approximations.

and (b). The arrival times of the different wave types at the observation point $[660]^T\,\mathrm{m}$ are given in table 5.4. The correct representation of the wave arrivals of the proposed method was already discussed in the paragraph before and will be not mentioned again. However, it must be mentioned that the Rayleigh pole is represented by a larger amplitude when mesh 4 is used for the numerical analysis. In figure 5.14(b), it can be noticed that results

due to any mesh match each other as long the single wave types didn't pass the observation point. After the wave have passed the observation point they diverge from each other. Of course, this is due to the fact that the far field is approximated in another fashion when a different number of waves is approximated. It can be noticed that the best results are obtained when the compressional- and shear wave are approximated (figure 5.14(a)). The best results mean that the deviation from the static solution is as small as possible. The worst results are obtained when only the compressional wave is approximated. Thus, in the following only the compressional- and shear wave will be approximated if not stated otherwise.

Radial approximation order Next, the influence of the order of the radial approximation polynomial $P_p^k(\xi_3)$ on the calculation will be considered. Therefore, the vertical displacement at the observation point $[6\,6\,0]^{\mathrm{T}}\,\mathrm{m}$ will be used for the comparative study. The spatial discretization for all calculations is done using mesh 2 (see figure 5.12(b)). The time step is chosen to be $\Delta t = 0.00062\,\mathrm{s}$, which results in a CFL-factor $\chi = 0.5$. In order to perform this analysis the CQM of Banjai and Sauter [18] had to be used. This has to be done since the proposed coupled time stepping scheme of section 4.5 exhibited numerical instabilities after some time steps when an approximation order $p \geq 2$ is used. These numerical difficulties also occurred when the whole domain (near- and far field) was applied to the CQM scheme described of section 3.3.2. Thus, the problem can not be attributed to the proposed Newmark-CQM coupling scheme. Also, different input parameters, as mesh size, time step size, dimension of the problem, and the kind of approximation polynomials (Lagrange, Legendre, Jacobi) didn't stabilized the numerical calculations. Nevertheless, the CQM of Banjai and Sauter [18] seems to be *immune* to the aforementioned instabilities. The main difference of this CQM compared to that of section 3.3.2 is that the system of algebraic equations has to solved for every frequency step and, hence, the solution (displacement) is transformed to the time domain.

The results of these calculations are plotted in figures 5.15(a) and (b). The calculation is performed using different radial approximations $p \in \{0,1,2,3,4\}$ and are referred by "CONST, FIRST, SECOND, THIRD, and FOURTH". It can be observed that the solution is nearly independent on the approximation order of the radial direction, only the results obtained when using a constant approximation order deviates from the other solutions when looking at times $t \leq 0.045\,\mathrm{s}$. Depending on the approximation order slightly different static solutions are approached. Nevertheless, the constant and first approximation order are closest to the analytical static solution. Thus, it is sufficient to use an approximation of first order and, thus, the proposed coupled time stepping of section 4.5 can be used to gain the time domain solution.

Characteristic length of infinite element $\overline{a}$ This paragraph investigates the influence of the proper choice of characteristic length $\overline{a}$ of the infinite element (see also equation

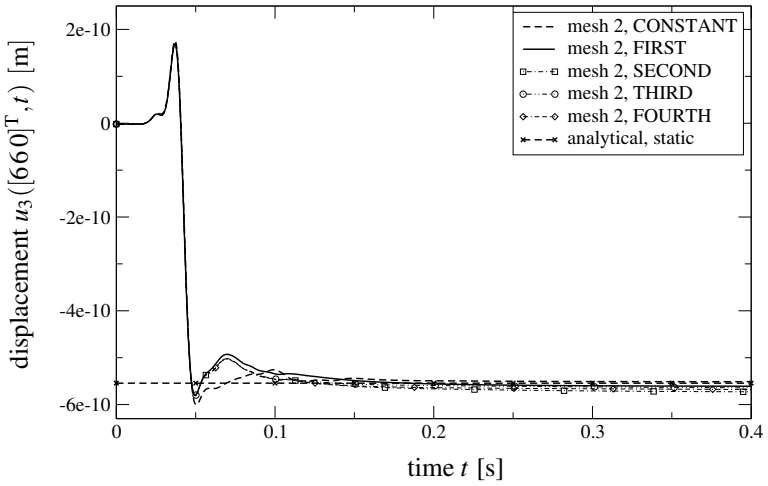

(a) Displacement u_3

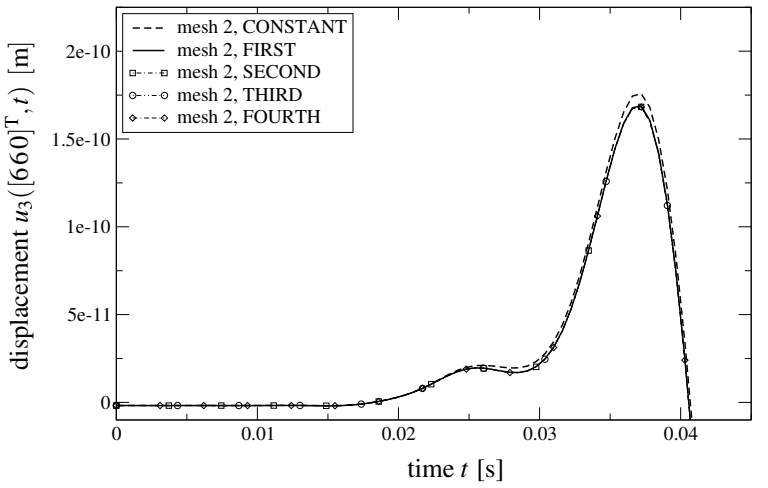

(b) Zoom section of 5.15(a) - Displacement u_3

Figure 5.15: Vertical displacement u_3 at observation point $[660]^T$ m for different radial approximation orders.

(4.20)). The computation is performed for various different sizes of characteristic lengths $\{0.5\overline{a}, 0.75\overline{a}, 1.0\overline{a}, 1.25\overline{a}, 2.0\overline{a}\}$. In order to give an imagination on how the spatial discretization looks like the meshes for the characteristic lengths $0.5\overline{a}$ and $2.0\overline{a}$ are sketched in figures 5.16(a) and (b), respectively. The radial approximation polynomial is chosen to be of first order. The spatial discretization of the near field corresponds to that of mesh 2 (see figure 5.10(b)). Also here, the time domain solution is again obtained by using the CQM of Banjai and Sauter [18]. As in the paragraphs before, the time step is chosen to be $\Delta t = 0.00062\,\mathrm{s}$. The vertical displacement of the observation point $[660]^T$ m is plotted in figures 5.17(a) and (b). As can be noticed in figure 5.17(b) the displacement is unaffected

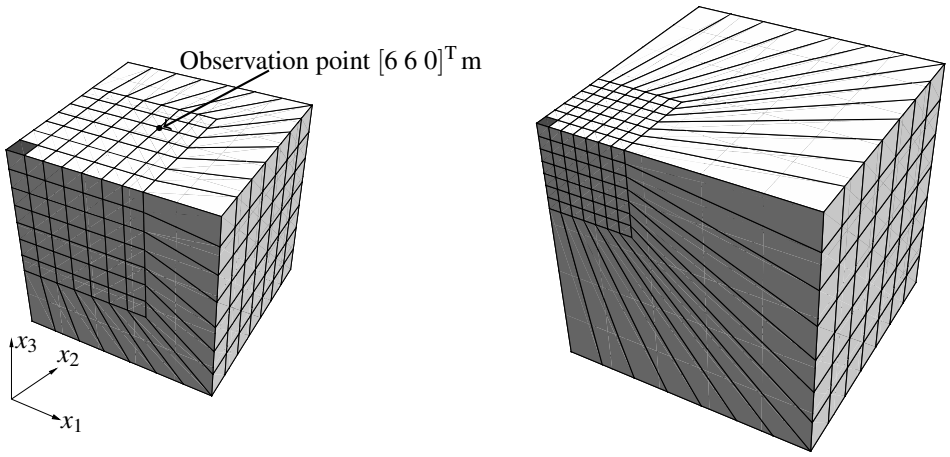

(a) Mesh 2: $0.5\overline{a}$ (b) Mesh 2: $2.0\overline{a}$

Figure 5.16: FEM-iFEM discretization with different characteristic lengths of the infinite element.

for any chosen characteristic length for observation times $t \leq 0.045\,\mathrm{s}$. This is not the case for the long time behavior. Depending on the characteristic length of the infinite element different static solutions are obtained, as can be noticed in figure 5.17(a). Thus, the nearly correct static solution is obtained when the characteristic length is approximately $1.0\overline{a}$. In this case the infinite element behaves in such a way as the source point is a singular point. This is for example the case when a single point force at the origin $[0\,0\,0]^{\mathrm{T}}\,\mathrm{m}$ is applied to the surface. Thus, due to the similarity to the here computed problem the correct behavior of the infinite element is, of course, only satisfied for a chosen characteristic length of $1.0\overline{a}$. Consequently, the characteristic length will be fixed to $1.0\overline{a}$ in the following.

Comparison to BEM In the following, the proposed numerical scheme will be validated by a comparison with a BEM calculation [123]. In order to do so, the vertical and horizontal displacement at the observation point $[6\,6\,0]^{\mathrm{T}}\,\mathrm{m}$ will be analyzed. Calculations using infinite elements are performed using the spatial discretizations mesh 1, mesh 2, and mesh 4.The time step size is chosen to be $\Delta t = 0.00062\,\mathrm{s}$ except for mesh 1, where $\Delta t = 0.00031\,\mathrm{s}$. The wave arrival times at the observation point $[6\,6\,0]^{\mathrm{T}}\,\mathrm{m}$ are listed in table 5.4. The time domain solution is computed using the presented coupled time stepping scheme of section 4.5. The Newmark parameters will be set to $\beta = 0.3025$ and $\gamma = 0.6$. The radial approximation polynomial is chosen to be of first order. Furthermore, the approximation of the compressional- and shear wave will be performed. Thus, the infinite elements are adjusted to the underlying problem. The vertical displacement u_3 is plotted in figures 5.18(a) and (b), whereas the horizontal displacement u_1 is plotted in figure

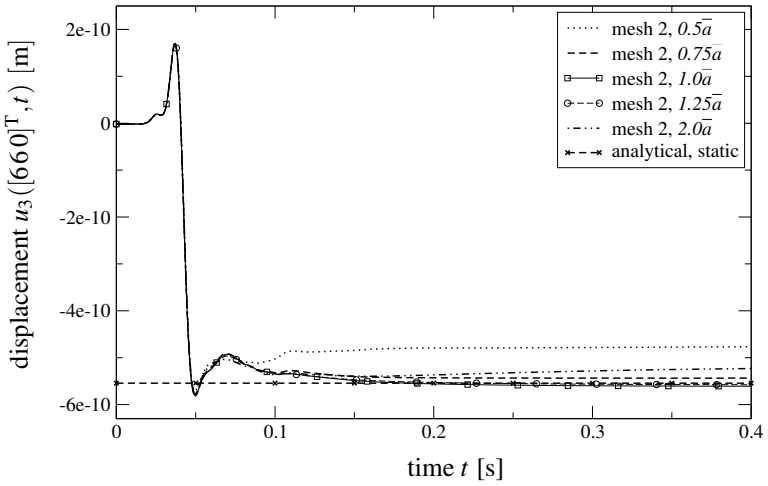

(a) Displacement u_3

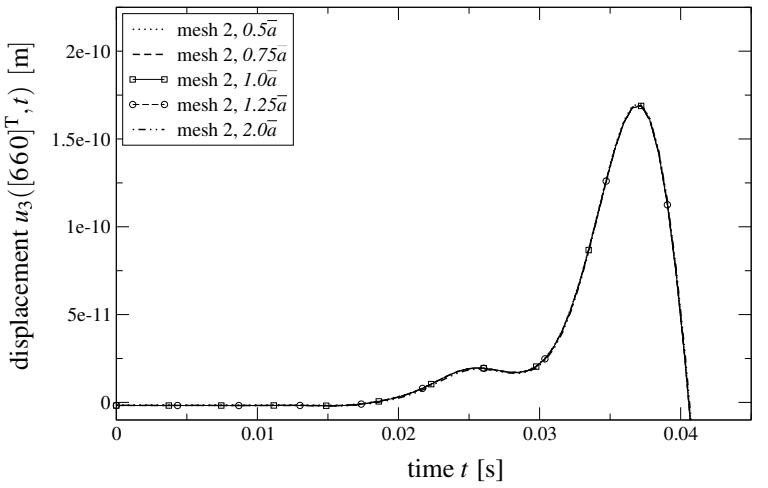

(b) Zoom section of 5.17(a) - Displacement u_3

Figure 5.17: Vertical displacement u_3 at observation point $[660]^T$ m for various sizes of characteristic length of the infinite elements $\bar{a}$.

5.18(c). The horizontal displacement u_2 is equal to u_1 at the observation point, due to the symmetry of the problem. In figure 5.18(b), the arrival of the compressional wave is clearly visible at time $t = 0.018$ s as well as the arrival of the shear- and Rayleigh wave at times $t = 0.030$ s and $t = 0.033$ s, respectively. In can be noticed that the single solutions coincidence properly. The small deviations, of course, occur due to different spatial- and time discretizations. Furthermore, the solutions obtained by using infinite elements to describe the far field behavior coincidence properly with the BEM solution and, thus, it can be concluded that the proposed method is adequate for unbounded domains. Moreover, it can be observed that the solutions of the cube meshes (mesh 1 and 2) nearly coincidence

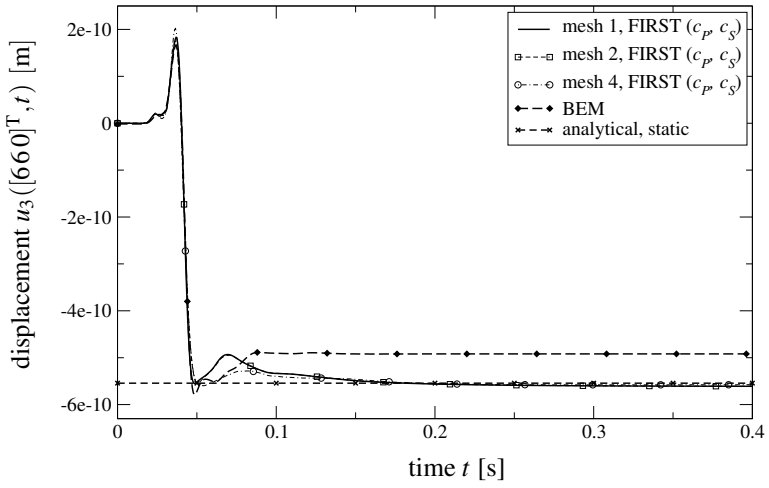

(a) Displacement u_3

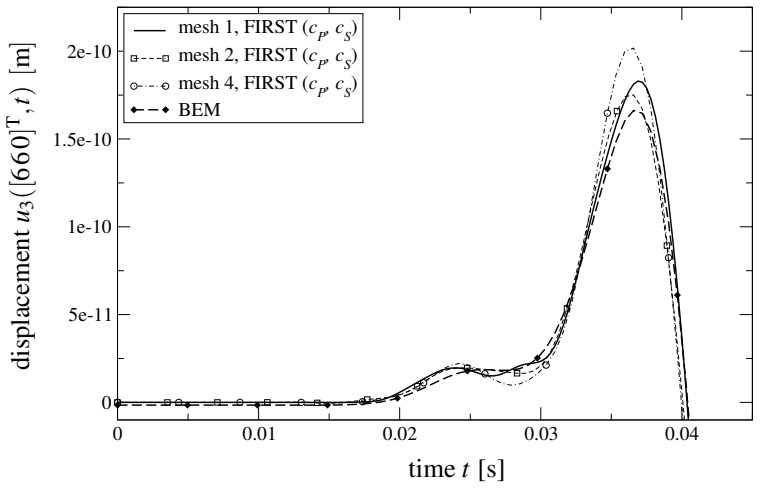

(b) Zoom section of 5.18(a) - Displacement u_3

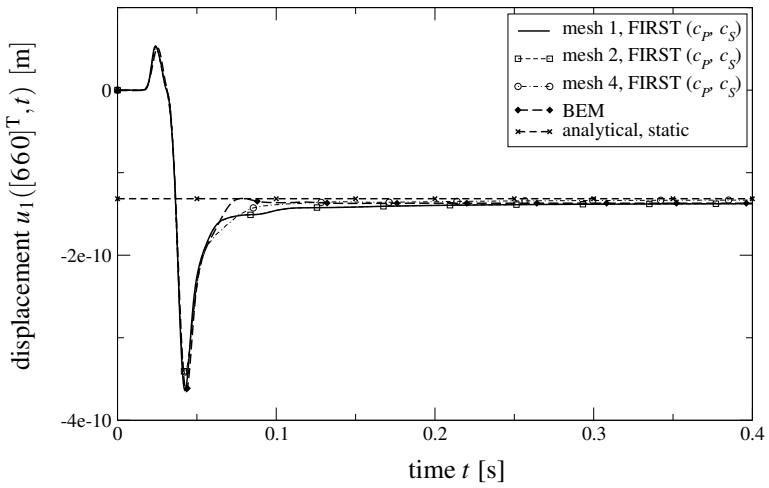

(c) Displacement u_1

Figure 5.18: Vertical- and horizontal displacement at observation point $[660]^T$ m.

with the solution of the 1/8-sphere (mesh 4). Consequently, the corner (point $[7\,7\,0]^{\mathrm{T}}$ m) of the cube-mesh doesn't affect the solution of the vertical displacement, despite the angles of incidence of the waves aren't normal to the boundary. This conclusion is also confirmed by the horizontal displacement u_1 (figure 5.18(c)). Reflected waves are clearly observable when the pure finite element mesh is used, as can be seen in figures 5.18(a) and (c). On the contrary the solutions using infinite elements approach the static solution, after the waves have passed the observation point. The static solution of the BEM calculation deviates from the analytical static solution. This is due to the fact that the BEM has to truncate the mesh at some point. This truncation pollutes the solution of the numerical approximation, as is discussed in more detail by, e.g. Rüberg [118].

Single point force This section will be closed with a comparison of the above obtained results of the elastic halfspace problem (figure 5.9) with the analytical solution due to a single point force given by Pekeris [108]. The point force $[0\,0\,-4]^{\mathrm{T}}\mathrm{H}(t)\,\mathrm{N}$ is applied at the origin $[0\,0\,0]^{\mathrm{T}}$ m, whereas the remaining boundary conditions are chosen as in the examples before. Additionally to the distributed load case, also the FEM-iFEM calculation will be performed with a point force. The calculation with the point force and the distributed force is performed for mesh 1 and mesh 2. The time step size is chosen as in the examples above. The Newmark parameters will be set to $\beta = 0.3025$ and $\gamma = 0.6$. The radial approximation polynomial is chosen to be of first order. Furthermore, the approximation of the compressional- and shear wave will be performed.

The vertical- u_3 and the horizontal displacement u_1 are plotted in figures 5.19 and 5.20, respectively. As can be observed the arrival of the compressional wave is well imitated by the numerical approximations. After the compressional wave the shear wave arrives causing an increasing amplitude. The arrival of the Rayleigh wave causes the amplitude to approach infinity, as it is apparently noticeable in the horizontal and vertical displacement, shown in figures 5.19 and 5.20, respectively. The approximated solutions due to the point force are rather wavily compared to the solution obtained by the distributed force. Nevertheless, the Rayleigh pole is better approximated by the point force. Especially at times around $t = 0.03\,\mathrm{s}$ the solution obtained by the distributed load reproduces the analytical solution nearly perfectly. After the waves have passed the observation point the solutions of the single numerical approximations approach the static solution in a sufficiently accurate manner, as can be noticed in figures 5.19 and 5.20. Comparing the different discretizations (mesh 1 and mesh 2), it is observable that only when the point force is applied the solutions diverge from each other considerably. This is not the case when the distributed force is applied. Here, the solutions coincidence properly. However, the proposed method is capable to reproduce the horizontal and vertical displacements in an appropriate manner.

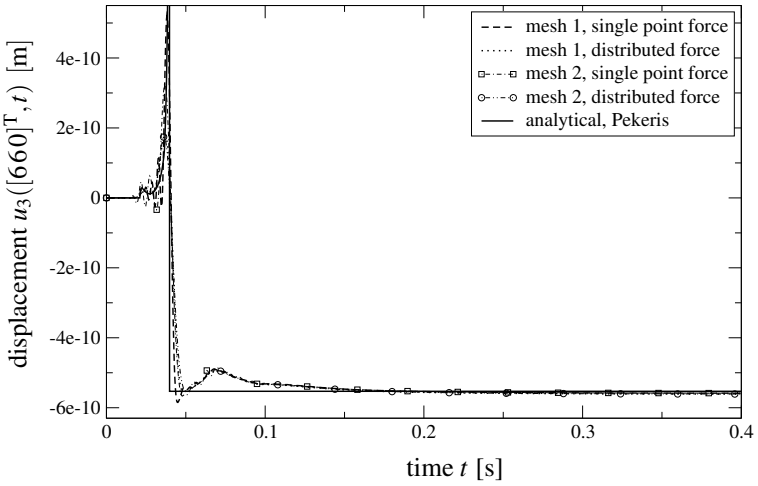

(a) Displacement u_3

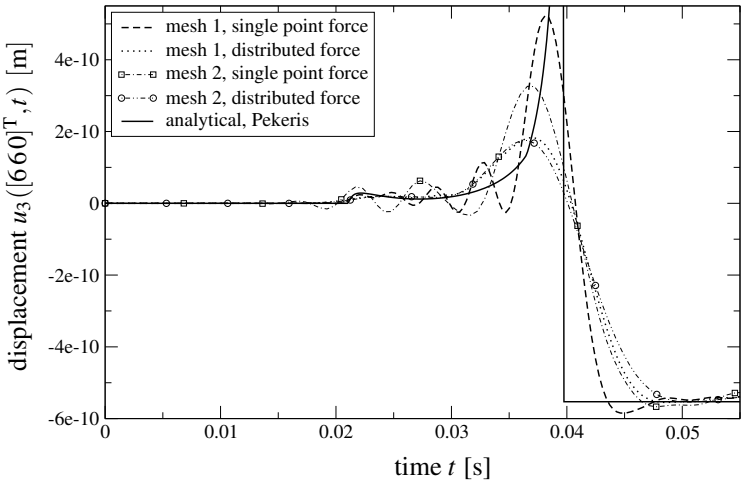

(b) Zoom section of 5.19(a) - Displacement u_3

Figure 5.19: Vertical displacement at observation point $[660]^T$ m due to a single point force (Pekeris [108]) and a distributed force.

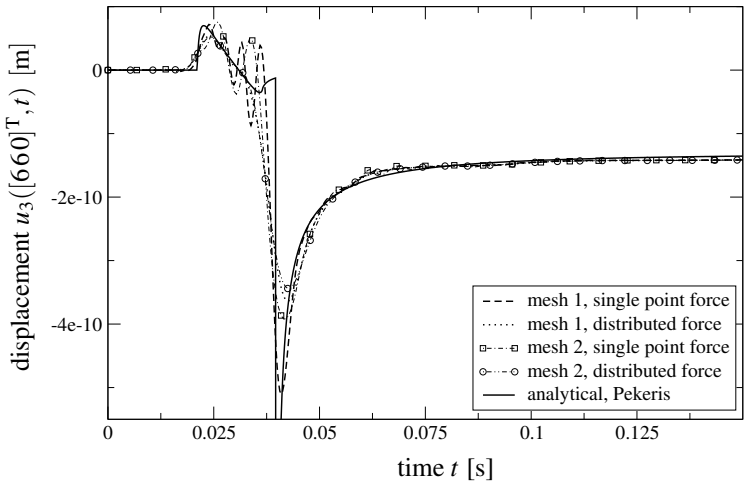

(a) Displacement u_1

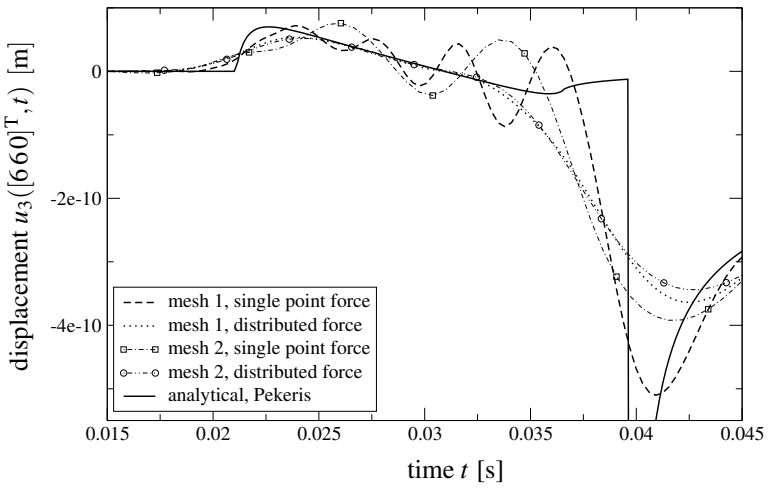

(b) Zoom section of 5.20(a) - Displacement u_1

Figure 5.20: Horizontal displacement at observation point $[660]^T$ m due to a single point force (Pekeris [108]) and a distributed force.

5.2 Poroelastodynamic problems

In order to investigate the performance of the proposed infinite element for the poroelastic case different test examples will be presented. The material data of the considered materials, a soil (coarse sand) and a rock (Berea sandstone), are given in table 5.6

	$K\ \left[\frac{\mathrm{N}}{\mathrm{m}^2}\right]$	$G\ \left[\frac{\mathrm{N}}{\mathrm{m}^2}\right]$	$\varrho\ \left[\frac{\mathrm{kg}}{\mathrm{m}^3}\right]$	$\phi\ [-]$	$K^s\ \left[\frac{\mathrm{N}}{\mathrm{m}^2}\right]$	$\varrho_f\ \left[\frac{\mathrm{kg}}{\mathrm{m}^3}\right]$	$K^f\ \left[\frac{\mathrm{N}}{\mathrm{m}^2}\right]$	$\kappa\ \left[\frac{\mathrm{m}^4}{\mathrm{Ns}}\right]$
rock	$8.0\cdot10^9$	$6.0\cdot10^9$	2458	0.19	$3.6\cdot10^{10}$	1000	$3.3\cdot10^9$	$1.90\cdot10^{-10}$
soil	$2.1\cdot10^8$	$9.8\cdot10^7$	1884	0.48	$1.1\cdot10^{10}$	1000	$3.3\cdot10^9$	$3.55\cdot10^{-9}$

Table 5.6: Material data of Berea sandstone (rock) and soil [91].

and are taken from Kim and Kingsbury [91]. In the following examples, it is also of interest to check the theoretical arrival times of the different waves which are present. This can be done, however, only for estimated wave speeds since the wave velocities are in general dependent on the Laplace parameter s (dispersive waves). Thus, wave velocities can be approximated for the special cases $\mathrm{s}\to 0$ and $\mathrm{s}\to\infty$, only. Taking the high frequency limit $\mathrm{s}\to\infty$ of equation (2.42) yields

$$(c_{1,2}^2)^\infty = \lim_{\mathrm{s}\to\infty} c_{1,2}^2 = A \pm \sqrt{A^2 - B}\,,$$

with

$$A = \frac{(4G+3K)\phi^2(\varrho_a+\varrho_f\phi)+3R(\varrho\phi^2-2\alpha\varrho_f\phi^2+\alpha^2(\varrho_a+\varrho_f\phi))}{6\phi^2\left(\varrho(\varrho_a+\varrho_f\phi)-\varrho_f^2\phi^2\right)}$$

$$B = \frac{(4G+3K)R}{3\left(\varrho(\varrho_a+\varrho_f\phi)-\varrho_f^2\phi^2\right)}\,,$$

whereas the low frequency limit $\mathrm{s}\to 0$ gives

$$(c_1^2)^0 = \frac{\alpha^2 R+\phi^2(K+\frac{4}{3}G)}{\varrho\phi^2}\,.$$

for the compressional waves. Note that the low frequency limit results in only one wave speed, which actually corresponds to the fast compressional wave, as can be noticed in table 5.7. This is obvious when taking into account the relation $\lim_{\mathrm{s}\to 0}\mathrm{s}\hat{f}(\mathrm{s}) = \lim_{t\to\infty} f(t)$ and considering that the slow compressional wave is highly damped. The high- and low frequency limit for the shear wave velocity are given by

$$(c_S^2)^\infty = \frac{G}{\varrho - \frac{\varrho_f^2\phi^2}{\varrho_a+\varrho_f\phi}}$$

and

$$(c_S^2)^0 = \frac{G}{\varrho} ,$$

respectively. The individual wave speeds of the soil and rock are listed in table 5.7. Additionally, the wave speeds are tabled when some fluid inertia terms are omitted as it is discussed in section 2.2.4. Actually, in this case only the low frequency limit exists. The Rayleigh wave speed c_R is approximated by equation (2.16) and, therefore the high and low frequency limits result from the frequency limits of the shear wave velocities. This approximation may be applied to porous materials as long as low frequency problems are considered, as investigated by Yang [147]. This is the case for many soil- and geomechanical applications.

	Approx. wave speeds [m/s]							
	c_1^∞	c_2^∞	c_1^0	c_2^0	c_S^∞	c_S^0	c_R^∞	c_R^0
	complete poroelastic formulation							
rock	3137.2	1036.5	3136.8	-	1600.1	1562.4	1458.8	1424.4
soil	1788.1	318.0	1689.6	-	247.9	228.1	229.9	211.5
	simplified poroelastic formulation (some fluid inertia neglected)							
rock	∞	-	3136.8	-	1562.4		1424.4	
soil	∞	-	1689.6	-	228.1		211.5	

Table 5.7: Approximated wave speeds for poroelastic materials.

5.2.1 One-dimensional poroelastic column

In this section, a one dimensional infinite poroelastic column as depicted in figure 5.6 will be investigated. The finite case is already discussed extensively by Schanz and Cheng [124] and, therefore, will be omitted here. The column is subjected to a time dependent total stress loading $\sigma^{\text{tot}}(0,t) = 1\,\text{N/m}^2 H(t)$, which acts in terms of a Heaviside step function in time. The boundary condition for the fluid phase is defined by setting the pressure to zero at the top of the column, i.e., $p(0,t) = 0\,\text{N/m}^2$. The analysis is performed using the complete u_i, p form (2.37). Thus, the discrete variational form is derived in Laplace domain as illustrated in section 3.2.5. This brings in the advantage that the performance of the proposed infinite element in section 4.3.2 can be compared to the analytical infinite element (4.24). Therefore, the near and far field are discretized in time by the CQM. The CQM formulation of Banjai and Sauter [18] is used, which brings in the advantage that the radial approximation is more flexible, as was worked out for the elastic case.

Since, the governing equations of the u_i, p form in time domain of section 2.2.4 are just an *simplification* of the original set of differential equations describing the porous material (cf. section 2.2.2), also a validation of this simplified model will be performed, i.e., the results of the analytical one-dimensional solution of the simplified model will be compared to the analytical one-dimensional solution obtained by using the complete set (2.37). The analytical one-dimensional solution of the simplified model is given in (A.21), whereas the analytical solution of the complete formulation is given in (A.16).

The near field is discretized with eight one-dimensional quadratic finite elements for the solid displacement and the pore pressure, whereas the infinite domain is approximated by a one-dimensional infinite element as presented in section 4.3.2. Both versions of infinite elements will be used, first, the version where *both compressional waves* are approximated (4.28) and, second, the version where only the *fast compressional wave* (4.29) is approximated. The radial approximation polynomial is chosen to be of constant order, i.e., $P_0^k = 1$. In order to validate the performance of the proposed infinite element the solution is compared to the analytical solution given by equation (4.22).

Moreover, a comparison is performed to results where the far field is represented by the *analytic infinite element* presented in section 4.3.1, whereas the near field is discretized using conventional finite elements. Both materials, as defined in table 5.6, will be used for the investigation. The time steps are chosen in such a way that the CFL-factor $\chi \approx 0.5$ is obtained. This can be done only approximately, since the wave speeds are frequency dependent. In order to obtain $\chi \leq 0.5$, the high frequency limit of the corresponding wave speeds of table 5.7 will be used for the calculation of the proper time steps. Thus, for the soil a time step of $\Delta t = 0.00014\,\mathrm{s}$, and for the rock a time step of $\Delta t = 0.00008\,\mathrm{s}$ is chosen.

In figures 5.21 and 5.22, the solid displacement $u(0,t)$ at the top of the column and the pore pressure $p(8\,\mathrm{m},t)$ at the position $x = 8\,\mathrm{m}$ is plotted for the soil and the rock, respectively. The results are denoted by "complete poro" for the calculation when the complete set of differential equations (2.37) are used and "simple poro" when the governing equations (2.29)-(2.31) are used. The calculation using the proposed infinite element is denoted as "FEM-only fast comp. wave (c_1)" when only the fast compressional wave is approximated using the shape functions (4.29) and as "FEM-both comp. wave (c_1, c_2)" when both compressional waves are approximated using (4.28). The comparison to the results when the analytical infinite element is attached to the finite element mesh is denoted by "FEM-analytical iFEM". It can be clearly observed that in every plot the different scenarios match each other. Thus, the governing equations (2.29)-(2.31) represent the behavior of the underlying poroelastic material in an appropriate way, since the results are equal to those of the complete analytical solution for the underlying porous material. Moreover, it can be noticed that the simplified approach of the infinite elements, where only the fast compressional wave is considered (shape functions (4.29)), is sufficient. This is obvious by taking a closer look at the wave weighting factors. For the investigated material the

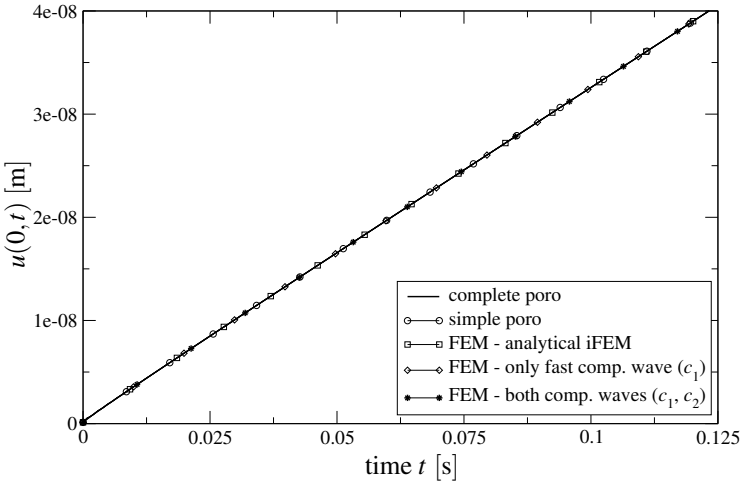

(a) Solid displacement - soil

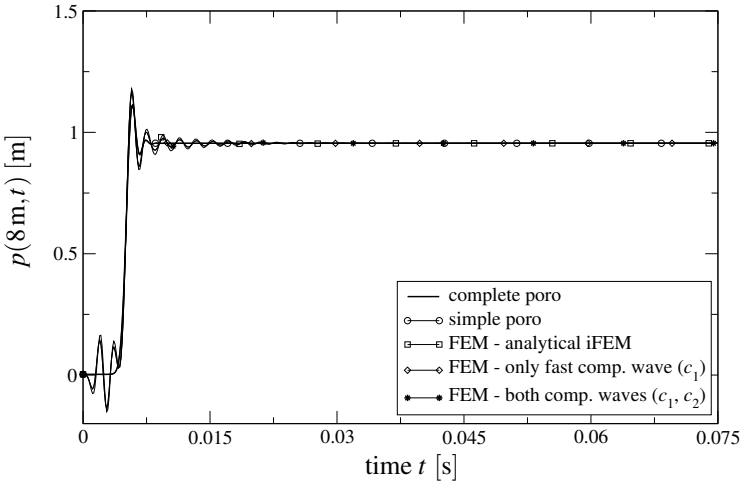

(b) Pore pressure - soil

Figure 5.21: Infinite poroelastic column - soil.

wave weighting factors are roughly $\hat{U}_1^{\mathrm{K}} = \hat{P}_1^{\mathrm{K}} \approx 1$ and $\hat{U}_2^{\mathrm{K}} = \hat{P}_2^{\mathrm{K}} \approx 0$. In figures 5.21(b) and 5.22(b), the arrival of the first compressional wave can be noticed which lifts the pore pressure within the poroelastic material. Of course, the pore pressure returns back to a equilibrium state $p(x,t \to \infty) = 0$ for an increasing observation time. This is due to the fact that the fluid gains enough time to trickle through the porous material, thus, the pore pressure relaxes with increasing time.

Concerning the soil, numerical oscillations at the beginning may occur when the pore pressure is considered as can be noticed in figure 5.21(b). These oscillations can be attributed

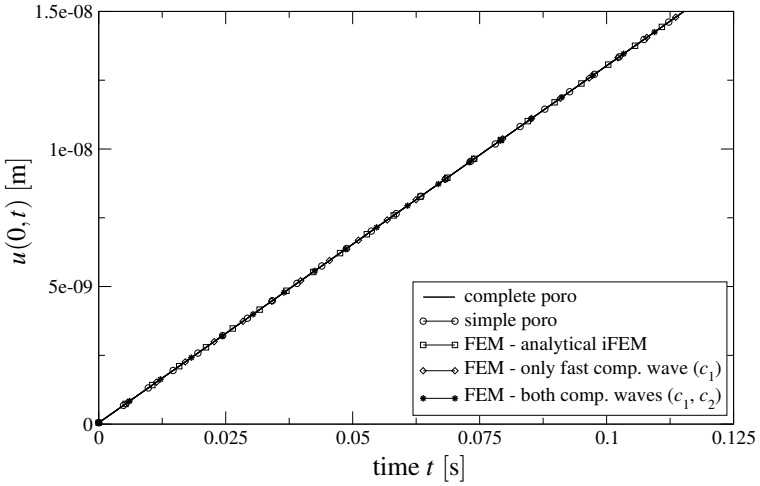

(a) Solid displacement - rock, $\kappa = 1.90 \cdot 10^{-10}\,\mathrm{m}^4/\mathrm{Ns}$

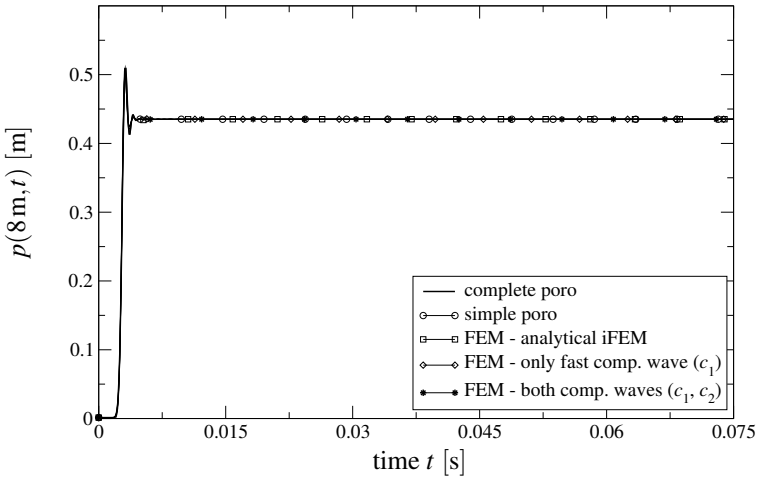

(b) Pore pressure - rock

Figure 5.22: Infinite poroelastic column - rock.

to the FEM part alone, since also the solution using the analytical infinite element features these numerical problems. They can be attributed to the fact that the soil behaves nearly incompressible [126], which results apparently in numerical difficulties. These instabilities are also known from the quasi-static consolidation, as worked out by Murad and Loula [104]. They concluded that the pore pressure oscillations arise from an unstable approximation of the incompressibility constraint on the initial condition. Furthermore,

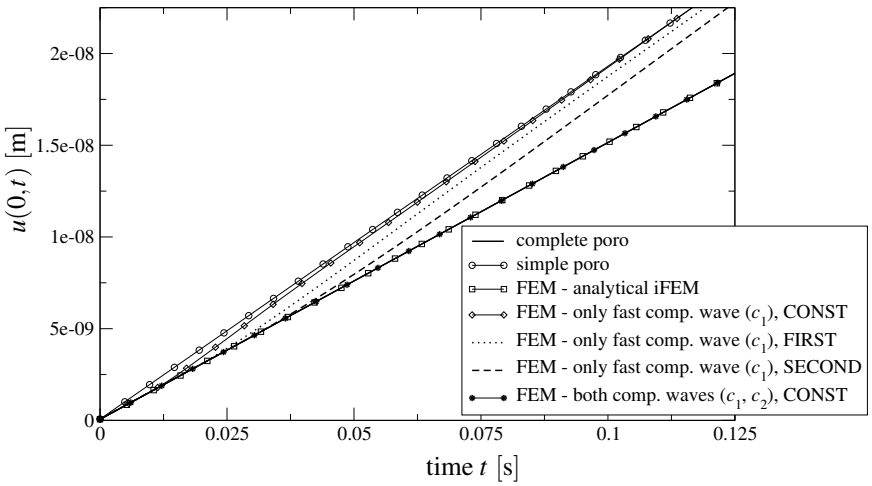

(a) Solid displacement - rock, $\kappa = 1.0\,\mathrm{m}^4/\mathrm{Ns}$

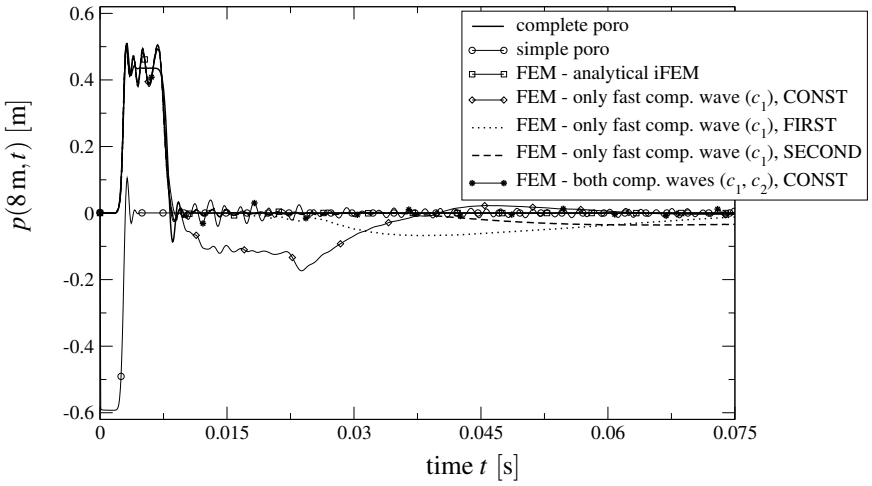

(b) Pore pressure - rock, $\kappa = 1.0\,\mathrm{m}^4/\mathrm{Ns}$

Figure 5.23: Infinite poroelastic column - rock.

they investigated that these oscillation decay in time as it is also the case in figure 5.21(b). They also proved stability and convergence of a backward Euler-Galerkin formulation for any combination of approximation order of the solid displacement and the pore pressure. Zienkiewicz and Shiomi [158] recommend to use reduced integration of appropriate submatrices to overcome these problems.

Up to now, only the fast compressional wave was detectable. In order to investigate the

test case when the second compressional wave is observable the permeability is altered to a large value, i.e., $\kappa = 1.0\,\mathrm{m}^4/\mathrm{Ns}$. This action reduces the damping of the system significantly and, thus, the second wave is detectable. The outcome of this artificial created scenario is plotted in figures 5.23. For this case, the governing equations (2.29)-(2.31), which are just an approximation of the complete set of governing equations, are not able to represent the behavior of the porous media in an appropriate manner, as can be noticed in figures 5.23(a) and 5.23(b). Especially, the pore pressure (figure 5.23(b)) is distorted evidently. Here, the pressure changes actually to negative values as soon as the step load is applied. When the fast compressional wave arrives at the observation point $x = 8\,\mathrm{m}$ the pressure returns to the steady state solution. The analytical solution is only approached sufficiently by the calculations when the analytical infinite element or the infinite element with both compressional waves is attached to the finite element mesh. The reduced damping of the systems is noticeable by oscillations when the numerical approximation schemes are used. When only the fast compressional wave is approximated using the shape functions (4.29) the results deviate as soon as the second compressional wave arrives at the observation point at time $t \approx 0.008\,\mathrm{s}$. Beside the constant radial approximation also a linear and quadratic radial approximation order is plotted in figures 5.23(a) and 5.23(b), denoted by the attached label “CONST”, “FIRST”, and “SECOND”, respectively. It can be verified that a higher approximation order can produce less deviation from the correct analytical solution. Nevertheless, to obtain sufficient accurate results the approximation of both compressional waves is absolutely essential.

5.2.2 Poroelastic halfspace

In the next example, a poroelastic halfspace is considered. The underlying material is assumed to be a rock. In a later step also a soil will be considered. The material data are given in table 5.6. A schematic representation of the problem is given in figure 5.9. Thus, the same problem will be considered as it was done for the elastodynamic case. As a starting point, to validate the performance of the infinite element, the u_i, p formulation will be used. The semi-discrete variational formulation is given in equation (3.44). This formulation suffices to represent the underlying porous material in an appropriate way, as shown for the one-dimensional case. In the following the influence of the number of approximated waves will be investigated. In addition to the two body waves the Rayleigh wave will be present in an unbounded poroelastic halfspace. As already investigated for the one-dimensional case the second compressional wave is highly damped and, therefore, not detectable for the underlying material. For this reason only the first compressional wave will be considered besides the shear- and Rayleigh wave and, thus, the shape functions (4.30) and (4.31) will be used. In order to validate the performance of the proposed infinite element the solid displacements u_i at point $[6\,6\,0]^{\mathrm{T}}\mathrm{m}$ are studied for the cases when only the fast compressional wave, the compressional- and shear wave, or when all wave types

(comp.-, shear-, and Rayleigh wave) are approximated. The corresponding curves are labeled as mentioned before in the following plots.

The calculation will be performed for two different spatial discretizations, namely mesh 1 and mesh 2, as depicted in figures 5.10(a) and 5.10(b), respectively. The detailed discretization parameters are summarized in table 5.3. The approximation order of the solid displacement u_i and the pore pressure p is chosen to be of the same order. The radial approximation polynomial P_p^k of the infinite elements is chosen to be of first order and, again, to be the same for the solid displacement and the pore pressure.

The applied load is assumed to be a vertical total stress t_i^{tot} which acts in terms of a Heaviside step function in time, i.e., the load is applied and kept constant. The load vector $\mathbf{t}^{\text{tot}} = [0\,0\,-1]^{\text{T}}\,\text{N/m}^2$ is applied on an area of $1.0\times1.0\,\text{m}^2$, whereas the remaining surface is traction free. The pore pressure p is assumed to be zero on the whole surface, i.e., $p(x_1,x_2,0) = 0$, and, thus, the surface is assumed to be permeable. On the symmetry planes, the x_1x_3- and x_2x_3-plane, the normal displacements are fixed and also the flux q_i is set to zero. Of course, at infinity the displacements u_i are assumed to be zero as well the pore pressure p.

A comparison is also performed to a pure finite element mesh (mesh 3, figure 5.10(c)), denoted as "FEM" in the following plots. An *additional layer* of 7 m thickness of conventional finite elements is attached, as depicted in figure 5.10(c), to attempt to simulate the far field. The bottom of the additional layer is fixed and impermeable, whereas the boundaries to the infinite side are assumed to be free to move, traction free, and impermeable.

The time integration is performed using the proposed coupled time stepping scheme presented in section 4.5. Furthermore, vanishing initial conditions are assumed. Concerning the Newmark time-stepping scheme the integration parameters are set to the values $\beta = 0.3025$ and $\gamma = 0.6$, which yields some numerical. The time step is chosen in such a way that a CFL-factor of $\chi \approx 0.75$ is achieved, i.e., $\Delta t = 0.00006\,\text{s}$ and $\Delta t = 0.00012\,\text{s}$ for mesh 1 and mesh 2, respectively.

Here, it is also of interest to check the theoretical arrival times of the different waves which are present. The wave velocity for both compressional-, the shear- and the Rayleigh wave are listed in table 5.7. Since the differential equations (2.29)-(2.31) are used to describe the behavior of the porous material only the low frequency limit of the fast compressional wave speed exists and, therefore, this limit is used for the calculation of the arrival times (cf. table 5.7). To calculate the arrival times of the different wave types the distance measure is performed from the outer corner point of the load area, i.e., $[1\,1\,0]^{\text{T}}\,\text{m}$. They are given in table 5.8. The arrival times of the different wave types at the observation point are given in column 1. In case if any reflection would take place at the transition from the near to the far field the arrival times at the observation point are given in column 2. Column 3 contains the arrival times from the truncated boundary of the pure finite element mesh.

	Wave speed [m/s]	Distance [m]		
		7.07	9.07	23.07
		Arrival time [s]	Approx. reflection time [s]	
			iFEM	FEM
Comp. wave c_P	3136.8	0.0023	0.0029	0.0076
Shear wave c_S	1562.4	0.0045	0.0058	0.015
Rayleigh wave c_R	1424.4	0.0050	0.0064	0.017

Table 5.8: Distance measure from load corner point $[1\,1\,0]^{\mathrm{T}}$ m to observation point $[6\,6\,0]^{\mathrm{T}}$ m with corresponding wave arrival times - rock.

The vertical solid displacement u_3 is shown in figure 5.24(a) and (b), whereas the horizontal solid displacement is depicted in figure 5.24(c). It can be observed that all calculations represent the arrival of the compressional wave at time $t = 0.023\,\mathrm{s}$ properly. The arrival of the shear wave is followed by the arrival of the Rayleigh wave at times $t = 0.0045\,\mathrm{s}$ and $t = 0.0050\,\mathrm{s}$, respectively. The number of different approximated waves has nearly no influence on the solutions when looking at the vertical solid displacement for times $t \leq 0.006\,\mathrm{s}$ (figure 5.24(b)). After the wave have passed the observation point the solutions approach the quasi-static solution, denoted as "quasi-static". The quasi-static solution results from a quasi-static u_i, p FEM-iFEM calculation. Here, the number of approximated waves affects the solutions and it can be observed that the approximation of the fast compressional- and shear wave yields the best results, as can be observed in figure 5.24(a). Furthermore, it can be seen that the solution of the pure finite element mesh deviates when the reflected compressional wave from the outer boundary arrives at time $t = 0.0076\,\mathrm{s}$. This deviation increases significantly when the reflected shear- and Rayleigh waves arrive at times $t = 0.015\,\mathrm{s}$ and $t = 0.017\,\mathrm{s}$. The aforementioned observations of the vertical solid displacement are also valid for the horizontal displacement u_1 as can be noticed in figure 5.24(c), which is, of course, the same as u_2 due to the symmetric properties of the problem.

Different poroelastic FEM formulations, comparison to BEM The proper functionality of the proposed infinite element of section 4.3.3 was till now validated only for the u_i, p-poroelastic formulation. Thus, in the following the introduced infinite element will be applied to the complete poroelastic FEM formulation as well to the irreducible u_i, w_i FEM formulation. Furthermore, the aforementioned calculations will be compared to a BEM calculation [102]. Again, the poroelastic halfspace, as sketched in figure 5.9 will be taken under consideration. The boundary conditions are chosen to be the same as in the calculations before. Furthermore, the time discretization is done in the same way, i.e., $\Delta t = 0.00012\,\mathrm{s}$. The spatial discretization is performed using the mesh sketched in figure 5.10(b), i.e., mesh 2 is taken. The poroelastic material is chosen to be a rock, where the

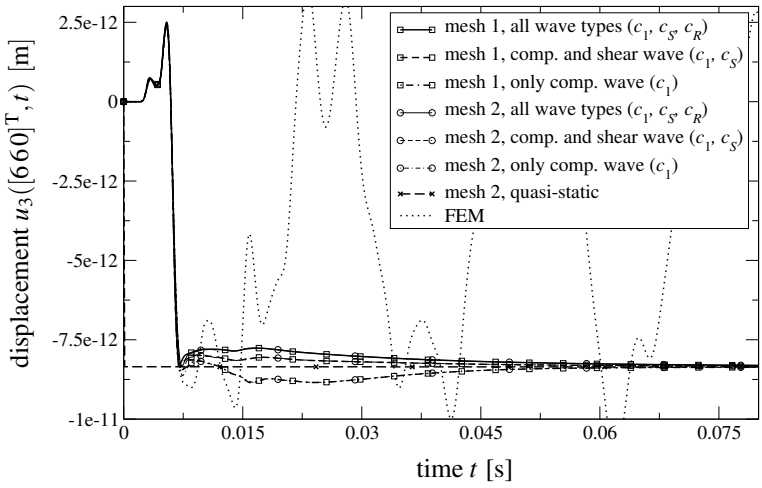

(a) Displacement u_3

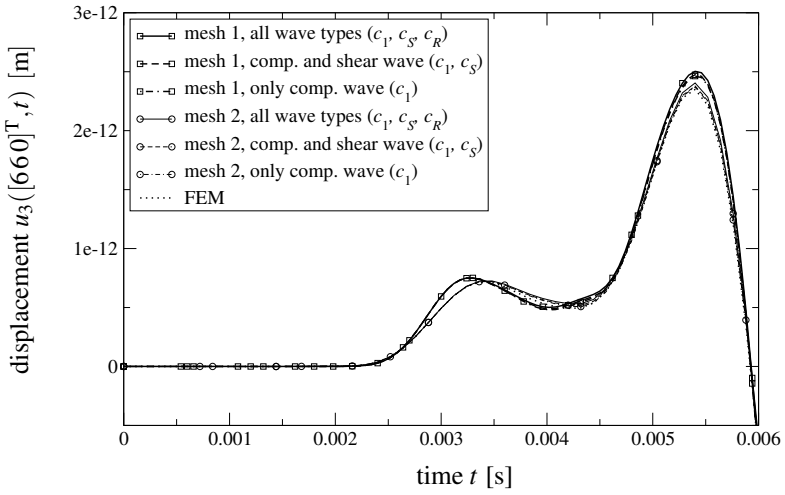

(b) Zoom section of 5.24(a) - Displacement u_3

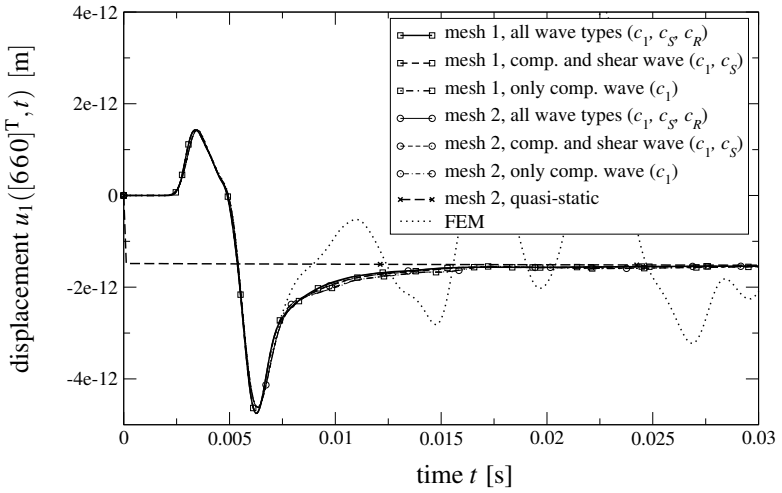

(c) Displacement u_1

Figure 5.24: Vertical- and horizontal displacement at observation point $[660]^T$ m.

material data are given in table 5.6. The wave arrival times of table 5.8 can be taken again to check them against the arrival times of the numerical simulations.

In figures 5.25(a) and (b), the vertical displacement u_3 at the observation point $[6\,6\,0]^{\mathrm{T}}$m is plotted, whereas the horizontal displacement u_1 is plotted in figure 5.25(c). Of course, the horizontal displacement u_2 is equal to the horizontal displacement u_1 at the observation point $[6\,6\,0]^{\mathrm{T}}$m due to the symmetric property of the problem. The u_i, p FEM formulation (3.44) is denoted as "u_i, p-formulation", the irreducible formulation u_i, w_i (3.42) by "u_i, w_i-formulation". The non-symmetric FEM formulation of the full form, i.e., the continuity equation is placed in the damping matrix (3.38), is denoted by "u_i, p, w_i-non-symmetric formulation", whereas the symmetric formulation (continuity equation is placed in the stiffness matrix (3.41)) is denoted by "u_i, p, w_i-symmetric formulation". The BEM calculation will be labeled as "BEM".

The wave arrival of the fast compressional wave at time $t = 0.0023\,\mathrm{s}$ is captured in an appropriate way by any numerical method. At time $t = 0.0045\,\mathrm{s}$ the shear wave arrives as can be clearly observed in figure 5.25(b) which overlaps with the arrival of the Rayleigh wave at time $t = 0.0050\,\mathrm{s}$. In figure 5.25(b), it can be observed that the u_i, p FEM formulation nearly coincides with the symmetric u_i, p, w_i FEM formulation. This statement is also valid for the u_i, w_i and non-symmetric u_i, p, w_i-poroelastic FEM formulation. Nevertheless, the deviation of the two pair of curves is small. After the waves have passed the observation point the single approximation methods approach the quasi-static solution (denoted as "quasi-static" in figures 5.25(a) and (c)). The quasi-static solution results from a quasi-static u_i, p FEM-iFEM calculation. The different FEM formulations also coincide well when considering the horizontal displacement in figure 5.25(c). Moreover, the different solutions agree proper to the BEM calculation, especially when the wave arrival times are observed. Nevertheless, the BEM approaches another quasi-static solution.

In conclusion, any Finite Element Formulation represents the physical behavior of the porous media in an appropriate way. Moreover, the governing equations (2.29)-(2.31) are capable of describing the porous material in a sufficient accurate manner as long the slow compressional wave is not detectable (cf. also section 5.2.1). Concerning the infinite element it can be stated that it represents the far field appropriate independent on the Finite Element Formulation.

Decay of Rayleigh wave In this paragraph, the decrease of the Rayleigh surface wave with depth will be investigated. To visualize this effect different points below the surface will be observed. They are located roughly at the same distance of 8.5 m measured from the origin $[0\,0\,0]^{\mathrm{T}}$ m. Thus, the arrival time of any wave type is the same for the different observation points. Actually, the observation points are located at $[6\,6\,0]^{\mathrm{T}}$ m, $[5.5\,5.5\,-3.25]^{\mathrm{T}}$ m, $[5\,5\,-4.75]^{\mathrm{T}}$ m, and $[4\,4\,-6.25]^{\mathrm{T}}$ m and will be labeled with their corresponding coordinates in the following plots. The calculations are performed with respect to the same

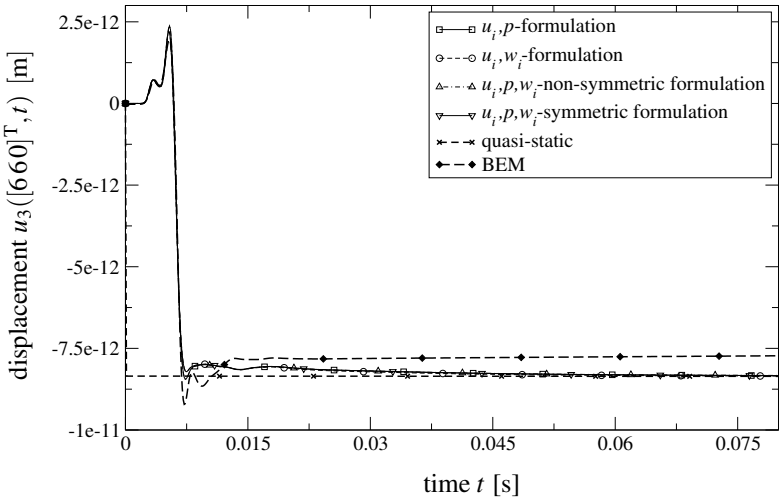

(a) Displacement u_3

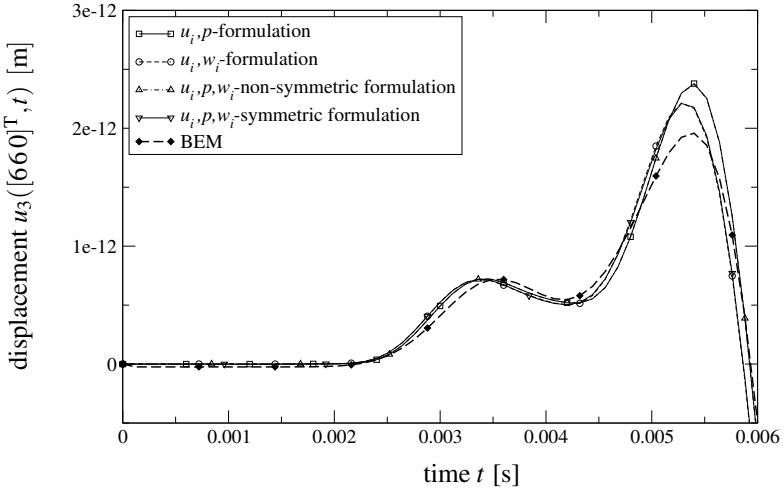

(b) Zoom section of 5.25(a) - Displacement u_3

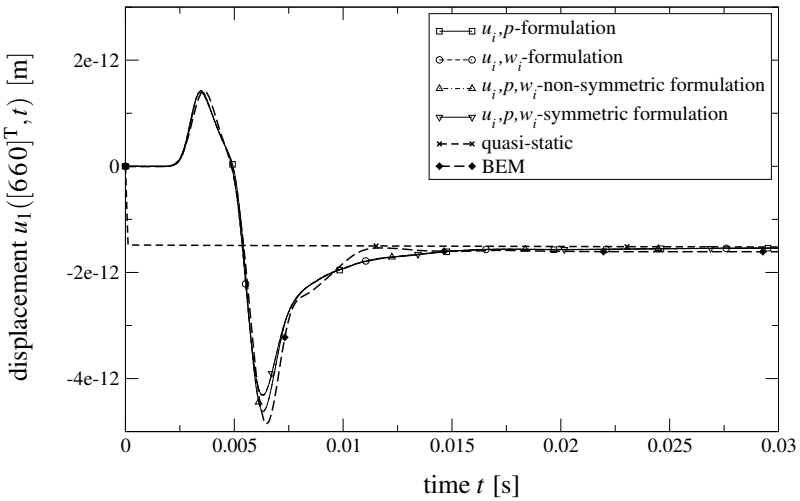

(c) Displacement u_1

Figure 5.25: Vertical- and horizontal displacement at observation point $[660]^T$ m. Comparison of different poroelastic FEM formulations.

assumptions as in the example above. However, the calculations are only performed using the spatial discretization defined by mesh 1. Moreover, the infinite element is adopted to approximate the fast compressional- and shear wave only, which suffices to obtain accurate solutions, as was investigated in the above examples. In figures 5.26(a) and (b), the

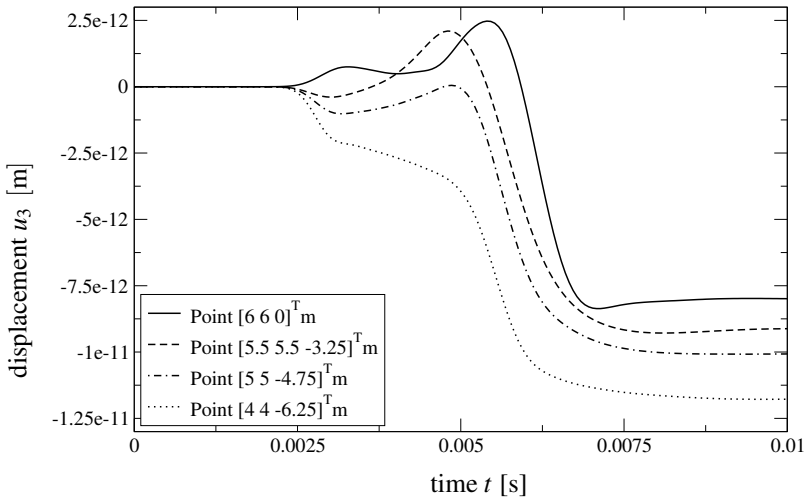

(a) Displacement u_3

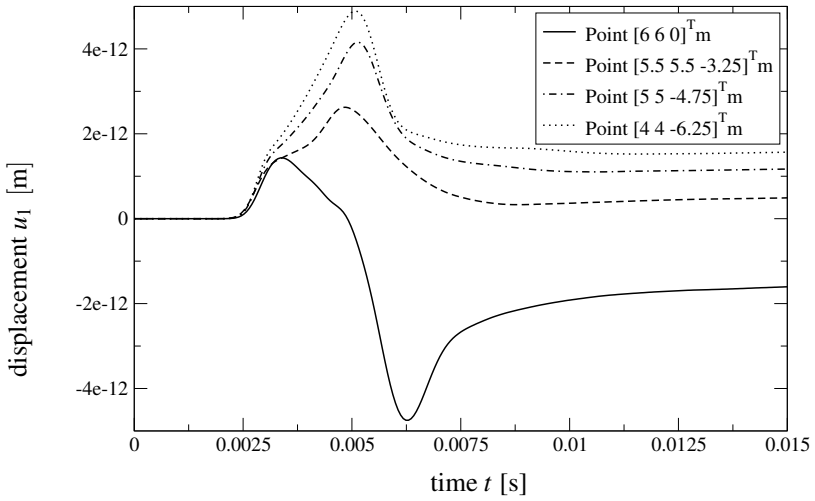

(b) Displacement u_1

Figure 5.26: Vertical- and horizontal displacement at different depths.

vertical- u_3 and horizontal u_1 displacement are plotted. The wave arrival times of the fast compressional-, the shear- and the Rayleigh wave are taken from column one of table 5.8. In figure 5.26(a), it can be clearly observed that with increasing depth the Rayleigh pole vanishes. The amplitude shift to the left, which can be observed in figure 5.26(b), may indicate that this amplitude is mainly caused by the shear wave, since this shift gets larger for increasing depths.

Halfspace - Soil So far, the underlying porous material was assumed to be a rock. In the following the infinite element will also be applied to a poroelastic halfspace where the material is assumed to be a soil. The material data of the soil are given in table 5.6. The governing equations (2.29)-(2.31) will be used to describe the behavior of the porous media, since for the underlying material this approximation yields sufficient accurate results as was shown in the one-dimensional example (cf. section 5.2.1). The corresponding FEM formulation is given by equation (3.44).

As in the case of the rock, the functionality of the infinite elements will be investigated by observing the solid displacements u_i at the observation point $[6\,6\,0]^{\mathrm{T}}\,\mathrm{m}$. The spatial discretization of the solid displacement and the pore pressure is performed in the same manner as for the case of the rock. The infinite elements will be adopted in such a way that either all wave types, i.e., the fast compressional-, the shear-, and Rayleigh wave, are approximated or that only the fast compressional and the shear wave are approximated. To approximate only the fast compressional wave is not sufficient as shown for the case of the rock. The respective curves will be labeled in the following plots as mentioned before. The boundary conditions are assumed to be the same as in the examples before.

For the time integration a CFL-factor of $\chi = 0.75$ is assumed. Thus, taking into account the wave speed of the fast compressional wave of the soil, given in table 5.7, a time step of $\Delta t = 0.00011\,\mathrm{s}$ and $\Delta t = 0.00022\,\mathrm{s}$ is obtained for mesh 1 and mesh 2, respectively. The calculations will be compared to a pure FEM solution (mesh 3) as it was also done for the case of rock. Here, the time step is chosen to be $t = 0.00022\,\mathrm{s}$. Furthermore, a comparison to a BEM calculation [102] is considered.

Also in this case the wave arrival of the numerical approximation method will be checked against the theoretical arrival times, calculated with the approximated wave speeds of table 5.7. The expected wave arrival times are calculated in the same way as for the case of the rock and are listed in table 5.9.

	Wave speed [m/s]	Distance [m]		
		7.07	9.07	23.07
		Arrival time [s]	Approx. reflection time [s]	
			iFEM	FEM
Comp. wave c_P	1689.6	0.0042	0.0054	0.014
Shear wave c_S	228.1	0.031	0.040	0.10
Rayleigh wave c_R	211.5	0.033	0.043	0.11

Table 5.9: Distance measure from load corner point $[1\,1\,0]^{\mathrm{T}}\,\mathrm{m}$ to observation point $[6\,6\,0]^{\mathrm{T}}\,\mathrm{m}$ with corresponding wave arrival times - soil.

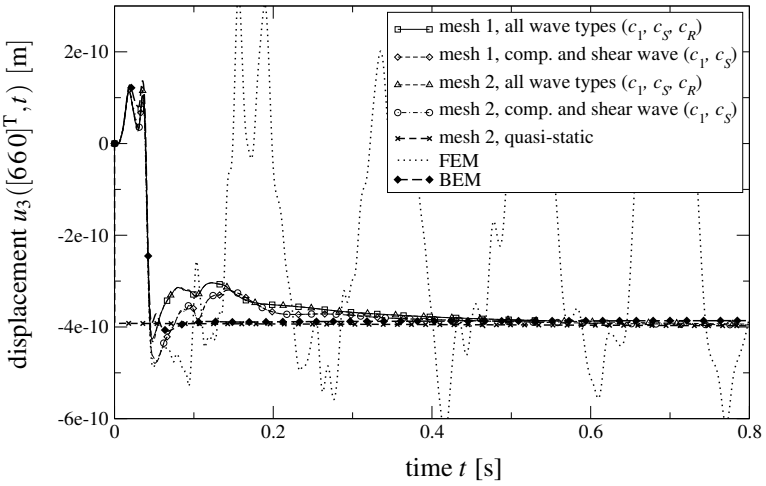

(a) Displacement u_3

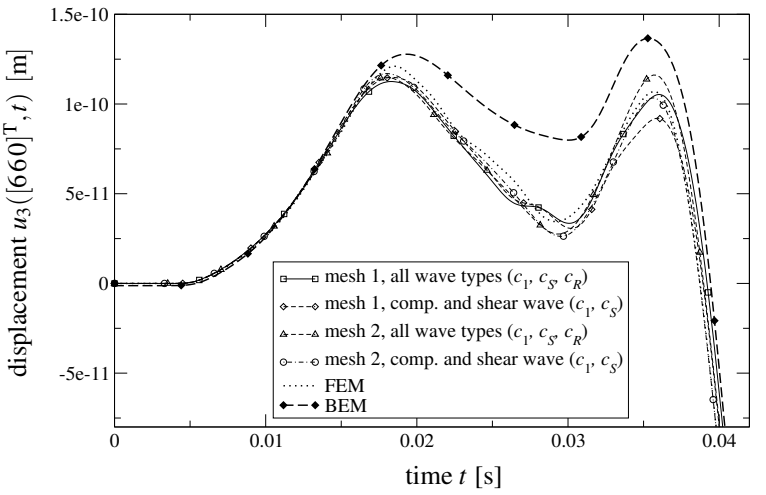

(b) Zoom section of 5.27(a) - Displacement u_3

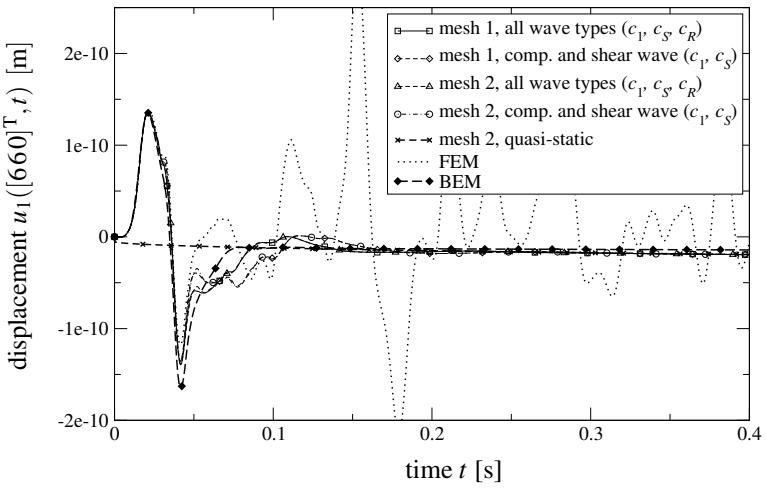

(c) Displacement u_1

Figure 5.27: Vertical- and horizontal displacement at observation point $[660]^T$ m - soil.

The displacements u_i at the observation point $[6\,6\,0]^{\mathrm{T}}\,\mathrm{m}$ are plotted in figures 5.27. The vertical solid displacement u_3 is shown in figure 5.27(a) and (b), whereas the horizontal solid displacement u_1 is depicted in figure 5.27(c). At time $t = 0.0042\,\mathrm{s}$ the arrival of the influence of the fast compressional wave can be noticed. The expected reflection of the fast compressional wave ($t = 0.014\,\mathrm{s}$) at the free boundary of the pure FEM calculation, due to the truncation of the spatial discretization, causes a slight deviation of this solution. Furthermore, from this time on the different calculations diverge from each other. This is in a way obvious, since now the infinite elements are activated and the infinite elements which approximate all three wave types possess another behavior as when only two waves are approximated. However, these deviations of the solutions to each other aren't observable for the case of a rock, as investigated in the example above. The Rayleigh pole can be clearly observed at time $t = 0.033\,\mathrm{s}$ which overlaps with the arrival of the shear wave ($t = 0.031\,\mathrm{s}$). For the soil the solutions differ in a greater amount from the BEM calculation as for the case of a rock (cf. figure 5.25(b)). However, this deviations are due to the fact that the infinite elements just approximate the wave behavior of the far field, whereas the BEM fulfills the wave equation exactly within the domain and certainly in infinity. Nevertheless, the results obtained by using the infinite elements are quite good compared to the pure finite element solution. As it can be realized in figure 5.27(b), the different spatial discretizations doesn't really affect the solution, as it was also the case for the rock. Actually, the Rayleigh pole is more emphasized when the coarser mesh (mesh 2) is used. After the waves have passed the observation point the solutions approach the quasi-static solution (denoted by "mesh 2, quasi-static") as can be identified in figures 5.27(a) and 5.27(c). Nevertheless, small reflections of the shear-, and consequently the Rayleigh wave, can be observed at times $t \geq 0.040\,\mathrm{s}$ and $t \geq 0.043\,\mathrm{s}$. This reflections may be caused since the waves are not perfectly transferred to the far field. This is in a way obvious since the infinite elements are just an approximation. These spurious reflections are greater when the soil is considered as for the rock. Nevertheless, compared to the pure finite element calculation the results obtained by using infinite elements are superior and, therefore, approve their necessity. For the case of the soil, the quasi-static solution of any infinite element calculation matches the BEM solution.

Elastic modeled poroelastic material In the following paragraph, the poroelastic material will be compared to two elastic models, namely the undrained and drained case. These two models represent an upper and lower bound of the poroelastic model. The drained material parameters are already defined in table 5.6. The definition of the undrained material parameters are taken from [60]. The undrained compression modulus is given by

$$K_u = K + \frac{K^s K^f \alpha^2}{K^f \alpha + \phi (K^s + K^f)} \,.$$

The undrained Poisson ratio and Young's modulus are defined by

$$\nu_u = \frac{3K_u - 2G}{2(3K_u + G)} , \qquad E_u = 3K_u(1 - 2\nu_u) ,$$

respectively. In table 5.10 the drained and undrained material parameters for a soil are given with the corresponding wave velocities.

	$K, K_u \left[\frac{\mathrm{N}}{\mathrm{m}^2}\right]$	$G \left[\frac{\mathrm{N}}{\mathrm{m}^2}\right]$	$\varrho \left[\frac{\mathrm{kg}}{\mathrm{m}^3}\right]$	$E, E_u \left[\frac{\mathrm{N}}{\mathrm{m}^2}\right]$	$\nu, \nu_u \, [-]$	$c_P \left[\frac{\mathrm{m}}{\mathrm{s}}\right]$	$c_S \left[\frac{\mathrm{m}}{\mathrm{s}}\right]$	$c_R \left[\frac{\mathrm{m}}{\mathrm{s}}\right]$
				soil				
drained	$2.1 \cdot 10^8$	$9.8 \cdot 10^7$	1884	$2.544 \cdot 10^8$	0.298	425.2	228.1	211.5
undrained	$5.248 \cdot 10^9$	$9.8 \cdot 10^7$	1884	$2.922 \cdot 10^8$	0.49	1689.6	228.1	217.2

Table 5.10: Material data of a soil modeled elastic.

The calculations are performed using the spatial discretization of mesh 2 (see figure 5.10(b)). The boundary conditions for the elastic models are taken as in the examples of the elastic halfspace (cf. section 5.1.3) and for the poroelastic model as in the examples above. Also, the temporal discretization is performed in the same manner, i.e., the time steps are chosen to obtain a CFL-factor of $\chi = 0.75$ for any model. Thus, a time step of $\Delta t = 0.00022\,\mathrm{s}$ for the undrained and poroelastic model and $\Delta t = 0.00088\,\mathrm{s}$ for the drained model is used. Concerning the infinite elements, the approximation of all three wave types is assumed for any model, i.e., the compressional-, shear-, and Rayleigh wave.

	Wave speeds $[\mathrm{m/s}]$			Wave arrival times $[\mathrm{s}]$		
	c_P, c_1	c_S	c_R	t_{c_P,c_1}	t_{c_S}	t_{c_R}
poroelastic	1689.6	228.1	211.5	0.0042	0.031	0.033
drained	425.2	228.1	211.5	0.017	0.031	0.033
undrained	1689.6	228.1	217.2	0.0042	0.031	0.0325

Table 5.11: Distance measure from load corner point $[1\,1\,0]^{\mathrm{T}}\,\mathrm{m}$ to observation point $[6\,6\,0]^{\mathrm{T}}\,\mathrm{m}$ with corresponding wave arrival times.

In figures 5.28, the solid displacements u_i are plotted. The wave arrival times at the observation point $[6\,6\,0]^{\mathrm{T}}\,\mathrm{m}$ for the single material models are, again, listed in compact form in table 5.11. The arrival of the compression wave of the poroelastic material at time $t = 0.0042\,\mathrm{s}$ can be clearly observed in figure 5.28(b), which coincidences with the arrival of the compressional wave of the undrained elastic model. The compressional wave of the drained model arrives at a later time $t = 0.017\,\mathrm{s}$. The shaky behavior of the history

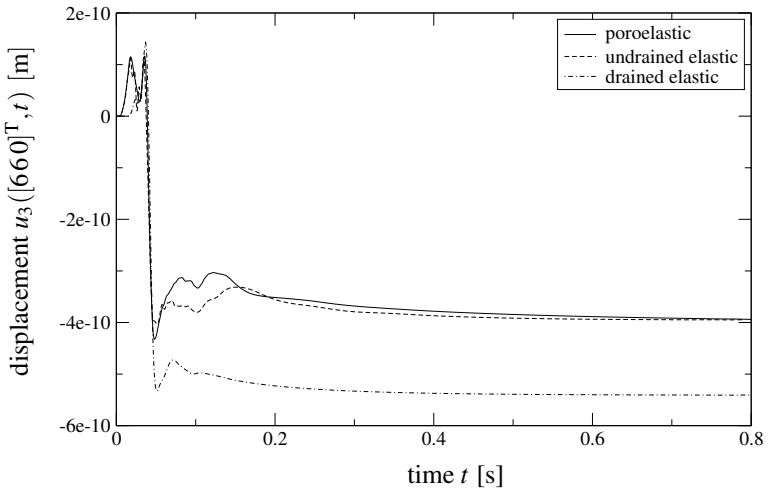

(a) Displacement u_3

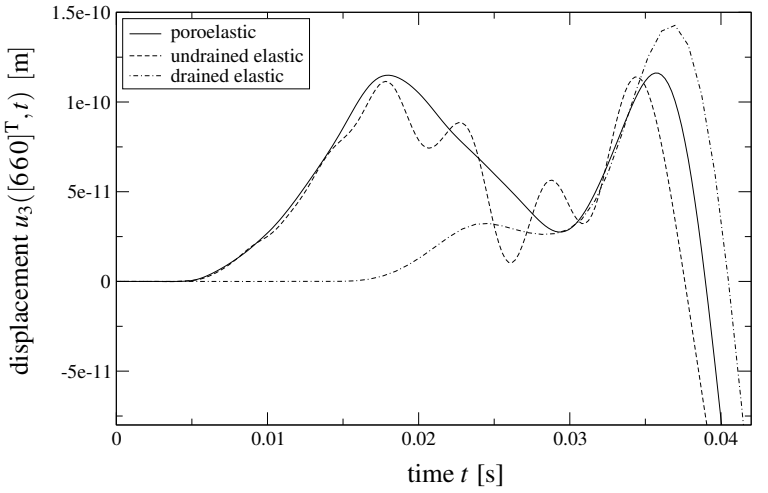

(b) Zoom section of 5.28(a) - Displacement u_3

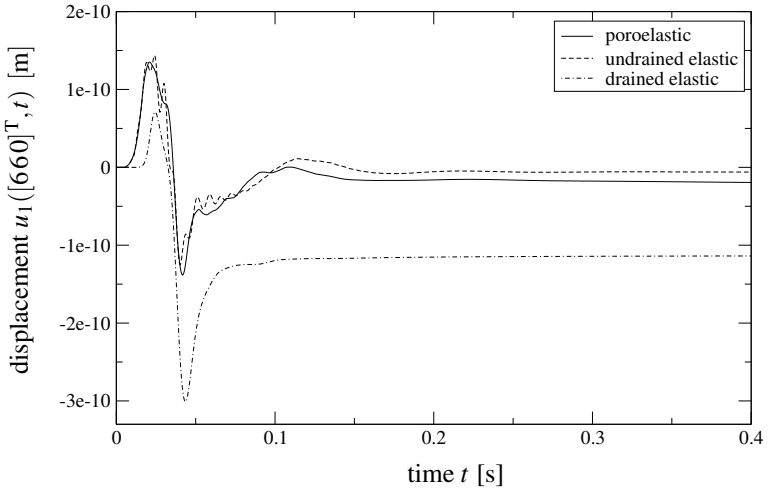

(c) Displacement u_1

Figure 5.28: Vertical- and horizontal displacement at observation point $[660]^T$ m - Comparison poroelastic and elastodynamic modeling of the soil.

plot of the undrained model may be attributed to the fact that this model behaves nearly incompressible as can be noticed when looking at the Poisson's ratio of $\nu = 0.49$. The arrival of the shear wave is the same for any model, since the shear modulus is the same for any material. The Rayleigh pole, which overlaps with the arrival of the shear wave, can be clearly observed in the vertical displacement (figure 5.28(b)) as well as in the horizontal displacement in figure 5.28(c). Whereas the Rayleigh pole is nearly the same for the poroelastic and undrained model, it is more pronounced for the drained model. After the waves have passed the observation point they approach the quasi static solution. When looking at the horizontal displacement, the poroelastic model lies in between the elastic solutions, i.e., they are an upper and lower bound. This statement is also valid for the vertical displacement, although the solution of the poroelastic material is slightly outside the upper bound of the undrained model. Actually, this deviation may be attributed to the numerical approximation scheme, which performs differently for the underlying material (cf. also section 5.1.3, where the elastic halfspace is considered). In conclusion, it can be stated that the one-phase elastic models of the poroelastic material are just a crude approximation.

5.2.3 Soil on a bedrock

Next, a saturated soil is considered of finite thickness resting on a bedrock, i.e., a poroelastic layer fixed at the bottom. The schematic representation of the problem is sketched in figure 5.29. The saturated porous layer, a soil, is assumed to be of 5 m thickness. The

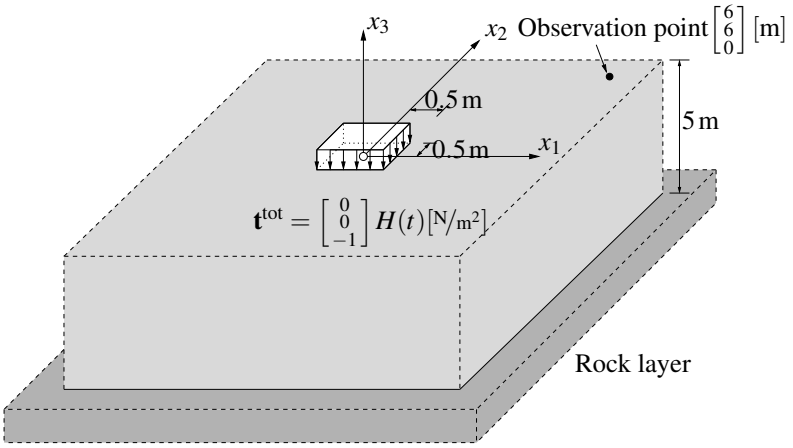

Figure 5.29: Schematic representation of the poroelastic halfspace resting on a rock layer.

material parameters of the soil are given in table 5.6. Below an impermeable bedrock is assumed, thus, the flux at this boundary and the displacements in any direction are assumed to be zero. The remaining boundary conditions are chosen to be same as for the poroelastic

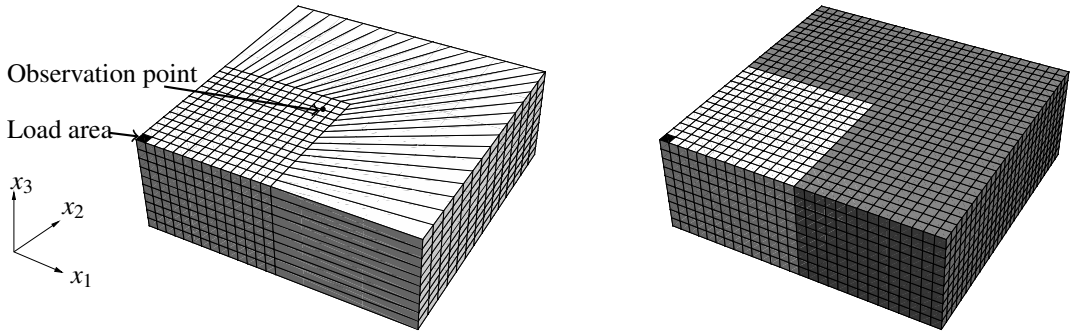

(a) Mesh 5: cube $7\times7\times5\,\mathrm{m}^3$

(b) Mesh 6: cube $7\times7\times5\,\mathrm{m}^3$ with attached pure FEM layer of 7 m thickness

Figure 5.30: Finite-infinite element discretizations.

halfspace, with the exception of the load vector. Here, the load vector $\mathbf{t}^{\mathrm{tot}} = [0\,0\,-1]^{\mathrm{T}}\,\mathrm{N/m^2}$ is applied on an area of $0.5\times0.5\,\mathrm{m}^2$. Again, the saturated poroelastic layer is modeled with the governing equations (2.29)-(2.31), thus, some fluid inertia terms are neglected. The spatial discretizations of the near- and far field are depicted in figures 5.30(a) and (b). The detailed discretization parameters are summarized in table 5.12. The spatial approximation of the solid displacement and the pore pressure are assumed to be of the same order. The calculation using infinite elements will be performed in such a way that either all wave types, i.e., the fast compressional-, the shear-, and the Rayleigh wave or just the fast compressional- and shear wave are approximated. These two calculations are labeled as "iFEM, all wave types (c_1, c_S, c_R)" and "iFEM, comp. and shear wave (c_1, c_S)", respectively.

Mesh label	mesh 5	mesh 6
Finite domain	$7\times7\times5\,\mathrm{m}^3$	$14\times14\times10\,\mathrm{m}^3$
h_e	0.25 m	0.25 m
Near field	1960 HEX20	1960 HEX20
Far field	280 iFEM	5880 HEX20
Degrees of freedom, u_i, p-formulation, P_p^k with $p=1$	41048	142100

Table 5.12: Spatial discretization parameters.

As in the examples before, the solid displacements u_i at the observation point $[6\,6\,0]^{\mathrm{T}}\,\mathrm{m}$ are investigated and compared to a BEM calculation [102] in order to validate the proposed infinite element. Additionally, a comparison is performed to a pure finite element mesh, denoted as "FEM" in the following plots. Here, an *additional layer* of 7 m thickness of conventional finite elements is attached as depicted in figure 5.30(b). The boundaries on the infinite side are assumed to be free to move, traction free, and impermeable.

For the underlying spatial discretization ($h_e = 0.25\,\mathrm{m}$) a time step of $\Delta t = 0.00011\,\mathrm{s}$ is chosen, which results in a CFL-factor of $\chi = 0.75$. As in the example before, the wave arrival times are inspected as well (see table 5.13). The distance measure is performed from the outer corner point of the load area, i.e., $[0.5\,0.5\,0]^{\mathrm{T}}\,\mathrm{m}$. Additionally, the arrival of reflected waves from the rock layer at the observation point are listed in column 4.

	Wave speed [m/s]	Distance [m]			
		7.78	9.78	23.78	12.67
		Arrival time [s]	Approx. reflection time [s]		
			iFEM	FEM	rock layer
Comp. wave	1689.6	0.0046	0.0058	0.014	0.0076
Shear wave	228.1	0.034	0.043	0.10	0.056
Rayleigh wave	211.5	0.037	0.046	0.11	0.060

Table 5.13: Distance measure from load corner point $[0.5\,0.5\,0]^{\mathrm{T}}\,\mathrm{m}$ to observation point with corresponding wave arrival times.

In figures 5.31(a)-(c), the vertical- and horizontal solid displacements are plotted over time. The expected arrival of the fast compressional wave is clearly observable at time $t = 0.0046\,\mathrm{s}$ in figure 5.31(b). The arrival of the compressional wave is followed by the arrival of the Rayleigh wave at time $t = 0.037\,\mathrm{s}$, which overlaps with the arrival of the shear wave at time $t = 0.034\,\mathrm{s}$. Due to fact that the load is applied on a smaller region, compared to the examples before, the Rayleigh pole is more pronounced. Whereas the expected arrival of reflected compressional waves from the rock layer ($t = 0.0076\,\mathrm{s}$) is nearly not detectable, the influence of reflected shear waves is clearly observable at time $t = 0.056\,\mathrm{s}$ in figure 5.31(b). Since the influence of the Rayleigh wave is decreasing with depth the displacement change at time $t = 0.060\,\mathrm{s}$ is essentially caused by the shear wave alone (arrival time $t = 0.056\,\mathrm{s}$). Since up to this time the influence of the compressional wave is of minor influence the deviation of the pure FEM calculation is relatively small. This behavior changes as the reflected shear- and Rayleigh wave from the FEM boundary reach the observation point at time $t = 0.10\,\mathrm{s}$ and $t = 0.11\,\mathrm{s}$. From this time on, the pure FEM results diverge from the calculation using infinite elements which can be clearly noticed in figures 5.31(a) and (c). Also, the behavior of the solution with the infinite elements differs from the BEM solution, which is due to the fact that the infinite elements

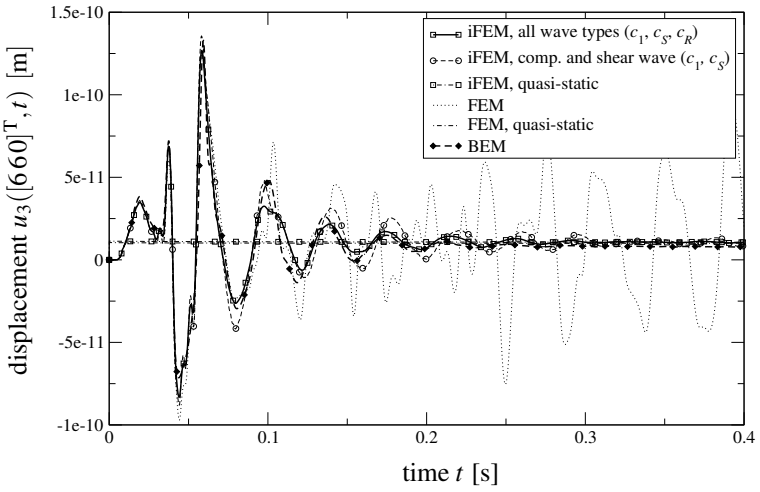

(a) Displacement u_3

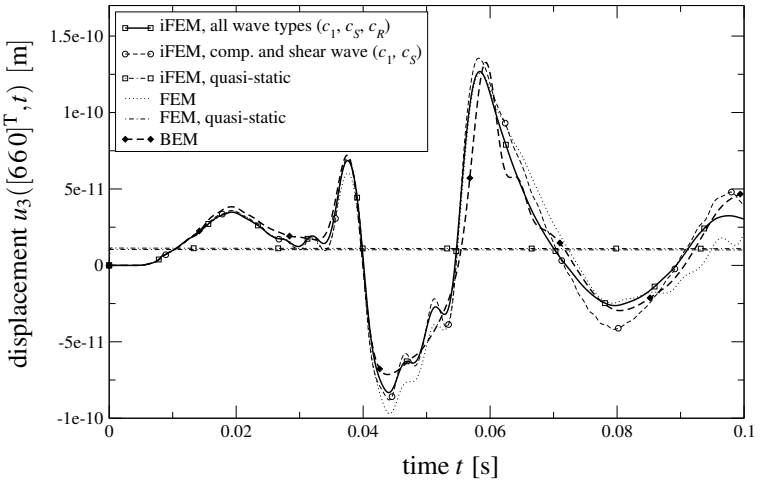

(b) Zoom section of 5.31(a) - Displacement u_3

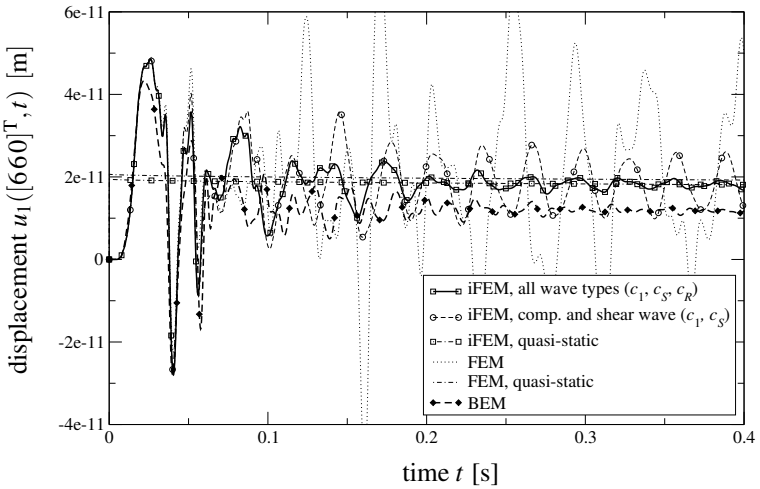

(c) Displacement u_1

Figure 5.31: Vertical- and horizontal displacement at observation point $[660]^T$ m.

just approximate the far field behavior. Consequently, the far field is represented in another fashion. With ongoing time the solutions approach the quasi-static equilibrium state since the introduced waves are transferred to infinity. Furthermore, the approximation of only the fast compressional- and shear wave yields not as good results as when all wave types are approximated as can be observed best when looking at the horizontal displacement in figure 5.31(c). In the pure FEM solution, still reflected waves can be noticed when the calculations using the infinite elements already approached the quasi-static equilibrium. Of course, when enough time has passed the damping due to the material will also cause this solution to approach the quasi-static equilibrium. It must be mentioned that the quasi-static solutions of the calculation with the infinite elements and the pure FEM coincidence proper. Only the BEM solution approaches another quasi-static equilibrium.

6 CONCLUSION

In the present work, an infinite element has been developed to be used in combination with finite elements to treat unbounded domains. The application of the proposed numerical approximation scheme has been performed to elastostatics, elastodynamics, poroelastodynamics, and quasi-static poroelasticity. The governing equations are derived under the assumption of linear kinematics as well as linear, homogenous, and isotropic material behavior. The poroelastic material is modeled based on Biot's theory. Compared to a pure elastic modeled soil, which is a common approximation in soil-mechanics, the governing equations describing the poroelastic material take into account the interaction between the solid skeleton and the interstitial fluid. Consequently, the unknown field variables are the solid displacement, the pore pressure, and the relative displacement of the fluid phase to the solid skeleton. Under the assumption of a compressible fluid the pore pressure can be eliminated, which yields the so-called irreducible form with the solid- and relative displacement as unknowns. If a further reduction of unknowns in time domain is desired the negligence of some fluid inertia terms is necessary. This simplified model yields the solid displacement and the pore pressure as primary variables. An elimination of the relative displacement without the negligence of any fluid inertia terms is possible in Laplace domain. The validity of the simplified model has been discussed in section 5.2.1. One can conclude that the simplified model is applicable to realistic, most common poroelastic material in the low frequency regime. Moreover, the wave speeds of plane body waves in an infinite elastic and poroelastic material are derived.

The treatment of unbounded domains with the proposed method has been performed in such a way that the domain of consideration is decomposed into a so-called near- and far field. Consequently, finite elements are used for the numerical approximation of the near field behavior, whereas the solution of the far field is approximated by the proposed infinite elements. Discrete variational formulations for the governing equations of an elastic and a poroelastic material are deduced. In case of the poroelastic material different approaches are discussed. Here, a symmetric as well as a non-symmetric finite approximation scheme has been recalled for the approximation of all three constituents, i.e., the solid displacement, pore pressure, and relative displacement. Furthermore, the finite element formulation for the irreducible (solid- and relative displacement are unknown) and the simplified form (solid displacement and pore pressure are unknown) are presented. Exemplarily, the finite element formulation in Laplace domain is performed for the case that the solid displacement and the pore pressure are the unknown variables. Here, the case is chosen where no negligence of fluid inertia terms is assumed.

The main topic of this thesis is devoted to the derivation of the infinite elements. The infinite elements have been constructed in such a way that they represent the far field behavior in an appropriate manner, i.e., they are defined in such a manner that they approximate the Sommerfeld radiation condition sufficiently. The Sommerfeld radiation condition ensures that outward traveling waves are transferred from the near- to the far field and that no incoming waves will appear. Hence, a wave-like behavior is attributed to the infinite elements to fulfill these requirements. To provide this wave-like behavior to the shape functions of the infinite elements they have to be formulated in Laplace domain. Thus, the existing waves can be approximated by the infinite elements with exponential functions, one for every present wave type. In the case of an elastic material a compressional- and a shear wave have to be considered. When investigating a poroelastic material two compressional- and one shear wave have to be taken into account. Additionally, for an elastic or poroelastic halfspace a surface wave, the so-called Rayleigh wave has to be considered. In the elastic case, the approximation of each wave type can be performed independently, whereas in the poroelastic case the two compressional waves are related to each other. This wave-relation has been taken from the analytical solution of a one-dimensional poroelastic column. Nevertheless, the slow compressional wave in a poroelastic material is highly damped and, thus, for realistic, most common poroelastic materials, not observable. Hence, a simplified model for a poroelastic infinite element has been presented which neglects the the slow compressional wave. This simplified model of the infinite element for poroelastodynamics exhibits the same structure as the infinite element for elastodynamics. Nevertheless, this simplified model is only applicable if the second wave is nearly not detectable, as it has been validated by a simple infinite one-dimensional example. Moreover, the infinite element is constructed in such a way that the radial approximation order is variable and independent of the approximation order of the finite portion. The approximation order of the finite portion of the infinite element is restricted to the approximation order of the near field, since a direct coupling (node to node coupling) is assumed between the finite and infinite elements. The correct long time behavior, i.e., the static and quasi-static solution of the elastic and poroelastic material, respectively, is ensured by the correct $1/r$-like mapping behavior, which is used for the mapping relation between the physical and local space.

Another crucial point is the numerical evaluation of the infinite element matrices, since in radial direction (direction to infinity) the functions to be integrated contain exponential terms due to the wave approximation. To overcome this difficulty, a Newton-Cotes type formula has been derived. The integration of the finite portion of the shape functions has been performed with the standard Gauß quadrature.

The temporal discretization of the near- and far field has been accomplished by two different integration schemes. The system of ordinary differential equations obtained by the spatial discretization by finite elements is treated by the Newmark method. On the other hand the far field is discretized with the proposed infinite elements. Their formulation is frequency dependent and, thus, a set of convolution equations is obtained by the infinite

element discretization. This set of equations is integrated by means of the convolution quadrature method. Next, the near- and far field has been combined using a direct coupling strategy. The resulting equation system is solved at every time step to obtain the time domain solution of the whole domain. This approach has been performed mainly for two reasons. First, the treatment of materially non-linear or large deformation problems is still retained within the near field. Second, the convolution quadrature requires to store the system matrices of every time step and, thus, this integration scheme demands respective computer storage.

Summarizing, the proposed infinite elements approximate the far field behavior in an adequate manner, which has been validated by different test examples. For the case of elastodynamics, the results obtained by the proposed numerical approximation scheme coincide well in either case, first, when they are compared to a boundary element calculation or, second, when they are compared to an analytical solution. However, when poroelastodynamic problems are considered the performance of the infinite elements is not as good as when elastodynamic problems are investigated. Here, small reflections are observable when the waves enter the transition from the near- to the far field. In this case, the boundary element method yields better results. The lack of accuracy, especially for the poroelastic material, can be attributed to the fact that the infinite elements just approximate the wave behavior of the far field, whereas the boundary element method fulfills the wave equation exactly within the domain and certainly in infinity. Furthermore, the numerical integration scheme exhibits numerical instabilities when the radial approximation is chosen to be higher than of first order. However, due to the fact that a higher radial approximation order does not yield better results this disadvantage can be confidently disregarded. As a consequence, future works should take care of the numerical instabilities of the numerical integration scheme. The best solution to solve this problem could be to formulate an infinite element directly in time domain, given the case that this can be realized at all. Another approach to eliminate the numerical instabilities of the time stepping scheme could be to use different time steps for the near- and far field. Thus, an optimized time step could be chosen for each domain. On the finite element side the treatment of material non-linearity or large deformations could be taken into account.

A ANALYTIC SOLUTIONS

A.1 Time domain solution of a finite elastic column

The time domain solution of an elastic column, as depicted in figure 4.1, will be accomplished using an inverse Laplace transformation of (4.3). Following the steps as shown by Graff [79] the series expansion

$$\frac{1}{1+\mathrm{e}^{-2\frac{\mathrm{s}}{c_P}\ell}} = \sum_{n=0}^{\infty}(-1)^n\,\mathrm{e}^{-2\frac{\mathrm{s}}{c_P}\ell n}$$

is inserted into (4.3) yielding

$$u(x,\mathrm{s}) = \frac{\hat{\sigma}c_P}{(K+\frac{4}{3}G)\mathrm{s}}\sum_{n=0}^{\infty}(-1)^n\left[\mathrm{e}^{-\frac{\mathrm{s}}{c_P}(2\ell n+x)} - a\,\mathrm{e}^{-\frac{\mathrm{s}}{c_P}[2\ell(n+1)-x]}\right]\,. \tag{A.1}$$

Using the Laplace transform relation [61]

$$\tfrac{B}{\mathrm{s}}\,\mathrm{e}^{-b\mathrm{s}} \bullet\!\!-\!\!\circ\, B\mathrm{H}(t-b)\,, \qquad B,b\in\mathbb{R}$$

yields together with equation (A.1) the time domain solution for an impulse load of the displacement. Of course, the aim is to obtain the solution for arbitrary loading. This will lead to convolution integrals of the form

$$u(t,x) = \int_0^t \mathscr{L}^{-1}\{\hat{u}(x,\mathrm{s})\}f(t-\tau)\,\mathrm{d}\,\tau\,. \tag{A.2}$$

Taking a Heaviside step function as loading, the occurring convolution integrals have the general form

$$\int_0^t B\mathrm{H}(\tau-b)\mathrm{H}(t-\tau)\,\mathrm{d}\,\tau = \begin{cases} 0 & \ldots\text{if } t<b \\ B(t-b) & \ldots\text{if } t>b\,, \end{cases}$$

which can be written as

$$\int_0^t B\mathrm{H}(\tau-b)\mathrm{H}(t-\tau)\,\mathrm{d}\,\tau = B(t-b)\mathrm{H}(t-b)\,.$$

Thus, the time domain solution according to a Heaviside step function can be evaluated term-by-term resulting in

$$u(x,t) = \frac{\sigma_0 c_P}{(K+\frac{4}{3}G)} \sum_{n=0}^{\infty} (-1)^n \Big[\mathrm{H}(t - \tfrac{1}{c_P}(2\ell n + x)) \mathrm{H}(t - \tfrac{1}{c_P}(2\ell n + x)) \Big] \\ - \mathrm{H}(t - \tfrac{1}{c_P}(2\ell(n+1) - x)) \mathrm{H}(t - \tfrac{1}{c_P}(2\ell(n+1) - x)) \big] \,. \tag{A.3}$$

In the solution (A.3), clearly one wave with the velocity c_P can be identified.

A.2 Time domain solution of an infinite elastic column

The time domain solution of equation (4.9), according to a Heaviside step function, is obtained in the same manner as for the finite column (cf. section A.1) and is given by

$$u(x,t) = \frac{\sigma_0 c_P}{(K+\frac{4}{3}G)} \left(t - \tfrac{x}{c_P}\right) \mathrm{H}\left(t - \tfrac{x}{c_P}\right) \,. \tag{A.4}$$

Also in this solution one wave with the velocity c_P can be observed but with the difference that only one outgoing wave exists.

A.3 Analytic solution of a finite poroelastic column

The analytic solution of a one-dimensional poroelastic column of length ℓ, as sketched in figure A.1, will be presented. The side walls and the bottom of the column are assumed to be impermeable and frictionless. Movement of the media is only permitted parallel to the side walls and the bottom, not perpendicular to them. Furthermore, the total stress σ_0^{tot} and the solid displacement u_0 are prescribed at the top and the bottom of the column, respectively. For the fluid phase the flux q_0 at the bottom and the pore pressure p_0 at the top of the column is applied. Here, the case will be presented where the solid displacement, the pore pressure, and the relative displacement are considered as unknowns.

In order to derive the analytic solution, equations (2.33), (2.35) and (2.34a) are recalled and restricted to a one-dimensional problem. Hence, three coupled scalar ordinary differential equations

$$\left(K+\tfrac{4}{3}G\right)\hat{u}_{,xx} - \alpha\hat{p}_{,x} - \mathrm{s}^2\varrho\hat{u} - \mathrm{s}^2\varrho_f\hat{w} = 0 \tag{A.5a}$$

$$\hat{w}_{,x} + \alpha\hat{u}_{,x} + \frac{\phi^2}{R}p = 0 \tag{A.5b}$$

$$\hat{p}_{,x} + \frac{\mathrm{s}^2}{\phi^2}\left(\phi\varrho_f + \varrho_a\right)\hat{w} + \mathrm{s}^2\varrho_f\hat{u} + \frac{\mathrm{s}}{\kappa}\hat{w} = 0 \tag{A.5c}$$

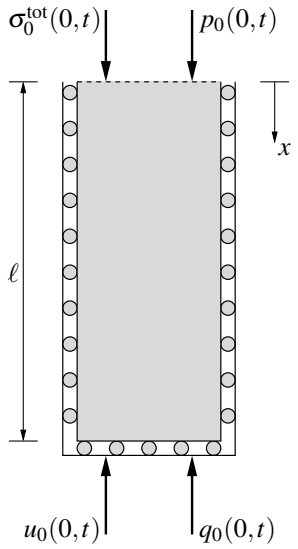

Figure A.1: One-dimensional poroelastic column

are obtained. Furthermore, vanishing body forces $\hat{F}$ and $\hat{f}^f$ are assumed. Note that equation (A.5c) is divided by the porosity ϕ after the fluid stress $\sigma^f = -\phi p$ was replaced by the pore pressure p. Additionally, the total stress σ^{tot} in equation (A.5a) was substituted using the relations (2.19) and (2.20). The boundary conditions in Laplace domain are

$$\begin{aligned} \hat{u}(\ell,\mathrm{s}) = \hat{u}_0 \quad \bullet\!\!-\!\!\circ \quad u_0\delta(t) = u(\ell,t), \qquad & \hat{p}(0,\mathrm{s}) = \hat{p}_0 \bullet\!\!-\!\!\circ p_0\delta(t) = p(0,t), \\ \hat{\sigma}^{\mathrm{tot}}(0,\mathrm{s}) = -\hat{\sigma}_0^{\mathrm{tot}} \bullet\!\!-\!\!\circ -\sigma_0^{\mathrm{tot}}\delta(t) = \sigma^{\mathrm{tot}}(0,t)\ , \quad & \hat{q}(\ell,\mathrm{s}) = \hat{q}_0 \bullet\!\!-\!\!\circ q_0\delta(t) = q(\ell,t)\ . \end{aligned} \tag{A.6}$$

The temporal behavior of the boundary conditions is assumed to be an impulse load. Also vanishing initial conditions are assumed in the above Laplace transformation. The homogeneous set of ordinary differential equations can be solved using the ansatz

$$\begin{bmatrix} \hat{u}(x,\mathrm{s}) \\ \hat{p}(x,\mathrm{s}) \\ \hat{w}(x,\mathrm{s}) \end{bmatrix} = \mathrm{e}^{\mathrm{s}\lambda x} C\mathbf{v} \tag{A.7}$$

with the corresponding Eigenvector $\mathbf{v}$ of the system matrix (A.8). The constant C scales the Eigenvector $\mathbf{v}$ to the specified boundary conditions. Inserting the ansatz function (A.7) into the set of differential equations (A.5) yields the eigenvalue problem

$$\begin{bmatrix} \mathrm{s}\left[\lambda^2(K+\frac{4}{3}G) - \varrho\right] & -\alpha\lambda & -\mathrm{s}\varrho_f \\ \alpha\mathrm{s}\lambda & \dfrac{\phi^2}{R} & \mathrm{s}\lambda \\ \mathrm{s}^2\varrho_f & \mathrm{s}\lambda & \dfrac{\mathrm{s}^2\varrho_f}{\beta} \end{bmatrix} \begin{bmatrix} Cv_1 \\ Cv_2 \\ Cv_3 \end{bmatrix} = \begin{bmatrix} 0 \\ 0 \\ 0 \end{bmatrix} \tag{A.8}$$

for λ. Note that in the above equation the abbreviation β from equation (2.36) is incorporated to achieve simpler expressions. The determinant of the above matrix (A.8) yields the characteristic equation

$$\underbrace{(K+\tfrac{4}{3}G)}_{A}\lambda^4 - \underbrace{\frac{\left[(K+\tfrac{4}{3}G)\varrho_f\phi^2 + R\beta\varrho + R\alpha(\alpha-2\beta)\varrho\right]}{R\beta}}_{B}\lambda^2 + \underbrace{\frac{\varrho_f(\rho-\beta\varrho)\phi^2}{R\beta}}_{C} \stackrel{!}{=} 0\,. \quad \text{(A.9)}$$

The characteristic equation (A.9) has the four complex eigenvalues

$$\lambda_1 = -\lambda_3 = \sqrt{\frac{B-\sqrt{B^2-2AC}}{2A}}\,, \quad \lambda_2 = -\lambda_4 = \sqrt{\frac{B+\sqrt{B^2-2AC}}{2A}}\,. \quad \text{(A.10)}$$

Thus, the solution can be written as

$$\begin{bmatrix}\hat{u}(x,\mathrm{s})\\ \hat{p}(x,\mathrm{s})\\ \hat{w}(x,\mathrm{s})\end{bmatrix} = \sum_{i=1}^{4} C_i\,\mathrm{e}^{\mathrm{s}\lambda_i x}\,\mathbf{v}^i = \sum_{i=1}^{4} C_i\,\mathrm{e}^{\mathrm{s}\lambda_i x}\begin{bmatrix}v_1^i\\ v_2^i\\ v_3^i\end{bmatrix} \quad \text{(A.11)}$$

with the yet unknown constants C_i and Eigenvectors $\mathbf{v}^i$. The Eigenvectors of the system are given by

$$\mathbf{v}^i = \begin{bmatrix}1\\ \frac{R\mathrm{s}(\alpha-\beta)\lambda_i\rho_f}{R\beta\lambda_i^2-\rho_f\phi^2}\\ \frac{\beta\rho_f\phi^2-R\alpha\beta\lambda_i^2}{R\beta\lambda_i^2-\rho_f\phi^2}\end{bmatrix} \quad \text{(A.12)}$$

and, therefore, only the four unknown constants remain to be adapted to the given boundary conditions. Hence, the solution (A.11) is inserted into the one-dimensional form of the constitutive equation (2.18)

$$\hat{\sigma}^{\mathrm{tot}}(x,\mathrm{s}) = (K+\tfrac{4}{3}G)\hat{u}_{,x}(x,\mathrm{s}) - \alpha\hat{p}(x,\mathrm{s}) = \mathrm{s}(K+\tfrac{4}{3}G)\sum_{i=1}^{4}\lambda_i C_i\,\mathrm{e}^{s\lambda_i x}\,v_1^i - \alpha\hat{p}(x,\mathrm{s}) \quad \text{(A.13)}$$

and into the one-dimensional form of Darcy's law (2.26)

$$\begin{aligned}\hat{q}(x,\mathrm{s}) &= -\kappa\left[\hat{p}_{,x}(x,\mathrm{s}) + \frac{\mathrm{s}^2}{\phi^2}\left(\phi\varrho_f + \varrho_a\right)\hat{w}(x,\mathrm{s}) + \varrho_f\mathrm{s}^2\hat{u}(x,\mathrm{s})\right]\\ &= -\kappa\left[\sum_{i=1}^{4}\mathrm{s}\lambda_i C_i\,\mathrm{e}^{\mathrm{s}\lambda_i x}\,v_2^i + \frac{\mathrm{s}}{\phi^2}(\phi\varrho_f+\varrho_a)\sum_{i=1}^{4}C_i\,\mathrm{e}^{\mathrm{s}\lambda_i x}\,v_3^i + \varrho_f\mathrm{s}^2\sum_{i=1}^{4}C_i\,\mathrm{e}^{\mathrm{s}\lambda_i x}\,v_1^i\right]\\ &= \sum_{i=1}^{4}\underbrace{\frac{\mathrm{s}\kappa\left(R\alpha{\lambda_i}^2-\varrho_f\phi^2\right)\left[\mathrm{s}\varrho_f\phi^2-\beta(\varrho_a+\varrho_f\phi)\right]}{\varrho_f\phi^4-R\beta{\lambda_i}^2\phi^2}}_{=:h_i}C_i\,\mathrm{e}^{\mathrm{s}\lambda_i x}\end{aligned} \quad \text{(A.14)}$$

with the introduced abbreviation h_i, which will be used in further expressions for a more condensed writing. The boundary conditions (A.6) are used to determine the unknown constants, which yields the following set of algebraic equations

$$\begin{bmatrix} \mathrm{e}^{\mathrm{s}\lambda_1\ell} & \mathrm{e}^{\mathrm{s}\lambda_2\ell} & \mathrm{e}^{-\mathrm{s}\lambda_1\ell} & \mathrm{e}^{-\mathrm{s}\lambda_2\ell} \\ v_2^1 & v_2^2 & -v_2^1 & -v_2^2 \\ \lambda_1 & \lambda_2 & -\lambda_1 & -\lambda_2 \\ h_1\,\mathrm{e}^{\mathrm{s}\lambda_1\ell} & h_2\,\mathrm{e}^{\mathrm{s}\lambda_2\ell} & h_1\,\mathrm{e}^{-\mathrm{s}\lambda_1\ell} & h_2\,\mathrm{e}^{-\mathrm{s}\lambda_2\ell} \end{bmatrix} \begin{bmatrix} C_1 \\ C_2 \\ C_3 \\ C_4 \end{bmatrix} = \begin{bmatrix} \hat{u}_0 \\ \hat{p}_0 \\ \frac{\alpha\hat{p}_0 - \hat{\sigma}^{\mathrm{tot}}}{\mathrm{s}(K+\frac{4}{3}G)} \\ \hat{q}_0 \end{bmatrix} .$$

The above equation system is now ready to be solved for the four unknown constants C_i, in general, with the aid of computer algebra. Finally, to obtain the solution, the resulting constants are inserted into (A.11) to gain the solution for the solid displacement, the pore pressure, and the relative displacement. Since the underlying system is of linear behavior, the superposition principle for different load cases can be used. For simplicity, in this thesis, the solution of the load case

$$\begin{aligned} \hat{u}(\ell,\mathrm{s}) &= 0\,, & \hat{p}(0,\mathrm{s}) &= 0\,, \\ \hat{\sigma}^{\mathrm{tot}}(0,\mathrm{s}) &= -\hat{\sigma}_0^{\mathrm{tot}}\,, & \hat{q}(\ell,\mathrm{s}) &= 0 \end{aligned}$$

will be investigated and the corresponding analytical solution is given by

$$\begin{aligned} \hat{u}(x,\mathrm{s}) &= \frac{\hat{\sigma}_0^{\mathrm{tot}}}{\mathrm{s}(K+\frac{4}{3}G)(v_2^2\lambda_1 - v_2^1\lambda_2)} \left[v_2^2 g(\mathrm{s},\lambda_1,x,\ell,1) - v_2^1 g(\mathrm{s},\lambda_2,x,\ell,1)\right] \\ \hat{p}(x,\mathrm{s}) &= -\frac{v_2^1 v_2^2 \hat{\sigma}_0^{\mathrm{tot}}}{\mathrm{s}(K+\frac{4}{3}G)(v_2^2\lambda_1 - v_2^1)\lambda_2} \left[g(\mathrm{s},\lambda_1,x,\ell,-1) - g(\mathrm{s},\lambda_2,x,\ell,-1)\right] \\ \hat{w}(x,\mathrm{s}) &= \frac{\hat{\sigma}_0^{\mathrm{tot}}}{\mathrm{s}(K+\frac{4}{3}G)(v_2^2\lambda_1 - v_2^1\lambda_2)} \left[v_2^2 v_3^1 g(\mathrm{s},\lambda_1,x,\ell,1) - v_2^1 v_3^2 g(\mathrm{s},\lambda_2,x,\ell,1)\right] \end{aligned} \tag{A.15}$$

with

$$g(\mathrm{s},\lambda,x,\ell,a) = \frac{\left(\mathrm{e}^{-s\lambda x} - a\,\mathrm{e}^{-\mathrm{s}\lambda(2\ell-x)}\right)}{\left(1+\mathrm{e}^{-2\mathrm{s}\lambda\ell}\right)},$$

where the real factor $a = \pm 1$ is introduced to handle the changing sign. To obtain the corresponding stress $\hat{\sigma}^{\mathrm{tot}}(x,\mathrm{s})$ and flux $\hat{q}(x,\mathrm{s})$, the solid displacement, the pore pressure, and the relative displacement have to be inserted into the constitutive equations (A.13) and (A.14). Taking a closer look on the Eigenvalues (complex roots) λ_i, one can observe that they are the inverse of the compressional wave velocities of the poroelastic media (see also section 2.2.7), i.e., $c_i = 1/\lambda_i$ with $i = 1,2$.

Accordingly, the solution consists of four superimposed compressional waves. Two waves are traveling with the wave speeds c_1, c_2 in positive x-direction and the other two are trav-

eling into the negative x-direction. Thus, in each direction a fast and a slow compressional wave with wave speed c_1 and c_2, respectively, can be observed.

To obtain a solution in time domain an inverse Laplace transformation has to be applied. A analytic Laplace transformation of solution (A.15) is not possible since the factor β is dependent on the Laplace parameter s and, consequently, the eigenvalues λ_i, the Eigenvectors $\mathbf{v}^i$, and h_i. Several methods exist in the literature and a comparison of different methods is given for example by Cheng et al. [49]. For the case that one function of the convolution integral (A.2) is given in Laplace domain only and the other one is given in time domain, than the convolution quadrature method, presented in section 3.3.2, is preferable to take.

A.4 Analytic solution of an infinite poroelastic column

Analytic solution of the full form u, p, w As shown in section 4.3.1, the general ansatz of the solution of an infinite poroelastic column reads as

$$\begin{bmatrix} \hat{u}(x,\mathrm{s}) \\ \hat{p}(x,\mathrm{s}) \\ \hat{w}(x,\mathrm{s}) \end{bmatrix} = C_3 \begin{bmatrix} v_1^3 \\ v_2^3 \\ v_3^3 \end{bmatrix} \mathrm{e}^{-\mathrm{s}\lambda_1 x} + C_4 \begin{bmatrix} v_1^4 \\ v_2^4 \\ v_3^4 \end{bmatrix} \mathrm{e}^{-\mathrm{s}\lambda_2 x} , \tag{A.16}$$

with the Eigenvectors defined in (A.12) and the Eigenvalues λ_1 and λ_2 from (A.10). The constants C_3 and C_4 are calculated in the same way as for the finite column with the exception that in this case only prescribed boundary conditions on the top of the infinite column are possible. The assumed boundary conditions

$$\hat{p}(0,\mathrm{s}) = 0 , \qquad \hat{\sigma}^{\mathrm{tot}}(0,\mathrm{s}) = -\hat{\sigma}_0^{\mathrm{tot}} , \tag{A.17}$$

yield the constants

$$C_3 = \frac{v_2^4 \hat{\sigma}_0^{\mathrm{tot}}}{(K+\frac{4}{3}G)\mathrm{s}(v_1^3 v_2^4 \lambda_1 - v_v^3 v_1^4 \lambda_2)} , \qquad C_4 = \frac{v_2^3 \hat{\sigma}_0^{\mathrm{tot}}}{(K+\frac{4}{3}G)\mathrm{s}(v_1^3 v_2^4 \lambda_1 - v_v^3 v_1^4 \lambda_2)} . \tag{A.18}$$

Note that in the case of the infinite column the total stress is given by

$$\hat{\sigma}^{\mathrm{tot}}(x,\mathrm{s}) = (K+\tfrac{4}{3}G)\hat{u}_{,x}(x,\mathrm{s}) - \alpha\hat{p}(x,\mathrm{s}) = \mathrm{s}(K+\tfrac{4}{3}G)\sum_{i=3}^{4} \lambda_i C_i \mathrm{e}^{s\lambda_i x} v_1^i - \alpha\hat{p}(x,\mathrm{s}) \tag{A.19}$$

and the flux by

$$\begin{aligned} \hat{q}(x,\mathrm{s}) &= -\kappa \left[\hat{p}_{,x}(x,\mathrm{s}) + \frac{\mathrm{s}^2}{\phi^2} \left(\phi\varrho_f + \varrho_a \right) \hat{w}(x,\mathrm{s}) + \varrho_f \mathrm{s}^2 \hat{u}(x,\mathrm{s}) \right] \\ &= \sum_{i=3}^{4} \underbrace{\frac{\mathrm{s}\kappa \left(R\alpha {\lambda_i}^2 - \varrho_f \phi^2 \right) \left[\mathrm{s}\varrho_f \phi^2 - \beta(\varrho_a + \varrho_f \phi) \right]}{\varrho_f \phi^4 - R\beta {\lambda_i}^2 \phi^2}}_{=:h_i} C_i \mathrm{e}^{\mathrm{s}\lambda_i x} . \end{aligned} \tag{A.20}$$

Note that in the equations (A.19) and (A.20) the relation $\lambda_3 = -\lambda_1$ is used to obtain a more compressed form.

Analytic solution of the simplified u, p model The analytical one-dimensional solution of the simplified poroelastic model presented in section 2.2.4 can be found in the work of Nenning and Schanz [105]. Thus, only the final result will be given here. Corresponding to the governing equations (2.29)-(2.31) the analytical solution in Laplace domain of an infinite column is given by

$$\begin{bmatrix} \hat{u}(x,\mathrm{s}) \\ \hat{p}(x,\mathrm{s}) \end{bmatrix} = C_3 \begin{bmatrix} v_1^3 \\ v_2^3 \end{bmatrix} \mathrm{e}^{-\mathrm{s}\lambda_1 x} + C_4 \begin{bmatrix} v_1^4 \\ v_2^4 \end{bmatrix} \mathrm{e}^{-\mathrm{s}\lambda_2 x} \ . \tag{A.21}$$

The Eigenvalues λ_i are the inverse of the compressional wave speeds, which are defined in (2.44), thus, $\lambda_i = {}^1/_{c_i}$ holds. The corresponding Eigenvectors are defined as

$$\mathbf{v}^i = \begin{bmatrix} 1 \\ \frac{(K+\frac{4}{3}G)\mathrm{s}\lambda_i^2 - \mathrm{s}\varrho}{\alpha\lambda_i} \end{bmatrix} = \begin{bmatrix} v_1^i \\ v_2^i \end{bmatrix} . \tag{A.22}$$

Assuming the prescribe boundary conditions of (A.17) yields the constants (A.18) with the components of the Eigenvectors (A.22). Whereas the stress is also given by equation (A.19), the flux is for the simplified model given by

$$\begin{aligned} \hat{q}(x,\mathrm{s}) &= -\kappa \left[\hat{p}_{,x}(x,\mathrm{s}) + \varrho_f \mathrm{s}^2 \hat{u}(x,\mathrm{s}) \right] = -\kappa \left[\sum_{i=3}^{4} \mathrm{s}\lambda_i C_i \, \mathrm{e}^{\mathrm{s}\lambda_i x} \, v_2^i + \varrho_f \mathrm{s}^2 \sum_{i=1}^{4} C_i \, \mathrm{e}^{\mathrm{s}\lambda_i x} \, v_1^i \right] \\ &= \sum_{i=3}^{4} \frac{\mathrm{s}^2 \kappa \left(\varrho - \alpha\varrho_f - (K+\frac{4}{3}G)\lambda_i^2 \right)}{\alpha} C_i \, \mathrm{e}^{\mathrm{s}\lambda_i x} \ . \end{aligned} \tag{A.23}$$

Again, in equation (A.23) the relation $\lambda_3 = -\lambda_1$ is used.

REFERENCES

[1] J. D. Achenbach. *Wave propagation in elastic solids*. North-Holland, 2005.

[2] T. Akiyoshi, K. Fuchida, and H. L. Fang. Absorbing boundary conditions for dynamic analysis of fluid-saturated porous media. *Soil Dynamics and Earthquake Engineering*, 13:387–397, 1994.

[3] T. Akiyoshi, X. Sun, and K. Fuchida. General absorbing boundary conditions for dynamic analysis of fluid-saturated porous media. *Soil Dynamics and Earthquake Engineering*, 17:397–406, 1998.

[4] B. Albers. Modelling of surface waves in poroelastic saturated materials by means of a two component continuum. Lecture notes, July 2004.

[5] J. Altenbach and H. Altenbach. *Einführung in die Kontinuumsmechanik*. B. G. Teubner Stuttgart, 1994.

[6] D. E. Amos. Algorithms 683: A portable FORTRAN subroutine for exponential integrals of a complex argument. *ACM Transactions on Mathematical Software*, 16 (2):178–182, 1990.

[7] D. E. Amos. Computation of exponential integrals of a complex argument. *ACM Transactions on Mathematical Software*, 16(2):169–177, 1990.

[8] C. Ashcraft and R. Grimes. SPOOLES: An object-oriented sparse matrix library. In *Proceedings of the ninth SIAM Conference on Parallel Processing for Scientific Computing*, page 10. Citeseer, 1999.

[9] H. G. Askar. Infinite elements for ground freezing problems. *Journal of Engineering Mechanics ASCE*, 110(2):157–172, 1984.

[10] R. J. Astley. Infinite elements for wave problems: a review of current formulations and an assessment of accuracy. *International Journal for Numerical Methods in Engineering*, 49:951–976, 2000.

[11] R. J. Astley and J.-P. Coyette. Conditioning of infinite element schemes for wave problems. *Communications in Numerical Methods in Engineering*, 17:31–41, 2001.

[12] R. J. Astley, J.-P. Coyette, and L. Cremers. Three-dimensional wave-envelope elements of variable order for acoustic radiation and scattering. Part II: Formulation in the time domain. *Journal of the Acoustical Society of America*, 103(1):64–72, 1998.

[13] R. J. Astley, G. J. Macaulay, J.-P. Coyette, and L. Cremers. Three-dimensional wave-envelope elements of variable order for acoustic radiation and scattering. Part I: Formulation in the frequency domain. *Journal of the Acoustical Society of America*, 103(1):49–63, 1998.

[14] J-L. Auriault, L. Borne, and R. Chambon. Dynamics of porous saturated media, checking of the generalized law of Darcy. *Journal of the Acoustical Society of America*, 77:1641–1650, 1985.

[15] I. Babuška. Error-bounds for finite element method. *Numerische Mathematik*, 16 (4):322–333, 1971.

[16] I. Babuška. The finite element method with Lagrangian multipliers. *Numerische Mathematik*, 20(3):179–192, 1973.

[17] S. Balay, K. Buschelman, W. D. Gropp, D. Kaushik, M. G. Knepley, L. C. McInnes, B. F. Smith, and H. Zhang. PETSc Web page, 2009. `http://www.mcs.anl.gov/petsc`.

[18] L. Banjai and S. Sauter. Rapid solution of the wave equation in unbounded domains. *Journal of Numerical Analysis, SIAM*, 47(1):227–249, 2008.

[19] U. Basu. Explicit finite element perfectly matched layer for transient three-dimensional elastic waves. *International Journal for Numerical Methods in Engineering*, 77(2):151–176, 2009.

[20] U. Basu and A. K. Chopra. Perfectly matched layers for time-harmonic elastodynamics of unbounded domains: theory and finite-element implementation. *Computer Methods in Applied Mechanics and Engineering*, 192:1337–1375, 2003.

[21] U. Basu and A. K. Chopra. Perfectly matched layers for transient elastodynamics of unbounded domains. *International Journal for Numerical Methods in Engineering*, 59:1039–1074, 2004.

[22] K.-J. Bathe. *Finite-Elemente Methoden*. 2., vollständig neu bearbeitete und erweiterte Auflage. Springer-Verlag, 2002.

[23] A. Bayliss and E. Turkel. Radiation boundary conditions for wave-like equations. *Communications on Pure and Applied Mathematics*, 33(6):707–725, 1980.

[24] W. Becker and D. Gross. *Mechanik elastischer Körper und Strukturen*. Springer-Verlag Berlin Heidelberg New York, 2002.

[25] G. Beer. Discussion of ref. [32](and author's reply). *Engineering Computations*, 1: 290–292, 1984.

[26] G. Beer and J. L. Meek. Infinite domain elements. *International Journal for Numerical Methods in Engineering*, 17(1):43–52, 1981.

[27] T. Belytschko, H. J. Yen, and R. Mullen. Mixed methods for time integration. *Computer Methods in Applied Mechanics and Engineering*, 17(18):259–275, 1979.

[28] T. Belytschko, P. Smolinski, and W. K. Liu. Stability of multi-time step partitioned integrators for first-order finite element systems. *Computer Methods in Applied Mechanics and Engineering*, 49(3):281–297, 1985.

[29] J.-P. Berenger. A perfectly matched layer for the absorption of electromagnetic waves. *Journal of Computational Physics*, 114:185–200, 1994.

[30] J. G. Berryman. Confirmation of Biot's theory. *Applied Physics Letters*, 37(4): 382–384, 1980.

[31] P. Bettess. *Infinite Elements*. Penshaw Press, Sunderland, 1992.

[32] P. Bettess and J. A. Bettess. Infinite elements for static problems. *Engineering Computations*, 1:4–16, 1984.

[33] P. Bettess and O. C. Zienkiewicz. Diffraction and refraction of surface waves using finite and infinite elements. *International Journal for Numerical Methods in Engineering*, 11(8):1271–1290, 1977.

[34] M. A. Biot. General Theory of Three-Dimensional Consolidation. *Journal of Applied Physics*, 12:155–164, 1941.

[35] M. A. Biot. Theory of Elasticity and Consolidation for a Porous Anisotropic Solid. *Journal of Applied Physics*, 26:182–185, 1955.

[36] M. A. Biot. Theory of Propagation of Elastic Waves in a Fluid-Saturated Porous Solid. II. Higher-Frequency-Range. *Journal of the Acoustical Society of America*, 28(2):179–191, 1956.

[37] M. A. Biot. Theory of Propagation of Elastic Waves in a Fluid-Saturated Porous Solid. I. Low-Frequency-Range. *Journal of the Acoustical Society of America*, 28 (2):168–178, 1956.

[38] G. Bonnet. Basic Singular Solutions for a Poroelastic Medium in the Dynamic Range. *Journal of the Acoustical Society of America*, 82(5):1758–1762, 1987.

[39] G. Bonnet and J.-L. Auriault. Dynamics of saturated and deformable porous media: Homogenization theory and determination of the solid-liquid coupling coefficients. *Physics of Finely Divided Matter*, pages 306–316, 1985.

[40] M. Bonnet. Boundary integral equation methods for solids and fluids, 1995.

[41] R. M. Bowen. Incompressible porous media models by use of the theory of mixtures. *International Journal of Engineering Science*, 18:1129–1148, 1980.

[42] R. M. Bowen. Compressible porous media models by use of the theory of mixtures. *International Journal of Engineering Science*, 20:697–735, 1982.

[43] D. Braess. *Finite Elemente*. Springer Berlin Heidelberg New York, vierte, überarbeitete und erweiterte Auflage, 2007.

[44] F. Brezzi. On the existence, uniqueness and approximation of saddle-point problems arising from Lagrangian multipliers. *RAIRO Anal. Numer*, 8(2):129–151, 1974.

[45] F. Brezzi and M. Fortin. *Mixed and hybrid finite element methods*. Springer Series in Computational Mathematics. Springer-Verlag, New York Inc., 1991.

[46] E. O. Brigham. FFT, Schnelle Fourier Transformation, 3. Auflage, 1987.

[47] P. J. Brown, S. Dey-Sakar, M. Batzle, E. Tang, G. McMechan, G. Steensma, and M. Peeters. Biot slow wave laboratory detection and seismic response. Accepted by the EAGE/SEG Research Workshop, Pau, France, 2001.

[48] J. Chen and G. F. Dargush. Boundary Element Method for Dynamic Poroelastic and Thermoelastic Analysis. *International Journal of Solids and Structures*, 32 (15):2257–2278, 1995.

[49] A. H. D. Cheng, P. Sidauruk, and Y. Abousleiman. Approximate inversion of the Laplace transform. *The Mathematica Journal*, 4(2):76–82, 1994.

[50] W. C. Chew, J.M. Jin, and E. Michielssen. Complex coordinate stretching as a generalized absorbing boundary condition. *Microwave and Optical Technology Letters*, 15(6):363–369, 1997.

[51] A. K. Chopra. *Dynamics of structures–Theory and applications to earthquake engineering*. Prentice–Hall, second edition, 2001.

[52] Y. K. Chow and I. M. Smith. Static and periodic infinite solid elements. *International Journal for Numerical Methods in Engineering*, 17:503–526, 1981.

[53] Z. Chuhan and Z. Chongbin. Coupling method of finite and infinite elements for strip foundation wave problems. *Earthquake Engineering and Structural Dynamics*, 15:839–851, 1987.

[54] J. Cipolla. Acoustic infinite elements with improved robustness. In *Proceedings of ISMA 2002*, pages 2181–2187. P. Sas and B. Van Hal, Katholieke Universiteit Leuven, 2002.

[55] R. D. Cook, D. S. Malkus, M. E. Plesha, and R. J. Witt. *Concepts and Applications of Finite Element Analysis*. John Wiley & Sons. Inc., fourth edition, 2001.

[56] R. Courant, K. Friedrichs, and H. Lewy. Über die partiellen Differenzengleichungen der mathematischen Physik. *Mathematische Annalen*, 100:32–74, 1928.

[57] P. J. Davis and P. Rabinowitz. Methods of numerical integration, 1984.

[58] R. de Boer. *Theory of Porous Media*. Springer-Verlag, Berlin, 2000.

[59] R. de Boer and W. Ehlers. Theorie der Mehrkomponentenkontinua mit Anwendungen auf bodenmechanische Probleme. Forschungsbericht aus dem Fachbereich Bauwesen, Heft 40, Universität - GH Essen, 1986.

[60] E. Detournay and A. H.-D. Cheng. *Fundamentals of Poroelasticity*, volume 2 of *Comprehensive Rock Engineering: Principles, Practice & Projects*. Pergamon Press, 1993.

[61] G. Doetsch. *Anleitung zum praktischen Gebrauch der Laplace-Transformation und der Z-Transformation*. R. Oldenbourg Verlag, München, Wien, 6. Auflage, 1989.

[62] D. Dreyer. *Efficient infinite elements for exterior acoustics*. PhD thesis, Technische Universität Hamburg-Harburg, 2004.

[63] D. Dreyer and O. von Estorff. Improved conditioning of infinite elements for exterior acoustics. *International Journal for Numerical Methods in Engineering*, 58(6): 933–953, 2003.

[64] D. Dreyer, S. Petersen, and O. von Estorff. Effectiveness and robustness of improved infinite elements for exterior acoustics. *Computer Methods in Applied Mechanics and Engineering*, 195:3591–3607, 2006.

[65] F. Durbin. Numerical inversion of Laplace transforms: an effcient improvement to Dubner and Abate's method. *The Computer Journal*, 17(4):371–376, 1974.

[66] W. Ehlers. Poröse Medien – ein kontinuumsmechanisches Modell auf der Basis der Mischungstheorie. Forschungsbericht aus dem Fachbereich Bauwesen 47, Universität - GH Essen, 1989.

[67] W. Ehlers. Grundlegende Konzepte in der Theorie Poröser Medien. *Technische Mechanik*, 16(1):63–76, 1996.

[68] C. Emson and P. Bettess. Application of infinite elements to external electromagnetic field problems. In *Proc. Int. Conf. Num. Meth. Coupled Problems, E. Hinton et al. (eds), Pineridge Press*, pages 887–902, 1981.

[69] B. Engquist and A. Majda. Absorbing boundary conditions for numerical simulation of waves. *Math. Comp.*, 31:629–652, 1977.

[70] B. Engquist and A. Majda. Radiation boundary conditions for acoustic and elastic wave calculations. *Communications on Pure and Applied Mathematics*, 32:313–357, 1979.

[71] G. Feltrin. *Absorbing boundaries for the time-domain analysis of dam-reservoir-foundation systems*. Birkhäuser, 1997.

[72] A. Gajo, A. Saetta, and R. Vitaliani. Evaluation of three- and two-field finite element methods for the dynamic response of saturated soil. *International Journal for Numerical Methods in Engineering*, 37(7):1231–1247, 1994.

[73] L. Gaul, M. Kögl, and M. Wagner. *Boundary Element Methods for Engineers and Scientists*. Springer-Verlag Berlin Heidelberg, 2003.

[74] K. Gerdes. The conjugated vs. the unconjugated infinite element method for the Helmholtz equation in exterior domains. *Computer Methods in Applied Mechanics and Engineering*, 152:125–145, 1998.

[75] D. Givoli. Non-reflecting boundary conditions. *Journal of Computational Physics*, 94:1–29, 1991.

[76] D. Givoli. Numerical methods for problems in infinite domains. *Studies in Applied Mechanics*, Elsevier, 1992.

[77] D. Givoli and J. B. Keller. A finite element method for large domains. *Computer Methods in Applied Mechanics and Engineering*, 76(1):41–66, 1989.

[78] D. Givoli, I. Patlashenko, and J. B. Keller. High-order boundary conditions and finite elements for infinite domains. *Computer Methods in Applied Mechanics and Engineering*, 143:13–39, 1997.

[79] K. F. Graff. *Wave Motion in Elastic Solids*. Oxford University Press, 1975.

[80] C. Hagen. *Wechselwirkungen zwischen Bauwerk, Boden und Fluid unter transienter Belastung*. PhD thesis, Technischen Universität Hamburg-Harburg, 2005.

[81] E. R. Hughes, T. G. Leighton, G. W. Petley, P. R. White, and R. C. Chivers. Estimation of critical and viscous frequencies for Biot theory in cancellus bone. *Ultrasonics*, 41(5):365–368, 2003.

[82] T. J. R. Hughes. *The Finite Element Method: Linear, Static and Dynamic Finite Element Analysis*. Dover Publications - Mineola, New York, 2000.

[83] D. L. Johnson, J. Koplik, and R. Dashen. Theory of dynamic permeability and tortuosity in fluid-saturated porous media. *Journal of Fluid Mechanics*, 176:379–402, 1987.

[84] M. Jung and U. Langer. *Methode der finiten Elemente für Ingenieure*. 1. Auflage. B. G. Teubner GmbH, Stuttgart/Leipzig/Wiesbaden, 2001.

[85] J. B. Keller and D. Givoli. Exact non-reflecting boundary conditions. *Journal of Computational Physics*, 82(1):172–192, 1989.

[86] N. Khalili, S. Valliappan, J. T. Yazdi, and M. Yazdchi. 1D infinite element for dynamic problems in saturated porous media. *Communications in Numerical Methods in Engineering*, 13(9):727–738, 1997.

[87] N. Khalili, M. Yazdchi, and S. Valliappan. Wave propagation analysis of two-phase saturated porous media using coupled finite-infinite element method. *Soil Dynamics and Earthquake Engineering*, 18:533–553, 1999.

[88] L. Kielhorn. Modellierung von Wellenausbreitung in porösen Böden: Dimensionslose Variablen für eine Randelementformulierung. Diplomarbeit, Institut für angewandte Mechanik - Technische Universität Braunschweig, 2004.

[89] S.-H. Kim, K.-J. Kim, and S. E. Blouin. Analysis of wave propagation in saturated porous media. I. Theoretical solution. *Computer Methods in Applied Mechanics and Engineering*, 191:4061–4073, 2002.

[90] S.-H. Kim, K.-J. Kim, and S. E. Blouin. Analysis of wave propagation in saturated porous media. II. Parametric studies. *Computer Methods in Applied Mechanics and Engineering*, 191:4075–4091, 2002.

[91] Y. K. Kim and H. B. Kingsbury. Dynamic characterization of poroelastic materials. *Experimental Mechanics*, 19(7):252–258, 1979.

[92] B. Kirk, J. W. Peterson, R. H. Stogner, and G. F. Carey. `libMesh`: A c++ library for parallel adaptive mesh refinement/coarsening simulations. *Engineering with Computers*, 22(3–4):237–254, 2006. `http://dx.doi.org/10.1007/s00366-006-0049-3`.

[93] J. Korsawe, G. Starke, W. Wang, and O. Kolditz. Finite element analysis of poroelastic consolidation in porous media: Standard and mixed approaches. *Computer Methods in Applied Mechanics and Engineering*, 195:1096–1115, 2006.

[94] R. S. Lakes and R. Witt. Making and characterizing negative Poisson's ratio materials. *International Journal of Mechanical Engineering Education*, 30:50–58, 2002.

[95] R. W. Lewis and B. A. Schrefler. *The Finite Element Method in the Static and Dynamic Deformation and Consolidation of Porous Media*. John Wiley and Sons, Chichester, 1998.

[96] C. Lubich. Convolution quadrature and discretized operational calculus I. *Numerische Mathematik*, 52:129–145, 1988.

[97] C. Lubich. Convolution quadrature and discretized operational calculus II. *Numerische Mathematik*, 52:413–425, 1988.

[98] J. Lysmer and R. L. Kuhlemeyer. Finite dynamic model for infinite media. In *Proceedings of the American Society of Civil Engineers (ASCE)*, pages 859–877, 1969.

[99] J. M. M. C. Marques and D. R. J. Owen. Infinite elements in quasi-static materially nonlinear problems. *Computers & Structures*, 18(4):739–751, 1984.

[100] F. Medina and J. Penzien. Infinite elements for elastodynamics. *Earthquake Engineering and Structural Dynamics*, 10:699–709, 1982.

[101] F. Medina and R. L. Taylor. Finite element techniques for problems of unbounded domains. *International Journal for Numerical Methods in Engineering*, 19:1209–1226, 1983.

[102] M. Messner and M. Schanz. A Regularized Collocation Boundary Element Method for Linear Poroelasticity. preprint No. 03/2010, `http://www.mech.tugraz.at/preprints`.

[103] W. Moser. *Transient coupled BEM–BEM and BEM-FEM analyses*. Monographic Series TU Graz: Structural Analysis. Verlag der Technischen Universität Graz, 2006.

[104] M. A. Murad and A. F. D. Loula. On stability and convergence of finite element approximations of Biot's consolidation problem. *International Journal for Numerical Methods in Engineering*, 37(4):645–667, 1944.

[105] M. Nenning and M. Schanz. Infinite elements in a poroelastodynamic FEM. preprint No. 02/2010, `http://www.mech.tugraz.at/preprints`.

[106] N. M. Newmark. A method of computation for structural dynamics. *JEMD*, 85: 67–93, 1959.

[107] A. Nur and J. D. Byerlee. An Exact Effective Stress Law for Elastic Deformation of Rock with Fluids. *Journal of Geophysical Research*, 76(26):6414–6419, 1971.

[108] C. L. Pekeris. The seismic surface pulse. *Proceedings of the National American Society*, 41:469–480, 1955.

[109] T. Pinto and J.-P. Coyette. Conjugated infinite elements for two-dimensional time-harmonic elastodynamics. *Journal of Computational Acoustics*, 8(3):473–493, 2000.

[110] T. J. Plona. Observation of a second bulk compressional wave in porous medium at ultrasonic frequencies. *Applied Physics Letters*, 36(4):259–261, 1980.

[111] R. Rajapakse and P. Karasudhi. An efficient elastodynamic infinite element. *International Journal of Solids and Structures*, 22(6):643–657, 1986.

[112] N. Ravichandran. *A framework-based finite element approach for solving large deformation problems in multi-phase porous media*. PhD thesis, University of Oklahoma, 2005.

[113] J. W. S. Rayleigh. On waves propagated along the plane surface of an elastic solid. *Proceedings of the London mathematical Society*, 17:4–11, 1887.

[114] B. D. Reddy. *Introductory Functional Analysis*, volume 27 of *Texts in Applied Mathematics*. Springer, New York, 1998.

[115] T. Ribeiro. *Elastoplastic Boundary Element Analysis with Adaptive Cell Generation*. Monographic Series TU Graz, 2006.

[116] W. Ritz. Über eine neue Methode zur Lösung gewisser Variationsprobleme der mathematischen Physik. *JRAM*, 135:1–61, 1908.

[117] S. Rjasanow and O. Steinbach. The fast solution of boundary integral equations. Mathematical and Analytical Techniques with Applications to Engineering, 2007.

[118] T. Rüberg. *Non-conforming FEM/BEM Coupling in Time Domain*, volume 3 of *Monographic Series TU Graz: Computation in Engineering and Science*. Verlag der Technischen Universität Graz, 2008.

[119] Y. Saad and M. H. Schultz. GMRES: A generalized minimal residual algorithm for solving nonsymmetric linear systems. *SIAM Journal on Scientific and Statistical Computing*, 7(3):856–869, 1986.

[120] Z. S. Sacks, D. M. Kingsland, R. Lee, and J. F. Lee. A perfectly matched anisotropic absorber for use as an absorbing boundary condition. *IEEE Antennas and Propagation Society magazine*, 43(12):1460–1463, 1995.

[121] M. Schanz. Eine Randelementformulierung im Zeitbereich mit verallgemeinerten viskoelastischen Stoffgesetzen. *Bericht aus dem Institut A für Mechanik*, 1, 1994.

[122] M. Schanz. Allgemeine numerische Methoden. Vorlesungsmanuskript, Technische Universität Braunschweig – Institut für Angewandte Mechanik, 2000.

[123] M. Schanz. *Wave Propagation in Viscoelastic and Poroelastic Continua: A Boundary Element Approach*, volume 2 of *Lecture Notes in Applied Mechanics*. Springer-Verlag, Berlin, Heidelberg, New York, 2001.

[124] M. Schanz and A. H.-D. Cheng. Transient wave propagation in a one-dimensional poroelastic column. *Acta Mechanica*, 145(1-4):1–18, 2000.

[125] M. Schanz and S. Diebels. A comparative study of Biot's theory and the linear Theory of Porous Media for wave propagation problems. *Acta Mechanica*, 161 (3-4):213–235, 2003.

[126] M. Schanz and D. Pryl. Dynamic fundamental solutions for compressible and incompressible modeled poroelastic continua. *International Journal of Solids and Structures*, 41(15):4047–4073, 2004.

[127] B. R. Simon, J. S.-S. Wu, and O. C. Zienkiewicz. Evaluation of higher order, mixed and hermitean finite element procedures for dynamic analysis of saturated porous media using one-dimensional models. *International Journal for Numerical and Analytical Methods in Geomechanics*, 10(5):483–499, 1986.

[128] B. R. Simon, J. S.-S. Wu, O. C. Zienkiewicz, and D. K. Paul. Evaluation of $u-w$ and $u-\pi$ finite element methods for the dynamic response of saturated porous media using one-dimensional models. *International Journal for Numerical and Analytical Methods in Geomechanics*, 10(5):461–482, 1986.

[129] L. Simoni and B. A. Schrefler. Mapped infinite elements in soil consolidation. *International Journal for Numerical Methods in Engineering*, 24:513–527, 1987.

[130] A. Sommerfeld. Die Greensche Funktion der Schwingungsgleichung. *Jahresbericht der Deutschen Mathematiker-Vereinigung*, 21:309–352, 1912.

[131] A. Sommerfeld. *Partial Differential Equations in Physics: lecture on theoretical physics*. Academic Press, New York, 1949.

[132] A. Sommerfeld. *Mechanik der deformierbaren Medien*, volume 2 of *Vorlesungen über theoretische Physik*. Akademische Verlagsgesellschaft Geest & Portig K.-G., Leipzig, 1957.

[133] O. Steinbach. *Stability estimates for hybrid coupled domain decomposition methods*. Springer-Verlag New York Inc, 2003.

[134] O. Steinbach. *Numerische Näherungsverfahren für elliptische Randwertprobleme: Finite Elemente und Randelemente*. Vieweg+Teubner Verlag, 2003.

[135] G. Strang and G. J. Fix. *An Analysis of the Finite Element Method*. Prentice-Hall, Inc., Englewood Cliffs, N. J., 1997.

[136] A. H. Stroud. *Numerical quadrature and solution of ordinary differential equations: a textbook for a beginning course in numerical analysis*. Springer, 1974.

[137] J. M. Sullivan Jr. and K. O'Neill. Application of infinite elements to phase change situations on deforming meshes. *International Journal for Numerical Methods in Engineering*, 33(9):1861–1874, 1992.

[138] B. Szabó and I. Babuška. *Finite Element Analysis*. John Wiley & Sons. Inc., New York, 1991.

[139] A. Toselli and O. B. Widlund. *Domain decomposition methods–algorithms and theory*. Springer Verlag, 2005.

[140] R. F. Ungless. An infinite finite element. *MA Sc Thesis, University of British Columbia*, 1973.

[141] O. von Estorff and M. Firuziaan. Nonlinear dynamic response by coupling BEM and FEM. *Engineering Analysis with Boundary Elements*, 24(10):715–725, 2000.

[142] K. von Terzaghi. Die Berechnung der Durchlässigkeit des Tones aus dem Verlauf der hydromechanischen Spannungserscheinungen. *Sitzungsbericht der Akademie der Wissenschaften (Wien): Mathematisch–Naturwissenschaftlichen Klasse*, 132: 125–138, 1923.

[143] E. W. Weisstein. Exponential Integral. *From MathWorld–A Wolfram Web Resource.* `http://mathworld.wolfram.com/ExponentialIntegral.html` and `http://functions.wolfram.com/GammaBetaErf/ExpIntegralEi`.

[144] K. Wilmanski. Porous Media at Finite Strains. The New Model With the Balance Equation for Porosity. *Archives of Mechanics*, 48(4):591–628, 1996.

[145] K. Wilmanski. A few remarks on Biot's model and linear acoustics of poroelastic saturated materials. *Soil Dynamics and Earthquake Engineering*, 26:509–536, 2005.

[146] Wolfram Research, Inc. *Mathematica, Version 6.0*. Champaign, Illinois, 2007.

[147] J. Yang. A note on Rayleigh wave velocity in saturated soils with compressible constituents. *Canadian Geotechnical Journal*, 38(6):1360–1365, 2001.

[148] Y.-B. Yang, S.-R. Kuo, and H.-H. Hung. Frequency-independent infinite elements for analysing semi-infinite problems. *International Journal for Numerical Methods in Engineering*, 39:3553–3569, 1996.

[149] H. R. Yerli, B. Temel, and E. Kiral. Transient infinite elements for 2d soil-structure interaction analysis. *Journal of Geotechnical and Geoenvironmental Engineering*, 124(10):976–988, 1998.

[150] C.-B. Yun, J.-M. Kim, and C.-H. Hyun. Axisymmetric elastodynamic infinite elements for multi-layered half-space. *International Journal for Numerical Methods in Engineering*, 38(22):3723–3743, 1995.

[151] Y. Q. Zeng, J. Q. He, and Q. H. Liu. The application of the perfectly matched layer in numerical modeling of wave propagation in poroelastic media. *Geophysics*, 66 (4):1258–1266, 2001.

[152] C. Zhao and S. Valliappan. A dynamic infinite element for three-dimensional infinite-domain wave problems. *International Journal for Numerical Methods in Engineering*, 36(15):2567–2580, 1993.

[153] C. Zhao and S. Valliappan. Transient infinite elements for contaminant transport problems. *International Journal for Numerical Methods in Engineering*, 37(7): 1143–1158, 1994.

[154] C.-B. Zhao, C.-H. Zhang, and G.-D. Zhang. Analysis of 3-d foundation wave problems by mapped dynamic infinite elements. *Science in China (Series A)*, 32(4): 479–491, 1989.

[155] Y. Zheng and X. Huang. Anisotropic Perfectly Matched Layers for Elastic Waves in Cartesian and Curvilinear Coordinates. Research report, Earth Resource Laboratory, Dept. of Earth, Atmospheric, and Planetary Sciences , Massachusetts Institute of Technology, 2002. URL `http://www-eaps.mit.edu/erl/research/report1/pdf2002/ZHENG.pdf`.

[156] O. C. Zienkiewicz. Basic formulation of static and dynamic behaviours of soil and other porous media. *Applied Mathematics and Mechanics*, 3(4):457–468, 1982.

[157] O. C. Zienkiewicz and P. Bettess. *Fluid Structure Interaction*, chapter 5. Numerical methods in offshore engineering. John Wiley, 1978.

[158] O. C. Zienkiewicz and T. Shiomi. Dynamic behaviour of saturated Porous Media; The generalized Biot Formulation and its Numerical Solution. *International Journal for Numerical and Analytical Methods in Geomechanics*, 8:71–96, 1984.

[159] O. C. Zienkiewicz and R. L. Taylor. *The Finite Element Method for Solid and Structural Mechanics*. Elsevier Butterworth-Heinemann, sixth edition edition, 2005.

[160] O. C. Zienkiewicz, C. T. Chang, and P. Bettess. Drained, undrained, consolidating and dynamic behavior assumptions in soils. *Geotechnique*, 30:385–395, 1980.

[161] O. C. Zienkiewicz, C. Emson, and P. Bettess. A novel boundary infinite element. *International Journal for Numerical Methods in Engineering*, 19(3):393–404, 1983.

[162] O. C. Zienkiewicz, K. Bando, P. Bettess, C. Emson, and T. C. Chiam. Mapped infinite elements for exterior wave problems. *International Journal for Numerical Methods in Engineering*, 21:1229–1251, 1985.

[163] O. C. Zienkiewicz, A. H. C. Chan, M. Pastor, D. K. Paul, and T. Shiomi. Static and dynamic behaviour of soils: A rational approach to quantitative solutions. I. fully saturated problems. *Proceedings of the Royal Society of London A, Mathematical and Physical Sciences*, 429(1877):285–309, 1990.

[164] O. C. Zienkiewicz, R. L. Taylor, and P. Nithiarasu. *The Finite Element Method for Fluid Dynamics*. Elsevier Butterworth-Heinemann, sixth edition edition, 2005.

[165] O. C. Zienkiewicz, R. L. Taylor, and J. Z. Zhu. *The Finite Element Method: Its Basis and Fundamentals*. Elsevier Butterworth-Heinemann, sixth edition edition, 2005.